



Ammonia-Based Energy Storage System for an Electrical Grid

A Design Study For Maui, HI, USA

Group 3

William Matthews

Enzia Schnyder

Lai Chong

Lewis Murray

Jing Yang

James Rhodes

April 23, 2018

Student Submission, University of Oxford
Engineering Science
Summer 2018
Third Year Project



DECLARATION OF AUTHORSHIP

You should complete this certificate. It should be bound into your third year project report, immediately after your title page. Three copies of the report should be submitted to the Chairman of examiners for your Honour School, c/o Clerk of the Schools, examination Schools, High Street, Oxford.

Name (in capitals):

College (in capitals): **Supervisor(s):**

Title of project (in capitals):

Page count (excluding risk and COSHH assessments):

Please tick to confirm the following:

I have read and understood the University's disciplinary regulations concerning conduct in examinations and, in particular, the regulations on plagiarism (*The University Student Handbook. The Proctors' and Assessors' Memorandum, Section 8.8*; available at <https://www.ox.ac.uk/students/academic/student-handbook>)

I have read and understood the Education Committee's information and guidance on academic good practice and plagiarism at <https://www.ox.ac.uk/students/academic/guidance/skills>.

The project report I am submitting is entirely my own work except where otherwise indicated.

It has not been submitted, either partially or in full, for another Honour School or qualification of this University (except where the Special Regulations for the subject permit this), or for a qualification at any other institution.

I have clearly indicated the presence of all material I have quoted from other sources, including any diagrams, charts, tables or graphs.

I have clearly indicated the presence of all paraphrased material with appropriate references.

I have acknowledged appropriately any assistance I have received in addition to that provided by my supervisor.

I have not copied from the work of any other candidate.

I have not used the services of any agency providing specimen, model or ghostwritten work in the preparation of this project report. (See also section 2.4 of Statute XI on University Discipline under which members of the University are prohibited from providing material of this nature for candidates in examinations at this University or elsewhere: <http://www.admin.ox.ac.uk/statutes/352-051a.shtml>.)

My contribution to the joint report does not exceed 30 pages (including all diagrams, photographs, references and appendices).

I agree to retain an electronic copy of this work until the publication of my final examination result, except where submission in hand-written format is permitted.

I agree to make any such electronic copy available to the examiners should it be necessary to confirm my word count or to check for plagiarism.

Candidate's signature: **Date:**

DECLARATION OF AUTHORSHIP

You should complete this certificate. It should be bound into your third year project report, immediately after your title page. Three copies of the report should be submitted to the Chairman of examiners for your Honour School, c/o Clerk of the Schools, examination Schools, High Street, Oxford.

Name (in capitals):

College (in capitals): **Supervisor(s):**

Title of project (in capitals):

Page count (excluding risk and COSHH assessments):

Please tick to confirm the following:

I have read and understood the University's disciplinary regulations concerning conduct in examinations and, in particular, the regulations on plagiarism (*The University Student Handbook. The Proctors' and Assessors' Memorandum, Section 8.8*; available at <https://www.ox.ac.uk/students/academic/student-handbook>)

I have read and understood the Education Committee's information and guidance on academic good practice and plagiarism at <https://www.ox.ac.uk/students/academic/guidance/skills>.

The project report I am submitting is entirely my own work except where otherwise indicated.

It has not been submitted, either partially or in full, for another Honour School or qualification of this University (except where the Special Regulations for the subject permit this), or for a qualification at any other institution.

I have clearly indicated the presence of all material I have quoted from other sources, including any diagrams, charts, tables or graphs.

I have clearly indicated the presence of all paraphrased material with appropriate references.

I have acknowledged appropriately any assistance I have received in addition to that provided by my supervisor.

I have not copied from the work of any other candidate.

I have not used the services of any agency providing specimen, model or ghostwritten work in the preparation of this project report. (See also section 2.4 of Statute XI on University Discipline under which members of the University are prohibited from providing material of this nature for candidates in examinations at this University or elsewhere: <http://www.admin.ox.ac.uk/statutes/352-051a.shtml>.)

My contribution to the joint report does not exceed 30 pages (including all diagrams, photographs, references and appendices).

I agree to retain an electronic copy of this work until the publication of my final examination result, except where submission in hand-written format is permitted.

I agree to make any such electronic copy available to the examiners should it be necessary to confirm my word count or to check for plagiarism.

Candidate's signature: **Date:**

DECLARATION OF AUTHORSHIP

You should complete this certificate. It should be bound into your third year project report, immediately after your title page. Three copies of the report should be submitted to the Chairman of examiners for your Honour School, c/o Clerk of the Schools, examination Schools, High Street, Oxford.

Name (in capitals):

College (in capitals): **Supervisor(s):**

Title of project (in capitals):

Page count (excluding risk and COSHH assessments):

Please tick to confirm the following:

I have read and understood the University's disciplinary regulations concerning conduct in examinations and, in particular, the regulations on plagiarism (*The University Student Handbook. The Proctors' and Assessors' Memorandum, Section 8.8*; available at <https://www.ox.ac.uk/students/academic/student-handbook>)

I have read and understood the Education Committee's information and guidance on academic good practice and plagiarism at <https://www.ox.ac.uk/students/academic/guidance/skills>.

The project report I am submitting is entirely my own work except where otherwise indicated.

It has not been submitted, either partially or in full, for another Honour School or qualification of this University (except where the Special Regulations for the subject permit this), or for a qualification at any other institution.

I have clearly indicated the presence of all material I have quoted from other sources, including any diagrams, charts, tables or graphs.

I have clearly indicated the presence of all paraphrased material with appropriate references.

I have acknowledged appropriately any assistance I have received in addition to that provided by my supervisor.

I have not copied from the work of any other candidate.

I have not used the services of any agency providing specimen, model or ghostwritten work in the preparation of this project report. (See also section 2.4 of Statute XI on University Discipline under which members of the University are prohibited from providing material of this nature for candidates in examinations at this University or elsewhere: <http://www.admin.ox.ac.uk/statutes/352-051a.shtml>.)

My contribution to the joint report does not exceed 30 pages (including all diagrams, photographs, references and appendices).

I agree to retain an electronic copy of this work until the publication of my final examination result, except where submission in hand-written format is permitted.

I agree to make any such electronic copy available to the examiners should it be necessary to confirm my word count or to check for plagiarism.

Candidate's signature: **Date:**

DECLARATION OF AUTHORSHIP

You should complete this certificate. It should be bound into your third year project report, immediately after your title page. Three copies of the report should be submitted to the Chairman of examiners for your Honour School, c/o Clerk of the Schools, examination Schools, High Street, Oxford.

Name (in capitals):

College (in capitals): **Supervisor(s):**

Title of project (in capitals):

Page count (excluding risk and COSHH assessments):

Please tick to confirm the following:

I have read and understood the University's disciplinary regulations concerning conduct in examinations and, in particular, the regulations on plagiarism (*The University Student Handbook. The Proctors' and Assessors' Memorandum, Section 8.8*; available at <https://www.ox.ac.uk/students/academic/student-handbook>)

I have read and understood the Education Committee's information and guidance on academic good practice and plagiarism at <https://www.ox.ac.uk/students/academic/guidance/skills>.

The project report I am submitting is entirely my own work except where otherwise indicated.

It has not been submitted, either partially or in full, for another Honour School or qualification of this University (except where the Special Regulations for the subject permit this), or for a qualification at any other institution.

I have clearly indicated the presence of all material I have quoted from other sources, including any diagrams, charts, tables or graphs.

I have clearly indicated the presence of all paraphrased material with appropriate references.

I have acknowledged appropriately any assistance I have received in addition to that provided by my supervisor.

I have not copied from the work of any other candidate.

I have not used the services of any agency providing specimen, model or ghostwritten work in the preparation of this project report. (See also section 2.4 of Statute XI on University Discipline under which members of the University are prohibited from providing material of this nature for candidates in examinations at this University or elsewhere: <http://www.admin.ox.ac.uk/statutes/352-051a.shtml>.)

My contribution to the joint report does not exceed 30 pages (including all diagrams, photographs, references and appendices).

I agree to retain an electronic copy of this work until the publication of my final examination result, except where submission in hand-written format is permitted.

I agree to make any such electronic copy available to the examiners should it be necessary to confirm my word count or to check for plagiarism.

Candidate's signature: **Date:**

DECLARATION OF AUTHORSHIP

You should complete this certificate. It should be bound into your third year project report, immediately after your title page. Three copies of the report should be submitted to the Chairman of examiners for your Honour School, c/o Clerk of the Schools, examination Schools, High Street, Oxford.

Name (in capitals):

College (in capitals): **Supervisor(s):**

Title of project (in capitals):

Page count (excluding risk and COSHH assessments):

Please tick to confirm the following:

I have read and understood the University's disciplinary regulations concerning conduct in examinations and, in particular, the regulations on plagiarism (*The University Student Handbook. The Proctors' and Assessors' Memorandum, Section 8.8*; available at <https://www.ox.ac.uk/students/academic/student-handbook>)

I have read and understood the Education Committee's information and guidance on academic good practice and plagiarism at <https://www.ox.ac.uk/students/academic/guidance/skills>.

The project report I am submitting is entirely my own work except where otherwise indicated.

It has not been submitted, either partially or in full, for another Honour School or qualification of this University (except where the Special Regulations for the subject permit this), or for a qualification at any other institution.

I have clearly indicated the presence of all material I have quoted from other sources, including any diagrams, charts, tables or graphs.

I have clearly indicated the presence of all paraphrased material with appropriate references.

I have acknowledged appropriately any assistance I have received in addition to that provided by my supervisor.

I have not copied from the work of any other candidate.

I have not used the services of any agency providing specimen, model or ghostwritten work in the preparation of this project report. (See also section 2.4 of Statute XI on University Discipline under which members of the University are prohibited from providing material of this nature for candidates in examinations at this University or elsewhere: <http://www.admin.ox.ac.uk/statutes/352-051a.shtml>.)

My contribution to the joint report does not exceed 30 pages (including all diagrams, photographs, references and appendices).

I agree to retain an electronic copy of this work until the publication of my final examination result, except where submission in hand-written format is permitted.

I agree to make any such electronic copy available to the examiners should it be necessary to confirm my word count or to check for plagiarism.

Candidate's signature: **Date:**

DECLARATION OF AUTHORSHIP

You should complete this certificate. It should be bound into your third year project report, immediately after your title page. Three copies of the report should be submitted to the Chairman of examiners for your Honour School, c/o Clerk of the Schools, examination Schools, High Street, Oxford.

Name (in capitals):

College (in capitals): **Supervisor(s):**

Title of project (in capitals):

Page count (excluding risk and COSHH assessments):

Please tick to confirm the following:

I have read and understood the University's disciplinary regulations concerning conduct in examinations and, in particular, the regulations on plagiarism (*The University Student Handbook. The Proctors' and Assessors' Memorandum, Section 8.8*; available at <https://www.ox.ac.uk/students/academic/student-handbook>)

I have read and understood the Education Committee's information and guidance on academic good practice and plagiarism at <https://www.ox.ac.uk/students/academic/guidance/skills>.

The project report I am submitting is entirely my own work except where otherwise indicated.

It has not been submitted, either partially or in full, for another Honour School or qualification of this University (except where the Special Regulations for the subject permit this), or for a qualification at any other institution.

I have clearly indicated the presence of all material I have quoted from other sources, including any diagrams, charts, tables or graphs.

I have clearly indicated the presence of all paraphrased material with appropriate references.

I have acknowledged appropriately any assistance I have received in addition to that provided by my supervisor.

I have not copied from the work of any other candidate.

I have not used the services of any agency providing specimen, model or ghostwritten work in the preparation of this project report. (See also section 2.4 of Statute XI on University Discipline under which members of the University are prohibited from providing material of this nature for candidates in examinations at this University or elsewhere: <http://www.admin.ox.ac.uk/statutes/352-051a.shtml>.)

My contribution to the joint report does not exceed 30 pages (including all diagrams, photographs, references and appendices).

I agree to retain an electronic copy of this work until the publication of my final examination result, except where submission in hand-written format is permitted.

I agree to make any such electronic copy available to the examiners should it be necessary to confirm my word count or to check for plagiarism.

Candidate's signature: **Date:**

Contents

1 Executive Summary	2	6.4 Sustainability and NO _x	98
2 Introduction	3	6.5 The Turbine Model	99
2.1 Outline	3	6.6 Turbine cycle modifications	103
2.2 What is an ESS?	3	6.7 Turbine Control	106
2.3 Location, and why implement an ESS?	3	6.8 PID Control	107
2.4 Project Aims	4	6.9 Turbine System Overview	111
2.5 Plant Structure	5	6.10 Safety & Risk	112
3 Air Separation	7	6.11 Costing	113
3.1 Introduction	7	6.12 Conclusions & Further Work	114
3.2 Plant Overview	8	7 Solid Oxide Fuel Cell System	115
3.3 Optimisation and Analysis	21	7.1 Introduction	115
3.4 Safety and Risk	30	7.2 Design Objectives	115
3.5 Sustainability	32	7.3 Operating Principles	115
3.6 Costing	32	7.4 Design Procedure	120
3.7 Conclusion & Further Work	32	7.5 Integrated Gas Turbine	125
4 Hydrogen Production	34	7.6 System Controller	129
4.1 Introduction	34	7.7 System Overview	132
4.2 Process Diagram	34	7.8 Cost Analysis	133
4.3 Dynamic System Response	36	7.9 Sustainability Analysis	133
4.4 Specification	36	7.10 Safety and Risk Analysis	134
4.5 Fundamentals	37	7.11 Further Considerations	134
4.6 Electrolyser Design	47	8 Heat Exchangers	136
4.7 Stack Number	53	8.1 Introduction	136
4.8 Thermal Model	53	8.2 Stream data	136
4.9 Electrolyser Control System	54	8.3 Design Problem	137
4.10 Hydrogen Storage	55	8.4 Pinch Design	138
4.11 System Simulation	57	8.5 Costing	140
4.12 Costing	58	8.6 Conclusion	140
4.13 Sustainability	60	9 Power Control and Plant Simulation	141
4.14 Safety	60	9.1 Introduction	141
4.15 Conclusion	62	9.2 Motivation	141
5 Ammonia Synthesis and Storage	65	9.3 Control Objectives	142
5.1 Introduction	65	9.4 System Dynamics	142
5.2 Review of Synthesis Methods	66	9.5 Plant Model in Simulink®	145
5.3 Thermodynamic Modelling	69	9.6 Plant Scaling	152
5.4 Mechanism and Kinetics	71	9.7 Plant-Controller Structure	152
5.5 Catalyst	74	9.8 PID Considerations	154
5.6 Reactor Design	75	9.9 LQR Problem Formulation	155
5.7 Additional Units	79	9.10 Controller and Plant Testing	158
5.8 Ammonia Storage	81	9.11 Secondary Controller - Virtual Inertia	161
5.9 Ammonia Cracker	83	9.12 Operation in Fail-States	162
5.10 Modelling, Optimising and Control	84	9.13 Risks and Challenges	162
5.11 Cost, Sustainability and Safety	86	9.14 Conclusion	164
5.12 Section Summary	89	10 Sustainability	165
6 Gas Turbine	93	11 Plant Safety	166
6.1 Introduction	93	12 Overall Financial Analysis	170
6.2 Gas Turbine Design	93	13 Conclusion	174
6.3 Limitations of Ammonia as a Fuel	95		

1 Executive Summary

This report provides an analysis and evaluation of the current and prospective sustainability, profitability and design requirements of an ammonia-based energy storage system for Maui, HI, USA. Methods of analysis include model simulation and validation, as well as plant costings and supply/demand matching. Other analysis include plant safety, sustainability as well as potential environmental impacts.

The report covers a range of current and emerging technologies and assesses their respective strengths and weaknesses. Currently, there is significant opportunity for the deployment of an energy storage system capable of meeting the island's 1.31 TWh annual demand whilst maintaining a profit margin of up to 64% at current energy prices. Total purchase cost is currently estimated to be \$6680 million.

The report finds that in order to best meet the initial criteria, the preferred design stages are the use of electrolysis to produce hydrogen and cryogenic air separation to produce nitrogen, using excess energy harvested from a wind farm. These can then be fed into an ammonia synthesis reactor producing liquid ammonia for storage. This in turn can be used to power a solid oxide fuel cell system and gas turbine to generate electricity on demand. The minimum lifetime of the plant is taken to be 25 years.

The report also investigates the limitations of the scope of the project when conducting analysis.

Some of the limitations include:

- The dependence on energy prices remaining high in Maui relative to the US average.
- The full environmental impact of the capital purchases have not been analysed.
- The decommissioning costs of the plant have not been considered.
- The impact of natural disasters beyond tropical storms have been excluded from the report.

2 Introduction

2.1 Outline

In this project a design draft of an ammonia-based Energy Storage System (ESS) is presented. The plant and wind farm have to power the island of Maui on its own, with no support from other generation units.

2.2 What is an ESS?

An Energy Storage System is a means of capturing excess energy in an electrical transmission grid to be used later. ESSs are seeing an increase in their potential use as many renewables only offer power intermittently. There is an upwards trend in amount of renewables used [?] meaning a method to supply consumers power all the time is needed.

2.3 Location, and why implement an ESS?

In the scenario given, the plant has to power a location with nothing more than an ESS and a wind farm. The location chosen (after considering various options through a multi-criteria analysis) was the island of Maui, Hawaii. The primary considerations leading to the choice of this location were:

Fuel Imports Hawaii is primarily powered by oil [?] which has to be imported by a fuel tanker.

Importing oil adds to the carbon footprint of the generation, as well as the cost of the power made. Eliminating the need to import a fuel via tanker should remove some of the cost associated with generation.

High Energy Price Hawaii has the highest electrical prices in the USA, at \$0.3114 per kWh (residential January 2018)[?]. The Next highest state is Rhode Island at \$0.2224 per kWh (residential January 2018)[?]. Average US electrical prices across the residential sector is \$0.1223 per kWh (January 2018)[?]. As Hawaii has almost triple the prices across the rest of the US, this seems like a good opportunity to penetrate the market with a more cost-effective solution that the consumers will back. Hawaii's population is high and it continues to grow year-on-year, meaning extra capacity will have to be built in to satisfy consumer's demands for the future. Of course, as technology and time progresses, the population grows more power-hungry.

Clean Energy Initiative On January 28, 2008, the State of Hawaii and the USDE (US Department of Energy) signed a 'Memorandum of Understanding' with the goal to use renewable resources such as wind, sun, ocean, geothermal and bio-energy to supply 70% or more of

Hawaii's energy needs by 2030 to reduce the State's dependence on imported oil.

Geography Windspeeds in the State of Hawaii are high making this an ideal location for wind power [?]. To supplement this, the U.S. Department of Energy identified Hawaii to have the potential to install 3,000 MW of wind power, capable of generating 12,000 million kWh per year [?]. Considering that the entire State used only 9,962 million kWh in 2011, this project seems feasible with efficient processes.

2.4 Project Aims

Fundamentally the plant must supply the consumers of Hawaii a stable energy supply, yet as with any engineering system there are more factors that must be considered. A set of project aims were produced and are set out below to outline what this plant has to achieve for it to be considered successful:

Sustainable Sustainability is very important in this plant, as it must be a better alternative to the current oil infrastructure, with the future in mind as well. Sustainability covers environmental and social considerations, which includes everything from reducing resource use, reducing pollution, as well as ensuring social acceptance. Sustainable design was considered for each process unit to maximise the sustainability metrics decided on, while delivering the specified material flow rates required for self-sufficient design.

Profitable For this design to be a viable suggestion of replacing Hawaii's oil infrastructure, it *must* be able to run a profit over the plant's lifetime, otherwise such a plant will not be attractive to investors.

Safe Running a large chemical plant has a lot of hazards associated with it, and careful consideration of these through HAZOP and risk analysis is required before an implementation of the plant can occur. For instance, the energy storage medium used, ammonia, can cause harm to people should a leak occur, careful planning with HAZOP and risk analysis can aid in making the plant safer and more socially acceptable.

Satisfies Demand For this plant to replace the current infrastructure it must run entirely by itself. The plant must generate and store ammonia, for use in a generation stage to satisfy local demand. The entire process flow is explored through component design sections below.

The extent to which the plant achieves each of these above aims is examined at the end of the report.

2.5 Plant Structure

The plant structure is setup as in Figure 1 and sub-divided into sections that are discussed below in detail. The most complex parts of the components are explored to see how the objective of supplying power to Maui can be achieved solely using wind power and storing energy in ammonia.

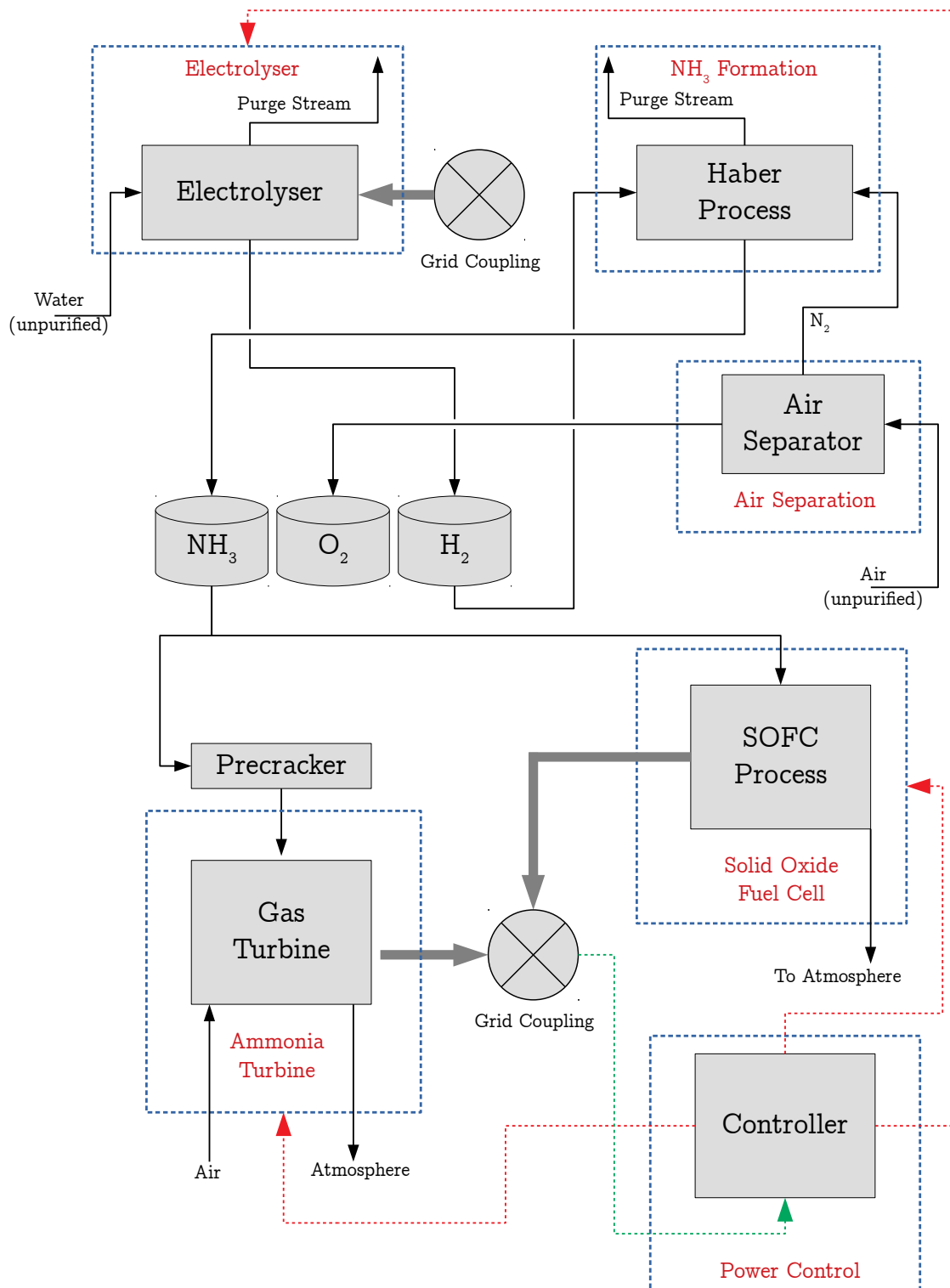


Figure 1: Diagram Showing Component Interconnections

3 Air Separation

3.1 Introduction

This section will briefly discuss the aim of the air separation part of the project, the goals to achieve as well as the two conventional air separation methods used in the industry.

3.1.1 Background

One of the two major inputs to the Haber-Bosch process for the ammonia synthesis part of the energy storage system is a high-purity stream of nitrogen. This section details the method used to process around 97,000 tpy (or 265.5 tpd) of dry air to produce around 74,000 tpy (or 202.8 tpd) of nitrogen at 99.99% purity to be further processed in the Haber-Bosch plant downstream, to produce 90,000 tpy of Ammonia.

3.1.2 Air Composition

The input to the processing plant is atmospheric air taken at ambient temperature and pressure (at 25°C and 1.013 bar). A water filter unit is in place to remove any water content in the input stream before air separation. Dry air composition at ambient conditions are shown in Table 1 [? ? ?].

Table 1: Air Composition and Properties

Species	Molecular Weight (kg kmol ⁻¹)	Mole Fraction	Boiling Point (K)	Specific Heat \tilde{c}_p (kJ kmol ⁻¹ K ⁻¹)
N ₂	28.01	78.08%	77.4	29.10
O ₂	32.00	20.95%	90.2	29.28
Ar	39.95	0.93%	87.3	20.77
CO ₂	44.01	0.03%	194.7	36.04
Other Gases	/	Trace	/	/
Air	28.96	100%	78.7	29.08

3.1.3 Production Methods

Conventional air separation plants adopt either Pressure Swing Adsorption (PSA) or Cryogenic Distillation to separate nitrogen (or oxygen, depending the purpose of the plant) from air.

Both methods have their own distinctive advantages and disadvantages, and a decision is made based on the following two criteria: production capacity and purity of desired product.

Pressure Swing Adsorption Pressure Swing Adsorption makes use of the differences in gas species' properties and their respective affinities for the adsorbent material under pressure to separate from a mixture of gases [?].

An adsorbent bed is used in a PSA column, which preferentially adsorbs nitrogen under pressure and allows other gases to be removed. After separation, adsorbent bed is regenerated by lowering column pressure, thus releasing the adsorbed nitrogen.

The PSA column operates as a batch process, hence as a conventional practice in the industry, two (or more) columns are ran in an alternating sequence to separate gases continuously.

Capacities of PSA plants can range from small scale of 100 m³/hr at 99.9% nitrogen purity to large scale of 9000 m³/hr at 97% nitrogen purity [?].

As this method does not satisfy the 99.99% nitrogen purity requirement, more in-depth details of this method is not investigated further.

Cryogenic Distillation Cryogenic Distillation makes use of the differences in gas species' boiling points and their respective volatilities under cryogenic temperatures to separate from a mixture of gases [?].

Depending on the purity requirements of products, design of one to three distillation columns is used, namely high-pressure column (HPC), low-pressure column (LPC) and argon column (ARC). Input stream of air is filtered and liquefied before entering the system distillation columns, producing high-purity nitrogen from the top of the column and oxygen-rich mixture from the bottom (assuming a two-column design).

Capacities of cryogenic distillation plants can range from small scale of 600 tpd to large scale of 40,000 tpd of nitrogen at very high purity; though the distillation columns' load range are highly inflexible with a low ramp-rate, it is not ideal to turn the unit off and on which poses a problem with varying wind supply.

This method satisfies both production capacity and purity requirements, hence the method is adopted for our plant and the design details are investigated further. To address the varying wind supply issue, the unit is designed to run continuously.

3.2 Plant Overview

This section includes the overall air separation plant schematic and goes over individual component of the plant. Working equations and design parameters are specified in this section, allowing optimisation and analysis in Section 3.3.

3.2.1 Plant Diagram

Conventional air separation units make use of multi-column system to fully separate air into its constituents. But to serve the goal of this project, a double-column system is more than sufficient to produce high-purity nitrogen and oxygen. A diagram of the air separation plant is shown overleaf in Figure 2, which is an adaption from a cryogenic air separation plant schematic by Linde Engineering [?].

3.2.2 Plant Components

Adapted from a cryogenic air separation plant schematic by Linde Engineering, the plant will contain the following components [?]:

Table 2: Cryogenic Plant Components

Component	Purpose
Mechanical air filter	Dust removal
Molecular sieve	H ₂ O and CO ₂ removal
Multi-stage compressors with intercoolers	Bring inlet to optimum temperature and pressure
Throttle (or expansion turbine)	Lower pressure to transition between HPC and LPC
High-pressure column	First-stage distillation
Low-pressure column	Second-stage purification
Reboiler and condenser units	Regulate column conditions
Heat exchangers	Using the cold product to cool inlet stream

Pre-Processing Filtering Before inlet air stream can enter the first distillation column for separation, it has to be processed to remove impurities that may adversely affect the performance of the plant, namely water vapour and CO₂.

A mechanical air filter is first used to remove solid air particulates by means of a woven fibrous membrane in a cylindrical cartridge (up to 0.5 µm). Air flows from outside in, accumulating dust on the exterior of the cylinder, which can be blown off by a reverse pulse of compressed air [?].

Water vapour can condense into ice in the cryogenic chambers, the build-up can cause blockage in the trays of distillation column, whilst CO₂ can poison the catalyst in Haber-Bosch process downstream. Hence both species are removed via the use of a molecular sieve, which uses microporous adsorbents like zeolite (up to 2 nm) and operates in a similar manner as PSA [?].

Multi-stage Compressors with Intercoolers In between the air filter and the molecular sieve, a multi-stage compressor will be used compress filtered inlet gas stream from 1.01 bar (i.e. atmo-

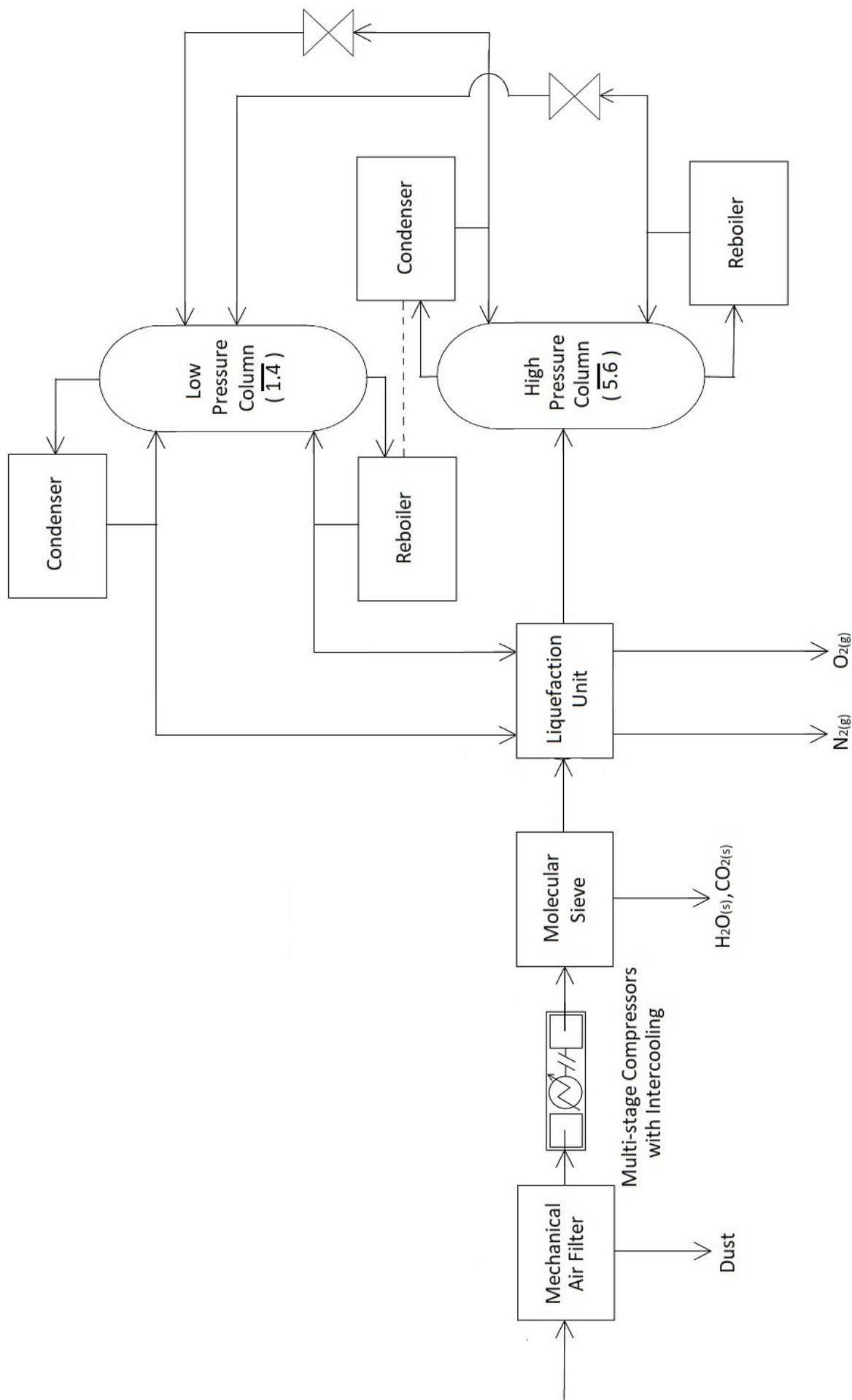


Figure 2: Overall Plant Schematic (adapted from Linde Engineering cryogenic air separation process)

spheric) to 5.6 bar. As the compression process is modelled to be adiabatic, temperature of the inlet stream will rise with compression, hence intercoolers are used to ensure maximum temperature in between compression is capped at 400 K to ensure minimal heat transfer and high compressor efficiency.

After the first compression, hot compressed gas is cooled to ambient temperature (298 K) using water as a coolant before subjected to further compression. This process is repeated if multiple stages of compression is required.

By using ideal gas law ($pv = RT$) and assuming polytropic process ($pv^\gamma = \text{constant}$), compression pressure ratio can be defined by Equation 1:

$$r_p = \frac{p_{out}}{p_{in}} = \left(\frac{T_{out}}{T_{in}} \right)^{\frac{1}{\gamma-1}} \quad (1)$$

It follows that single-stage work input can be defined by Equation 2:

$$W_{in} = \frac{\gamma}{\gamma-1} \dot{m} c_p T_{in} \left(r_p^{\frac{\gamma-1}{\gamma}} - 1 \right) \cdot \frac{1}{\eta_{mech}} \quad (2)$$

where \dot{m} is inlet stream mass flow rate (= 265.5 tpd of dry air, or 3.07 kgs^{-1}), c_p is the specific heat capacity of air mixture, T_{in} is the inlet temperature, γ is the Poisson constant (where $\gamma = 1.4$ for adiabatic process) and η_{mech} is the mechanical efficiency of compressor (assuming 90% efficient).

Specific heat capacity of air mixture at constant pressure changes with varying temperature, from $1.01 \text{ kJ kmol}^{-1}\text{K}^{-1}$ at 298K to $1.07 \text{ kJ kmol}^{-1}\text{K}^{-1}$ at 400K (at constant pressure of 5 bar) [?]. As there is only a small increase in value, $1.01 \text{ kJ kmol}^{-1}\text{K}^{-1}$ is used to simplify calculations.

Abiding by the temperature cap, first stage compresses inlet air stream from 1 bar to 2.80 bar, with predicted compressor work of 1229 kW. Second stage compresses air stream from 2.80 bar to 5.60 bar, with predicted compressor work of 787 kW. This gives a total of 2016 kW of compressor work before liquefaction.

Liquefaction Unit Inlet air stream has to be cooled and fully liquefied before feeding into the HPC for separation. But with the low boiling point of species, it is difficult to find a refrigerant that can be used to achieve the goal. Hence a modified Linde-Hampson liquefaction cycle is used as shown in Figure 3 [?].

Inlet air stream is compressed from 5.60 bar to 50 bar in another multi-stage compressor with intercooling, but for simplicity this compression process will be modelled as isothermal compression (state 1 → 2). After compression, inlet air stream will be cooled using both the vapour stream from

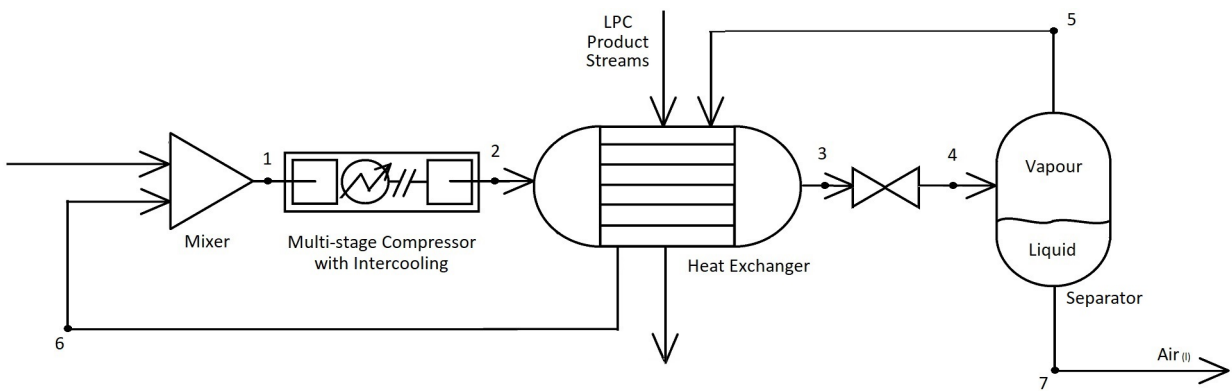


Figure 3: Modified Linde-Hampson Liquefaction Cycle

the separator and the two product streams from LPC (state $2 \rightarrow 3$, with reference to Figure 2) in a series of heat exchangers. This will cool the inlet air stream to cryogenic temperature at 50 bar, which will then be put through a throttle for isentropic expansion to 5.6 bar (state $3 \rightarrow 4$). Inlet air stream is now in saturated liquid-vapour state and can be separated by state in the separator. Liquid stream (state 7) is extracted from the bottom of the separator and can now enter the HPC for first-stage separation; whilst vapour stream (state 5) is recycled, cold is extracted (state $5 \rightarrow 6$) and mixed in with incoming inlet air stream to be liquefied again.

This process is depicted in a temperature-entropy diagram of air as shown in Figure 4. Note that each node correspond to their respective streams in the liquefaction unit diagram in Figure 3.

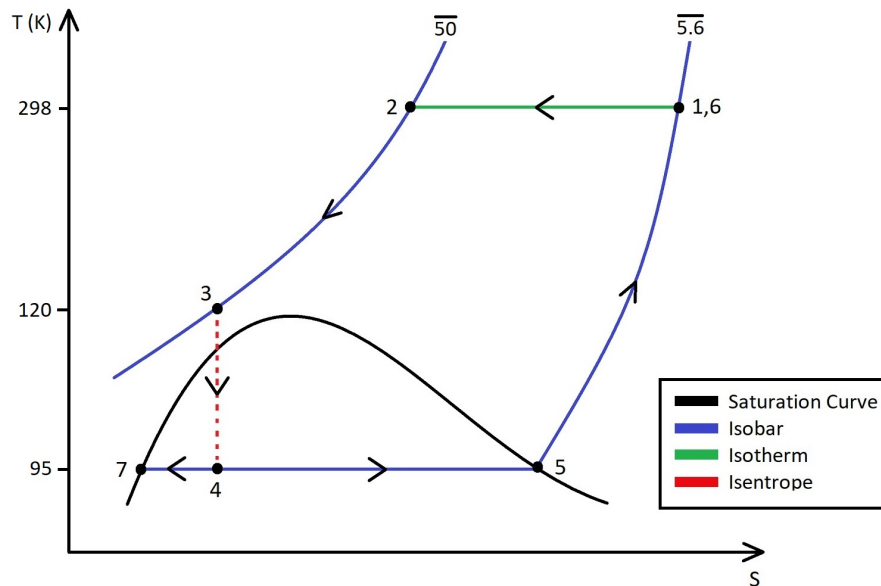


Figure 4: Temperature-Entropy Diagram of Linde-Hampson Liquefaction Cycle

Most temperature and pressure conditions are already well-defined, except the temperature at state 3. If the temperature is increased at state 3, less heat exchange is required between the cold and

hot streams hence a smaller heat exchanger can be used (i.e. reduction in capital cost); the downsides of this decision are losing more work at the throttle as well as smaller fraction of the stream is liquefied thus requiring a larger recycle stream (i.e. lower efficiency). For simplicity, the temperature at state 3 is fixed at 120 K so that the application of such a liquefaction cycle can be analysed. Having the temperature and pressure conditions at each state, enthalpy and entropy values of the air mixture can be found at each state. As no suitable thermodynamic data can be found of air mixture at cryogenic conditions, linear combination of enthalpy and entropy data of nitrogen and oxygen will be used instead. These are compiled into Table 3.

From state 3 to state 4, supercritical fluid undergoes isentropic expansion hence entropy remains constant throughout as the state changes to saturated liquid-vapour. This information can be used to find the liquid fraction x of the saturation liquid-vapour, using entropy values at state 5 (fully saturated vapour) and 7 (fully saturated liquid) using Equation 3, which is found to be around 66%.

Hence, 34% of the initial air stream is not liquefied and is recycled.

$$x = \frac{s_4 - s_5}{s_7 - s_5} \quad (3)$$

Enthalpy at state 4 (h_4) can be found in a similar way using Equation 4, and is found to be -1.4006 kJmol^{-1} .

$$h_4 = x h_7 + (1 - x) h_5 \quad (4)$$

Table 3: Thermodynamic Properties of Air Mixture at Different States [?]

State	Pressure (bar)	Temperature (K)	Enthalpy (kJmol^{-1})	Entropy ($\text{Jmol}^{-1}\text{K}^{-1}$)
1	5.6	298	8.6307	180.0013
2	50	298	8.3503	160.9482
3	50	120	-1.0827	106.0736
4	5.6	95	-1.4006	106.0736
5	5.6	95	1.0850	132.3265
6	5.6	298	8.6307	180.0013
7	5.6	95	-2.6882	92.7981

Note that the values in the database take 298.15 K and 1 bar as datum, hence some values in Table 3 are negative.

Isothermal compression work can be found by using Equation 5,

$$W_{in} = \dot{m}RT \ln \left(\frac{p_{out}}{p_{in}} \right) \cdot \frac{1}{\eta_{mech}} \quad (5)$$

where gas constant for air is $0.287 \text{ kJkg}^{-1}\text{K}^{-1}$ [?] and η_{mech} is the mechanical efficiency of compressor (assuming 90% efficient).

Heat exchanges can be found by using Equation 6,

$$\Delta Q = \dot{m}(h_{out} - h_{in}) \quad (6)$$

where $\Delta Q > 0$ means heat addition and $\Delta Q < 0$ means heat extraction.

From state 1 to state 2, compressor work required is found to be 637 kW.

From state 2 to state 3, 1000 kW of heat is extracted from inlet air stream when cooled in heat exchanger. Such heat extraction will have to be supplied by LPC cold product streams as well as cold recycled vapour stream from separator.

From state 5 to state 6, vapour stream from separator can extract 272 kW of heat; the rest of the heat to be extracted (728 kW) will be from using LPC cold product streams. The calculation is explored further when analysing distillation column design.

Distillation Column As a 99.99% nitrogen purity is required, a two-column design is investigated.

The reason behind this decision is due to the fact that under different pressure, nitrogen-oxygen mixture has different boiling points and volatilities, as listed below [?]:

Table 4: Boiling points and volatilities of nitrogen-oxygen mixture under different pressures

Pressure (bar)	Boiling Point (K)	Volatility α
1.4	80.40	3.68
5.6	95.28	2.46

Note that the values above are found by interpolation using the data of a binary 80% nitrogen-20% oxygen mixture.

Referring back to Table 4, argon has a boiling temperature close to that of oxygen and far from that of nitrogen. This implies that most of the argon in the inlet stream will likely end up in the oxygen-rich stream. And as the concentration of argon is significantly lower than both nitrogen and oxygen in inlet stream, the assumption of a binary-mixture consisting of only nitrogen and oxygen (over a ternary-mixture) is justified.

By combining Raoult's Law ($p_i = x_i p_i^*$) and Dalton's Law ($p_i = y_i P$), a relationship linking vapour mole fraction y_i to liquid mole fraction x_i can be found:

$$y_i = \frac{\alpha x_i}{1 + (\alpha - 1)x_i} \quad (7)$$

Using the relationship, two vapour-liquid equilibrium (VLE) line of the nitrogen-oxygen mixture is plotted on MATLAB, as shown in Figure 5.

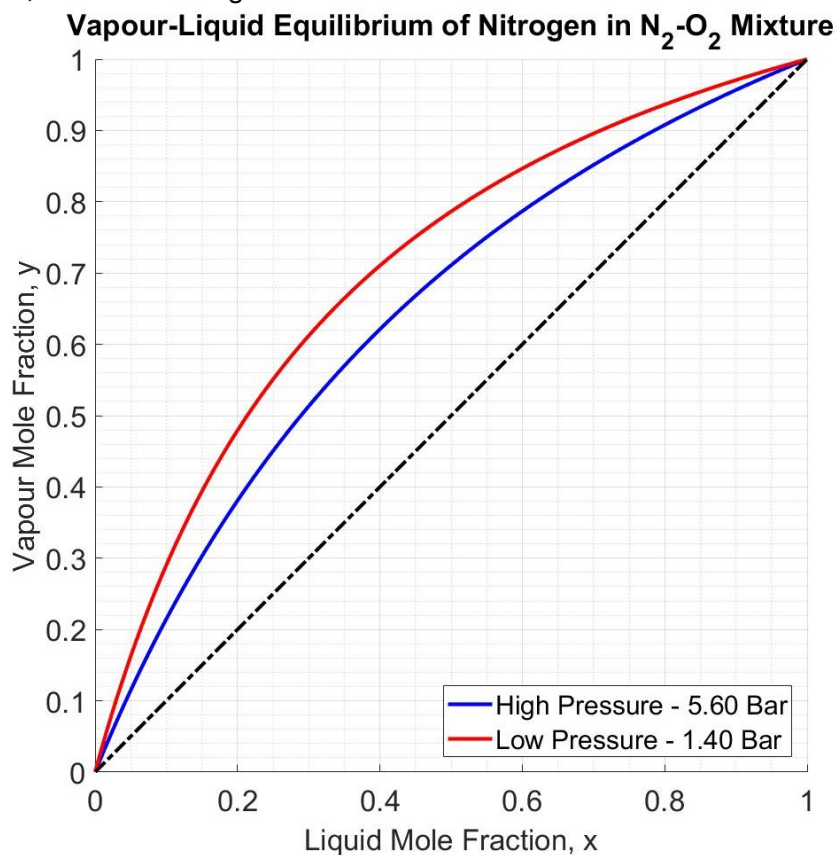


Figure 5: Vapour-Liquid Equilibrium of nitrogen in 80% nitrogen-20% oxygen mixture

From Figure 5, it can be seen that the VLE line at lower pressures moves away from the hypothetical $y = x$ dotted line, implying that nitrogen vapour is more enriched at lower pressures; this benefit, however, is offset by the lower boiling points at lower pressures. Hence a two-column design can allow a preliminary distillation in HPC (at 5.6 bar and 95.28 K) before a further purification in LPC (at 1.4 bar and 80.40 K).

McCabe-Thiele Construction can be used to calculate the number of equilibrium stages required for separation in the two columns, by setting the distillate and bottom products' purities, with the following assumptions:

1. Molar heat of vapourisation is the same for feed components at each independent equilibrium stage. Hence for each mole of vapour condensed, one mole of liquid is vapourised (i.e. equal molar overflow).
2. Vapour and liquid streams are assumed to be saturated at their respective boiling points with respect to their equilibrium position.
3. Negligible heat losses or mixing effects.

By specifying the purity requirements and feed conditions, operating lines and feed lines can be found by taking control volumes and considering mass balances around different sections of the column and feed inlets. Figure 6 shows the variables used for operating lines and feed lines functions.

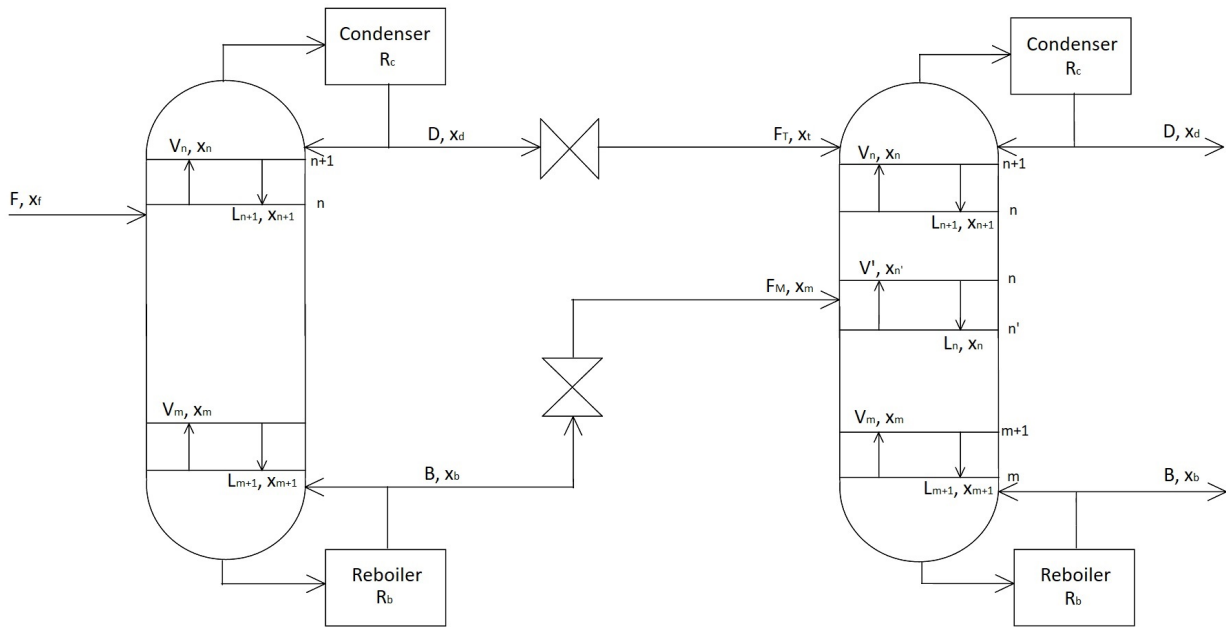


Figure 6: Diagrams of HPC and LPC with labels

Note that capital letters represent molar flow rates (with L for Liquid, V for Vapour, D for Distillate, B for Bottom, F_T for Top Feed and F_M for Middle Feed), whilst x and y represent liquid and vapour mole fractions respectively.

With reference to Figure 6, top operating line (TOL, for rectifying section) and bottom operating line (BOL, for stripping section) are defined by Equation 8 and 9:

$$y_n = \left(\frac{L_{n+1}}{V_n} \right) x_{n+1} + \left(\frac{D}{V_n} \right) x_d \quad (8)$$

$$y_m = \left(\frac{L_{m+1}}{V_m} \right) x_{m+1} - \left(\frac{B}{V_m} \right) x_b \quad (9)$$

where n represents the stages at the top of the column and m represents the stages at the bottom.

Alternatively, TOL and BOL can be expressed in terms of condenser and reboiler reflux ratios, R_c ($= \frac{L_{n+1}}{D}$) and R_b ($= \frac{V_m}{B}$), giving Equation 10 and 11:

$$y_n = \left(\frac{R_c}{R_c + 1} \right) x_{n+1} + \left(\frac{1}{R_c + 1} \right) x_d \quad (10)$$

$$y_m = \left(\frac{R_b + 1}{R_b} \right) x_{m+1} - \left(\frac{1}{R_b} \right) x_b \quad (11)$$

Reflux ratios are chosen by multiplying the minimum reflux ratio the system requires by a factor k , hence $R = kR_{min}$, which is typically 1.2 to 1.5 times of minimum reflux ratio [?]. With a higher reflux ratio, fewer trays are required for separation hence a shorter column and lower initial capital investment. The trade-off, however, is increased condenser and reboiler work hence higher running cost. A value for reflux ratio factor of 1.2 is chosen for the initial analysis.

Feed line(s) (q-line) is defined by Equation 12:

$$y_q = - \left(\frac{q}{1-q} \right) x_q + \left(\frac{1}{1-q} \right) x_f \quad (12)$$

where $q (= \frac{h_d - h_f}{h_{vap}})$ is the heat needed to one mole of feed to saturated vapour condition divided by molar enthalpy of feed. Note that for fully saturated liquid, $q = 1$ hence the q-line has infinite gradient and therefore will be a vertical line; for fully saturated vapour, $q = 0$ hence the q-line has zero gradient and therefore will be a horizontal line.

Applicable only to LPC, middle operating line (MOL, between the two feed inlets) is defined by Equation 13.

$$y' = \left(\frac{L'}{V'} \right) x' + \left(\frac{D}{V'} \right) x_d - \left(\frac{F_T}{V'} \right) x_T \quad (13)$$

Two useful information to have are minimum condenser reflux ratio and minimum theoretical number of equilibrium stages. Minimum condenser reflux ratio can be found by setting the operating lines to intersect the q-line on the vapour-liquid equilibrium curve (i.e in a pinched condition at infinite equilibrium stages); whilst minimum theoretical number of equilibrium stages can be found by setting the column in total condenser reflux (i.e. at infinite reflux) such that operating lines align with $y = x$ line.

For a real life application, the separation process may exhibit non-ideal behaviour due to uneven mixing or non-uniform vapour-liquid composition.

The model can be improved by applying a Murphree Tray Efficiency of 70% to ensure thorough separation at each equilibrium stage. Murphree Tray Efficiency can be directly apply to the steps of the McCabe-Thiele construction with Equation 14:

$$E_{mv} = \frac{y_{out} - y_{in}}{y_{eq} - y_{in}} \quad (14)$$

$$y_{out} = E_{mv} (y_{eq} - y_{in}) + y_{in}$$

A MATLAB script was written to automatically follow the operating line functions and construct the

McCabe-Thiele plots for both HPC and LPC, which can be used to calculate the number of stages required, reflux ratios used and feed locations. An initial simulation is ran to produce two McCabe-Thiele plots which are shown in Figure 7.

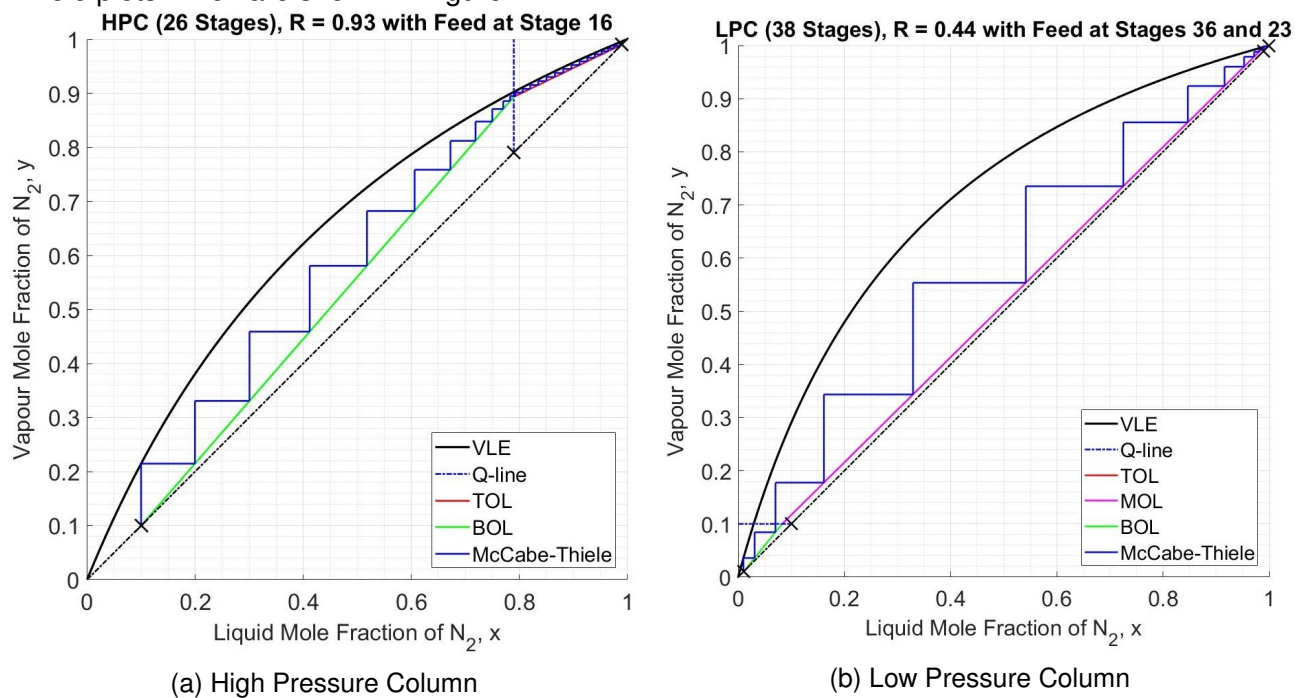


Figure 7: McCabe-Thiele Construction

Figure 7a shows the McCabe-Thiele construction for the initial HPC design with the following parameters (on the basis of nitrogen purity):

1. Feed purity $x_f = 79\%$ (fully saturated liquid)
2. Distillate purity $x_d = 99\% (= x_t \text{ in LPC})$
3. Bottom purity $x_b = 10\% (= x_m \text{ in LPC})$
4. Minimum condenser reflux ratio $R_{min} = 0.93$ ($R = 1.2R_{min}$)

Feed is assumed to be fully saturated liquid as the stream enters the column for separation, and two product streams are extracted from top and bottom of the column. In this configuration, mole flow rates $D = 0.0822 \text{ kmols}^{-1}$ and $B = 0.0238 \text{ kmols}^{-1}$.

As this is the first stage of distillation, distillate stream of HPC is used as the top feed for LPC and bottom stream of HPC is used as the middle feed for LPC, for a second stage of purification.

Distillate and bottom streams are put through separate throttles to lower their pressures, transitioning from 5.6 bar to 1.4 bar, in between HPC and LPC. As distillate stream is assumed to be fully saturated liquid whilst bottom stream is assumed to be fully saturated vapour, isentropic expansion in the throttles induce saturated liquid-vapour states in both streams. The processes can be visualised

by Figure 8.

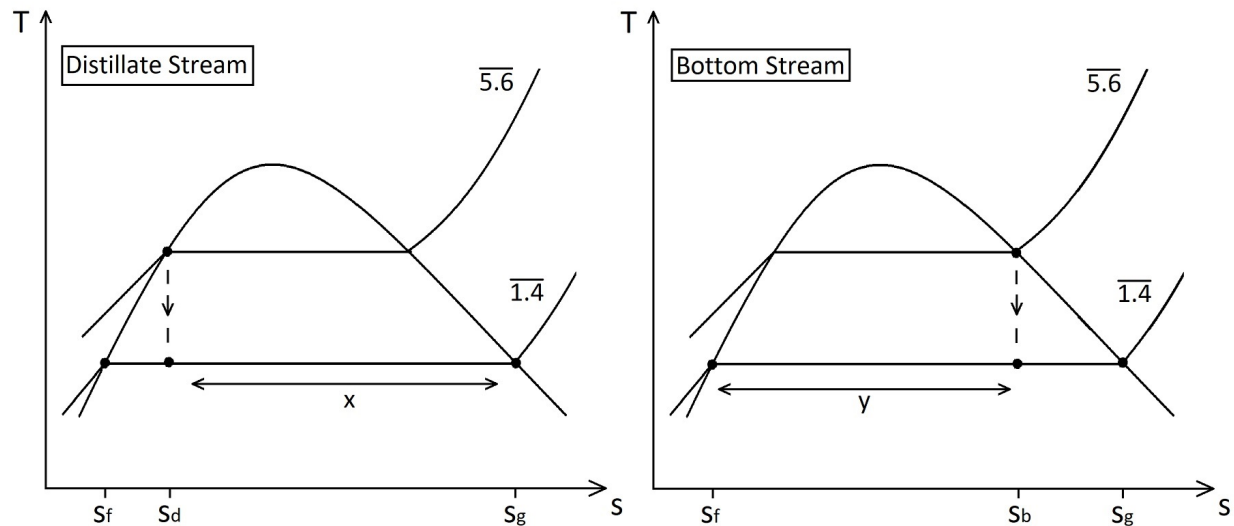


Figure 8: Temperature-Entropy Diagram of the Transition in between HPC and LPC

Through the use of the following equations,

$$x = \frac{s_d - s_g}{s_f - s_g} \quad (15)$$

$$y = \frac{s_b - s_f}{s_g - s_f}$$

and entropy data in Table 5, liquid fraction x (correspond to distillate stream) and vapour fraction y (bottom stream) can be found.

Table 5: Entropy Data for Distillate and Bottom Stream

Stream	s_i (5.6 bar)	s_f (1.4 bar)	s_g (1.4 bar)	x or y
Distillate	91.841	81.611	149.892	85%
Bottom	159.956	95.892	167.748	89%

This shows that neither of the streams are fully saturated, as distillate stream contains 85% saturated liquid and bottom stream contains 89% saturated vapour after throttling. This implies that the feed lines will no longer be perfectly vertical (fully saturated liquid) or horizontal (fully saturated vapour); but with only a 10% difference, there is an observable difference but the impact on the separation process should be small. Hence for simplicity of analysis, both streams are assumed to be fully saturated when they enter LPC.

Figure 7b shows the McCabe-Thiele construction for the initial LPC design with the following parameters (on the basis of nitrogen purity):

1. Top feed purity $x_t = 99\%$ (fully saturated liquid)
2. Middle feed purity $x_m = 10\%$ (fully saturated vapour)
3. Distillate purity $x_d = 99.99\%$
4. Bottom purity $x_b = 1\%$
5. Minimum condenser reflux ratio $R_{min} = 0.44$ ($R = 1.2R_{min}$)

Top feed is assumed to be fully saturated liquid and middle feed is assumed to be fully saturated vapour as the streams enter the column for purification. This allows two purified product streams to be extracted from top and bottom of the column. In this configuration, mole flow rates $D = 0.0836 \text{ kmols}^{-1}$ and $B = 0.0225 \text{ kmols}^{-1}$.

Although this design satisfies the product streams purity and supply requirements, operating lines in LPC are near total reflux conditions despite only running at 1.2 times of minimum reflux ratio. This is due to the fact that HPC produces a much larger distillate stream than bottom stream, which contributed to the imbalance of vapour and liquid feed streams as inputs to LPC.

The two major contributors to the cost of operation of the distillation columns are the number of equilibrium stages in the columns and the reflux ratios the columns are running at. The number of equilibrium stages directly relates to the dimensions of the column and insulation required, whilst the reflux ratios directly relate to the reboiler and condenser thermal loads and sizes.

In order to reduce the column operational cost, further investigation into the design details of the column will be discussed in Section 3.3 ("Optimisation and Analysis").

Distillation Column Reboiler and Condenser The two-column system uses two sets of reboiler and condenser units to regenerate liquid and vapour flows in the columns. As the liquid mixture flows down the column and gathers at the bottom, a portion of the flow is vapourised by the reboiler and forms the rising vapour stream. Similarly, the vapour stream rising to the top of the column is condensed by the condenser to replenish the liquid stream. This forms the cycle of stripping and rectifying in the column.

There is an integrated design between HPC condenser and LPC reboiler. Adopted from Linde Engineering cryogenic plant [?], the design is redrawn in Figure 9.

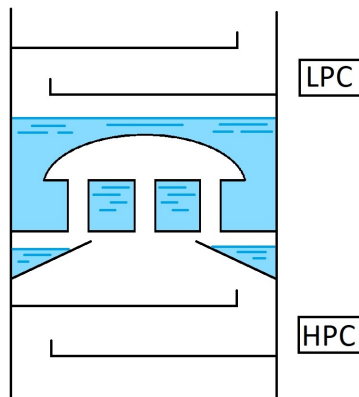


Figure 9: Special Inter-Column Reboiler-Condenser Configuration

The boiling point of pure nitrogen at 5.6 bar is higher than the boiling point of pure oxygen at 1.4 bar, hence the refrigeration required to condense nitrogen at the top of HPC can be supplied by boiling the oxygen at the bottom of LPC. This replenishes both the liquid stream in HPC and vapour stream in LPC. With this configuration, no external thermal load is required, hence it maximises the thermal efficiency of the system.

3.3 Optimisation and Analysis

This section details the process to improve the system by optimising the two-column design and balancing heat of streams.

3.3.1 Distillation Column Optimisation

In section 3.2.2 ("Distillation Column"), a preliminary set of parameters are introduced to allow initial analysis of the distillation. The set of parameters are as follows:

1. HPC distillate purity $x_d = 99\%$ ($= x_t$ in LPC)
2. HPC bottom purity $x_b = 10\%$ ($= x_m$ in LPC)
3. Reflux ratio factor $k = 1.2$ (applies to both columns)

As shown previously, the system running at this set of parameters is not very efficient. It can be improved by running simulations on different parameters and hence find an optimal set of operating conditions.

HPC Distillate Stream Purity The first parameter to optimise is the HPC distillate stream purity x_d . The distillate stream of HPC is the first step for nitrogen purification. It is to be isentropically ex-

panded in a throttle before entering the rectifying section of LPC, forming the main body of the liquid stream travelling down the column.

Simulations are to be ran at HPC bottom purity x_B of 10% and reflux ratio factor k of 1.2. The minimum distillate purity allowed by the VLE curve is 90%, hence simulations are ran at 1% interval in the range of 90% to 99% to test out the impact on the system.

Figure 10a shows the change in number of stages required by the system, while Figure 10b shows the change in reflux ratios required by system.

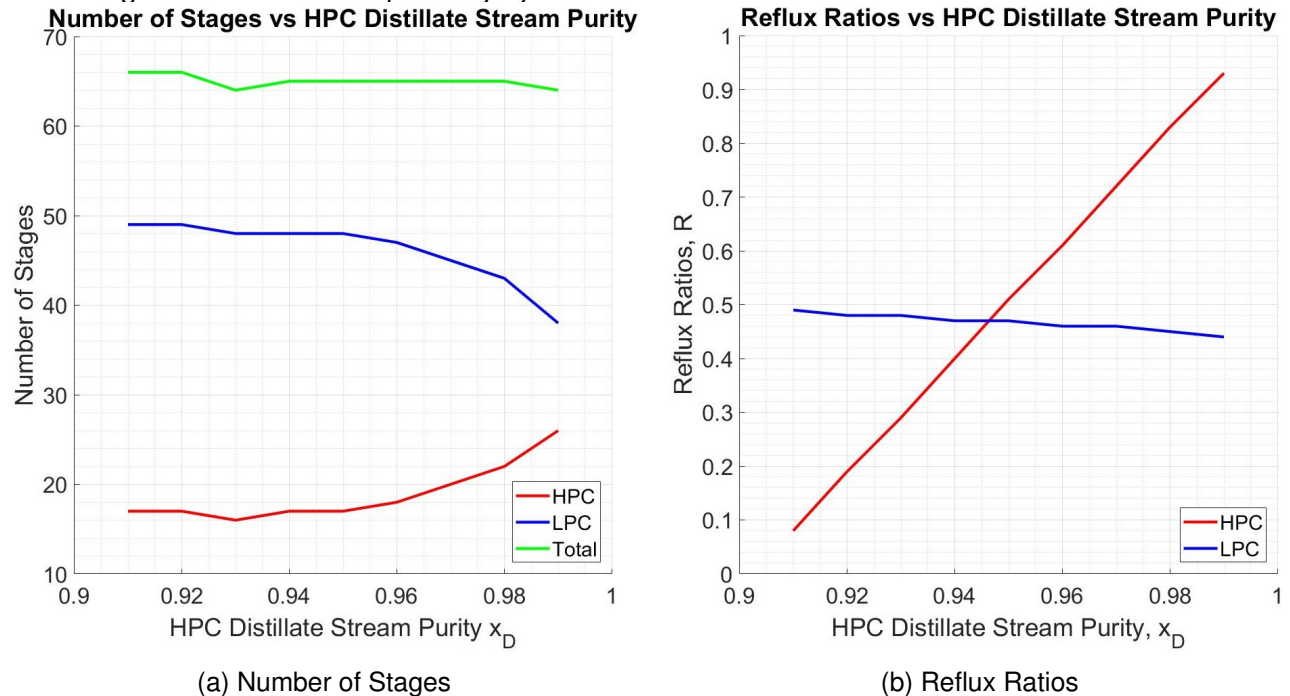


Figure 10: Optimising HPC Distillate Stream Purity

From Figure 10a, it is shown that as the purity x_D increases, number of stages required by HPC (denoted by red line) increases whilst that of LPC (denoted by blue line) decreases. The total stages required (denoted by green line) stayed relatively constant, with the lowest number of stages required at purity of 93% and 99%.

From Figure 10b, it is shown that as the purity x_D increases, reflux ratios required by HPC (red) increases rapidly whilst that of LPC (blue) decreases slightly.

An extra set of data on the stream flow rates between the two columns is also generated, which showed insignificant changes and hence is not presented.

Considering the effects on the number of stages and reflux ratios by running simulation on HPC distillate purity, 93% was chosen to be the optimal condition.

HPC Bottom Stream Purity The second parameter to optimise is the HPC bottom stream purity x_d . The bottom stream of HPC is the first step for oxygen purification. It is to be isentropically

expanded in a throttle before entering the stripping section of LPC, forming the main body vapour stream travelling up the column.

Simulations are to be ran at HPC distillate purity x_D of 93% and reflux ratio factor k of 1.2. The minimum bottom purity allowed by the VLE curve is 70%, hence simulations are ran at 10% interval in the range of 10% to 70% to test out the impact on the system.

Figure 11a shows the change in number of stages required by the system, while Figure 11b shows the change in stream flow rates in between the two columns.

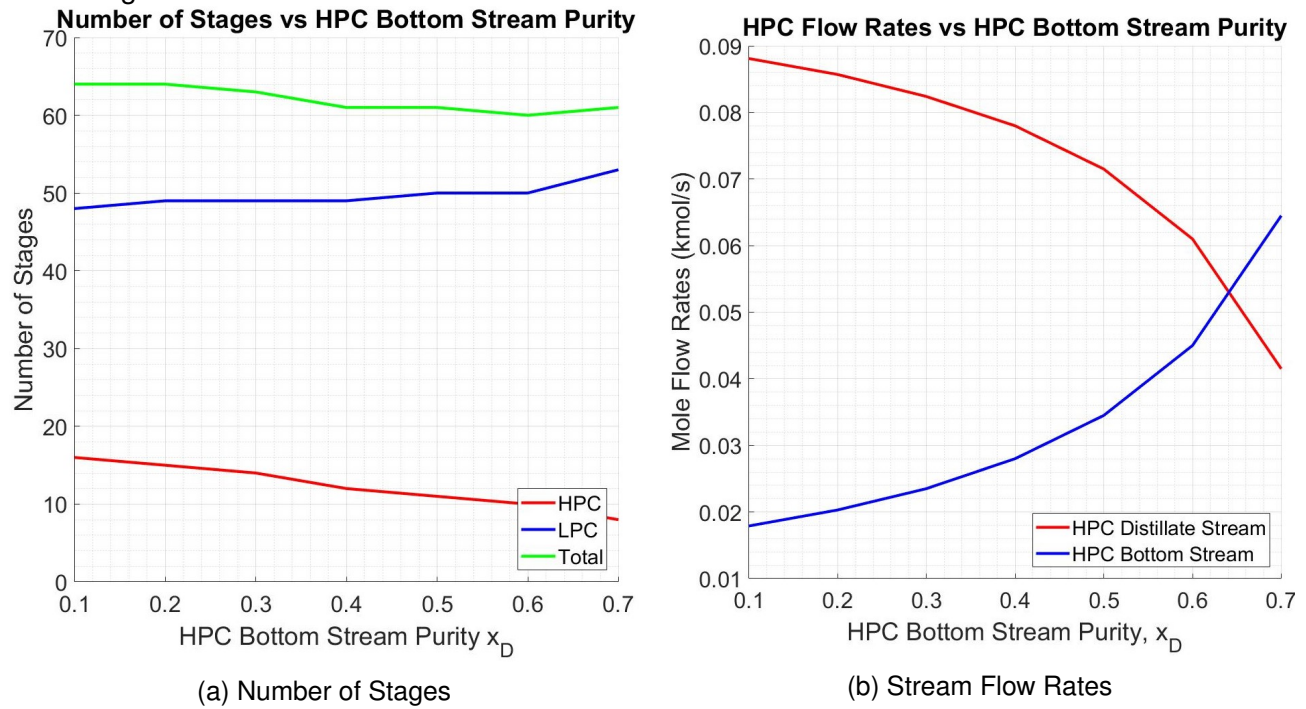


Figure 11: Optimising HPC Distillate Stream Purity

From Figure 11a, it is shown that as the purity x_B increases, number of stages required by HPC (denoted by red line) decreases whilst that of LPC (denoted by blue line) increases. The total stages required (denoted by green line) stayed relatively constant, with the lowest number of stages required at purity of around 60%. Further stimulation at 1% interval between 60% to 70% showed that the lowest number of stages applies to purity conditions of 61% to 65%.

From Figure 11b, it is shown that as the purity x_B increases, HPC distillate stream flow rate (denoted by red line) decreases whilst that of HPC bottom stream (denoted by blue line) increases. The two curves cross at 65% purity, which implies equimolar flow out in top and bottom section of the column. This is a high-efficient condition as supply of vapour and liquid streams in LPC are matched, thus minimising reboiler and condenser duty.

An extra set of data on the reflux ratios between the two columns is also generated, which showed no changes and hence is not presented.

Considering the effects on the number of stages and HPC output stream flow rates by running sim-

ulation on HPC bottom purity, 65% was chosen to be the optimal condition.

Reflux Ratio Factor The third parameter to optimise is the reflux ratio factors for both HPC and LPC. To simplify the analysis, the same reflux ratio factor is to be applied to both HPC and LPC. Simulations are ran at HPC distillate purity x_D of 93% and HPC bottom purity x_B of 65%. From [?], optimum reflux ratios are often within the range of 1.2 to 1.5 times of minimum reflux ratio, but for cryogenic system this might not be the case [?]; hence simulations are ran at 0.1 interval in the range of 1.1 to 2.0 to test out the impact on the system.

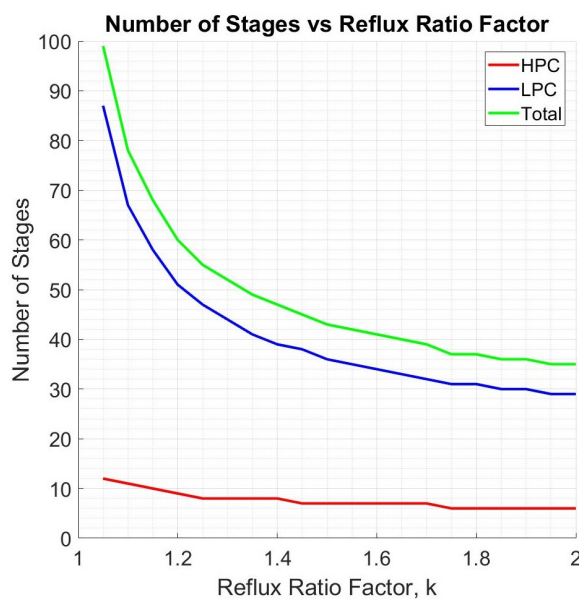


Figure 12: Number of Stages

From Figure 12, it is shown that as the reflux ratio factor k increases, number of stages required by HPC (denoted by red line) decreases slightly whilst that of LPC (denoted by blue line) decreases rapidly. The total stages required (denoted by green line), heavily influenced by LPC, also decreases rapidly and plateaued towards factor of 2.0.

As number of stages relates to column dimensions and reflux ratio factor relates to reboiler and condenser loads, this information will be used in Section 3.3.3 ("Cost Analysis") later.

3.3.2 Design Dimensions

Heat Exchanger Plate-fin heat exchangers are used to transfer heat between cold and hot streams. As a simplification to the analysis, condensers and reboilers are also modelled as heat exchangers.

The surface area can be found using Equation 16.

$$A_s = \frac{\Delta Q}{U\Delta T_m} \quad (16)$$

where $U\Delta T_m$ is taken to be 11250 Btu hr⁻¹ft⁻² (or 35.49 kWm⁻²).

Distillation Column Design dimensions of the distillation columns are controlled by the reflux ratios. With higher reflux ratios, wider columns are needed to accommodate larger vapour and liquid streams inside the column; but the columns will be shorter as fewer equilibrium stages are needed. These two dimensions, diameter and height, can directly affect both the capital cost and the operating cost of the system. A cost analysis study is required to find an optimum balance between the two.

In both HPC and LPC, a 24-inch (or 0.61 m) tray spacing assumption is used. It is common practice to leave additional spaces of 5 ft (or 1.52 m) both at the top of the column as vapour-liquid disengaging space and bottom as liquid sump [?]. Equation 17 relates the height of the column H (in m) to the number of equilibrium stages required N :

$$H = 0.61N + 3.04; \quad (17)$$

The column diameter is selected to ensure vapour velocity is within 60% of flooding velocity. Making the assumption that liquid density is much larger than vapour density, i.e. $\rho_f >> \rho_g$, vapour velocity can be expressed as Equation 18 [?]:

$$v = \frac{F}{\sqrt{\rho_g}} \quad (18)$$

where F is a constant that can be found by carrying out force balance of weight against drag on an arbitrary particle. $F = 1.51$ is assumed for 24-inch tray spacing with 60% flooding [?].

Volumetric flow rate Q can be expressed in vapour molar flow rate V and in vapour velocity v in Equation 19. Equating these two Equations and substituting in Equation 18, column diameter can be found in Equation 20.

$$Q = \frac{V \cdot MW_g}{\rho_g} = \left(\frac{1}{4} \pi D^2 \right) v \quad (19)$$

$$D = \sqrt{\frac{4V \cdot MW_g}{\pi F \sqrt{\rho_g}}} \quad (20)$$

where vapour molar flow rate is linked to reflux ratio by $V = (R + 1)D$, MW_g is the molecular weight of gas and ρ_g is the vapour density.

3.3.3 Cost Analysis

The costing of the system will be analysed using Guthrie correlations, which make use of a cost index commonly used in chemical process industries called Marshall and Swift Cost Index, or M&S. Although the publishing of M&S has been discontinued in scientific journal '*Chemical Engineering*' from 2012, Guthrie correlations can still provide a simple analysis on the total installed cost of each major component.

Using past M&S values from [?] and [?], dating back to 1975, data showed a general linear trend that can be extrapolated to give a hypothetical M&S value of around 1450 for the year 2018. This value will be used in the cost analysis in this section.

Total installed cost of reboilers and condensers are modelled using Equation 21, assuming they act as independent heat exchangers to simplify analysis [?].

$$C_{\text{hex}} = \left(\frac{M\&S}{280} \right) (101.3) (A_s^{0.65}) \cdot (2.29 + F_c) \quad (21)$$

where A_s is the heat exchanger surface area and $F_c = 5.06$ is the overall correction factor that relates to design type (kettle reboiler), design pressure (sub-10-bar operation) and design material (stainless steel). Note that area in the equation is expressed in ft^2 , hence a conversion factor is applied ($\text{ft}^2 = 0.0929 \text{ m}^2$).

Total installed cost of distillation column is separated into two costs, cost for the pressure vessels and cost for the internal components (e.g. trays), using Equation 22 and 23 respectively [?].

$$C_{\text{col,ves}} = \left(\frac{M\&S}{280} \right) (101.9) (D^{1.066}) (H^{0.802}) \cdot (2.18 + F_c) \quad (22)$$

where D is the distillation column diameter, H is the distillation column height and $F_c = 2.36$ is the correction factor that relates to design material (stainless steel) and design pressure (sub-7-bar operation). Note that dimensions in the equation are expressed in ft and ft^2 , hence a conversion factor is applied (1 ft = 0.3048 m).

$$C_{\text{col,int}} = \left(\frac{M\&S}{280} \right) (4.7) (D^{1.55}) (H) \cdot F_c \quad (23)$$

where $F_c = 4.50$ is the correction factor that relates to tray spacing (24-inch), tray type (bubble-cap trays) and tray material (stainless steel).

Using cost Equations 21-23, a graph of fixed and operating costs of running the two-column distillation system against reflux ratio factor k is plotted, shown in Figure 13. With increasing reflux ratio

factor, operating cost (i.e. condenser and reboiler duties) rises steadily whilst fixed cost (i.e. cost of distillation columns) decreases sharply at low factor values. The total cost of operation is the summation of both fixed and operating cost. A black cross on the graph indicates the minimum total cost of USD 676,000 at reflux ratio factor of 1.75, which is the optimum point of operation.

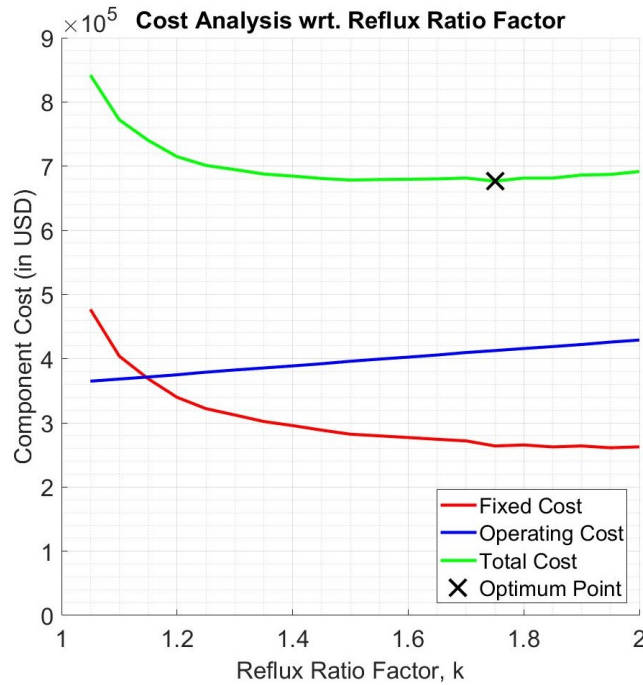


Figure 13: Distillation Column Cost with respect to varying Reflux Ratio Factor

With a reflux ratio factor of 1.75, new McCabe-Thiele plots can be generated for the two distillation columns, which are shown in Figure 14.

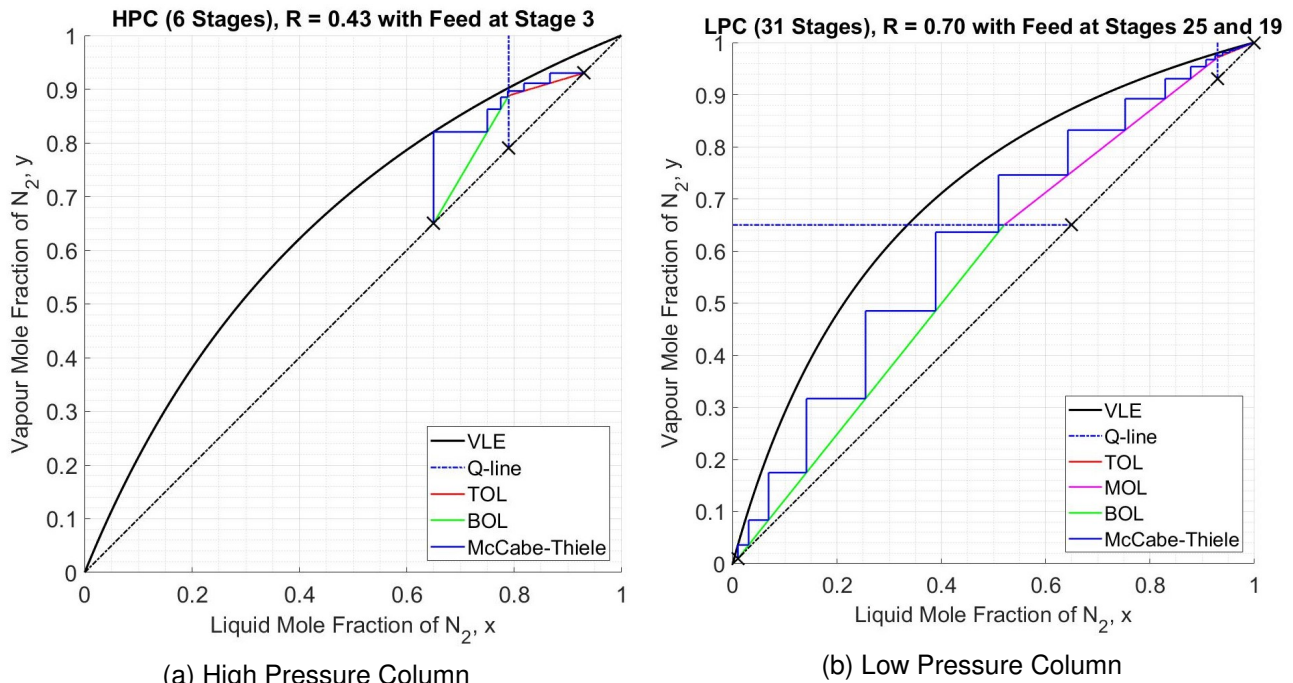


Figure 14: McCabe-Thiele Construction

Total installed cost of compressors can be found by Equation 24 [?].

$$C_{\text{comp}} = \left(\frac{M\&S}{280} \right) (517.5) (P^{0.82}) \cdot (2.11 + F_c) \quad (24)$$

where D is the distillation column diameter , H is the distillation column height and $F_c = 1.00$ is the correction factor that relates to compressor design type (centrifugal compressor). Note that power in the equation is expressed in bhp, hence a conversion factor is applied (1 bhp = 0.7457 kW).

3.3.4 Heat Balance

For a cryogenic distillation system to be efficient, heat duties are to be kept internal within the distillation columns. Heat can be balanced and redistributed to warm up a cold stream (in a reboiler) or cool down a hot stream (in a condenser).

Section 3.2.2 ("Liquefaction Unit") briefly discussed the use of LPC cold product streams to extract heat from inlet air stream, and summarised with a leftover of 728 kW of heat yet to be extracted.

The issue will be addressed in this section.

Reboiler and Condenser Each distillation column has its own set of reboiler and condensers. For simplicity of analysis, they are modelled as heat exchangers such that their duty can be expressed as Equation 25a and 25b respectively, in terms of heat required for vaporise liquid at the top and bottom of the columns.

$$Q_b = V_m \cdot \tilde{h}_{fg} = BR_b \cdot \tilde{h}_{fg} \quad (25a)$$

$$Q_c = V_n \cdot \tilde{h}_{fg} = D(R_c + 1) \cdot \tilde{h}_{fg} \quad (25b)$$

where \tilde{h}_{fg} is the vaporisation heat of mixture, generalised by equation $\tilde{h}_{fg} = xh_{fg,N_2} + (1 - x)h_{fg,O_2}$. Running both columns at reflux ratio factor of 1.75, duty and outlet stream temperatures are tabulated in Table 6 [?].

Table 6: HPC and LPC Heat Duty in kW [Temperature in K]

	HPC	LPC
Condenser	368.75 [96.51]	678.81 [80.21]
Reboiler	-447.77 [100.7]	-595.65 [93.40]

Note that positive heat duties represent heat extraction by the unit (i.e. stream is cooled down) whilst negative heat duties represent heat addition (i.e. stream is heated up).

As previously discussed in Section 3.2.2 ("Distillation Column Reboiler and Condenser"), heat ex-

traction required in HPC condenser can be supplied by LPC reboiler, whilst the heat addition in re-boilers can be supplied by heat exchange with inlet air stream.

Outlet Streams Outlet streams are considered cold when compared to inlet air stream, with LPC distillate stream at 80.21K and LPC bottom stream at 93.40K.

Amount of heat that can be extracted using the two streams can be expressed in Equation 26.

$$\Delta Q = \dot{m}c_p(T_{out} - T_{in}) \quad (26)$$

where specific heat capacity $c_p = 57.62 \text{ Jmol}^{-1}\text{K}^{-1}$ for distillate stream (value for pure nitrogen at 1.4 bar) and $c_p = 54.69 \text{ Jmol}^{-1}\text{K}^{-1}$ for bottom stream (oxygen at 1.4 bar) [?]. T_{out} is taken to be 288K as the streams exit the plant.

Using Equation 26, distillate stream can extract 1001 kW of heat whilst bottom stream can extract 239 kW of heat, which is more than the 728 kW of heat extraction required.

3.3.5 Control

There are several important parameters to control in a cryogenic plant, e.g. input and output flow rates and product streams' purity. As the cryogenic distillation system is designed for a specific flow rate to produce high-purity nitrogen for the Haber-Bosch plant downstream, the main focus of the control session will be on the distillate flow rate of the system.

A conventional reference tracking control loop is shown in Figure 15.

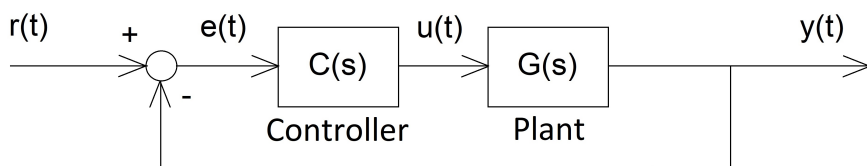


Figure 15: Simple Control Loop for Reference Tracking

System can be modelled using a second-order transfer function, generalised in Equation 27 [?].

$$G(s) = \frac{Ke^{-Ds}}{(1 + \tau_1 s)(1 + \tau_2 s)} \quad (27)$$

where K is the steady-state gain, D is the dead-time of the system and time coefficients are the lag-time.

Using time coefficients from a similar plant, the values are $\tau_1 = 250$ mins and $\tau_2 = 15$ mins respectively.

tively [?]. And for simplicity of analysis, it is assumed that $K = 1$ and $D = 0$.

For controller $C(s)$, a Proportional-Integral-Derivative (PID) controller will be used, generalised in Equation 28.

$$C(s) = P + I \frac{1}{s} + D \frac{N}{1 + N \frac{1}{s}} \quad (28)$$

A step input is used and the control loop is modelled on Simulink, where P , I , D and N values are found using the Simulink tuner. These values, along with the controller performance, are tabulated in Table 7.

Table 7: PID Controller

(a) Parameters		(b) Performance	
P	1.4197	Rise Time	209 min
I	0.0100	Peak Time	471 min
D	-1.7761	Settling Time	782 min
N	0.7993	Overshoot	7.19%

Figure 16 shows the transient performance of the control loop, showing highly unresponsive behaviour to step changes. Settling time of around 12 hours implies that the column should not be subjected to changes lightly.

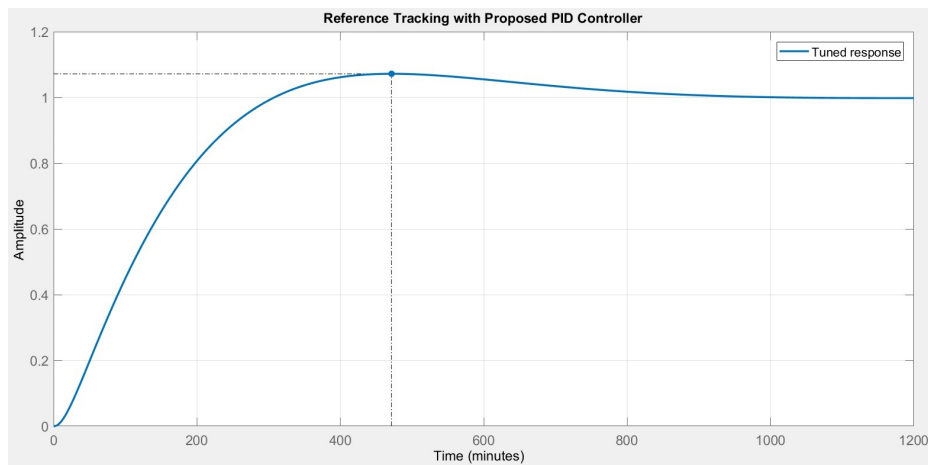


Figure 16: Reference Tracking with Proposed PID Controller

3.4 Safety and Risk

There are a few associated hazards when a cryogenic distillation plant is in operation, namely direct exposure to cryogenic material, oxygen-enriched air, asphyxiation in confined spaces and explosion due to rapid expansion of liquefied gas.

To ensure the safety of workers and general public, a HAZOP study, tabulated overleaf in Table 8, is conducted to identify sources of hazards and methods are devise to reduce the risks.

Table 8: HAZOP Study of the Cryogenic Plant

Guideword	Deviation	Possible Causes	Consequences	Action Required
NO	No feed	- Filter malfunction - Obstruction in pipes or valves - Compressor malfunction	- Halted production	- Regular maintenance of pipes and valves - Regular cleaning or replacement of filter - Regular maintenance of compressor
LESS	Smaller feed stream	- Blocked filter - Obstruction in pipes or valves - Compressor malfunction	- Smaller product streams	- Regular maintenance of pipes and valves - Regular cleaning or replacement of filter - Regular maintenance of compressor
LESS	Lower temperature in columns	- Heat-exchanger malfunction - Reboiler malfunction	- Flooding in trays and liquid sump - Impure products	- Regular maintenance of heat-exchanger and reboilers - Regulate temperature with sensors
LESS	Lower pressure in columns	- Compressor malfunction - Leakage in system	- Impure products - Escape of cryogenic materials - Creation of oxygen-enriched/deficient atmosphere	- Regular maintenance of compressors and leakage testing - Regulate pressure with sensors - Ensure good ventilation in confined spaces
MORE	Larger feed stream	- Damaged filter - Compressor malfunction	- Build up of material in system - Impure products	- Regular maintenance of compressor and replacement of filter - Regulate flow with sensors - Use of pressure-relief valves
MORE	Higher temperature in columns	- Intercooler malfunction - Condenser malfunction - Damaged column insulation	- Expansion of liquid in columns - Impure products - Increased load on condensers	- Regular maintenance of heat-exchanger and condensers - Regulate temperature with sensors
MORE	Higher pressure in columns	- Compressor malfunction - Throttle malfunction	- Impure products - Build up of pressure in columns - Potential explosion	- Regular maintenance of compressors - Regulate pressure with sensors - Use of pressure-relief valves

3.5 Sustainability

The air separation unit takes in atmospheric air as an input, implying that the raw materials are easily accessible and naturally obtainable.

During the pre-processing filtration of inlet air stream, 44 tpy of CO_2 is filtered out using a molecular sieve. But as this small amount of CO_2 is taken out directly from air, the disposal does not contribute to an increase in net CO_2 level in the atmosphere. It is also worth noting that this CO_2 generation is significantly lower than that of conventional coal power plants.

Hence it is suffice to conclude that the air separation operation of this plant has minimal negative environmental impact, and is therefore highly sustainable.

3.6 Costing

The main cost of running a cryogenic plant comes from the capital cost of compressors, capital cost of other components and operating cost of production are relatively low in comparison.

Most cryogenic distillation plants are designed to be self-sufficient by using hot and cold streams effectively, the plant is design to be independent from the grid, hence operating costs are essentially negligible.

A rough estimate on the costings of different plant components are summarised in Table 9.

Table 9: Costing Estimate of Cryogenic Plant Components

Component	Cost (in USD)
Mechanical Air Filter [?]	\$44,000
Molecular Sieve [?]	\$92,000
Compressors [?]	\$8,431,000
Heat Exchangers [?]	\$102,000
Separator [?]	\$50,000
High Pressure Column [?]	\$68,000
Low Pressure Column [?]	\$197,000
Condensers [?]	\$206,000
Reboilers [?]	\$207,000
Total	\$9,397,000

3.7 Conclusion & Further Work

A double-column design is adopted to perform air separation and produce two high-purity product streams continuously. The cryogenic distillation plant is expected to produce around 74,000 tpy of nitrogen at 99.99% purity to be used to synthesize ammonia in Haber-Bosch plant downstream, and 23,000 tpy of oxygen at 99% purity to be used in ammonia gas turbine.

For the plant to be implemented in reality, more in-depth analysis is required in several areas: col-

umn vessel and insulation materials, different operating conditions of columns, alternative liquefaction system and heat balance of streams. Regardless, this section on cryogenic distillation of air was overall successful.

4 Hydrogen Production

4.1 Introduction

Hydrogen gas is required to be fed into the ammonia synthesis process before being converted to energy. The production of hydrogen is currently dominated by the steam reforming of methane gas which depends on the finite fossil fuel resources that also produce greenhouse gases. Water electrolysis combined with renewable energy is sustainable, produces almost zero carbon dioxide and is able to produce hydrogen at a high purity ($> 99.9\%$). However, water electrolysis only represents 4% of global hydrogen productions.[1] This is largely due to high investment cost and energy efficiency problem. There are currently three main types of electrolysis: alkaline electrolysis, polymer electrolyte membrane electrolysis (PEM) and solid oxide electrolysis cell (SOEC). Only the first two types are commercially mature and available. Alkaline electrolysis is chosen because it has the largest power capacity to match the scale of this project. Alkaline electrolysis also has much lower investment cost and larger durability compared with PEM. As the maximum power supply (276MW) is far above the power capacity of any commercial electrolyzers (typical range is 3 - 6MW[2]), multiple electrolyzers are installed in parallel. The main objective of the design is to increase the system efficiency while maintaining the required hydrogen production rate. The aim of this chapter is to lay a theoretical basis, present a detailed model and examine the recent trends in alkaline electrolysis.

4.2 Process Diagram

The process flow diagram in Figure 17 shows the electrolytic cell and its surrounding facilities, including water treatment, electrolyte recirculation, AC to DC rectifier, output gas treatment, and facilities for temperature and pressure control. The electrolytic cell is the most important component and it also consumes most of the energy supplied. A detailed CAD drawing is shown in the next page.

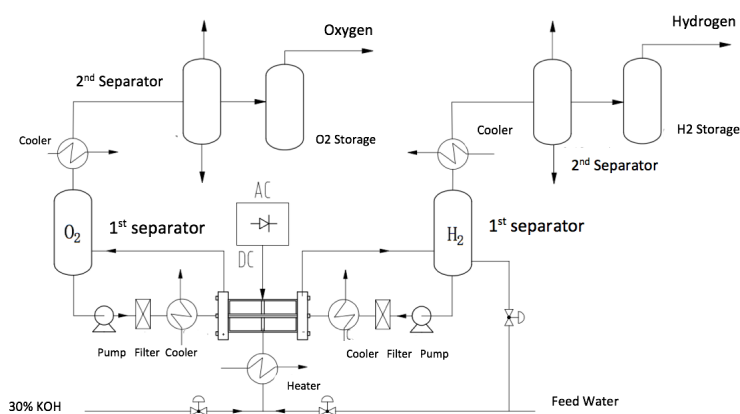
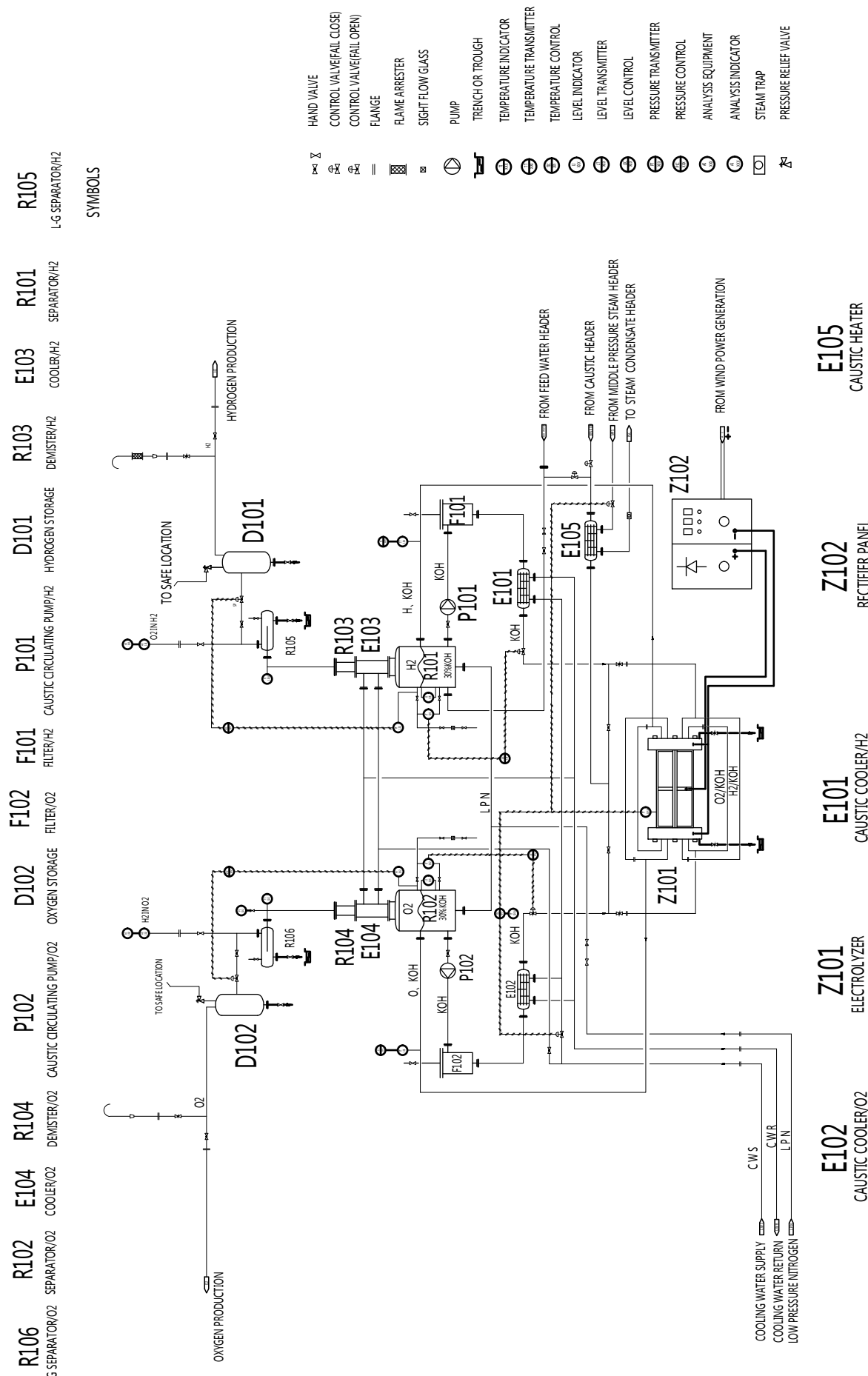


Figure 17: Overview of the system



4.3 Dynamic System Response

Because the power output from the wind farm is variable, intermittent and unpredictable, the electrolyser is required to cover a wide load range (typical load range is 100% - 20%[3]). Some alkaline electrolyzers can operate at a small overload, but they are not considered here because they lower lifetime and efficiency. The lower limit is set for gas purity concerns: if the wind energy is below a minimum limit, the electrolyser can be either shut down or operate at a standby mode (energy is supplied to the stack to maintain a minimum hydrogen production rate).[3] A complete shutdown would require a time-consuming start-up process while operating at the standby mode lowers efficiency, and therefore a compromise has to be made. In this model, the electrolyzers have multiple stacks that can be shut down independently and automatically in order to reduce the minimum power input requirement and thus improve the system flexibility. In addition, the electrolyser also needs to have a fast response in order to capture the peaks of the energy supply. Despite the dynamic nature of hydrogen production, the hydrogen consumption rate of the ammonia synthesis process is constant and therefore a hydrogen storage system is also required to store the excess energy.

4.4 Specification

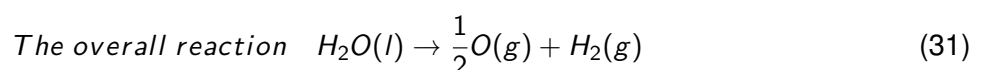
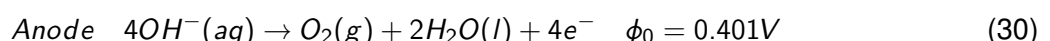
In industry, the typical electrical energy input efficiency is 54 kwh/kg_{H_2} .[4] The mean hydrogen production rate is set at a surplus to the hydrogen consumption rate to ensure that a constant hydrogen flow from the storage can be achieved. The water conversion rate is assumed to be 80%. Table 10 shows the flow rate and power requirement as well as the system and dynamic operation parameters. The hydrogen purity requirement is high because oxygen could adsorb on the surface of the ammonia synthesis catalyst and poison it. [5]

Table 10: System Specification

Flow rates & Power			
Maximum	H_2 flow rate($kmol/s$)	H_2O consumption(m^3/h)	Power(MW)
Mean	0.71	65.7	276
Minimum	0.25	23.6	99
System & Dynamic			
Purity	99.5 to 99.9998 %	System Lifetime	25 years
Ramp-up %($fullload$)/second	10	Ramp-down %($fullload$)/second	10
Start-up time	20min	Load range	20% - 100%

4.5 Fundamentals

Electrolysis is a non-spontaneous redox reaction that is carried out in the electrolytic cell, with the electrolyser filled with electrolytes (anion and cation) to improve conductivity. When a DC current passes through the electrodes, hydrogen is produced at the cathode, and oxygen is generated at the anode. The electrolyser is divided into the anode chamber and the cathode chamber by the diaphragm, with electrodes placed in each chamber. The reaction in alkaline solution is as follows:



The molar rate of hydrogen production for cells connected in series can be determined by considering Faraday's law, which presents as:[2]

$$f_{\text{H}_2} = \eta_F \frac{N_{\text{cell}} I_{\text{cell}}}{zF} = \eta_F \frac{N_{\text{cell}} j A}{zF} \quad (32)$$

where η_F is the Faraday efficiency, F is Faraday's constant, z is the number of electrons transferred(2 in this reaction). N_{cell} is the number of cells, I_{cell} is total current, j is current density, and A is cell area. It is shown in the equation that the production rate is directly proportional to the current.

4.5.1 Thermodynamics

The electrolysis process is an endothermic reaction, the enthalpy change is expressed as:[2]

$$\Delta H = \Delta G + T \Delta S \quad (33)$$

where ΔG is the Gibbs free energy change, which is the energy required to split water and is therefore the minimum electrical energy required. $T \Delta S$ represents thermal energy, and ΔS is the change of the reaction entropy. Under standard conditions (1 atm, 25° C), $\Delta H^0 = 285.8 \text{ kJ/mol}$, $\Delta S^0 = 163.14 \text{ J/mol}$. Therefore, $\Delta G^0 = 237.2 \text{ kJ/mol}$.[2] With increasing temperature, the energy required for decomposing water is reduced. This is why high temperature electrolysis method is adopted for the electrolysis process. The minimum voltage required (the reversible voltage) can be calculated by:[2]

$$U_{\text{rev}} = \frac{-\Delta G}{zF} \quad (34)$$

The reversible cell voltage at standard condition is therefore 1.23V. In reality, the actual voltage required is usually greater than this due to irreversibility. Therefore it is important to consider the thermoneutral voltage, which is the voltage at which the reaction is neither endothermic nor exothermic.

$$U_{tn} = \frac{-\Delta H}{zF} \quad (35)$$

At standard conditions, $U_{tn} = 1.48V$. Between 1.23V and 1.48V, the reaction is endothermic.

4.5.2 Reversible Voltage

The reversible cell voltage is the minimum potential required for water decomposition, and it can be calculated by:[1]

$$U_{rev}(T, p) = U_{rev}(T) + \frac{RT}{zF} \ln \left[\frac{(p - P_w)^{1.5} P_w^*}{P_w} \right] \quad (36)$$

The first term represents reversible voltage at atmospheric pressure and can be shown as:[1]

$$U_{rev}(T) = 1.50342 - 9.956 \times 10^{-4}T + 2.5 \times 10^{-7}T^2 \quad (37)$$

The second term shows the effects of pressure due to the wet gases being in contact with the electrolyte vapour near the electrode, which is a function of electrolyte vapour P_w and pure water pressure P_w^* . R is the universal gas constant.[1]

$$p_w = T^{-3.498} \exp \left(37.93 - \frac{6426.32}{T} \right) \exp(0.016214 - 0.13802M + 0.19330\sqrt{M}) \quad (38)$$

$$p_w^* = T^{-3.4159} \exp \left(37.043 - \frac{6275.7}{T} \right) \quad (39)$$

where M is the molarity of the electrolyte solution, and it can be expressed as a function of temperature and concentration($W_t\%$) by:[1]

$$M(T, W_t\%) = \frac{W_t\% (183.1221 - 0.56845T + 984.5679 \exp(W_t\%/115.96277))}{100 \times 56.105} \quad (40)$$

Figure 18 shows the effects of temperature and pressure on reversible voltage as well as the variation of P_w and P_w^* with temperature.

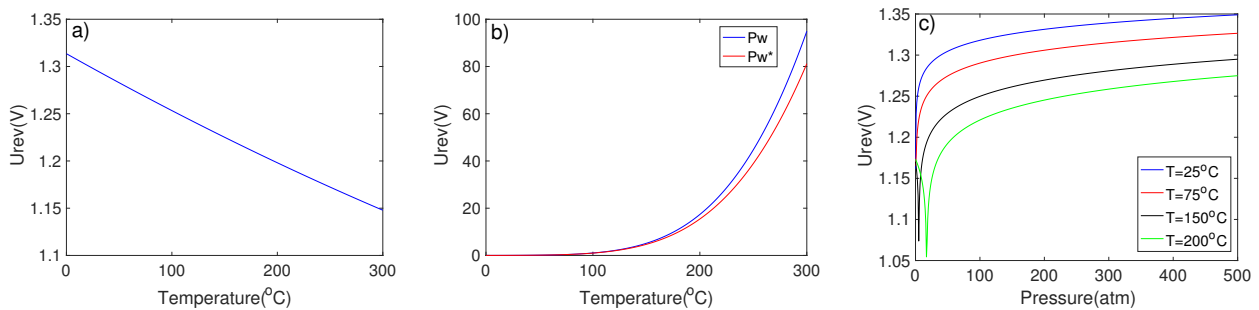


Figure 18: a) Variation of reversible voltage with temperature; b) P_w and P_w^* with temperature; c) pressure at various temperature, assuming 25% concentration

4.5.3 Electrochemistry

The actual cell voltage would be higher than the reversible energy as a result of irreversibility of the process. The cell voltage is the sum of reversible voltage, overpotential due to ohmic losses, activation overpotential and concentration overpotential. The concentration overpotential is small and therefore not considered in this model.

$$U_{cell} = U_{rev} + U_{ohm} + U_{act} + U_{con} \quad (41)$$

4.5.4 Ohmic Overpotential

Each component in the electrolytic cell can be modelled as an electrical conductor. When current passes through the conductors, there is ohmic power loss due to the resistivity of the conductors which will lead to a heating effect. Since the electrolysis reaction is endothermic, some of the heat can be utilised within the system. While most ohmic energy is lost in the electrolytic solution, the membrane, wirings, electrodes and bubble effects also form part of the electrical resistance. The heat generated can be evaluated by $Q = UI = I^2R$, where R can be computed by:

$$R = \frac{I}{A\kappa} \quad (42)$$

where $\kappa (S/m)$ is the conductivity of the solution.

The total ohmic loss is the sum of all components in the electrolysis cell.

$$R_{total} = R_{electric} + R_{anode} + R_{cathode} + R_{bubble} + R_{ions} + R_{membrane} \quad (43)$$

For the electrolytic solution, the area specific resistivity of the electrolyte can be calculated by:[6]

$$r_{ions} = \frac{\delta_{el}}{\sigma_{el}(T, M)} \quad (44)$$

where δ_{el} represents the electrolyte layer thickness and σ_{el} represents the conductivity of the solution which varies with temperature and molarity. The conductivity of electrolyte varies with temperature, concentration and composition. The specific conductivity of electrolyte (S/m) can be estimated by:[6]

$$\sigma_{el} = (A(M) + B(M^2) + C(MT) + D(\frac{M}{T}) + E(M^3) + F(M^2T^2)) \times 100 \quad (45)$$

where M represents the molarity in mol/L, and T is Temperature in Kelvin, and A-F are constants.

It can be seen from Figure 19 that the conductivity increases when concentration is higher, this is

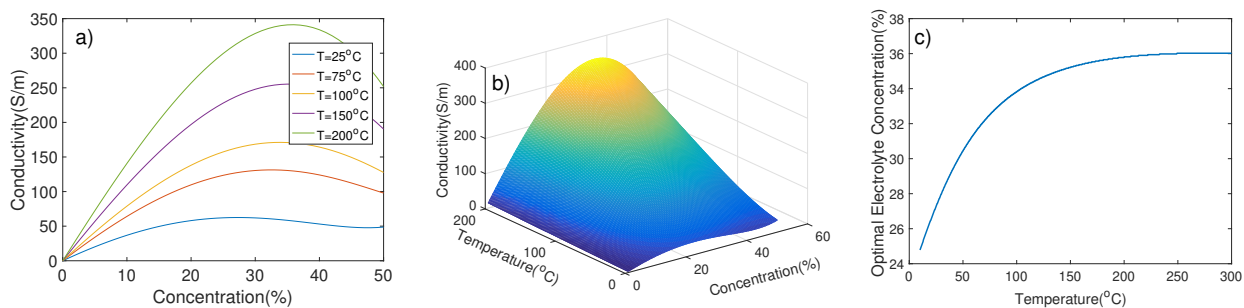


Figure 19: a) Variation of conductivity with temperature and concentration. b) 3D plot. c) the optimal concentration of electrolyte with temperature

due to the increase in the number of unit ions per volume in the solution. However the conductivity of the solution has a limit, and once that limit is reached, the conductivity starts decreasing with increasing concentration. It can also be shown that the conductivity increases with increasing temperature, because an increase in temperature may also cause an increase in the number of ions in solution due to dissociation of molecules. Also noteworthy is the existence of an optimal concentration which increases with increasing temperature: at above 200 degree Celsius, the optimal concentration reaches around 36%. In reality, the electrolyte concentration is usually around 25 - 30 % due to considerations on corrosion. The ohmic overpotential from electrolytic solution is therefore:

$$U_{ohm} = r_{ions} \times J \quad (46)$$

where J is the superficial current density.

4.5.5 Resistance of the Membrane

An empirical fitting of the resistance of the 0.5mm Zirfon based membrane and the temperature is presented as:[7]

$$R_{mem} = \frac{0.06 + 80e^{T/50}}{10000S_m} \quad (47)$$

where Sm is the membrane surface in cm^2 .

4.5.6 Activation Overpotential

In reality, the efficiency of alkaline electrolysis is further reduced by electrode kinetics, making the actual electrode potential higher than the reversible potential. The difference is called the activation overpotential. This represents the kinetic barriers that need to be overcome for the gas evolution reactions at each electrode. Various experiments have shown that the overpotential for oxygen evolution reaction (OER) is much higher than for that the hydrogen evolution reaction (HER), and it depends heavily on the catalytic properties of electrode materials. [8] There are many other factors that influence the overpotential, including temperature, current density, concentration and impurity of the solution. The corresponding current density can be calculated using the Butler-Volmer equation: [9]

$$J = J_0[e(\frac{\alpha_a}{RT}zFU_{act,a}) - e(\frac{\alpha_c}{RT}zFU_{act,c})], \quad (48)$$

where J is the current density, J_0 is the exchange current density, which represents current at equilibrium, the oxidation and reduction reaction rates are opposite and equal, resulting in zero net current, and $\alpha_{a/c}$ is the charge transfer coefficients. The charge transfer coefficients are related by temperature by:[7]

$$\alpha_a = 0.0675 + 0.00095T, \alpha_c = 0.1175 + 0.00095T \quad (49)$$

For large overpotential, this can be approximated by the Tafel equation[10]

$$U_{act,a/c} = 2.3026 \frac{RT}{zF\alpha_{a/c}} \log\left(\frac{J}{J_0}\right). \quad (50)$$

The exchange currents density is found experimentally, which can be significantly different depending on the electrode composition and temperature. The activation overpotential can be decreased by using catalysts, and this will be discussed later in the report. The activation overpotential at cathode and anode and the effects of temperature are shown in Figure 20 . It can be shown that the activation overpotential increases with temperature, but this effect is quite small.

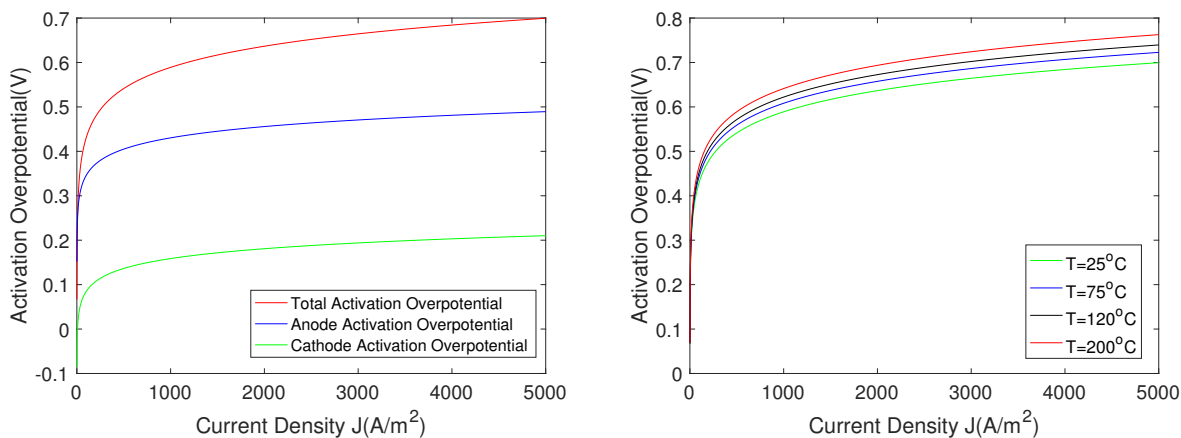


Figure 20: Activation Overpotential at cathode and anode(left); effects of temperature(right)

4.5.7 Bubble Effects

When hydrogen and oxygen are produced at the electrodes, bubbles will partially adhere to the electrodes, making a fraction of the surface electrochemically inactive so that current is applied to a smaller area. The effective surface area of the electrodes is:[11]

$$S_{eff} = S(1 - \theta) \quad (51)$$

where θ is the bubble coverage ratio on electrode surface, with values between 0 and 1. As a result, the actual current density is greater than the superficial one, their relationship is:[11]

$$J_a = \frac{J}{S_{eff}} = \frac{J}{1 - \theta} \quad (52)$$

where J_a is the actual current density, J is the superficial current density. An empirical equation has been developed from experimental data that relates bubble coverage and superficial current density [11]

$$\theta = 0.023\left(\frac{J}{A m^{-2}}\right)^{0.3} \quad (53)$$

Apart from current density, the bubble coverage also depends upon several other factors such as the rate of gas evolution at the electrode surface.[11] The total activation potential combined with bubble effects can be calculated by[7]

$$U_{act-\theta} = 2.3026 \frac{RT}{zF\alpha_{a/c}} \log\left(\frac{J}{J_0}\right) - 2.3026 \log(1 - \theta) \quad (54)$$

where the second term on the RHS represents the bubble effects. Another important effect of bubble formation is the reduction of electrolyte conductivity, which will increase the ohmic resistance of

the electrolyte. The effective conductivity can be calculated using the Bruggman equation:[12]

$$\sigma_B = \sigma_0(1 - \alpha_{total})^{1.5} \quad (55)$$

where α_{total} is the void fraction, which is the fraction of volume occupied by the gas. σ_0 is the conductivity without any bubbles and α_{total} is the total void fraction. Unlike many other models that were developed from assuming equal-sized spheres, the Bruggman model was derived assuming many different bubble sizes. As can be seen from Figure 21c), the conductivity reduces rapidly with increasing void fraction. When temperature = 120°C for example, a void fraction of 0.37 halves the conductivity. The void fraction is related by bubble coverage by[10]

$$\alpha_{total} = \frac{2}{3}\theta \quad (56)$$

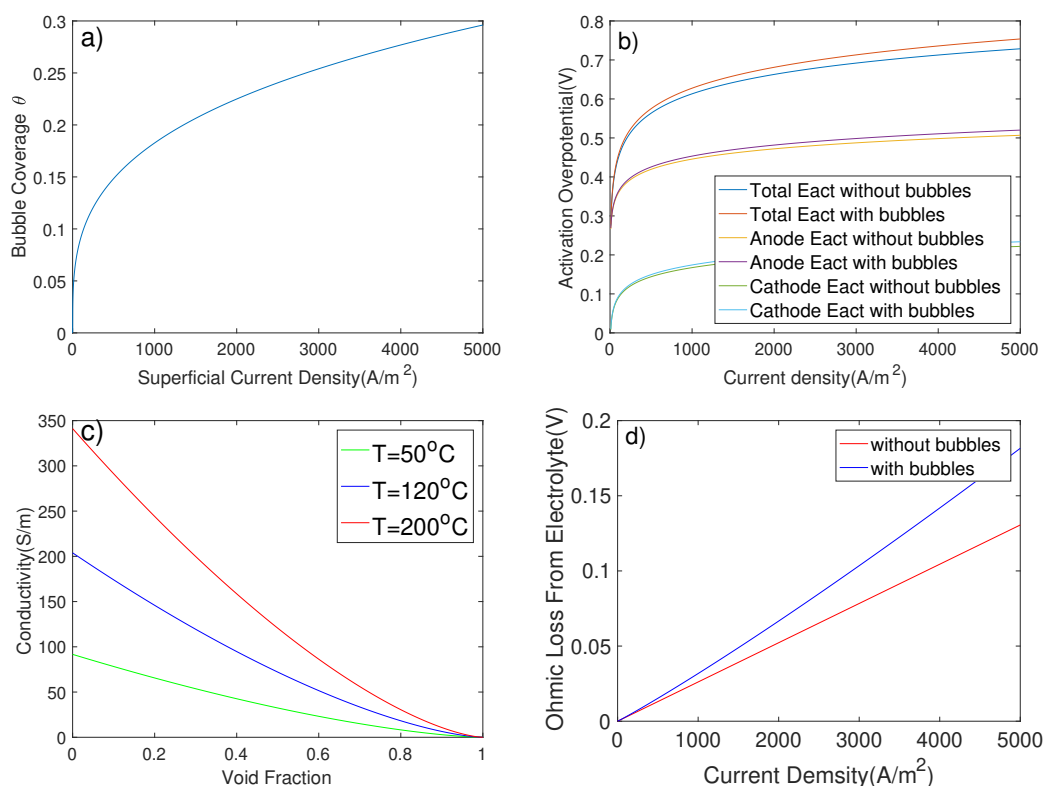


Figure 21: a)Bubble coverage against current density. b) Activation Overpotential taking into account the bubble effects at electrodes against current density. c)Conductivity against void fraction d) Ohmic voltage loss from electrolyte with and without bubbles

4.5.8 Overall Cell Voltage and Optimum Operating Conditions

The polarisation curve of the alkaline electrolysis cell is plotted in Figure 22a), it is observable that the total cell voltage increases with higher current density. This is largely due to the increased contribution from ohmic losses, especially from bubble formation, whereas the curve for activation po-

larisation actually becomes flatter at higher current density. This means that a lower current density will lower the energy consumption and thus increase the system efficiency. However, the hydrogen production rate, which increases with higher current density, is also an important factor to consider along with the system efficiency. Electrolyser degradation and safety issues also influence the choice of current density. The rate of electrolyser degradation increases rapidly with higher current density and this will thus increase the investment cost. The large amount of heat produced as a result of higher current density, if poorly managed, can be dangerous. In addition, gas crossover is more significant at low current density, and this is because although the amount of gases crossing over the membrane remains the same, there are smaller amounts of gases produced to dilute the effects. The result is a highly flammable mixture once it reaches a certain limit. In industry, a compromise has to be made. The current density is usually kept between $1000 - 3000 A/m^2$. [13]

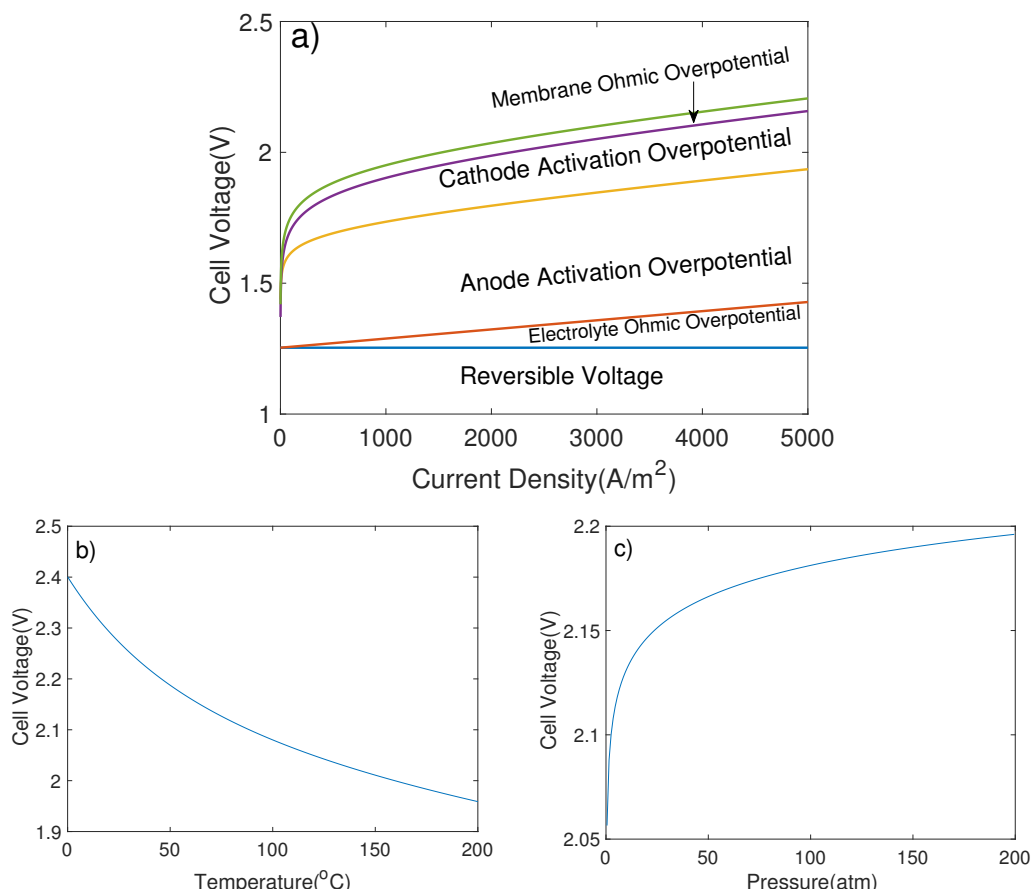


Figure 22: a) Total cell voltage showing cumulative effects of reversible voltage, activation and ohmic overpotential. b) Total cell voltage against temperature. c) Total cell voltage against pressure

Raising the operating temperature is one of the most effective ways to improve efficiency. As can be seen in Figure 22 b), increasing the operating temperature reduces the cell voltage, as a result of decreased reversible voltage, higher ionic conductivity, and lower activation overpotential due to enhanced electrode surface kinetics. However, a high temperature can lead to high corrosion risk

which will require more expensive materials. Also, the water loss from evaporation increases with higher temperature. Conventional electrolysis system is operated around 80 - 90°C, just below the boiling point of water.[14] There are two major ways to further elevate the operating temperature, the first way is to use a pressurised system which will increase the boiling point of electrolyte, and in industry this is usually kept at 120-150°C.[14] The second way is to carry out steam electrolysis which can increase the temperature even further to a level of above 500°C.[14] However this method has not become commercialized in industry due to its high economic cost.

Pressure is another very important parameter, increasing operating pressure has several positive effects apart from allowing for higher operating temperature. A high pressure would reduce the size of bubbles, and gases increase in solubility with increased pressure. This will reduce the ohmic loss from bubble formation. Obtaining pressurised hydrogen is also more energy efficient during the compression process. Also, higher operating pressure makes the process of hydrogen drying easier. However, at high pressure, there is more gas crossover due to diffusion since the partial pressure of both gases have increased. A high pressure also slightly increases the operating cell voltage. In industry, hydrogen production at a pressure of up to 30 bar is commercial available, and this can be achieved by using a feed-water pump.[2]

4.5.9 Electrolyser Efficiency

Efficiency is one of the key design objectives for the electrolysis system. There are three main efficiencies to consider depending on how the system is assessed.[13] The voltage efficiency is the proportion of effective voltage for water decomposition to the overall cell voltage and presents as:

$$\eta_{voltaic} = \frac{E_{anode} - E_{cath}}{U_c} \quad (57)$$

A more commonly used expression is the Faradic efficiency, which relates the reversible voltage to the overall cell voltage, it also represents the percentage of the actual to theoretical hydrogen production. Its value is usually lower than 1 which means that there exist the consumption of energy that does not contribute to the hydrogen production due to the parasitic currents in the system. [13]

$$\eta_{Faradic} = \frac{\Delta G}{zFU_c} = \frac{U_{rev}}{U_c} \quad (58)$$

The thermal efficiency takes into account the thermal energy and can be calculated by

$$\eta_{Thermal} = \frac{\Delta H_{t,p}}{zFU_c} = \frac{U_{th}}{U_c} \quad (59)$$

where $\Delta H_{t,p}$ is the enthalpy change of water decomposition. The thermal efficiency is 100% if the cell voltage is equal to the thermoneutral voltage. When cell voltage is higher than U_{th} , the efficiency is lower than 100%, and the process is exothermic. A thermal efficiency of over 100%, which is when the cell voltage is below the thermoneutral voltage, is theoretically achievable in high temperature steam electrolysis but is generally unpractical for alkaline electrolysis system. Under standard conditions, $U_{rev} = 1.23V$ and $U_{th} = 1.48V$. The relationship between U_{rev} and U_{th} against current density is plotted in Figure 23 a).

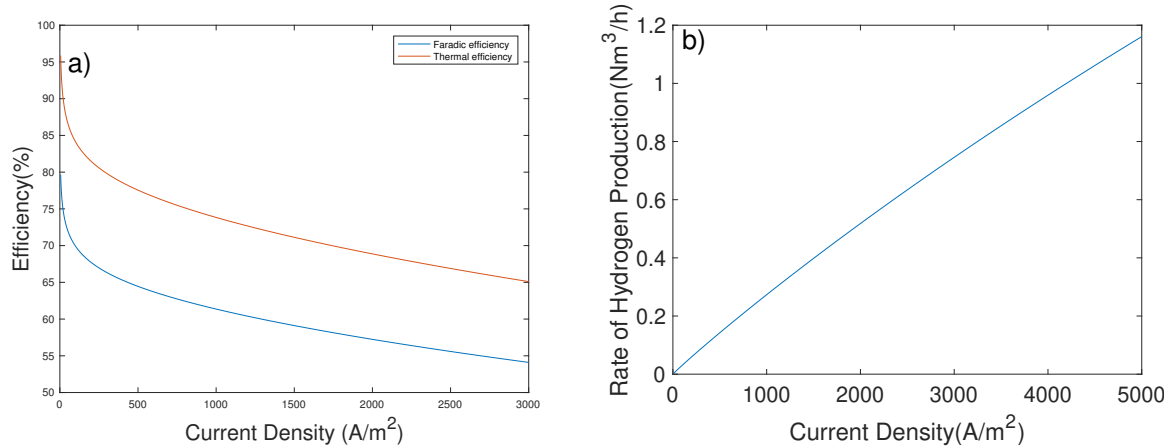


Figure 23: a)Comparison of Faradic and Thermal efficiency. b)Hydrogen production rate (single cell)

As discussed before, a compromise has to be made between efficiency and hydrogen production rate, which is shown in Figure 23 b).

Another important parameter for the electrolysis process is the specific energy consumption, which can be calculated for a given time interval t as:[15]

$$C_E = \frac{\int_0^t N_{cell} I_{cell} V_{cell} dt}{\int_0^t f_{H2} dt} \quad (60)$$

Finally, the electrolyser efficiency or the HHV efficiency can be calculated using the specific energy consumption by:[15]

$$\eta_E = \frac{HHV \text{ of Hydrogen}}{C_E} \quad (61)$$

where HHV is the higher-heating-value of hydrogen. It assumes that the energy absorbed by water can be released and reused in the system by converting water back to its initial standard conditions. However, recovering the full higher-heating value is not practical in reality. The electrical-energy effi-

Table 11: Operating conditions and key parameters.

Temperature	120 – 150°C
Cell area	1m ²
Pressure	30 bar
Membrane thickness	0.5mm
Electrode thickness	2cm
Electrode height	45cm
Electrolyte and Concentration	KOH 30%
Minimum/Maximum current density	1500/5000 A/m ²
Minimum/Maximum Cell voltage	1.98/2.25V
η_F at Minimum/Maximum load	62% / 56%
$\eta_{Thermal}$ at Minimum/Maximum load	75%/67%
HHV efficiency at Minimum/Maximum load	76%/68%
Minimum/Maximum Flow rate(per cell)	0.0048mol/s ⁻¹ /0.0145mol/s ⁻¹

ciency can be calculated using the higher-heating voltage.[16] [15]

$$\eta_E = \frac{V_{HHV}}{V_{cell}} \quad (62)$$

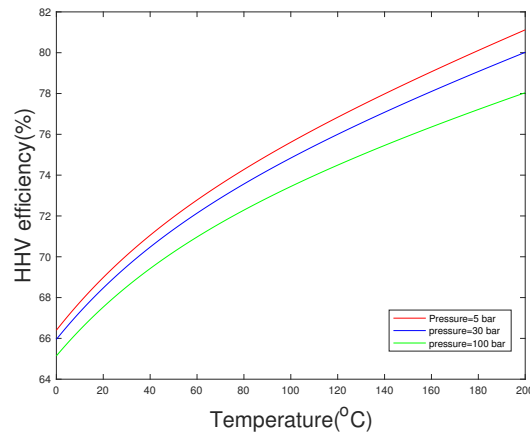


Figure 24: Variation of HHV efficiency against temperature at different pressure

The HHV efficiency at different temperatures and pressures with fixed current density is shown in Figure 24, It can be seen that the efficiency increases with increasing temperature and decreases with pressure. A summary of operating conditions and key parameters are shown in Table 11.

4.6 Electrolyser Design

4.6.1 Configuration

Currently there are two types of electrolyser configuration: unipolar and bipolar, which is shown in Figure 25. In a unipolar configuration (or tank-type), the electrodes with the same polarity are connected in parallel, therefore the total cell voltage is the same as the voltages of individual cells, and

Table 12: Pros and cons of monopolar and Bipolar configuration.[17] [15]

Unipolar	Bipolar
Advantages	
Simple design and therefore easy to fabricate	The compact structure reduces electrolyte ohmic loss, thus improves efficiency
Do not have parasitic currents	Operate at higher temperature and pressure
Cells can be individually isolated and carry out maintenance	Operate at higher current density which increases rate of production
Low maintenance requirement	Small requirement in space
Disadvantages	
Large Ohmic losses due to high currents and low voltages	Parasitic currents which cause efficiency loss and corrosion problems
Large space required	High requirements in precision and complex system design
Large limitation in raising operating temperature and pressure	Production needs to be stopped for maintenance
Difficult to achieve small interelectrode gaps	Requirement for electrolyte circulation
Heavy intercell busbars	Requirement for external gas/electrolyte separator

the total current is the sum of currents in each cell. A bipolar electrolyser usually has a larger number of cells with the electrodes connected in series, and the electrodes each have both the positive and negative polarities. So current is the same in each cell and at the terminals. Unipolar electrolyzers operate at a low voltage level of 1.9 - 2.5 V,[18] but they require a high level of current. On the other hand, bipolar configuration requires a low current but a voltage of $V_{cell} \times (n - 1)$, which is about 35-600V.[18] V_{cell} is the voltage for each cell and n is the number of electrodes. The industrial electrolyzers are mostly bipolar electrolyzers. The pros and cons of each type of configuration are shown in Table 12.

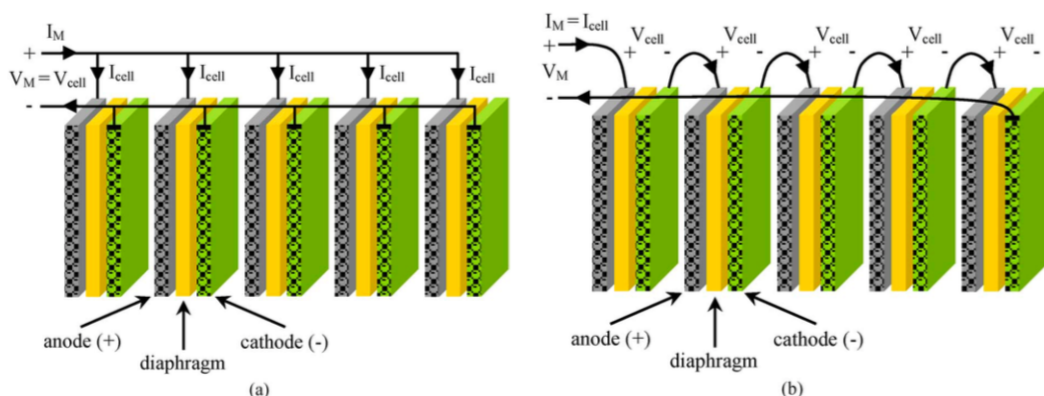


Figure 25: Electrolyser configuration a)Monopolar configuration; b)Bipolar configuration.[18]

4.6.2 Cell Geometry

Apart from adjusting the operating conditions, proper choice of cell geometry is another way to improve performance. Some of the key design parameters include size of inter-electrode gap, height and inclination of electrodes. The smaller the gap between the electrodes, the smaller the volume of the electrolyte and thus the lower the ohmic overpotential. However, in the conventional configuration, reducing the inter-electrode gap could increase the contribution of cell resistance from gas bubbles, making the optimal gap to be larger than 2mm. This problem can be solved by adopting zero-gap configuration.[19]A series of experiments[20] were conducted to identify the effects of electrode height and inclination, and it has been found that although selecting larger electrodes will enlarge the surface area and thus the current path, when the current density is large, higher efficiency can be achieved using smaller electrodes. This is because bubbles tend to accumulate at higher parts of the cell, increasing the void fraction. The experiments also showed that placing the electrodes at perfectly vertical position reduces the ohmic overpotential.

Zero-gap Configuration The zero gap cell involves two porous electrodes that are compressed and in contact with the membrane (Figure26), making the inter-electrode gap the same as the thickness of the membrane(< 0.5 mm).[19]The bubbles are released from the rear of the electrodes, which also reduces the contribution of cell resistance from the gas bubbles. Between the porous electrode and the bipolar plate is the gas diffusion layer, which not only provides an electrical connection, but also allows the feed of the electrolyte and the release of oxygen and hydrogen.This configuration can be assembled by depositing a catalyst layer onto the electrode, and then compressed onto the membrane, and finally gaskets are assembled to avoid leaking.The disadvantage of this configuration is the increased potential for the gas bubbles to block the electrode-membrane interface.

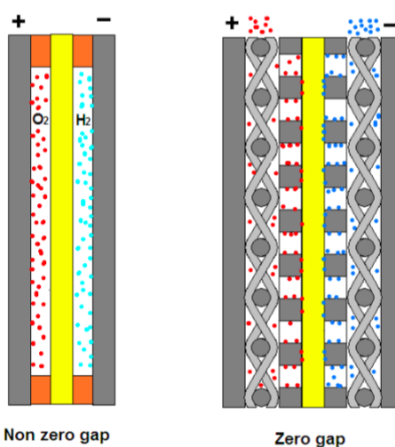


Figure 26: Zero-gap and non zero-gap configuration[23]

4.6.3 Electrode Material

The anode material must have good conductivity, high catalytic activity, good mechanical stability, resistance to electrolyte corrosion, in addition to an acceptable cost. Currently, the most commonly used anode is nickel or nickel based alloy. Nickel has good corrosion resistance compared with stainless steel or iron electrode and low price in alkaline medium. At the same time, nickel has high oxygen evolution potential and high oxygen evolution efficiency. One way to improve efficiency is to increase the electrode surface area in order to reduce the real current density and thus the activation overpotential. For example, a porous anode can be developed by sintering nickel powders, it has been shown that the porous high-surface area anodes have lower oxygen evolution overpotential than smooth anodes under elevated temperature and pressure (30 bars, 200°C). Sintered, porous nickel coating is another way to reduce overpotential which involves a lower sintering temperature. It has also been shown that an increase in coating thickness will raise the exchange current density and reduce the overpotential. Comparable effects in overpotential reduction can be achieved by using Raney alloys such as Raney nickel, Raney cobalt or Raney nickel-cobalt which will be covered with Ni or Co oxides during electrolysis.[21] [22]

The cathode materials for hydrogen production in early age were mainly Pt, Pd and its alloys. Although these alloys have very low hydrogen evolution overpotential, they are expensive and can not be widely used to popularise. So industry prefers inexpensive, low hydrogen overpotential alternatives such as Raney nickel or nickel based alloys like NiMo, NiSe and NiS_2 . For cathode, the electrocatalyst's behaviours depend on its ability to adsorb hydrogen atoms, which is related to the strength of the metal hydrogen bond (M-H). [23] A stronger M-H bond would reduce the HER activation energy. However, if the adsorption energy is too high, the desorption of hydrogen becomes difficult. Therefore, a suitable M-H bond strength is required for the cathode. It can be seen from Figure

27 that Pt has the highest activity, and Ni also have suitable bond strength while being inexpensive at the same time. Zhang et al.[24] compared the electrocatalytic activities of several nickel-based alloys (Ti/NiM where M represents different metals and Ni foil is the substrate). It can be shown from Figure 28 that Ti/NiPt electrode has the highest catalytic activity, and they are all relatively stable. Ti/NiCo is the most suitable choice when electrolytic activity, stability and cost are all taking into account. In this model, Raney nickel anode and Ti/NiPt cathode are adopted.

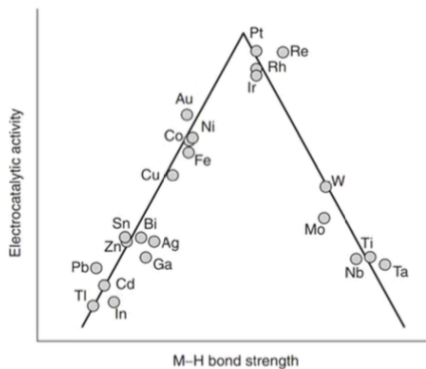


Figure 27: Electrocatalytic activity against M-H bond strength[23]

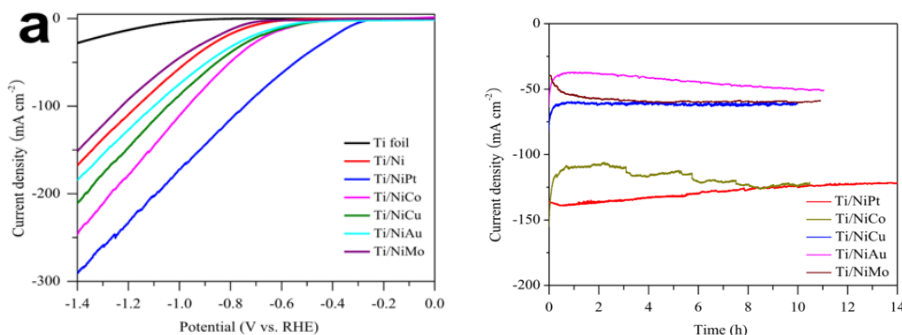


Figure 28: Polarization curve for Ti/NiM electrode(left); Long term stability of catalytic Ti/NiM electrode for HER recorded at 1V(right) [24]

4.6.4 Electrolyte and Ionic Activator

The selection criteria for the electrolyte include: high ionic conductivity; does not decompose chemically under supplying voltage; lower volatility so is not removed with the product gas. Alkaline electrolyte is adopted instead of acid electrolyte because the alkaline electrolytes have less issues with corrosion. KOH and NaOH solutions are common electrolyte choices, and KOH solution has higher specific conductivity than NaOH and is therefore used in this model. Although re-circulation of electrolyte is designed, there will be some electrolyte loss in reality through gases. It is therefore necessary to adjust the amount of electrolyte in the cell. The energy consumption can be further reduced by the addition of an ionic activator. Lj et al. [25] investigated the effect of adding an Novel

ternary Ni – Co – Mo based ionic activator to the alkaline KOH solution. It has been found that the electrolyzer with in-situ activated electrolyte has an efficiency about 15% higher than the standard KOH solution, and an energy consumption saving of about 17%. The energy saving is proved to be more efficient at higher temperatures and current densities. During electrolysis, metal composites are electrodeposited in-situ on cathode surface and exhibit better catalytic activity for hydrogen evolution reaction than those electro- deposited ex-situ.

4.6.5 Separator

The diaphragm (or microporous separators), which is made of electrically insulating and hydrophilic materials, is used to separate the cathode and anode to prevent short circuit. The diaphragm also needs to be have high ionic conductivity for the hydroxide ions to pass through, while preventing the diffusion of hydrogen and oxygen gas bubbles, as well as unhindered intermixing of hydrogen saturated catholyte and oxygen saturated anolyte. Other requirements include low ohmic resistance and high resistance to corrosion in the alkaline environment. Asbestos membrane was used for a long time in the industry, however it has low resistance to corrosion and was forbidden because of its toxicity. A large number of inorganic and organic substitutes have been studied and currently Zirfon is the most widely used diaphragm. It contains the hydrophilic and inorganic ZrO_2 power and polysulfone network to increase the mechanical strength. The typically thickness of Zirfon diaphragm is 0.3mm, which is much thinner than the asbestos diaphragms. It also has a low ionic resistance($0.1\text{--}0.2\Omega cm^2$)[26] In industry, the Zirfon diaphragm usually has a temperature limit of 120°C.[27]

Ion exchange membrane can also be used as separator in water electrolysis, with the cation exchange membranes being more resistant than anion exchange membranes in alkaline environment and at elevated temperature. The cell is divided into two hydraulically separated compartments. The cation exchange membranes have negatively charged functional groups such as $-SO_3^-$ or $-COOH$, and therefore only allows cations to pass through. [28] The typical pores size is about 10^{-9} to 10^{-8}m .[29] Nafion perfluorosulfonate ion exchange membrane demonstrates promising performance. It has been shown that the performance can be improved by reducing the separator thickness, and increasing the operating temperature. One advantage of this type of separator is that it allows a very high operating temperature (220 - 250 °C) before it loses stability.[30] However, the biggest disadvantage is the high cost.[31]

4.6.6 Ultrasound-aided Electrolysis

Another way to enhance the energy efficiency is through coupling electrolysis with ultrasonic field. Li et al.[32] investigated the effects of ultrasound on alkaline water electrolysis. The results showed that the cell voltage was lower in the presence of ultrasound, especially at higher current density and lower electrolyte concentration. The experiment also indicated that the enhancement of the efficiency was generally greater at higher electrolyte concentration. The efficiency of Hydrogen production was increased in the range of 5 to 18% at higher current density under ultrasonic field and energy saving was up to 10 to 25%. Other forms of external fields, such as magnetic field and super gravity field also have the effects of improving energy efficiency. The application of external field is useful because it accelerates the bubble detachment in the process. [33]

4.7 Stack Number

The electrolyzer is designed so that the maximum hydrogen flow rate can be achieved (with a slight surplus) when all electrolyzers are turned on and switched to their full capacity. Assuming a typical cell area of 1 m^2 . The total number of cells required is 48970. Theoretically it is preferable to use a larger number of stacks with fewer cells in one stack, since this can reduce the power loss by reducing the minimum allowed input power. However, the cost of a large amount of stacks could be quite high and they would also take up a large amount of space. Figure 29 shows the theoretical cumulative hydrogen production in January with different stack number. It can be seen that when the stack number is above 200, the hydrogen waste is less than 5%. Therefore a stack number of 200 (which could be divided into different electrolyzers) and 245 cells per stack is an appropriate choice.

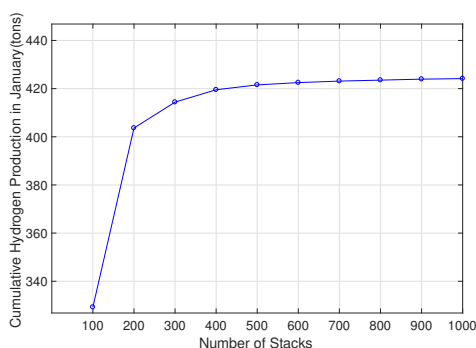


Figure 29: Theoretical cumulative hydrogen production in January against number of stacks

4.8 Thermal Model

A lumped thermal capacitance model is established to determine the temperature of the electrolyte, which affects the V-I characteristics and system efficiency. The general energy balance can be rep-

resented by:[1]

$$C_t \frac{dT}{dt} = \dot{Q}_{gen} - \dot{Q}_{exch} - \dot{Q}_{cool} \quad (63)$$

where

$$\dot{Q}_{gen} = N_c(U - U_{tn})I \quad (64)$$

$$\dot{Q}_{exch} = \dot{n}_{H_2} C_p^{H_2}(T - T_a) + \dot{n}_{O_2} C_p^{O_2}(T - T_a) + \dot{n}_{H_2O} C_p^{H_2O}(T - T_{in}^w) \quad (65)$$

$$\dot{Q}_{cool} = \dot{m}_f C_p^f(T_o^f - T_{in}^f) \quad (66)$$

where \dot{n}_i is the molar flow rates of product gases and water, \dot{m}_f is the mass flow rate of the cooling water. N_c is the number of cells in series and C_p^f is the thermal capacity of fluid at constant pressure. At steady state, $\frac{dT}{dt} = 0$, thus the required cooling water flow rate can be calculated, which is around 9 tons per hour for each stack. The above equations can also be used to predict the time required for the electrolyte to be heated up to the required temperature, or used in temperature controller design which will be covered in the next session.

4.9 Electrolyser Control System

A control system needs to be installed in the electrolyser to keep it working properly. The CAD drawing at the start of this session included control logics such as temperature, pressure and level control. A limiter is installed between the power source and electrolyser in order to prevent the low level power from passing through. The temperature control is designed to maintain the desired temperature. This can be achieved by controlling the flow rate of cooling water. Apart from the internal heat generated, a heater is also added as an additional heat source for better control. When the temperature is higher than the desired value, the cooling water flow rate increases to transfer heat more quickly. Pressure is controlled to approximately 30 bar using pumps and pressure relief valves. Level controllers are installed in the electrolyser tank and gas-liquid separator to monitor the liquid level in the vessel to prevent leakage current and ensure that liquid in the separator is not carried to the next equipment. Due to space limit, only temperature control will be discussed here. Closed loop PID control is the control mode most often associated with temperature controllers.[34] To achieve better performance, a fuzzy PID model is adopted here. It is based on PID control algorithm and fuzzy control algorithm, which achieves fuzzy adjusting the PID parameters.[35] The Simulink model is shown in Figure 30.

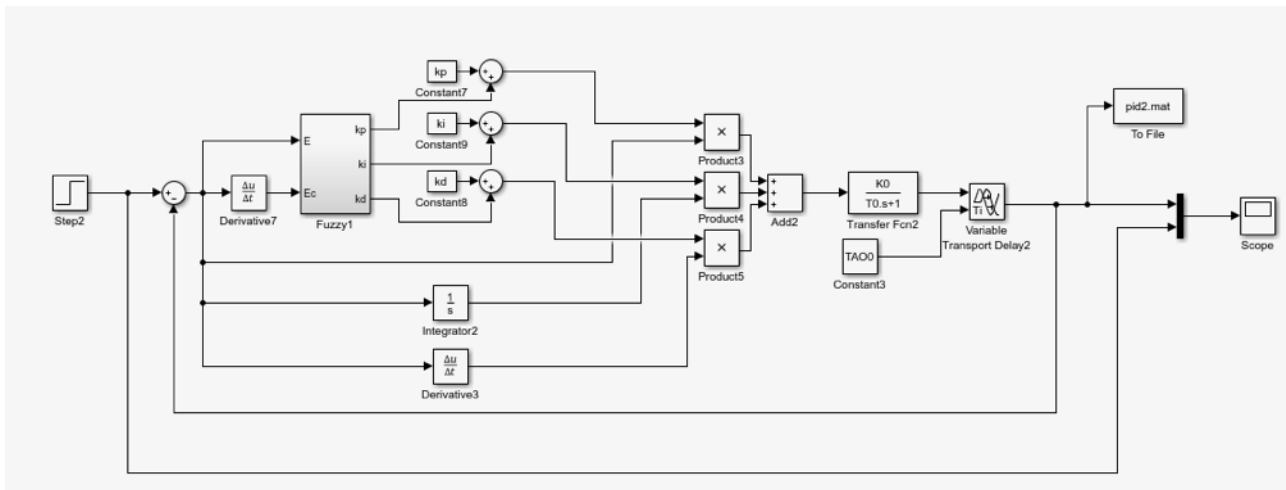


Figure 30: Fuzzy PID block diagram

The four equations in the thermal model session can be used to determine the transfer function, which is in the form of

$$G(s) = \frac{K}{T_s \times s + 1} \quad (67)$$

In reality, there should also be a time lag $e^{-\tau s}$ term in the temperature control system. The comparison between traditional PID controllers and fuzzy PID controllers are shown in Figure 31.

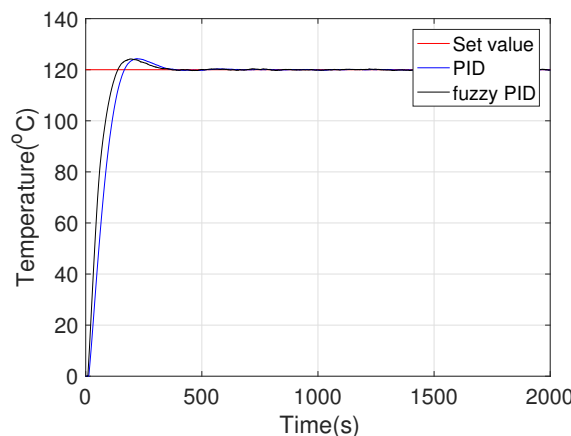


Figure 31: Comparison between PID and fuzzy PID controller under sensor noise

Both controllers have satisfactory performance with the fuzzy PID controller having faster response to changing temperature and smaller overshoot

4.10 Hydrogen Storage

The hydrogen storage system is required to supply the ammonia synthesis reactor with a constant hydrogen flow rate. There are three major ways to store the hydrogen gas produced , as compressed

gas(above ground or underground), as a liquid or forming chemical bonding in solids(usually as metal hydrides). When choosing a storage method, energy required, cost and safety are the major factors to consider and this is shown in Table 13.

Table 13: Hydrogen storage method comparison[36][37][38][39]

	Compressed Gas(700 bar)	Underground	Cryogenic Liquid	Metal Hydride (NaAlH ₄)
Energy Required(MJ/kg)	10.8	1.5	43	15
Storage Cost(\$/kg)	0.29	0.197	1.48	0.116
Safety	High risk of fire or leak	Lower risk, potential leak due to cracks in rock	Risk of Overpressure	Zero Explosion Probability

Storage as a compressed gas using the gas steel cylinders is the most simple and commercially mature storage method, and is therefore adopted in this model. Isothermal compression($\Delta T = 0$) is the ideal case as it requires minimum work input compared with isentropic compression, which is adiabatic. Several stages of compression is adopted to achieve the required compression ratio (a final pressure of 700-800 bar with high strength materials) and the compressed gas needs to be cooled down after each stage. The specific compression work can be calculated by [3]

$$w_i = RTZ \ln\left(\frac{p_2}{p_1}\right) \quad (68)$$

where Z is the compressibility factor, and it is used here since the compressed gas is non-ideal. Z is a function of temperature and pressure but is assumed to be constant here for simplicity. T is the temperature which is kept constant, $\frac{p_2}{p_1}$ is the compression ratio, where p_1 is 30 bar. The compression work for different compression ratio is shown in Figure 32. At a final pressure of 700 bar, the compression work is 4.3 MJ/kg. In reality, the number should be higher than this since the process is not perfectly reversible or isothermal.(typical value is 10.8kJ/kg[38])

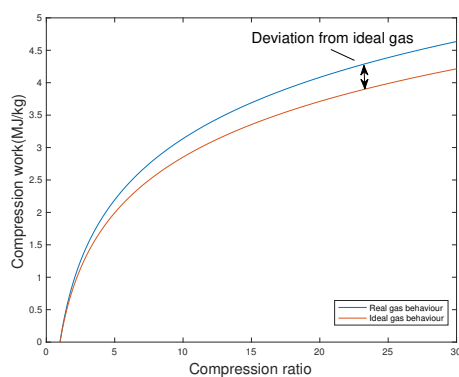


Figure 32: Compression work as a function of compression ratio

Underground storage in salt cavern has been developed for compressed hydrogen gas. It has the benefits of increased storage capacity, low cost and safer operation. However, if a cavern is not already available, the cost of digging and reinforcing can be quite high, and the storage location is also restricted by geological factors.[40] Although liquid hydrogen has a higher energy density compared with compressed gas, liquifying hydrogen is rarely adopted as a storage method since a large amount of energy is required to achieve a very low temperature(-252°C), it also needs fairly expensive heat-insulating materials. Metal hydrides is formed when a host metal is bonded with hydrogen atom to form a compound. When hydrogen needs to be recovered, the compound is supplied with heat to break the bonds. This method can significantly increase the energy density and also has lower risk compared with other storage methods. However, the cost of storage is quite high and strongly bonded hydrogen is hard to be recovered.[41]

4.11 System Simulation

A system simulation is carried out based on power input profile, demonstrating the results for 120 hours in November 2016. Figure 33 shows the changes of HHV efficiency and the ratio of power input and maximum input with time. As can be seen, the HHV efficiency is at a level of around 73% for most of the time and increases when the power input is low. The gaps represent the time period when the power input is below the minimum allowed limit. Note that some power is lost during the AC to DC rectifier stage, the conversion efficiency is assumed to be 90%. For simplification, the simulation assumed zero start-up time, zero response time and constant temperature at 120°C. Figure 34 demonstrates the cumulative production of hydrogen in this time period. Comparing this with the constant hydrogen consumption rate, the storage capacity requirement can be calculated.

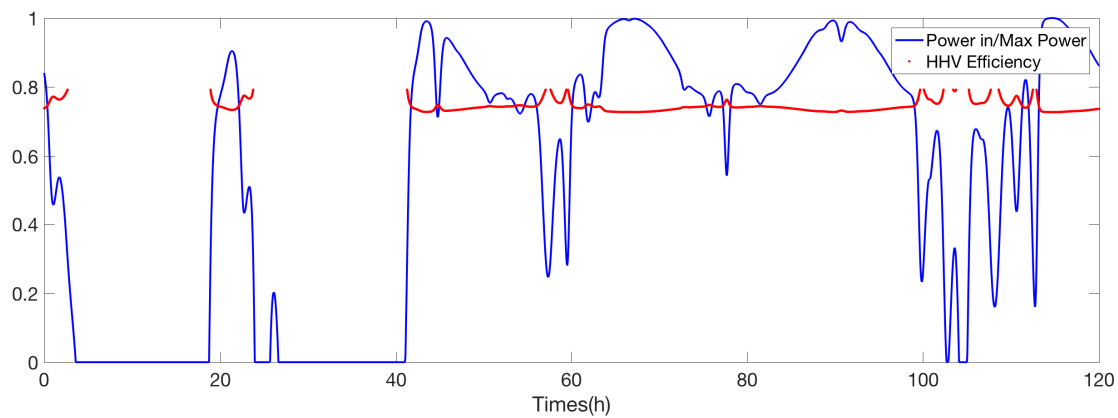


Figure 33: HHV efficiency and Power/ Power max

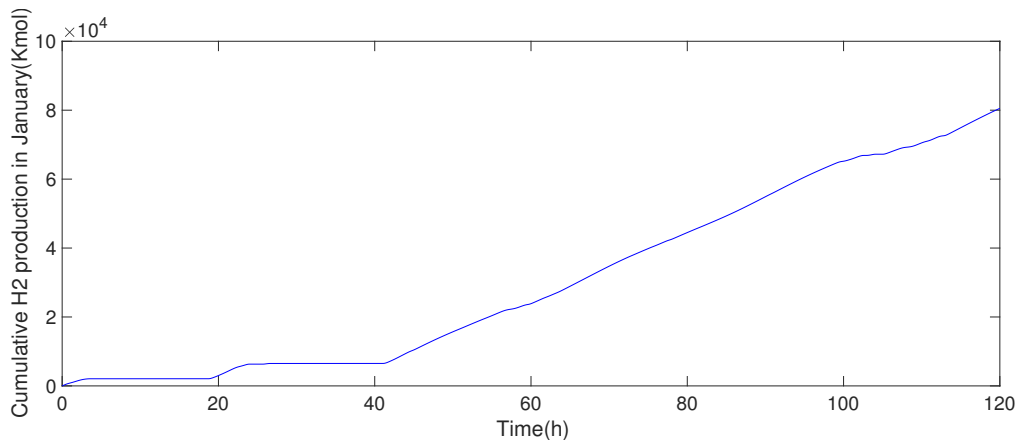


Figure 34: Cumulative production of hydrogen

4.12 Costing

A rough capital cost estimate of the hydrogen production system is shown in Table 14. The total capital cost include direct field cost, indirect field cost and home office/miscellaneous cost. There will also be operating costs such as water and maintenance. Most materials need to be transported, installed and maintained, which would involve associated labour cost, it is assumed as 10% of the material cost for static equipment, and 5% for rotating equipment. The component costs are estimated from industry sources.[42] [43] [44]

Table 14: System Costings

	Labour \$	Material \$	Total \$
Direct Field Cost			
Equipment Cost			
Vessels	19,380	193,800	213,180
Compressor	421,550	8,431,000	8,852,550
Drums/Filters	91,720	917,200	1,008,920
Stacks	522,590	5,225,900	5,748,490
Heat Exchangers	5,100	102,000	107,100
Pumps	735	14,700	15,435
Subtotal Major Equipment	1,061,075	14,884,600	15,945,675
Bulk Material Cost			
Civil/Structure/Architectural			
Foundations		38,379	38,379
Roads/Pavings		9,080	9,080
Buildings		213,507	213,507
Structural Steels		16,350	16,350
Piping/Instruments			
Pipe	4,605	46,050	50,655
Fittings	1,235	12,350	13,585
Valves	10,034	100,340	110,374
Cables	3,805	38,050	41,855
Instruments	2,270	22,701	24,971
Control Valves	6,540	65,402	71,942
Electrical			
Cables	3,405	34,050	37,455
DCS cabinet	6,502	65,020	71,522
Paintings			
Piping painting	7,720		7,720
Equipment painting	12,350		12,350
Insulation			
Piping Insulation	27026		27026
Equipment Insulation	27026		27026
Subtotal Bulk Materials	58,466	661,279	719,745
Total Direct Field Materials	1,119,541	15,545,879	16,665,420
Indirect Field Cost			
Construction management	45,403		45,403
Cranes	78,750		78,750
Scaffolding	40,646		40,646
Total Indirect Field Costs	164,799		164,799
Home Office/Miscellaneous			
Detailed Engineering	41,818		41,818
Start-up	12,121		12,121
Total Costs Excluding UAP	1,338,279	15,545,879	16,884,158
Unallocated Provision			249,300
Total Project Cost			15,795,179

4.13 Sustainability

The Paris Agreement has set a target to limit the global temperature rise to 2°C above the pre-industrial level, corresponding to a Carbon budget of 790GtC.[45] It has become a necessity for countries to develop long-term decarbonisation strategies. Therefore alkaline electrolysis derived by renewable energies has a great potential to become a more vital hydrogen production strategy due to its sustainable nature. Water is the only material input to the system and no greenhouse gases such as carbon dioxide will be produced in the electrolysis process. The water source comes from seawater and thus a desalination process is required. Desalination is a sustainable solution to freshwater shortage. On the negative side, however, the process is expensive and the desalination effluents could damage the environments. The electricity comes from wind power station which is also sustainable. While alkaline electrolysis has a lower energy efficiency than the conventional hydrogen production methods such as natural gas reforming, the continuous advances in the electrolysis technologies could lower the production costs and make it more competitive and widely used in large scale projects.

4.14 Safety

The major risk in the electrolysis plant is the flammable mixture of oxygen and hydrogen gases. Hydrogen has the NFPA 704's highest rating of 4 on the flammability scale. [46] This can happen if the gas crossover during the electrolysis is above the allowed limit, or if hydrogen is leaked to the air which is difficult to detect since its colourless, odourless, and tasteless. Hydrogen gas has a flammability range of 4-75% in the air and it also has a very low ignition energy(as low as $17\mu\text{J}$).[2] To avoid this problem, before driving the hydrogen production equipment, it is necessary to fill the system with nitrogen until the oxygen content of the system is less than 1%; Hydrogen leak alarm devices need to installed and electrolysis room should be set explosion-proof lights. Hydrogen flames are also nearly invisible, so flame detectors are needed. Also, all the equipment should be well grounded to prevent static electricity, which can cause hydrogen combustion and explosion. The leakage of the alkaline electrolyte is another potential risk. The HAZOP analysis is shown below.

Table 15: HAZOP Analysis

Deviation	Causes	Unmitigated Consequences	Likelihood	Risk Ranking	Recommendations
More Flow	Hydrogen/oxygen control valve failure	Cell reaction pressure drop, Electrolysis efficiency will be affected	Middle	Low	Add high flow alarm to respond.

	Cooling Water hand valves fully open by human error	No Hazard identified			
	Caustic control valve failure	High level in cell, lead to overpressure, potential fatality	Low	High	Add high level alarm to respond; Add high high level interlock to trip reaction cell.
	Feed water valve fully open by human error	Flooding in the separator	Low	Low	Add high level alarm to respond;
	Nitrogen hand valve open by human error	Production unqualified.	Low	Low	Add blind flange between the two hand valves.
Less Flow	Hydrogen/oxygen control valve failure	Overpressure;lead to vessel/cell rupture; potential fatality	Low	High	Add high pressure alarm to respond. Add high Pressure interlock to trip reaction cell.
	Cooling Water hand valves fully closed by human error	Material corrosion; mechanical failure; production unqualified	Low	Middle	Add high temperature alarm for the production to response.
	Caustic control valve failed; fully closed	Low level in cell, lead to reaction stop; leakage current	Low	Middle	Add Low level alarm to respond.
	Feed water valve fully closed by human error	Low level in cell, lead to reaction stop	Low	Low	Add Low level alarm to response.
	Pump Failure	Backflow of gases, causing flammable gas mixture	Low	High	Use valves to prevent gas backflow.
	Facility Leakage	Hydrogen leak into facilities, risk of explosion	Low	High	Install hydrogen sensor and leak alarm for emergency shut down.
	Valve or pipe blockage	Bursting of pipes	Low	High	Install blockage detectors.
	Water level too low	Leakage current	Low	High	Check the level controller.
No flow	Refer to less flow				
Reverse Flow	Caustic source shut down due to unknown reason	Hydrogen reverse to caustic system, causing jet fire if leaked, potential people injury	Low	Middle	Add check valve.
	Feed water source shut down due to unknown reason	Hydrogen reverse to feed water system, causing jet fire if leaked, potential people injury	Low	Low	Add check valve.
High Pressure	Pressure control system fails; Blockage; Pump failures	Facilities breakdown, potential explosion; low gas purity	Low	High	Pressure sensor installed for emergency shutdown
Low Pressure	Pump fails; pressure controls fails; leak in reactor	Electrolyte boils if operating above 100°C; more work at hydrogen storage stage	Low	Middle	Check the pumps; Check for any leakage
High Temperature	Cooling water flow rate too low; Heat exchanger malfunction	Material corrosion and mechanical failure such as membrane rupture; Electrolyte boiling	Low	High	Check the cooling water valves Check temperature controller
Low Temperature	Cooling water flow rate too high; Heat exchanger malfunction	Low efficiency	Low	Low	Check the cooling water valves Check temperature controller

Rupture/Leak	Tube rupture in cooler	High pressure cooling water, could cause jet fire if leaked	Low	Middle	Add pressure relieve valves
Contaminants/Composition	Water deionization stage malfunction	Side reactions; reduce lifetime	Low	Middle	Add analyser for feed water quality
Chemical Hazards	Electrolyte concentration too high	Cell or pipeline leakage; corrosion of membrane and electrodes	Low	High	Upgrade materials. Check recirculation pump Install PH meter linked to alarms

4.15 Conclusion

Alkaline electrolysis integrated with wind energy to produce hydrogen is a mature technology with a great potential to reach a larger production scale. The system performance can be improved by operating at elevated pressures and temperatures, as well as adopting the latest technology such as zero-gap configuration. The materials chosen are both cost-effective and able to maximize efficiency. The system is able to produce hydrogen gas at a high purity with an HHV efficiency of around 73%, and is able to respond to dynamic wind power input with a wide load range. The plant is sustainable and generally cost-effective. With the continuous development of more advanced electrolysis technology and the upward trend of using renewable energies globally, the system will be able to operate at a higher efficiency and larger scale to become more competitive than the traditional hydrogen production methods.

References

- [1] M. Hammoudi, C. Henao, K. Agbossou, Y. Dube, M.L. Doumbia, New multi-physics approach for modelling and design of alkaline electrolyzers
- [2] Joonas Koponen, Review of water electrolysis technologies and design of renewable hydrogen production systems
- [3] Hydrogen Science and Engineering, Materials, Processes, Systems and Technology, Wiley-VCH
- [4] Study on development of water electrolysis in the EU Fuel Cells and Hydrogen Joint Undertaking
- [5] V. L. KuchaevE. N. ShapatinaA. K. Avetisov, Mechanism of oxygen poisoning of ammonia synthesis catalyst
- [6] R.J. Gilliam,, J.W. Graydonb, D.W. Kirkb, S.J. Thorpea, A review of specific conductivities of potassium hydroxide solutions for various concentrations and temperatures
- [7] Christian Henao, Kodjo Agbossou, Mhamed Hammoudi, Yves Dub, Alben Cardenas, Simulation tool based on a physics model and an electrical analogy for an alkaline electrolyser
- [8] Richard L. Doyle and Michael E.G. Lyons, The Oxygen Evolution Reaction: Mechanistic Concepts and Catalyst Design

- [9] Milewski, J, Guandalini, G Campanari, S 2014, Modeling an alkaline electrolysis cell through reduced-order and loss-estimate approaches?, *Journal of Power Sources*, vol. 269, pp. 203211.
- [10] Hammoudi, M, Henao, C, Agbossou, K, Dub, Y, Doumbia, M 2012, New multi-physics approach for modelling and design of alkaline electrolyzers, *International Journal of Hydrogen Energy*, vol. 37, no. 19, pp. 1389513913.
- [11] H.Vogt, R.J, Balzer, The bubble coverage of gas-evolving electrodes in stagnant electrolytes
- [12] Kitipong Tangphanta, Kaokanya Sudapraserta, z, and Suthin Channarong, Mathematical Modeling of Electrical Conductivity in Electrolyte Solution between Two Gas Evolving Electrodes
- [13] Kai Zeng 1, Dongke Zhang,Recent progress in alkaline water electrolysis for hydrogen production and applications
- [14] R. L. LERoY, INDUSTRIAL WATER ELECTROLYSIS: PRESENT AND FUTURE
- [15] Alfredo Ursua, Member IEEE, Luis M. Gand, and Pablo Sanchis, Member IEEE, Hydrogen Production From Water Electrolysis: Current Status and Future Trends
- [16] RodneyL. LeRoy and ChristopherT. Bowen, The Thermodynamics of Aqueous Water Electrolysis
- [17] Tilak, B, Lu, P, Colman, J, Srinivasan, 1981, Chapter 1 Electrolytic production of hydrogen, in: Bockris, J, Conway, B, Yeager, E & White, R, Comprehensive treatise of electrochemistry, volume 2: Electrochemical processing, Plenum Press, New York.
- [18] A. Ursua, B, Hydrogen production with alkaline electrolyzers: Electrochemical modelling, electric power supplies and integration with renewable energies,[(in Spanish) Ph.D. dissertation, Dept. Electr.
- [19] Robert Phillips,a and Charles W. Dunnill, Zero Gap Alkaline Electrolysis Cell Designs for Renewable Energy Storage as Hydrogen Gas
- [20] N. Nagai, M. Takeuchi,T. Kimura, T. Oka, Existence of optimum space between electrodes on hydrogen production by water electrolysis
- [21] D. E. Hall, Electrodes for Alkaline Water Electrolysis, Inco Research & Development Center, Incorporated, Sterling Forest, Suern, New York 10901
- [22] D. E. Hall, Alkaline Water Electrolysis Anode Materials, American Cyanamid Company, Chemical Research Laboratories, Stamford, Connecticut 06904
- [23] Kjartansdttir, Cecila Kristn; Moller, Per, Development of Hydrogen Electrodes for Alkaline Water Electrolysis
- [24] High-efficiency and stable alloyed nickel based electrodes for hydrogen evolution by seawater splitting, Zhang,Li,Yang,Fa,Ge. *Journal of Alloys and Compounds*.732 (2018) 248-256
- [25] Ivana M.PerovicPetar Z.LausevicGvozden S.TasicBojan B.RadakVladimir M.Nikolic,Sladjana Lj.MaslovaraMilica P.Marceta Kaninsk, Novel ternary Ni-Co-Mo based ionic activator for efficient alkaline water electrolysis
- [26] Ph. VERMEIREN, W. ADRIANSENS, J. P. MOREELS and R. LEYSEN, EVALUATION OF THE ZIRFONj SEPARATOR FOR USE IN ALKALINE WATER ELECTROLYSIS AND Ni-H, BATTERIES
- [27] Nicolas Guillet and Pierre Millet, Alkaline Water Electrolysis
- [28] Hanna Jaroszek, Piotr Dydo, Ion-exchange membranes in chemical synthesis, a review

- [29] Diogo M. F. Santosl,; Csar A. C. Sequeiral; Jose L. Figueiredo, Hydrogen production by alkaline water electrolysis
- [30] YEO, S. C. EISENBERG, A. 1977. Physical Properties and Supermolecular Structure of Perfluorinated Ion-Containing (Nafion) Polymers. *Journal of Applied Polymer Science*, 21, 875-898.
- [31] Karel Vazac, Martin Paidar, Martin Roubalk, Karel Bouzek, Impact of the Cation Exchange Membrane Thickness on the Alkaline Water Electrolysis
- [32] Sheng-De Li, Cheng-Chien Wang, Chuh-Yung Chen, Zhancheng Guo, Water electrolysis in the presence of an ultrasonic field
- [33] Mingyong Wang, Zhi Wang, Xuzhong Gong, The intensification technologies to water electrolysis for hydrogen production
- [34] Appendix F: PID Temperature Control https://www.lakeshore.com/Documents/LSTC_appendixF_I.pdf
- [35] WANG Haiqing, JI Changying, LIU Tongzhao, GAO Feng, XIAN Jieyu, Modeling and Simulation of Fuzzy Self-tuning PID Temperature Control System
- [36] Zehra Yumurtac and Nur Bekiroglu, Yildiz Technical University Mechanical Engineering Faculty, TR 34349, Besiktas Istanbul, ECONOMICAL ANALYSIS OF GASEOUS AND LIQUID HYDROGEN STORAGE AND TRANSPORTATION
- [37] L. Kit Heung, L. Kit Heung, Savannah River Technology Center Aiken, SC 29808 USA Using Metal Hydride to Store Hydrogen
- [38] Monterey Gardiner, Energy requirements for hydrogen gas compression and liquefaction as related to vehicle storage needs, https://www.hydrogen.energy.gov/pdfs/9013_energy_requirements_for_hydrogen_gas_compression.pdf
- [39] L. Kit Heung Savannah River Technology Center Aiken, SC 29808 USA, Using Metal Hydride to Store Hydrogen, <https://pdfs.semanticscholar.org/b781/192e2624db103d1b615502dd44354eff9b52.pdf>
- [40] Above Ground Vs. Underground Storage Tanks: Pros and Cons, <http://www.communicationsetc.net/above-ground-vs-underground-storage-tanks-pros-and-cons/>
- [41] Wade A. Amos, National Renewable Energy Laboratory, Costs of Storing and Transporting Hydrogen
- [42] David Milligan and Judy Milligan. Matches' process equipment cost estimates. [Online] <http://matche.com/equipcost/Default.html>, 2014. [Accessed 10/4/18].
- [43] <http://kkft.bme.hu/htms/kornykozp/Cost.of.Equipments.pdf>. [Accessed 15/4/18]
- [44] L. Bertucciolo, E. Chan, D. Hart, F. Lehner, B. Madden, and E. Standen, "Development of Water Electrolysis in the European Union: Final Report," Fuel Cells and Hydrogen Joint Undertaking, Final Report, Feb. 2014.
- [45] Kentaro Tamura, PhD Leader, Climate and Energy Area Institute for Global Environmental Strategies (IGES), Paris Agreement: From Low Carbon to Decarbonization.
- [46] https://en.wikipedia.org/wiki/Hydrogen_safety [Accessed 15/4/18]

5 Ammonia Synthesis and Storage

5.1 Introduction

5.1.1 Overview

This section encompasses the processes required to produce and store the quantities of ammonia needed to meet the electricity demand of Maui. This includes both the ammonia synthesis stage and the long-term storage methods required in meeting demand, as well as a brief design of an ammonia cracker. However, it is wise to consider the overall need for the production and storage of ammonia. Hydrogen is produced from wind energy in electrolysis. In theory, this can be stored directly and used to fuel a gas turbine or fuel cell, thus the need for ammonia is not immediately clear. However, a comparison of the properties of the hydrogen and ammonia in Table 16 shows significantly higher energy density of ammonia, as well as the pressure and temperature requirements being significantly closer to atmospheric conditions. This in turn means the cost of storage infrastructure and power requirements are hugely more economical in the case of ammonia.

Table 16: Hydrogen and Ammonia energy storage properties and the conditions required [4]

Substance	Liq. energy density	Boiling point	High Pres. energy density	Pres. req.
H ₂	9.98 MJ/L	-253°C	2.96 MJ/L	300 bar
NH ₃	15.37 MJ/L	-33°C	13.77 MJ/L	8.58 bar

Therefore, in order to store a large enough quantity to power Maui in the absence of an alternative power source it is of clear practical and economic benefit to use ammonia as the medium for long-term energy storage when compared to hydrogen. It is noted that despite the benefits of ammonia over hydrogen storage other methods of energy storage such as pumped hydroelectric are also possible, but outside the scope of this analysis.

5.1.2 List of Design Objectives

The overall objective is to design a synthesis and storage system capable of meeting island energy demand during the absence of wind. This can be broken down into five main design objectives by which to measure success;

1. The process must be of sufficient scale to meet long term average energy demand, whilst meeting the peak demands of the power generation stages.
2. The process should be environmentally beneficial in comparison to traditional power plants.

3. The safety of the design must be prioritised.
4. The process must be as economical in order to be financially competitive.
5. The design of the plant must be realistic using technologies that are feasible for the size and lifetime of the plant.

In meeting scale requirements of the process; an initial year long demand requirement for stored energy was calculated in the control and energy matching design process (section 47) gave both a requirement for the year-long average demand for ammonia and the maximum energy storage requirement during an absence of wind energy. These requirements are shown in Table 17. Using the known efficiencies of the power generation stages and their respective duties an annual demand for ammonia can be calculated using the lower heating value (LHV) of ammonia. Supply-demand matching was also used to calculate the maximum storage required throughout the year, giving the scale requirements for the design process.

As defined by the power demand of Maui, Hawaii the annual power is set to average at a plant output of 36.6MW. Accounting for combined generation efficiency in the ammonia-to-power stage of 61.7% this translates into a daily average ammonia output of 227.6 metric tonnes. To account for minor degradation of the process a capacity of 250 tpd will be designed.

Table 17: Design requirements of synthesis stage

Yearly output	Average output	Storage required	Power stage efficiency	LHV NH ₃
83058 tNH ₃	227.6 tpd	15000 tNH ₃	61.7 %	18557 MJ/t

5.2 Review of Synthesis Methods

In order to best choose the overall design process a literature review of a number of methods was conducted in order to establish the process that best satisfies the objectives. These can then be compared with one another to establish the most suitable overall process.

5.2.1 Haber Process

The most well-established method for producing ammonia is that developed on in 1913 by Fritz Haber at BASF. This involved the reaction of N₂ and H₂ feed gases over a heterogenous solid iron catalyst at high temperature and pressure. The most common catalyst in this process is Fe magnetite. Whilst this process is well established and easily scalable with current production capacities exceeding 3000tpd [3], its low single-pass conversion and large ramp-up time makes it difficult for demand matching, meaning the process is usually run as a continuous process. Despite this

a large number of improvements have been made to this process and with the addition of a recycle stream overall conversion rates above 95% are now regularly achieved. Developments in the catalyst composition used in the reactor has led to lower pressure reactors and higher single pass conversion rates. Perhaps the most significant of these has been the development of wüstite as an alternative to magnetite as the iron precursor in the catalyst. This has shown clear advantages in terms of ammonia first pass conversion at lower temperatures and pressures and for similar material promoters[29] [23].

5.2.2 KAAP Ruthenium-Based Synthesis

A growing competitor to the iron-based synthesis route is an ammonia synthesis production route in which a ruthenium based catalyst is used in place of the iron. Despite known usage in ammonia synthesis since 1917, it was not until 1972 that Ozaki et. al. demonstrated visibly higher activity in ammonia synthesis converters using Ru as an active component. This has led to research into its use as a catalyst and in 1992 the development of the Kellogg Advanced Ammonia Process (KAAP) industrial process for Ru-based ammonia synthesis [32]. This process is typically able to operate under significantly lower pressures and feed ratios than iron-based catalysts, meaning a clear economic advantage in terms of reactor and pressure vessel design. The trade-off is the scarcity of ruthenium and thus the significantly higher cost of the catalyst. This can be shown in Table 18 below [22].

The cost of ruthenium being over 50 times greater than that of iron is a huge factor in the cost of the reactor. Furthermore, the degradation of the ruthenium by high concentrations of hydrogen can mean the cost of replacing the catalyst is also greater.

Table 18: Comparison of Ammonia Synthesis Catalysts

Catalyst	Availability	Cost (USD/m ³)*	T/ °C	H ₂ /N ₂ ratio	Energy consumption (Gj/t)
Fe	abundant	4750	350-525	2-3	~27
Ru	scarce	254100	325-450	under 2	~27

*converted from CNY data at March 2018 exchange rates

5.2.3 Electrocatalysis

An alternate method of producing ammonia is to use electrocatalysis reaction. This is a non-spontaneous thermodynamic reaction:



This reaction can be powered directly from an electrical source and has shown similar efficiency to established synthesis methods under normal temperatures and pressures [22]. In theory this would be a hugely advantageous design process as it would remove the need for hydrogen electrolysis. In recent years this has been a growing field with research into materials for electro-catalysts and electrolytes, however, whilst developments are being made to increase capacity of such systems to 12.5 t/year, current technology are limited to 0.1 kg/year [11]. Obstacles such as low current efficiency and conversion rates make this technology one in need of further development.

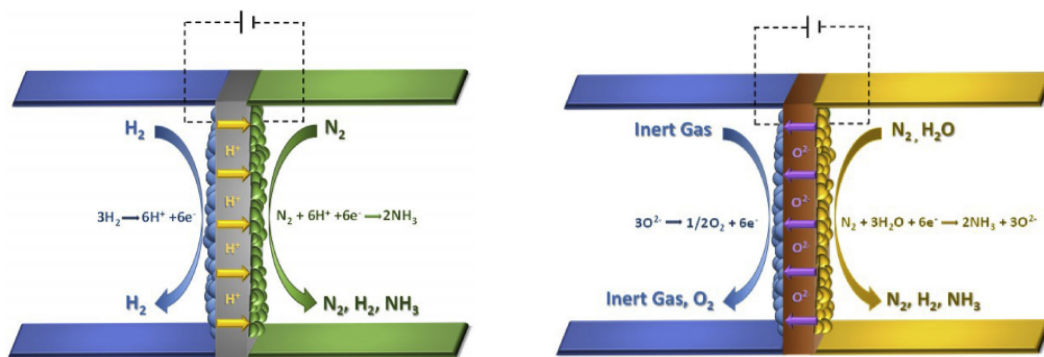


Figure 35: Electrochemical ammonia synthesis - anode (l), cathode (r) [21]

5.2.4 Photocatalytic Synthesis

Using the same principles of photosynthesis the photocatalytic reaction of nitrogen and water to form ammonia and oxygen can be achieved at room temperature and atmospheric pressure with the addition of solar energy. However, despite ongoing research into this field and a number of photocatalysts available, the scale of this process would currently be unable to meet the ammonia requirement of the plant [22].

5.2.5 Method Comparison

Due to the diversity of methods available comparison of these methods will be done using multi-criteria analysis (Table 19), due to the lack of comprehensive data from the electrocatalysis and photocatalysis methods. For simplicity the methods are given a design rating from 1-4 for each of the design objectives. These are then weighted to produce an overall rating for each of the reviewed methods. Safety was not included in this analysis due to the lack of comparative data.

The weightings were justified with feasibility being the most important due to the need to ensure that only methods able to meet the technological requirements are used. Whilst new and emerging technologies were considered in the design process priority was given to methods that have been

Table 19: Multi-criteria analysis table for reviewed ammonia synthesis methods

Method	Scale	Environmental	Economic	Feasibility	Total
Fe based Haber	4	3	4	4	30
Ru based KAAP	4	3	3	4	29
Electrocatalysis	2	4	2	2	20
Photocatalytic synthesis	1	4	1	1	14
Weighting	2	2	1	3	

The Fe-based Haber process was chosen for the synthesis stage.

successfully implemented on medium and large scale processes, laboratory condition processes whilst considered were only chosen if there was a clear method in up-scaling to industrial levels and the benefits of doing so were significantly greater than established industrial processes. This was due to the need for reliability of power supply, especially considering the island location of the power plant and the lack of alternative power sources. The next most important considerations were environmental and scale requirements. This is due to the need to ensure that the methods are able to be scaled sufficiently without the need for large numbers of parallel systems. Environmental was also given a medium weighting of 2 due to its importance in the overall design requirements. Finally, economic was given the lowest ranking on this design process due to the fact that only comparative cost estimates can be found without specific design analysis. The sensitivity of the measurements to changes in score or weighting should also be considered. From the total results only the KAAP process is within 4 points of the Haber total, thus an single unit change in any one rating will only affect the overall optimum if the change was a direct improvement of the KAAP process over the Haber.

5.3 Thermodynamic Modelling

In order to make design choices a model for the synthesis of ammonia Haber process must be developed. To produce ammonia an exothermic reversible reaction takes place between hydrogen and nitrogen;



To better understand the nature of the reaction the thermodynamic are be considered in the following sections.

5.3.1 Equilibrium Constant

The equilibrium constant K_a for ammonia synthesis was first calculated by Gillespie and Beattie (1930)[12] and is a function of the reaction temperature T .

$$\log K_a = -2.69/\log(T) - 5.52 \times 10^{-5}T + 1.85 \times 10^{-7}T^2 + \frac{2001.6}{T} + 2.69 \quad (71)$$

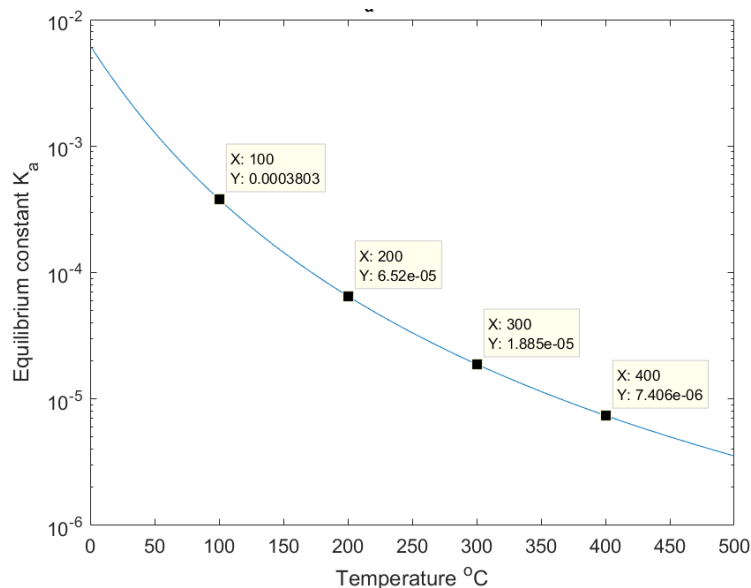


Figure 36: Equilibrium constant K_a of ammonia synthesis reaction at varying temperature

This clearly shows a decrease in the concentrations of products as the temperature increases; thus concurring with the Le Chatelier's principle that the equilibrium of reaction will shift to counteract the rise in temperature. This would suggest that a low reaction temperature would favour a high product yield at equilibrium. The governing mass balance within the reactor is:

$$\dot{n}_{i,in} + \dot{n}_{i,form} = \dot{n}_{i,out} + \dot{n}_{i,accum} \quad (72)$$

where \dot{n}_i are the molar flow rates for specie i , $\dot{n}_{i,in} = \dot{n}_{i,feed} + \dot{n}_{i,recycle}$ and $\dot{n}_{i,out} = \dot{n}_{i,prod} + \dot{n}_{i,recycle} + \dot{n}_{i,purge}$

5.3.2 Reaction Mixtures

When calculating the properties of $N_2:H_2:NH_3$ streams throughout the system a rule of mixtures is used. Eqn. 73 gives the specific heat of a reaction mixture where x_i are the mole fractions in the

stream and $C_{p,i}$ are their respective specific heats.

$$C_{p,mix} = x_{N_2} C_{p,N_2} + x_{H_2} C_{p,H_2} + x_{NH_3} C_{p,NH_3} \quad (73)$$

The specific heats $C_{p,i}$ can be given by the polynomial temperature correlation, Eqn. 74.

$$C_{p,i} = a + bT + cT^2 + dT^3 \quad (74)$$

Clearly a Thermodynamic model alone would suggest that to produce high outputs of ammonia the reaction low temperatures should be chosen. However, this model is insufficient without also considering the rate at which this reaction would occur.

Table 20: Specific heat coefficients [26]

Coef.	N_2	H_2	NH_3
a	28.9	29.11	27.568
b	$-0.1571 * 10^{-2}$	$-0.1916 * 10^{-2}$	$2.5630 * 10^{-2}$
c	$0.8081 * 10^{-5}$	$10.4003 * 10^{-5}$	$0.99072 * 10^{-5}$
d	$-2.873 * 10^{-9}$	$-0.8704 * 10^{-9}$	$-6.6909 * 10^{-9}$

5.4 Mechanism and Kinetics

For a large scale process such as the Haber process with a large product output the rate at which the reaction occurs is a significant limitation on the product output of the plant. This is due to the fact that over a limited reaction time the reactants do not have sufficient time to reach a thermodynamic equilibrium.

5.4.1 Reaction Mechanism

The reaction mechanism of the ammonia synthesis stage was key in understanding the kinetics of reaction, determining the rate of reaction and the effectiveness of a catalyst. The mechanism for the synthesis reaction is shown in Fig. 37 [18].

Where $*$ denotes the formation of an adsorption site. Experimental studies have found the adsorption of nitrogen to be rate determining in this process leading to an understanding of the microkinetics of the rate of reaction. This is due to the energy required to break the strong N_2 triple bond.

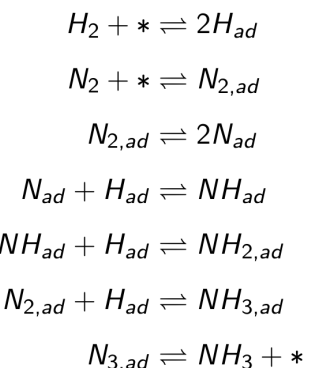


Figure 37: Synthesis mechanism

5.4.2 Rate of Reaction

Numerous models [1] for the synthesis rate of reaction r have been established, however, the most widely used is the Temkin equation [14]. Since its discovery a number of different forms of the equation have now been developed. This analysis uses the Dyson and Simon form for its simplicity and the limited experimental data required to simulate results [7].

$$r_{NH_3} = K_2 \left[K_a^2 \times f_{N_2} \left(\frac{f_{H_2}^3}{f_{NH_3}^2} \right)^\alpha - \left(\frac{f_{NH_3}^2}{f_{H_2}^3} \right)^{\alpha-1} \right] \quad (75)$$

Where the rate is a function of the fugacities f , the well-known equilibrium constant K_a , empirical constant α and K_2 defined by the Arrhenius law: where k_{20} and E_2 are found experimentally and R is the gas constant.

$$K_2 = k_{20} e^{-E_2/RT} \quad (76)$$

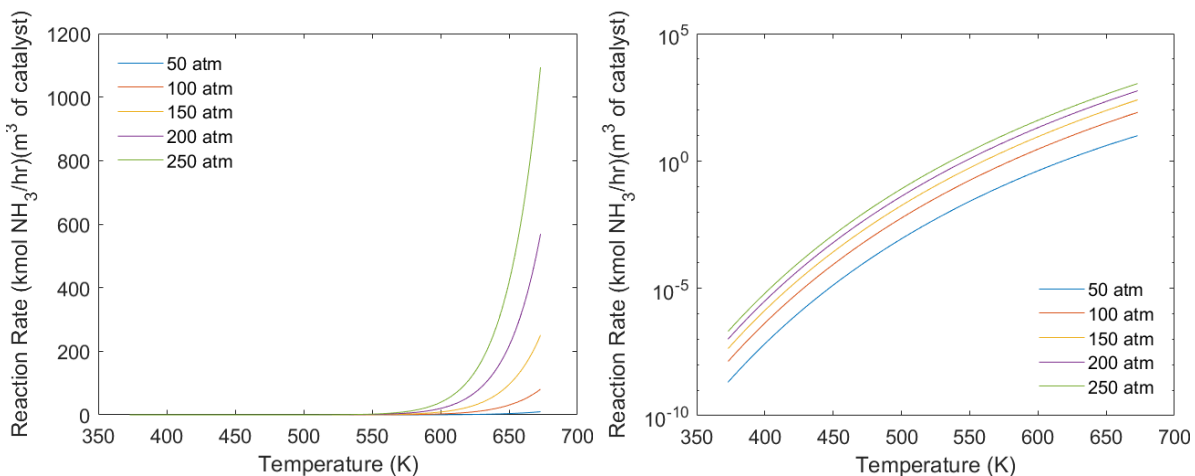


Figure 38: Reaction rate of ammonia synthesis

Figure 38 shows a significant increase in the rate of reaction as temperature increases, thus whilst the thermodynamic equilibrium decreases with temperature the rate of reaction increases. It is clear that as pressure increases the rate does also. The Temkin equation it is undefined when no ammonia is present due to the f_{NH_3} term in the denominator. Clearly this does not follow the thermodynamic principles of a reverse reaction. Thus to resolve this a small amount ($\leq 1\%$) of ammonia was included in the initial reactants; the reactor will be run at steady state conditions.

5.4.3 Fugacities

The fugacities f_i of the respective gases can be calculated from the pressure P and mole fraction of ammonia Z using:

$$f_{N_2} = P\gamma_{N_2} \frac{a}{3\delta} (1 - b_2 Z) \quad (77)$$

$$f_{H_2} = P\gamma_{H_2} a (1 - b_1 Z) \quad (78)$$

$$f_{NH_3} = P\gamma_{NH_3} \times Z \quad (79)$$

Where $a = \frac{3\delta}{3+1}$, $b_1 = \frac{i_0 + 0.5 + (0.5/\delta)}{1-i_0}$, $b_2 = \frac{i_0 - 0.5 + 1.5\delta}{1-i_0}$ and 3δ is the H/N ratio. Fugacity coefficients γ can be calculated using the Cooper (1967) and Newton (1935) expressions given as:

$$\gamma_{N_2} = 0.93432 + 0.3102 \times 10^{-3}T + 0.2959 \times 10^{-3}P - 0.2707 \times 10^{-6}T^2 + 0.4775 \times 10^{-6}P^2 \quad (80)$$

$$\gamma_{H_2} = \exp\{e^{-3.840T^{0.125}+0.541P} - e^{-0.126T^{0.5}-15.98P^2} + 300[e^{-0.01190T-5.94}(e^{-P/300} - 1)\} \quad (81)$$

$$\gamma_{NH_3} = 0.1439 + 0.2029 \times 10^{-2}T - 0.4488 \times 10^{-3}P - 0.1143 \times 10^{-5}T^2 + 0.2761 \times 10^{-6}P^2 \quad (82)$$

The sensitivity of the fugacity coefficients to temperature can be seen on Figure 39. This shows that as temperature decreases and pressure increases the behaviour of gases becomes increasingly non-ideal.

5.4.4 Modelling

The kinetics were implemented in ASPEN using a Langmuir-Hinshelwood-Hougen-Watson (LHHW) model, simulating the surface mechanisms during reaction.

This is commonly used for modelling heterogeneous reactions with a solid catalyst and fluid reactants. For ASPEN simulation the model must be given in the form [30]:

$$\text{Rate} = \frac{(\text{Kinetic factor})(\text{Driving force})}{(\text{Absorption})} \quad (83)$$

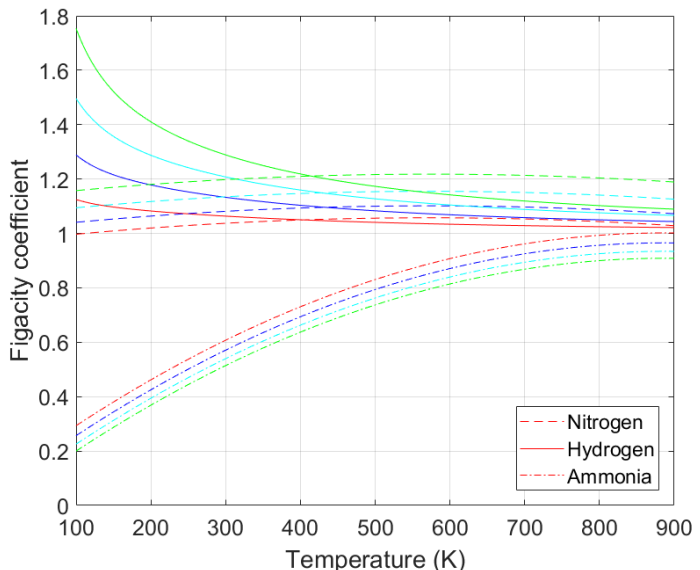


Figure 39: Variation of fugacity coefficients with temperature

In this form and using the Dyson and Simon form of the Temkin equation the absorption term can

be set to unity and the kinetic factor to K_2 , giving a driving force expression:

$$\text{Driving force} = K_a^2 \times f_{N_2} f_{H_2}^{3\alpha} f_{NH_3}^{-2\alpha} - f_{NH_3}^{(2\alpha-2)} f_{H_2}^{(3-3\alpha)} \quad (84)$$

Using the experimental values for k_{20} and E_2 in Eq. 76 to calculate K_2 and then the Gillespie and Beattie equation (Eq. 75) to calculate K_a and an experimental value of $\alpha = 0.5$ a kinetic model for the reaction was formed. Initial simulations of this model in a PFR reactor in aspen at a first approximation of industrial conditions ($p=100\text{bar}$ $T=400^\circ\text{C}$) giving a first pass conversion of $\approx 25\%$ NH_3 .

5.5 Catalyst

In modelling the rate of reaction Dyson and Simon accounted for the flow of reactants through a reactor. To account for the presence of a solid catalyst an effectiveness factor ξ_c was used such that an effective rate ($r_{eff} = \xi_c r_{NH_3}$) through the reactor could be calculated using the following assumptions [7]; The catalyst particles can be considered as spheres. The diffusion coefficients of each component are independent of position within a particle, particles are isothermal and Knudsen diffusion is not experienced. Giving the equation:

$$\xi_c = \frac{(\text{molar flux of component } i \text{ across surface}) \times (\text{surface area of catalyst pellet})}{(\text{vol. of catalyst pellet}) \times (\text{rate of formation of component } i \text{ at surface})} \quad (85)$$

Throughout the past 100 years an Fe-based magnetite (Fe_2O_3) precursor with a variety of oxidic promoters have been the principal catalyst used industrially in ammonia synthesis [22]. However, recently a number of additional catalysts have been developed; involving the use of a various other materials as promoters including ruthenium and bimetallic nitrides. These were considered during the

initial design of the plant due to their higher yields of ammonia at reduced pressures, but drawbacks included both the high cost and limited availability in the case of ruthenium. Considering the island location of the power generation facility the availability of resources was a key factor in the choice of catalyst. On balance, the additional cost of these materials are substantially higher than iron and thus greatly increase both the initial capital costs of the plant but also the running costs of the plant due to the increased material costs. Thus an alternative wüstite (Fe_{1-x}O) iron catalyst was chosen for the ammonia synthesis stage. This was chosen due to the increased reaction rate at lower op-

Table 21: Wüstite catalyst [29]

A301 particle size	1.5-3.0mm
Bulk density	3.25 g/cm ³
BET surface area	16.6 m ² /g
K_{20}	0.874×10^{16}
E_2	44.9 kcal/mol

erating pressure than the traditional magnetite promoter thus reducing the pressure needed for the reactor and the capital costs required. The catalyst in use will be the A301 catalyst manufactured by Shangyou Catalyst Co. Ltd.

Table 22: A301 Catalyst composition

Compound	Fe oxide	Al ₂ O ₃	K ₂ O	CaO	Others*
A301 (%)	93.0	2.7	0.8	2.8	0.7

*Impurities in raw material

5.6 Reactor Design

The synthesis reactor is central to the design of the process as it is within that the synthesis reaction takes place. In order to maintain close to optimum conditions a two bed reactor with intercooling between them was chosen. This enables the products of the first bed to return to a lower temperature before entering the second stage.

5.6.1 Reactor Sizing

The reactor consists of two reactor stages with inter-stage indirect cooling. Both reactor inlet stages are designed as fixed bed reactors with an even catalyst spacing throughout.

The overall volume of the reactor V , can be given by Eq. 86: where r is the rate of reaction, ρ_{cat} is the packing density of the catalyst and \dot{m} the mass flow rate [3].

$$V = \frac{\dot{m}}{1000\rho_{cat}r} \quad (86)$$

Rearranging the steady flow energy equation for an adiabatic reactor with no shaft work ($Q, W_s = 0$) gives an energy balance within the reactor: where ΔH_{reac} is the heat of reaction per mol_{NH₃} and x is the distance along the reactor.

$$\frac{dT_{reac}}{dx} = \frac{(-\Delta H_{reac})A_{cat}}{\dot{m}_{mix}C_{p_{mix}}} r_{NH_3} \quad (87)$$

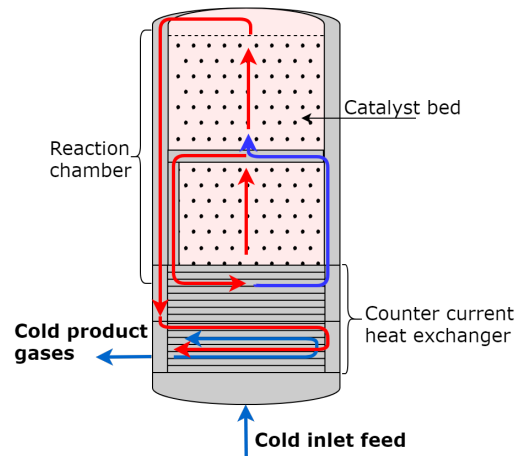


Figure 40: Two stage reactor

Table 23: Reactor sizing

Reaction rate r	ρ_{cat}	\dot{m}_{NH_3}	V	L_T	D_T
$1.3838 * 10^{-4} \frac{kg_{NH_3}}{s^{-1} kg_{cat}^{-1}}$	3.25 kg/L	3.22 kg/s	7.16 m ³	2.74 m	1.83 m

5.6.2 Dimensions and Pressure Drop

Pressure drop across a reactor can be calculated using the Ergun equation [10]:

$$\frac{\Delta p}{L} = \frac{150\mu(1-\epsilon)^2}{D_p^2\epsilon^3}v_s + \frac{1.75(1-\epsilon)\rho}{D_p\epsilon^3}v_s^2 \quad (88)$$

where Δp is the pressure drop across the length L of the bed, μ is the fluid viscosity, ϵ is the void space in the bed (taken as $\epsilon = 0.5$ [10]), ρ is the density of the fluid, D_p is the particle diameter and v_s is the superficial velocity of the fluid where $v_s = \frac{Q}{A} = \frac{\text{volumetric flow rate}}{\text{bed cross sectional area}}$.

Table 24: Reactor dimensions and pressure drop

Reactor bed	Volume m ³	Length m	Diameter m	Thickness mm	Δp atm
1	3.28	1.25	1.83	47.0	4.30
2	3.91	1.49	1.83	47.0	4.08

Modelling the outlet temperature against reactor length in Figure 41 for a single bed with an input temperature of 400 °C and a diameter $D_1 = 1.83$ m shows a change in the reactor profile up to $L_1=1.25$ m: after this point increasing the reactor length no longer increases the NH₃ yield thus this was chosen as a suitable length for the first stage. Using this first stage design a second bed could be subsequently designed; a larger bed was required to optimise ammonia yield. Simulating the reactor bed on ASPEN an optimum length of $D_2=1.82$ m and $L_2=1.49$ m was chosen as after this point there was no significant increase in performance with reactor length, giving a first pass conversion of 34.2% [8]. Furthermore, under a reactor pressure of 150 bar the thickness of the walls must be sufficient to withstand the high internal pressures of reaction.

5.6.3 Material Selection

In order to calculate the thickness of material required the internal reactor forces must be measured, as must the operating temperatures. Simulation shows the peak temperature of normal operation of the reactor remains below 700 °C. Therefore a material with a melting point significantly higher than this is required. Due to the corrosivity of NH₃ to a number of metals high-yield steel was chosen as the material for construction of the vessel.

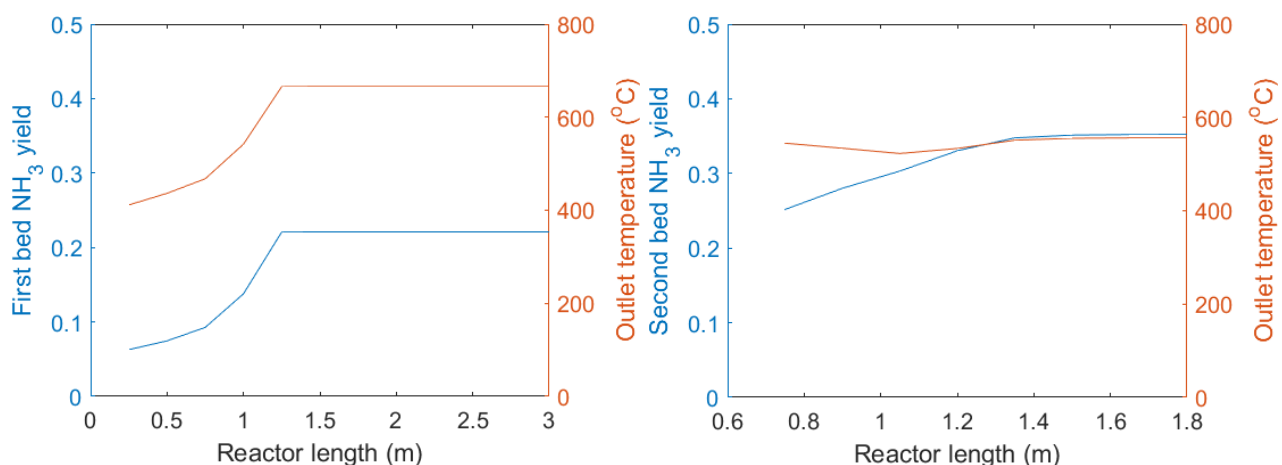


Figure 41: First (l) and second (r) reactor temperature and yield profile with length

Table 25: Properties of high yield steel [16]

Density	Melting point	Yield stress	Ultimate tensile strength	Cost
7850 kg/m ³	1500 °C	400 MPa	600 MPa	\$896/ton [24]

To ensure the reactor material can withstand the reactor pressures it must both withstand the hoop and longitudinal stresses within the reactor such that:

$$\frac{\sigma_{yield}}{S.F.} \geq \sigma_L = \frac{PD}{4t} \text{ and } \frac{\sigma_{yield}}{S.F.} \geq \sigma_H = \frac{PD}{2t} \quad (89)$$

where a safety factor of 2 is taken. This gives the condition that for high yield steel $t \geq 46.9 \text{ mm}$, the thickness of the vessel is taken to be 47 mm. For the leak before break failure condition: where B is wall thickness and K_c is the critical stress intensity factor.

$$\sigma_{yield} < \frac{K_c}{(\pi B)^{0.5}} \quad (90)$$

5.6.4 Heat Exchanger

For the two stage reactor design intermediary cooling is key factor in ensuring the exothermic synthesis reaction does not result in an unwanted temperature increase, thus shifting the equilibrium of reaction further towards the reactants. There were two main methods considered in literature. These were direct quench cooling and heat exchanger indirect cooling.

Quench Cooling Direct quench cooling involves the addition of cold feed mixtures during the reactor stages in order to reduce the reactor temperature at each stage. This means that only a fraction of the total feed enters the first reactor stage.

Indirect Cooling Indirect cooling involves a heat exchanger passing the hot product gases past the cold feed gases in order to raise the temperature of the feed gases. This means the entire feed stream passes through all reactor stages and thus the time in the reactor is maximised.

Design The chosen method for cooling configuration was the indirect cooling due to the maximisation of reaction time. This is supported by empirical analysis [28]. The heat exchanger used in the reactor is a counter-current heat exchanger with steady state heat transfer. From this it is possible to derive an energy balance equation [19];

$$\frac{dT_c}{dx} = \frac{UA}{\dot{m}_i C_p^i L} (T_h - T_c) \quad (91)$$

$$\frac{dT_h}{dx} = \frac{UA}{\dot{m}_o C_p^o L} (T_h - T_c) \quad (92)$$

In which T_c and T_h are the respective cold inlet and hot outlet streams. A is the area for heat transfer to occur and U is the overall heat transfer coefficient of the heat exchanger ($290.35 \text{ W m}^{-2} \text{ K}^{-1}$) [9], whilst C_p are the specific heat capacities for the respective inlet and outlet streams of gas mixtures (Eqn. 73) and \dot{m} are the mass flow rates of the respective streams. Along a heat exchanger of length L where x is the relative position along it. If we then assume $\dot{m}_i c_p^i$ is equal to $\dot{m}_o c_p^o$ and similarly $\frac{UA}{\dot{m}_i C_p^i}$ does not depend on x ; then the above expressions can be simplified in order to give the temperature at the reactor inlet and outlet:

$$T_r^i = \frac{T_i + \frac{UA}{\dot{m}_i C_p^i} T_r^o}{1 + \frac{UA}{\dot{m}_i C_p^i}} \quad (93)$$

$$T_o = \frac{T_r^o + \frac{UA}{\dot{m}_i C_p^i} T_i}{1 + \frac{UA}{\dot{m}_i C_p^i}} \quad (94)$$

The aim of the heat exchanger is twofold. The first of these is to heat up the feed of the product gases to a significantly high temperature to allow for a suitable rate of reaction. This is done by running the hot product gases in counter current to the feed gases. The second use of the heat exchanger is in a two-stage reactor system as an intermediary cooler for the product gases. This brings the temperature down to one in which the reaction equilibrium maintains a increased fraction of ammonia products.

5.7 Additional Units

5.7.1 Separator

In order to remove the fraction of ammonia from the product mixture, the relatively high boiling point of ammonia was used to remove liquid ammonia at high pressure and low temperature in a separator. This separates liquid droplets from gas particles by using gravity separation to allow the gaseous products to leave from the top outlet whilst liquid ammonia is removed from the bottom outlet in a vertical separator (Fig. 42).

To separate liquid ammonia from the product gases The Souders-Brown design equations were used to equate the drag force F_D exerted by gas flow to the gravity force of the droplet weight F_G [6] [17]. Assuming plug flow $F_D = F_G$. Substitution of expressions for the forces on a spherical droplet give the maximum gas velocity, V_{Gmax} using the Souders-Brown method [34]; K_s is found experimentally.

$$V_{Gmax} = K_s \sqrt{\left(\frac{\rho_L - \rho_G}{\rho_G} \right)} \quad \text{when } K_s = \sqrt{\left(\frac{4g D_P}{3C_D} \right)} \quad (95)$$

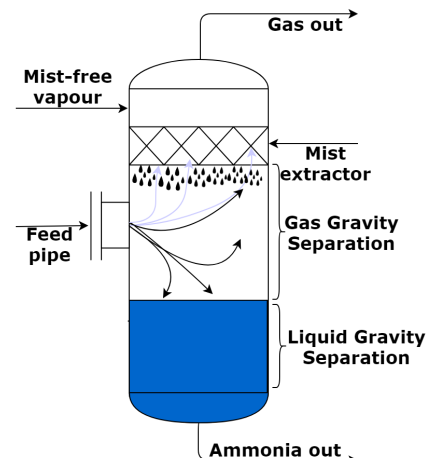


Figure 42: Vertical separator

$$D_{min} = \sqrt{\left(\frac{(4/\pi)q_a}{F_G V_{Gmax}} \right)} \quad (96)$$

Using a mist extractor - a horizontal wire mesh pad in a vertical separator used to coalesce the liquid into droplets large enough to drop from the mesh pad, $K_s = 0.12$. For a length/diameter ratio of 4/1 to reduce the material required in construction. And using a industrial standard HY-80 steel the separator can be modelled as a thin walled pressure vessel to calculate the required wall thickness of the tank [16].

$$\sigma_{yield} = \frac{pr}{t} \quad (97)$$

For an internal pressure of 140 bar, known material and dimensions of the separator can be sized.

Table 26: Separator design summary

K_s	V_{Gmax}	D_{min}	F_G	H	Vol
0.12	74kW	0.594 m	1	2.296 m	0.636 m ³

5.7.2 Compressor

In order to obtain the high operating pressures required for ammonia synthesis centrifugal compressors are used both in the feed streams and in the reactor inlet stream. The feed compressor is used to raise the pressure of the feed gases to the pressure of the recycle stream. Whilst the reactor inlet compressor raises the pressure to account for the pressure drop across the reactor. In this analysis the compressors are assumed to be driven by electric motors, however, turbine powered compressors are also possible, had the gas turbine generator been run continuously for power generation, this would also have been considered. For an isentropic compressor the total output temperature can be calculated from Eqn. 98 [26].

$$T_{out} = T_{in} \left[\left(\frac{P_2}{P_1} \right)^{\frac{1}{N}} \right]^{\left(\frac{n-1}{n} \right)} \quad (98)$$

The total compression power required \dot{W}_{comp} is given by Eqn. 99

$$\dot{W}_{comp} = \frac{\dot{W}_{fluid}}{\eta_{comp}} = \frac{1}{\eta_{comp}} TN \frac{n}{n-1} R \dot{m} \left(\left[\left(\frac{P_2}{P_1} \right)^{\frac{1}{N}} \right]^{\left(\frac{n-1}{n} \right)} - 1 \right) \quad (99)$$

Where T is the input temperature, N is the number of compressor stages, n is the polytropic exponent, R the specific gas constant, \dot{m} is the mass flow rate and P_1 and P_2 are the respective inlet and outlet pressures. η_{comp} is the overall compressor efficiency which is the product of mechanical and isentropic efficiencies such that $\eta_{comp} = \eta_{is}\eta_m$. Standard efficiencies of centrifugal compressors are taken as $\eta_{is} = 0.85$ and $\eta_m = 0.95$ [28].

Table 27: Combined compressor power requirements of plant

Compressor	T_{in} (K)	n	P_2/P_1	N	\dot{W}_{fluid}	\dot{W}_{comp}
1	298	1.40	25	2	1084 kW	1342 kW
2	513	1.40	5.6	2	892 kW	1104 kW
3	565	1.40	1.07	1	77 kW	95 kW
Total					2053 kW	2541 kW

The total cooling power, \dot{Q} can be found in order to size the intercooling heat exchangers: where $C_{p,mix}$ is found from Equation 73.

$$\dot{Q} = \dot{m}(N-1)(T_{out} - T_{in})C_{p,mix} \quad (100)$$

5.7.3 Purge

In order to limit the build-up of inert gases within the synthesis loop, a fraction of the recycle loop is purged. However, due to the cost of obtaining feed gases it is beneficial to keep the purge fraction small. After simulating a number of purge fractions on ASPEN a fraction of 5% of the recycle stream was chosen. This purge stream is comprised of mostly H₂ and N₂ feed gases. Considering the high energy requirement of the electrolyser hydrogen recovery of this stream is in both environmental and economic interest. For this stage there are two main methods; membrane technology and cryogenic separation, with the former generally requiring a lower initial investment whilst the latter provides a greater energy efficiency [27]. Further economic evaluation of this process is outside the scope of this design.

5.8 Ammonia Storage

Storage of liquid ammonia product is vital in matching the supply and demand sides of the plant. Thus the scale of this storage must be one of the largest stores in the plant. Liquid ammonia has a boiling point of -33.3°C at atmospheric conditions, however, this can be increased by pressure storage. This requires a compromise to be made between low temperatures and high pressures in which to store ammonia. A review of current large-scale ammonia storage methods (Bartels,2008)[4] highlights the main trade-off between high pressure and low temperature storage being the high capital cost of building high pressure vessels against the increased energy requirements and thus running costs of maintaining low temperature storage.

As calculated in section 9.6 the maximum capacity for required ammonia storage is 15000 tonnes at maximum capacity.

5.8.1 Low Temperature Storage

Storage of NH₃ at low temperature and ambient pressure is commonly used for large scale storage due to higher ammonia/steel ratio and thus a reduction in capital cost. At atmospheric pressure approximately 43 tonnes of ammonia can be stored per tonne of steel. This massively reduces the capital cost on steel. Despite this other factors must also be considered, mainly boil-off rate due to heat transfer from the environment. The mass of evaporated ammonia and thus the boil-off rate is

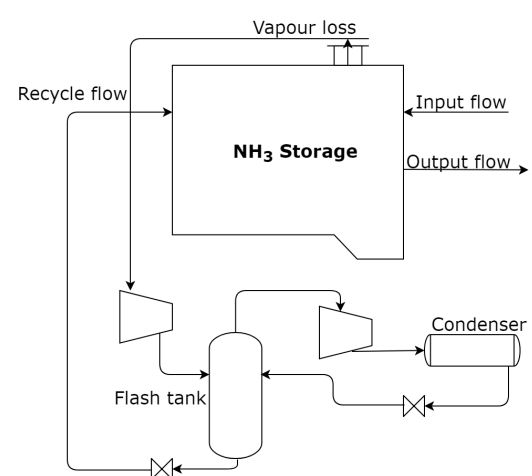


Figure 43: Cold NH₃ storage cycle

given as;

$$\dot{N}H_3_{evap} = \frac{\dot{Q}}{\Delta H_{vap}} \quad (101)$$

$$\text{Boil-off (\%)} = \frac{N}H_3_{evap}}{N}H_3_{storage} \quad (102)$$

This is typically below a conservative estimate of 0.1% per day [5]. Giving a maximum boil-off of 15 t/d. Using an ammonia refrigeration cycle system for 15000 tonnes a storage tank of at least $21.997 \times 10^3 \text{ m}^3$ would be required (density of liquid ammonia, $\rho_{NH_3(l)}=681.9 \text{ kg/m}^3$)[15].

5.8.2 High Pressure Storage

Pressure storage does not suffer from evaporation losses or cooling costs. However, it is limited by its structural mechanics and this material used for construction of the pressure vessel. To increase capacity more vessels are required. Bartels shows that in order to store ammonia at an ambient temperature of 20°C, a pressure of 8.58 bar would need to be maintained. However, the limiting size of a steel pressure vessel is calculated to be approximately 270t. The recommended ratio is about 2.8 ton NH₃ stored for every tonne of steel.

5.8.3 Design

High pressure storage would require 55 pressure vessels using over 5000 tonnes of steel, thus cold storage is a preferred option due to environmental and economic benefits.

Table 28: Comparison of ammonia storage methods

Ammonia Storage - 15000 tonnes required		
Properties	High pressure	Low temperature
NH ₃ Energy density (MJ/L)	13.77	15.37
Ammonia/Steel ratio	2.8	43
Pressure required (bar)	8.58	Atmospheric
Temperature required (°C)	20	-33.3
Storage efficiency	100%	96.3%
Tanks required	55	1
Steel required (tonnes)	5357	349

In order to minimise the heat transfer the surface area/volume ratio of the storage tank must be minimised. Despite the optimal ratio of a spherical tank the 3d nature of the shape would cause significant structural issues in building a sufficiently large container, thus a 3D projection of a 2 dimensional shape is preferred for vertical support. The optimal shape of this design is a cylindrical storage tank. For a maximum volume of $21.997 \times 10^3 \text{ m}^3$ the optimum radius/height ratio is $\frac{h}{r} = 2$ giving a radius, $r = 15.184\text{m}$ and height, $h = 30.38\text{m}$ steel containers. Insulated double containment tanks

are used to minimise heat transfer and to ensure toxic vapours are not released in the case a rupture. The outer tank is made from concrete. Estimation of the hydrostatic pressure at the bottom of the storage container can be given by the equation:

$$P_h = \rho g h \quad (103)$$

In the case of ammonia the pressure on the bottom of the tank would be 203.144 MPa of additional pressure. Thus a suitable steel thickness would have to be chosen to withstand this. Designing the refrigeration system using the compressor design equations and with a flash tank liquid holdup time of 10m the condenser can be sized using [26]; where H is the specific mass enthalpy.

$$\text{Area} = \frac{\dot{m}H}{U_{cond}T_{LMTD}} \quad (104)$$

Table 29: Storage refrigeration cycle design summary

Flow rate \dot{m}	Compressor power	Flash volume	Condenser area
0.17 kg/s	74kW	0.31 m ³	69.7 m ²

5.9 Ammonia Cracker

In order to produce feed gases for the gas turbine the liquid ammonia must first be decomposed into N₂ and H₂ in the endothermic reaction [20].



This requires the addition of heat due to the endothermic nature of the reaction and thus must be conducted in a furnace with a nickel catalyst to achieve the conversions required for decomposition.

Due to the high peak demands of the 3 gas turbines a small amount of the cracked gas is stored. This is done to reduce the peak requirement of the cracker. The standard capacity of an industrial cracker is 1000 m³/h at operating conditions the plant would require 26 SINCE-GAS ANH units at a cost of \$260000 per unit [33].

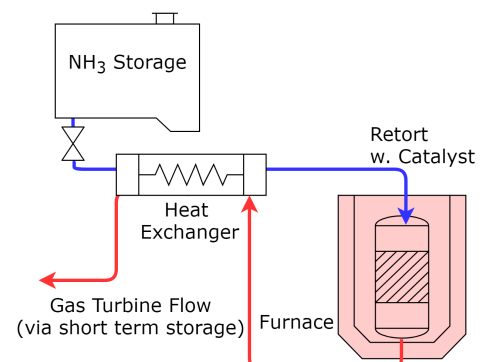


Figure 44: Ammonia cracker flow network

Table 30: Ammonia cracker design requirements

Peak NH ₃ mass flow demand	32.815 kg/s
Average NH ₃ mass flow rate required	0.1648 kg/s
Ramp-up time of SOFC	0.5h
Maximum theoretical capacity required	59067 kg/SOFC ramp-up
Minimum turbine down-time	2h
Capacity requirement of cracker	5.469 kg/s
Cracked gas storage requirement	49.223 ton
Total cost of cracker	\$6,760,000
Operating pressure	0.5 - 1.0 bar

5.10 Modelling, Optimising and Control

This section addresses the methods used in modelling, optimising and controlling the process in order to achieve peak operating conditions.

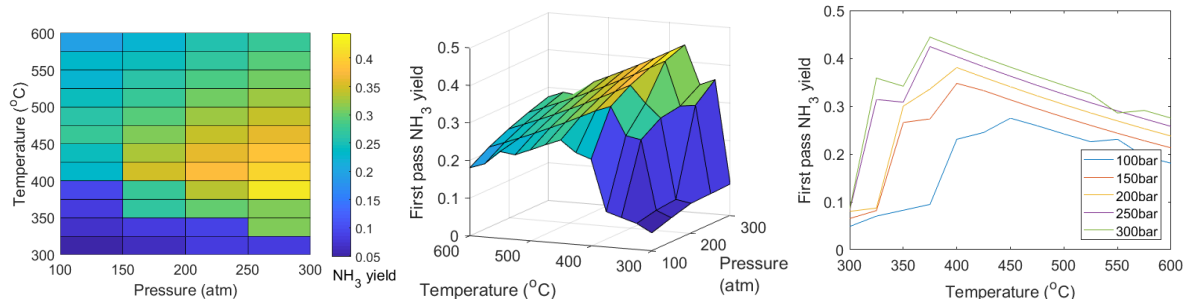


Figure 45: Ammonia single pass yield as function of temperature and pressure

5.10.1 MATLAB Modelling

MATLAB was used to initialise the model and plot the changes of reactor conditions. This was used to visualise relationships between a small number of variables over a variety of conditions.

5.10.2 ASPEN simulation

In order to optimise the pressure and temperature conditions, a number of simulation conditions were trialled using ASPEN plus. Thus measuring the first pass ammonia yield of the reactor at varying operating conditions. Plotting these results shows a peak in NH₃ yield at a temperature of 400 °C. Increasing pressure clearly is shown to increase yield, however, above a pressure of 150 bar there is a fall in the rate of increase. From this analysis the reactor operating point was set at 150bar and 400 °C. This was due to the desire to maximise first pass NH₃ yield whilst keeping the plant as economically viable as possible. The flow model used for simulation can be seen in Figure 46.

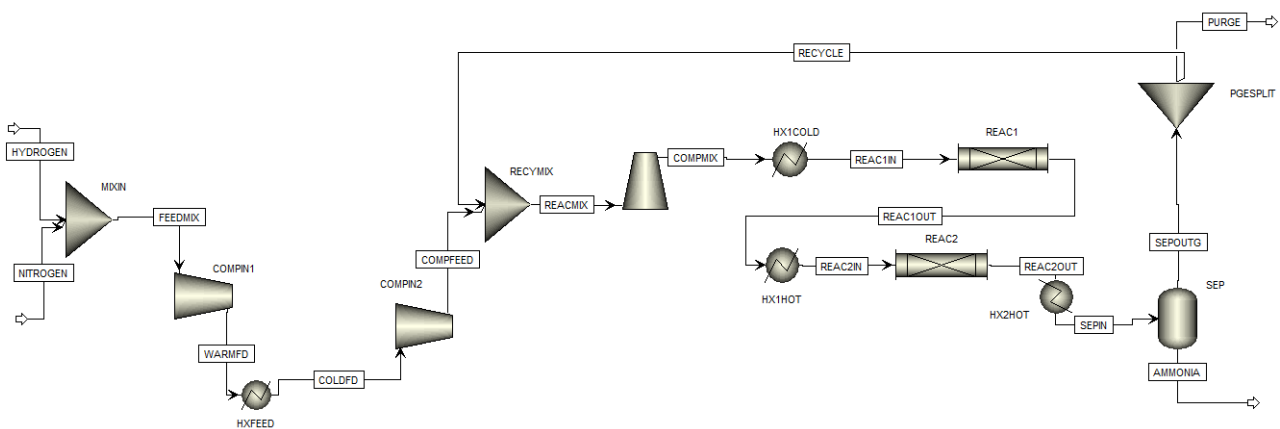


Figure 46: ASPEN model of synthesis reaction

5.10.3 Model Limitations

There are a number of limitations of the overall model for the process, the most of important of which are summarised here.

- The lack of a comprehensive process simulation on ASPEN. This is due to the difficulty in matching variable demand data into the simulation. Thus only the synthesis stage was simulated.
- The simulation limitations, a number of stages - in particular the ammonia cracker was limited to a rudimentary design.
- We have conveniently assumed steady state operation without analysis or process ramping that may be required for maintenance.
- The model assumed that yearly average supply was constant and gave no consideration to a growing power demand.

5.10.4 Plant Control

The ammonia synthesis process is designed to run at steady state conditions and thus the need for plant control on this process is limited. The overall plant supply/demand matching control has been designed in section 9.6. However, to ensure safe operating temperatures of the reactor an emergency quench feed can be used to lower the reactor feed temperature. Above a threshold safe output temperature of $T_{th}=700^{\circ}\text{C}$ a control feed is used to lower the reactant temperature. Energy required for cooling per $^{\circ}\text{C}$ required is:

$$\frac{\dot{Q}}{T} = \dot{m}C_{p,mix} \quad (106)$$

A full control system for the ammonia synthesis process using quench cooling is given by Araujo [2]. However, in this design only the emergency reactor control system is considered (Fig. 47).

5.11 Cost, Sustainability and Safety

In this section only the capital cost assessment for the design stage was conducted. For plant operating costs see section 12.

5.11.1 Capital Cost

An economic analysis of the ammonia synthesis and storage system requires an assessment of the costs associated with each stage of the design. In this analysis module factor costing method was used for the costing of components [31]. Where the purchasing cost C_p^o of equipment in USD is given by the equation [3]:

$$\log_{10} C_p^o = K_1 + K_2 \log_{10}(A) + K_3 (\log_{10}(A))^2 \quad (107)$$

Where K_1, K_2, K_3 are defined in Table 31. Thus the bare module cost C_{BM} (direct and indirect costs from purchase and installation) can be calculated from:

$$C_{BM} = C_p^o F_{BM} = C_p^o (B_1 + B_2 F_M F_P) \quad (108)$$

Where F_M and F_P are the respective material and pressure factors and B_1, B_2 are constants defined by design. Data for these constraints can be found in data sets and ASME tables [31]. The overall capital cost of this stage is estimated to be \$15.5 m with the highest cost being the pre-built ammonia crackers - accounting for over 43% of process cost.

5.11.2 Process Sustainability

Whilst the overall system sustainability is covered later in this report. The ammonia synthesis and storage stage of this project has been one in which no external inputs have been used besides the environmentally produced hydrogen and nitrogen in order to make liquid ammonia. In addition to this recycling the outlet streams has in some cases increased overall output efficiency by a factor of 3, whilst reducing waste streams.

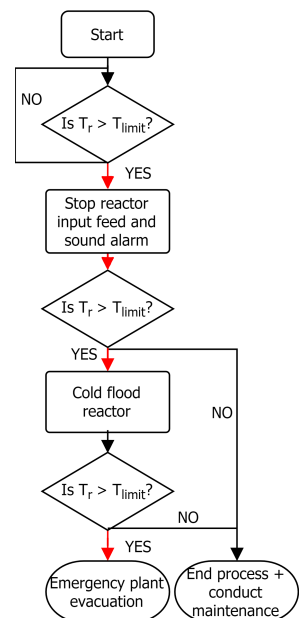


Figure 47: Reactor emergency control

Table 31: Cost summary of all components within the ammonia synthesis and storage process

Component	A	K_1	K_2	K_3	C_p^o	F_{BM}	C_{BM}
Synthesis loop							
Reactor	7.16 m ³	4.0152	0.4485	0.1074	\$ 0.005 m	118.18	\$ 0.591 m
Compressors	2541 kW	2.2897	1.3604	-0.1027	\$ 0.538 m	5.80	\$ 3.120 m
Separator	0.636 m ³	3.4974	0.4485	0.1074	\$ 0.003 m	118.18	\$ 0.306 m
Storage							
Steel Tank	21997 m ³	4.8509	-0.3973	0.1445	\$ 0.708 m	4.5	\$ 3.186 m
Concrete Tank	26699 m ³	4.8509	-0.3973	0.1445	\$ 0.839 m	1.5	\$ 1.259 m
Compressor	74 kW	2.2897	1.3604	-0.1027	\$ 0.030 m	4.4	\$ 0.132 m
Condenser	69.2 m ²	4.0336	0.2341	0.0497	\$ 0.043 m	2.99	\$ 0.129 m
Cracker							
Cracker	-	-	-	-	\$ 6.760 m	-	\$ 6.760 m
Total	-	-	-	-	-	-	\$ 15.482 m

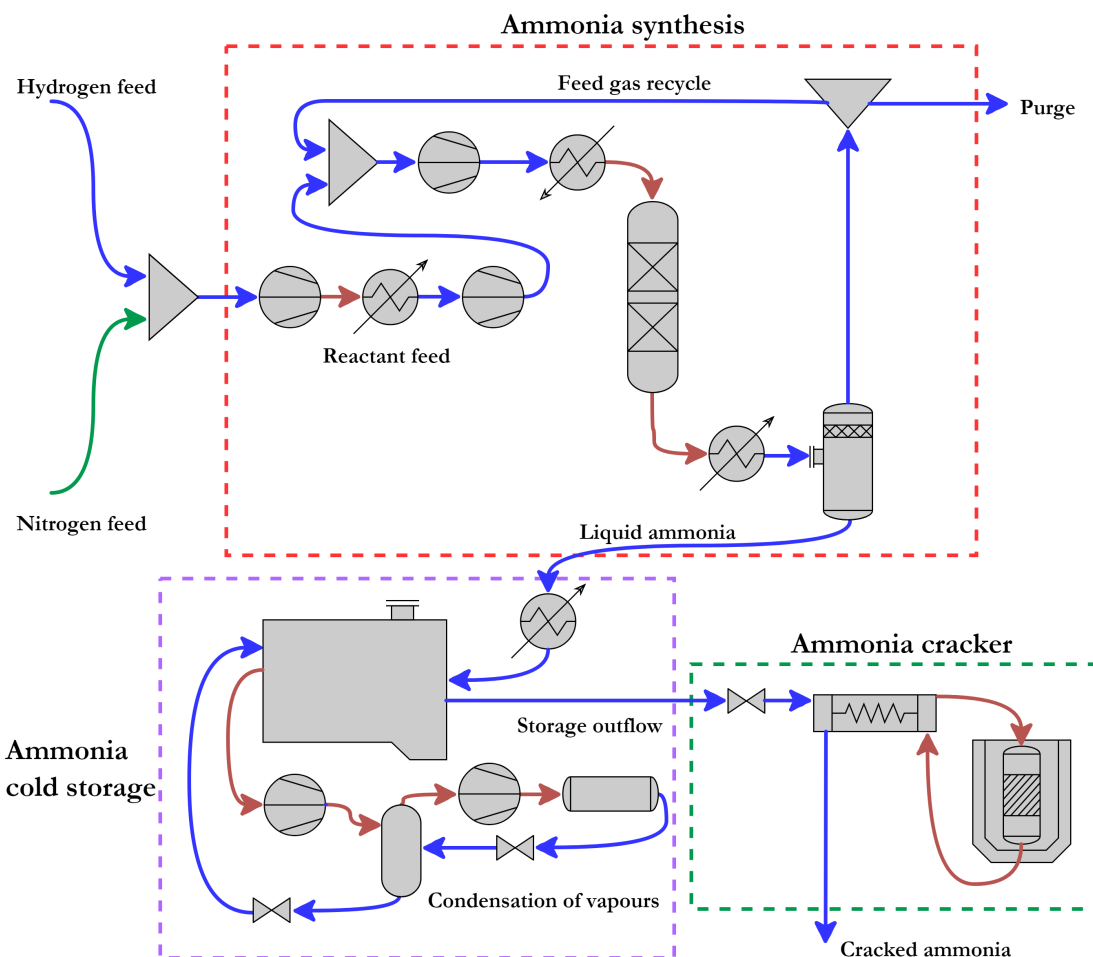


Figure 48: Flowsheet of process

Table 32: HAZOP analysis of synthesis stage

Line	Dev.	Cause	Consequences	Action
Reactor	No	Valve stuck/blocked	Rapid temperature change, Catalyst damage, Reaction rate fall.	Measure temperature with a thermocouple and flow rate continuously with alarm and shut down system, catalytic testing.
	Less	Low output concentration, Reactor leakage, Temperature fall	Release of reactants, fall in output. Explosive ammonia/air mixture.	Measure concentrations of gases outside of the reactor to detect any leakage of reactants. Catalyst replacement.
	More	Overpressure Overtemperature	Vessel failure, release of reactor gases.	Pressure and temperature sensors and warnings, complete shutdown at system before critical level reached. Alarm system in place.
H. Exch.	No	Valve stuck, blockage	Pipe burst - gas leak	Flow path redundancy in HX.
	Less	Low heat exchange - damage to surface plate, low flow rate.	Fall in output, damage to HX.	Thermocouple to measure temperature profile of flow. Regular maintenance.
	More	High flow rate, high temperature	Overheating of reactor.	Measure flow temperature. Regular maintenance.
Compr.	No	No flow - pump blockage, no power supply, complete pressure loss - leak of compressor	Gas leak into atmosphere, reduction in reaction conversion	Gas monitoring outside chamber, regular maintenance.
	Less	Low compression level - low power supply/blockage in system	Inefficient operation, damage to pump.	Filter of feed, flow rate and pressure monitoring.
	More	Overcompression, power surge, control failure, high flow rate	Damage to compressor pump, pipe rupture.	Power buffer systems. Warning and detection alarms.
Separ.	No	No output flow - separator leak	No ammonia output, gas leak	Continuous monitoring of pressure, temperature and flow rates. Regular inspection.
	Less	Temperature too high	Mesh damage, low yield.	Regular stream testing. Periodic inspection.
	More	Temperature too low	Power wastage in cooling.	Thermocouple to measure vessel temperature.
Storage	No	No	Failure power generation stages	Monitoring of storage levels, low storage warning.
	Less	Refrigeration failure of vessel	Building up of pressure - burst vessel	Leak before burst design of storage tank. Pressure relief valve.
	More	Buildup of pressure in container - failure of gas release valve	Vessel failure/bursting. Explosive ammonia/air mixture.	Redundancy in release valves, regular inspection. Pressure monitoring inside vessel.

5.12 Section Summary

5.12.1 Results and Conclusion

During the final design iteration of the synthesis stage a first pass conversion rate of 34% can be achieved after optimization. This is achieved at a pressure of 150bar and a reactor inlet temperature of 400 °C. Figure 46 shows the final stage ammonia synthesis stage ASPEN flow diagram. This is a high first pass conversion relative to industrial averages and is achieved by using high pressure and improved catalyst in relation to the industrial standard. The ammonia synthesis, whilst a well established process requires careful design and optimisation due to the specific design requirements. The use of ASPEN and MATLAB has allowed for the creation of a dynamic modelling system that has enabled the conversion rate of ammonia to be optimised, whilst design of the storage requirements and power generation needs of the plant has enabled this stage to be designed to minimise the waste output of the plant through stream recycles. This achieves an overall conversion rate nearly 3 times than that of a first pass yield.

Table 33: Design summary

NH ₃ production rate	257 tpd
NH ₃ storage capacity	15000 t
Capital cost of process	\$15.5 m
Single-pass NH ₃ conversion	34%
Overall NH ₃ conversion rate	96%
Operating pressure	150 bar
Operating temperature	400 °C
Storage pressure	1 bar
Storage temperature	-33 °C

In conclusion, this section of the reactor is vital in providing the long term energy storage. This has meant that scale and reliability have been prioritised in the design, whilst minimising environmental impact and maximising economic efficiency. This satisfies the initial design objectives and meets the needs of respective processes elsewhere in the plant.

5.12.2 Further Design

Whilst this design has addressed all the initial requirements, there are further improvements that could be made to the process. One of these would be to design a large scale cracker, this may have led to cost reductions over the current design. Finally, recycling the hydrogen content within the purge stream, would not only reduce output wastage but also improve the overall process efficiency.

References

- [1] L. Aparicio and J. Dumesic. Haber Bosch overall + conv. *Amm. Nitrate Proj.*, 1(9):452, 2008.
- [2] A. Araújo and S. Skogestad. Control structure design for the ammonia synthesis process.

- Computers and Chemical Engineering*, 32(12):2920–2932, 2008.
- [3] R. Bañares-alcántara and M. Fiaschetti. Analysis of Islanded Amm.-based Energy Sto. Sys. (Oct.):1–150, 2014.
- [4] J. R. Bartels. A feasibility study of implementing an Ammonia Economy. *Digital Repository @ Iowa State University*, (December):102, 2008.
- [5] V. Belapurkar. Boil-Off in Refrigerated Amm. Tanks. pages 1–4, 2016.
- [6] J. M. Campbell. Gas-Liquid Separators Sizing Parameter. (December 2014):1–16, 2015.
- [7] D. C. Dyson and J. M. Simon. A kinetic expression with diffusion correction for ammonia synthesis on industrial catalyst. *Ind. and Eng. Chem. Fundamentals*, 7(4):605–610, 1968.
- [8] S. S. Elnashaie. Response To Comments On Simulation and Optimization of an Industrial Ammonia Reactor. *Ind. and Eng. Chem. Research*, 28(8):1267, 1989.
- [9] S. S. E. H. Elnashaie, A. T. Mahfouz, and S. S. Elshishini. Digital simulation of an industrial ammonia reactor. *Chemical Engineering and Processing*, 23(3):165–177, 1988.
- [10] S. Ergun and A. A. Orning. Fluid Flow through Randomly Packed Columns and Fluidized Beds. *Industrial & Engineering Chemistry*, 41(6):1179–1184, 1949.
- [11] W. Gellett, S. Szymanski, and P. Onsite. High Efficiency Low Cost Production Electrochemical Ammonia Production. *NH3 Fuel Conference, CA*, 2016.
- [12] L. J. Gillespie and J. A. Beattie. The thermodynamic treatment of chem. equilibria in systems comp. of real gases. *Jou. of the Amer. Chem. Soc.*, 52(11):4239–4246, 1930.
- [13] R. F. Griffiths and G. D. Kaiser. Production of dense gas mixtures from ammonia releases. *Jnl. of Haz. Mat.*, 6(1-2):197–212, 1982.
- [14] U. Guacci, F. Traina, G. Buzzi Ferrarla, and R. Barisone. On the Apln. of the Temkin Eqn. in the Eval. of Cat. for the Amm. Synt. *Ind. and Eng. Chem.*, 16(2):166–176, 1977.
- [15] V. Hacker, , K. Kordesch, and W. Vielstich. Amm. crackers. *Facilities*, 3:121–127, 2003.
- [16] A. M. Howatson, P. G. Lund, and J. D. Todd. Engineering Tables and Data. 1972.
- [17] T. B. Jekel, D. T. Reindl, and J. M. Fisher. Gravity Separator Fundamentals and Design. *Ammonia Refrigeration Convention & Exhibition*, (1998):23, 2001.

- [18] J. R. Jennings. Catalytic Ammonia Synthesis. Fundamentals and Practice. *Springer Science & Business Media*, page 451, 1991.
- [19] A. Jinasena, B. Lie, and B. Glemmestad. Dynamic Model of an Amm. Synt. Reactor Based on Open Inf. *9th EUROSIM Con. on Mod. and Sim. Oulu*, pages 943–948, 2016.
- [20] J. Kim, D. Um, and O. Kwon. Hydrogen production from burning and reforming of ammonia in a microreforming system. *Energy Conversion and Management*, 56:184–191, 2012.
- [21] V. Kyriakou, I. Garagounis, and E. Vasileiou. Progress in the Electrochemical Synthesis of Ammonia. *Catalysis Today*, 286:2–13, 2017.
- [22] H. Liu. Ammonia synthesis catalyst 100 years: Practice, enlightenment and challenge. *Cuihua Xuebao/Chinese Journal of Catalysis*, 35(10):1619–1640, 2014.
- [23] H. Z. Liu, X. N. Li, and Z. N. Hu. Development of novel low temperature and low pressure ammonia synthesis catalyst. *Applied Catalysis A: General*, 142(2):209–222, 1996.
- [24] Meps. Regional Steel Prices & Indices Country Steel Prices Steel Data. pages 1–2, 2018.
- [25] R. Michaels and R. Corp. Emer. Plan.: Crit. Eval. of AEGLs for Amm. 17(2):179–, 1998.
- [26] E. R. Morgan. Techno-Economic Feasibility Study of Ammonia Plants Powered by Offshore Wind. *University of Massachusetts - Amherst, PhD Dissertations*, page 432, 2013.
- [27] M. Ojha and A. K. Dhiman. Problem , Failure and Safety Analysis of Amm. Plant : a Review. *Int. Review of Chem. En.*, 2(October):631–646, 2010.
- [28] M. Penkuhn and G. Tsatsaronis. Comparison of different amm. synt. loop configurations with the aid of advanced exergy analysis. *Energy*, 137:854–864, 2017.
- [29] N. Pernicone, F. Ferrero, I. Rossetti, L. Forni, P. Canton, and P. Riello. Wustite as a new precursor of industrial amm. synt. cat. *App. Catalysis A: General*, 251(1):121–129, 2003.
- [30] A. Plus. Aspen Plus Ammonia Model. 2008.
- [31] J. A. S. Richard Turton, Richard C. Bailie, Wallace B. Whiting. *Analysis, Synthesis and Design of Chemical Processes Third Edition*, volume 53. 2013.
- [32] I. Rossetti, N. Pernicone, F. Ferrero, and L. Forni. Kinetic study of ammonia synthesis on a promoted Ru/C catalyst. *Ind. and Eng. Chem. Research*, 45(12):4150–4155, 2006.
- [33] Since Gas. Automatic Ammonia Cracker for Hydrogen Generation. pages 4–6, 2018.

- [34] M. Souders and G. G. B. Design of Fractionating Columns: I. Entrainment and Capacity. *Ind. and Eng. Chem.*, 26(1):98–103, 1934.
- [35] G. P. Williams. Safety perf. in amm. plants: VI. *Proc. Saf. Prog.*, 18(2):78–81, 1999.

6 Gas Turbine

6.1 Introduction

A gas turbine system will be used in tandem with the SOFCs network to respond to sharp spikes in demand as gas turbines have a much shorter rise time so can be switched to full capacity quickly while the SOFC network slowly ramps up. It will burn the pre-cracked ammonia mixture in air to produce power. This section will first go through the design considerations and requirements of the turbine, followed by an explanation of the model used to find salient values and the final model results. The control problem of a step change in reference value for the turbine was also explored as well as an economic, environmental and safety analysis of the turbine system.

6.2 Gas Turbine Design

From analysis of the energy demand profile of Maui in Section 9.6, it was concluded that the maximum turbine output required was 250MW. As the main purpose of the turbine is to respond quickly to sharp changes in demand, the most important design parameter is the rise time rather than efficiency. Minimal environmental impact is also very important as this is one of the main design targets of the ESS. Other considerations are reliability, cost, safety and ease of operation/maintenance. The design parameters that can be chosen in optimising the turbine are equivalence ratio, turbine size, adiabatic flame temperature, cycle design, materials used and pressure ratio.

The three different turbine configurations considered were:

1. A single combined cycle 250MW turbine.
2. A single simple cycle 250MW turbine.
3. Three parallel simple cycle 90MW turbines.

A multi-criteria analysis was performed to judge which configuration was the most suitable, as shown in Table 1.

Table 34: Multi-criteria analysis of the different turbine configurations

Configuration	Weighting	Single combined cycle	Single simple cycle	Multiple simple cycle
Cost	4	2	5	5
Efficiency	3	5	3	3
Flexibility	2	3	3	4
Rise time	5	3	4	5
Total		44	55	62

Weightings and scores were given as follows, with each point being rated out of 5 with 5 being the

most desirable outcome:

Cost - 4: This is very important as the plant must be economically feasible to be built. However, the gas turbine is only a fraction of the total plant cost. Combined cycle plants are much more expensive than simple cycle at around 600-900 \$/kW compared to 300-350 \$/kW [?]. For simple cycle turbines, there is a very small difference in cost/kW across the turbine sizes of interest so they were both scored at 5. Operation and maintenance costs are slightly lower for combined cycle and do not vary in cost/kW across single cycle turbines but these are less significant due to the low usage of the gas turbine in this plant. [?] Therefore the combined cycle option was given a low score of 2 and the simple cycle options were given high scores of 5.

Efficiency - 3: Efficiency is important as it determines how much energy will need to be put into the turbine to achieve a given output, which determines the flow rate of ammonia required and factors heavily into operation costs. However, as most of the energy generated by the plant will come from the SOFCs, it is weighted less heavily. The gas turbine will also be used at peak demand time when electricity prices are high. Combined cycle systems are significantly more efficient than simple cycle at around 55% compared to 40% so option 1 was given a score of 5. For simple cycle turbines, 250MW turbines are only marginally more efficient than 90MW turbines (around 1%). However, the parallel configuration of option 3 would allow the turbines being used to operate at full load (and maximum efficiency) more of the time so they were both given scores of 3.

Flexibility - 2: The turbine system will operate at a variable load so it must be flexible. It has a low weighting as variations in flexibility are relatively small across the three options. The large turbines are more limited due to their minimum operating loads (around 46% for combined cycle and 43% for simple cycle) [?]. The small parallel turbines give greater flexibility as they do not all have to be used at a given time and can continue to be used at 66% of full load under maintenance periods. The modular system also allows more turbines to be added or removed depending on long term changes in energy demand of Maui [?].

Rise time - 5: A fast rise time is essential as the main purpose of the turbine system is to provide power during large surges in demand. Combined cycle performs with the greatest rise time (around 25 minutes [?]) as the steam cycle heats up slowly. Simple cycle turbines have a much faster rise time, which decreases with size. Option 3 will have the fastest rise time as the 3 turbines will be able to ramp up in parallel. From similar sized turbines, this will be around 6.5 minutes [?] compared to 11 minutes for a larger turbine [?]. [?]

Other factors: Other factors such as environmental impact, safety and ease of operation were not included as there was a smaller difference in impact across the three options.

The analysis shows that option 3, three parallel 90MW turbines, was the most suitable for this project, although the margins were close and option 2 could also feasibly be used. Option 1 would be more suitable for a project with a greater weighting on efficiency (i.e. if the turbine was the sole power generator of the plant).

6.3 Limitations of Ammonia as a Fuel

Ammonia provides many challenges as a combustible fuel. Its high ignition energy, high heat of vapourisation and low lower calorific value (LCV) mean that a lot of energy must be put into combustion. Additionally, it also has narrow flammability limits, limiting the range of equivalence ratios that can be used. Different methods considered to mitigate this were [?]:

1. **Mixing hydrocarbons into the ammonia** - This would improve combustion properties but at the cost of a high negative environmental impact due to the carbon emissions and the impact of extracting and transporting natural gas to the plant [?].
2. **Burning a mixture of ammonia and hydrogen** - The burning properties of hydrogen are much better than ammonia. A precracker can be used to partially dissociate the ammonia into hydrogen and nitrogen so that a mixture of the three gases is run through the combustion chamber. As hydrogen is much easier to combust than ammonia, a dissociation ratio can be chosen to achieve combustion properties comparable to that of hydrocarbons [?].
3. **Oxygen enriched combustion of ammonia** - Oxygen enriched combustion is a common technique used to decrease the energy input needed to burn fuels, and it has been shown to increase fuel consumption at equal stoichiometric ratios [?]. By adding excess oxygen, which can be taken as a waste product from the electrolyser or air separator, the mass flow rate of the air will also decrease, improving cycle efficiency.
4. **Gas turbine modifications** - A standard gas turbine can be modified to burn ammonia, which would include using a higher input ignition energy and larger size to accommodate for decreased air flow rate due to the lower flame stability of ammonia. However, this would be very expensive in both capital and operating costs [?].

It was decided to use methods 2 and 3 together to improve ammonia combustion. A precracker will be used to partially dissociate the ammonia coming from storage, which will be burnt in the combustion chamber with air and the waste oxygen from the electrolyser.

6.3.1 Dissociation Ratio

To find the appropriate dissociation ratio, the properties of ammonia and hydrogen were compared with conventional fuels diesel and gasoline as shown in Table 35.

Table 35: The burning properties of ammonia, hydrogen, diesel and gasoline [?]

Fuel	LCV (MJ/kg) [?]	Ignition energy (mJ)	Stoichiometric AFR by mass	Autoignition temperature (°F)	Flame speed (cm/s)
NH_3	18.6	9.0	0.1653	1200	33
H_2	120.1	0.18	0.0292	1170	300
Diesel	42.8	0.3	0.068	500	100
Gasoline	42.5	0.3	0.068	800	100

A trade-off must be found between optimising burning properties and having too much hydrogen, which will lead to an unstable, rapid burning and high combustion temperatures.

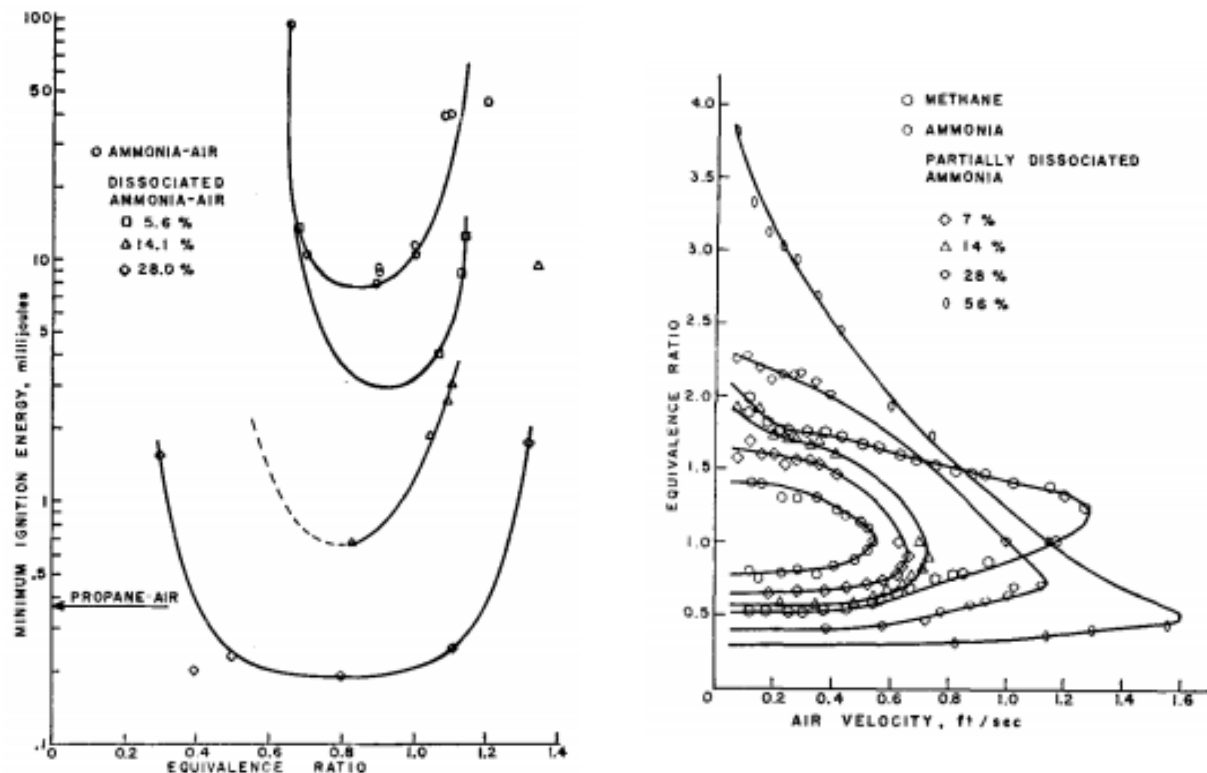


Figure 49: (a) The ignition energy and (b) flame-stability properties of methane-air, ammonia-air and partially dissociated ammonia-air [?]

Figure 49 suggests that 28% dissociation still had a minimum ignition energy higher than that of propane-air (8mJ compared to 0.37mJ at a similar equivalence ratio), which suggests a higher dissociation is required. Li et. al. (2014) [?] also showed that 54.5% dissociation had a similar burning velocity to methane. The mixture should behave similarly to natural gas, which is composed of methane (93.9%), ethane (4.2%) and propane (0.3%) [?], so that no modifications need to be

made to the turbine. Therefore a dissociation of 38% will be used with dissociation reaction:



Assuming that dry air is made of 79% N_2^* and 21% O_2 , where N_2^* is used to represents all components of air other than oxygen, the stoichiometric combustion reaction for one mole of pre-cracked ammonia is:



6.3.2 Mixture Properties

Properties of the new mixture are summarised in Table 36. The molar mass and lower calorific value were calculated using a weighted sum of the relevant mixture components i.e.

$$M_{r,mix} = \sum_{i=1}^N x_i M_{r,i} \quad (111)$$

where $M_{r,i}$ is the molar mass and x_i is the mole fraction of the i -th component of the mixture.

Lower flammability limits (LFL) and upper flammability limits (UFL) are the limits by volume percentage where combustion can occur. The flammability limits of the mixture were calculated using Le Chatelier's mixing rule [?]:

$$FL_{mix} = \frac{1}{\sum_{i=1}^N \frac{x_i}{FL_i}} \quad (112)$$

where FL_i is the upper or lower flammability limit of the i -th component of the mixture. The volume percentage of H_2/NH_3 at stoichiometric combustion is 24%, which falls comfortably in the flammability limits.

Table 36: Properties of the ammonia-air mixture. Due to its inert nature, the nitrogen formed in precracking ammonia were excluded in the calculations for flammability limits and calorific value [?].

	Mr (kg/kmol)	LCV (MJ/kg) [?]	LCV (MJ/kmol)	LFL	UFL
H_2	2.02	120.1	242.6	4.0	75.0
NH_3	17.03	18.6	316.8	15.0	28.0
H_2/NH_3 mixture	10	28.6	281.3	6.47	40

6.4 Sustainability and NO_x

Although energy and resources have to be consumed in order to manufacture the turbine system, the vast majority of sustainability concerns come from ammonia combustion. Burning ammonia will not emit the carbon dioxide and methane that conventional fossil fuel plants produce. However, there is a high potential for NO_x emissions due to the nitrogen content of ammonia. NO_x is harmful to humans as it can penetrate lung tissue, leading to respiratory disease. It is also very harmful to the environment due to its reactive nature, and can cause acid rain, water quality deterioration and smog [?]. NO_x also has a very high global warming potential of 310 compared to carbon dioxide and methane's potentials of 1 and 21 respectively [?]. Therefore emissions must be minimised in the design of the plant to achieve sustainability goals.

There are 3 main mechanisms of NO_x emissions [?]:

- 1. Thermal NO_x:** Thermal NO_x is produced when the triple bond in N₂ dissociates at high temperatures and reacts with oxygen in the air. It has a threshold temperature of around 1700K for gas turbines. Where combustion exceeds this temperature it can also be minimised by limiting residence time in the reactor, as the high activation energy required means it is a much slower reaction than the actual combustion. Thermal NO_x production is also proportional to the square root of the combustion pressure.
- 2. Flame generated NO_x:** This is associated with primary combustion reactions and occurs when nitrogen from the air combines with fuel then gets oxidised by the air with the fuel. The reaction is very fast, so is independent of residence time. It can be controlled using ideal premixing conditions and low temperature.
- 3. Fuel bound NO_x:** This is due to nitrogen atoms in ammonia reacting with oxygen during combustion. This can be controlled using the air fuel ratio in the same way as flame generated NO_x. Both very lean and rich mixtures can be used to control emissions depending on the dissociation ratio as shown in Figure 50. For NH₃/H₂ combustion, this has the largest impact on total NO_x emissions [?].

All three mechanisms have a large temperature dependence and it has been shown that NO_x emissions in NH₃/H₂ decrease significantly as temperature is reduced. From Figure 50, emissions can also be seen to decrease sharply around a fuel-air equivalence ratio of 0.65 for a 38% NH₃ mixture. A number of methods were considered to reduce NO_x emissions including catalytic reduction of NO_x and using a dry low emissions turbine, but the most cost effective and reliable method was judged to be limiting the adiabatic flame temperature to 1700K (the thermal NO_x threshold tempera-

ture [?]) by burning the mixture in lean conditions with a high mass flow rate of air.

The other exhaust gases coming from the turbine are water vapour and nitrogen, therefore only other negative environmental impacts of the gas turbine would come from indirect emissions from manufacture.

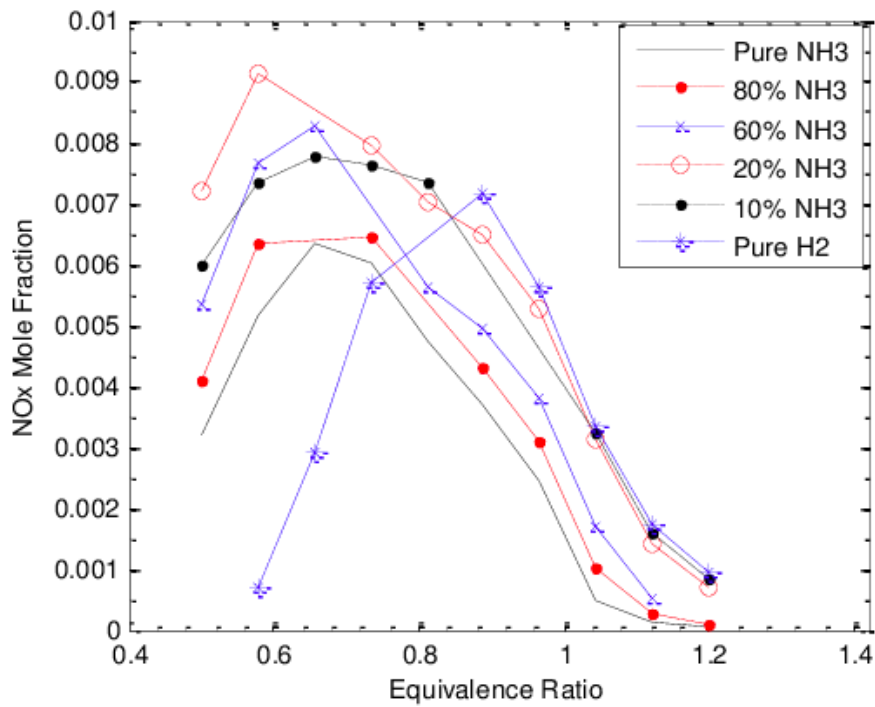


Figure 50: The effect of premixing conditions and fuel-air equivalence ratio on NO_x production when NH_3/H_2 mixtures are burned [?].

6.5 The Turbine Model

MATLAB was used to model the turbine in a modular approach, where each component was modelled using a separate function. The initial conditions were that the compressor would take in ambient air (298K, 101kPa) and that the adiabatic flame temperature should not exceed 1700K. A Brayton cycle was used to model the turbine and derivation of governing equations follows that of Ireland (2017) [?].

6.5.1 Cycle Efficiency

Cycle efficiency η_{cycle} represents the amount of work extracted per unit of heat put into the system.

$$\eta_{cycle} = \frac{w_{out} - w_{in}}{q_{in}} \quad (113)$$

where w_{out} is the total amount of work out of the system (from the turbine), w_{in} is the total work put into the system (through the compressor) and q_{in} is the total heat put into the combustion chamber.

6.5.2 Wobbe Number

The Wobbe number is a measure of the energy output of a given fuel. It can be used as an indicator describing interchangeability of different fuels to be used in combustors and is defined as follows [?]:

$$W_B = \frac{LCV}{\sqrt{G_S}} \quad (114)$$

Where LCV is the lower calorific value of the fuel ($MJkg^{-1}$), G_S is the specific gravity of the fuel relative to air. The NH_3/H_2 mixture was calculated to have a Wobbe number of $49.1 MJN^{-1}m^{-3}$, which is very close to the Wobbe number of natural gas which is $48.52 MJN^{-1}m^{-3}$ [?], and well within the Wobbe variation limits of a typical $90 MW$ gas turbine of $\pm 30\%$ [?] indicating that it should burn as propane would in the combustor.

6.5.3 Pressure Ratio

The pressure ratio r_p of a gas turbine determines cycle temperatures and therefore work input and outputs. Variation in net cycle efficiency was calculated and plotted against a pressure ratio from 1 to 35. It can be compared to the Joule cycle efficiency, which represents the maximum efficiency that can be extracted for a given pressure ratio. The specific work input, work output and net work output were also plotted with the different pressure ratios. An r_p of 21 was chosen as this results in the maximum efficiency as illustrated in Figure 51.

6.5.4 Compressor

Both centrifugal and axial flow compressors were considered for the plant, but the axial flow compressor was chosen in the end as its high efficiency and flow rate makes it more suitable for the large scale of the plant. The compressor was modelled as adiabatic and isentropic ($Pv^\gamma = k$). The air was modelled as a perfect gas ($Pv = RT$), such that:

$$\frac{T_{2s}}{T_1} = r_p^{\frac{\gamma-1}{\gamma}} \quad (115)$$

T_1 and T_{2s} are the inlet temperature and the isentropic outlet temperatures respectively (K).

Using the definition of compressor isentropic efficiency $\eta_c = (h_{2s} - h_1)/(h_2 - h_1)$, the compressor work in is therefore:

$$W_c = \frac{\dot{M}_a \tilde{C}_P}{\eta_c} (T_{2s} - T_1) \quad (116)$$

where \dot{M}_a is the molar flow rate of air ($kmols^{-1}$) and \tilde{C}_P is the molar specific heat capacity at a con-

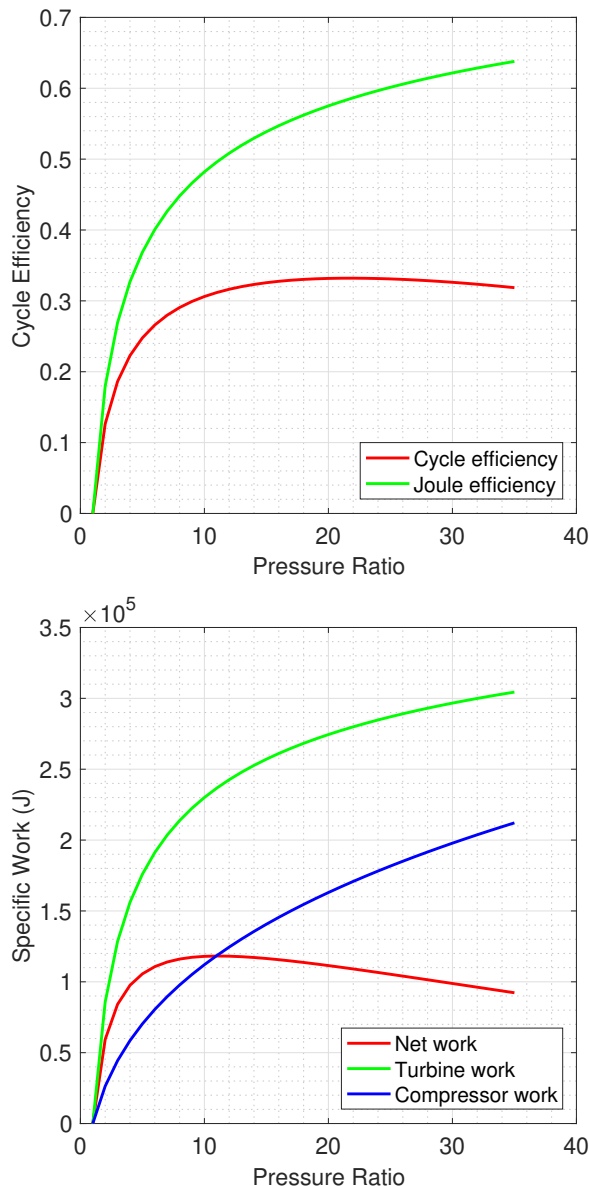


Figure 51: (a) The actual (red) and joule (green) cycle efficiency across different pressure ratios and (b) the turbine specific work output (green), the net specific work output (red) and the compressor specific work input (blue).

stant pressure of air ($\text{kJ kmol}^{-1} \text{K}^{-1}$). Using an r_p of 21, an isentropic efficiency of 0.85 [?] and taking the input air at ambient conditions, the compressor outlet temperature was calculated to be 757.1K.

6.5.5 Combustor

The combustion chamber can be assumed to be adiabatic. For complete combustion and no heating losses, the adiabatic flame temperature can be calculated using:

$$\tilde{\zeta}_{PP}(T_{2P} - T_0) = \tilde{\zeta}_{PR}(T_{1R} - T_0) - LCV \quad (117)$$

Where T_{2P} and T_{1R} represent the temperatures of the products and reactants (K), T_0 represents the reference temperature 288K, \tilde{C}_{PP} and \tilde{C}_{PR} represent the heat capacity at constant pressure of the combustion products (kJK^{-1}) and reactants and LCV is the lower calorific value at a constant pressure of the H_2/NH_3 mixture ($kJkmol^{-1}$). The heat capacities were calculated using the rule of mixtures $\tilde{C}_{P,mix} = \sum x_i \tilde{C}_{P,i}$ where x_i is the molar fraction of each component.

The heat input Q_{in} to the compressor must also be calculated to find the efficiency.

$$Q_{in} = \dot{M} \tilde{C}_P \Delta T \quad (118)$$

Where \dot{M} is the molar flow rate into the combustion chamber ($kmols^{-1}$), \tilde{C}_P is the average specific heat capacity of the reactants and the products ($kJkmol^{-1}K^{-1}$) and ΔT is the difference in temperature across the combustion chamber (K).

6.5.6 Air-Fuel Equivalence Ratio

The Air-fuel equivalence ratio λ is defined as the ratio of actual and stoichiometric fuel to oxidiser ratio. It determines the energy released for a combustion reaction as well as exhaust products:

$$\lambda = \frac{m_{air}/m_{fuel}}{(m_{air}/m_{fuel})_{stoich}} \quad (119)$$

where m_{air}/m_{fuel} is the molar ratio of air to fuel. Variations in λ must satisfy the lower and upper flammability limits of 6.5-40% [?], which correspond to λ in the range of 0.447 to 4.77, within these flammability limits the equivalence ratio can be varied to control the combustion temperature. Taking the flame temperature as the limiting value from Section 6.4 (1700K) and a combustor inlet temperature of 757K, the required equivalence ratio was found to be 2.5 as shown in Figure 52.

6.5.7 Turbine

The turbine is where power is generated, it is coupled to a generator to provide electrical power. An axial-flow turbine will be used for the plant as it is more suitable than radial inflow turbines for large flow rates. The turbine model was used to calculate the molar flow rate of pre-cracked ammonia required for the power demand of 90MW. The turbine was also modelled as adiabatic and isentropic, and the exhaust as a perfect gas, leading to:

$$\frac{T_{4s}}{T_3} = r_p^{\frac{\gamma-1}{\gamma}} \quad (120)$$

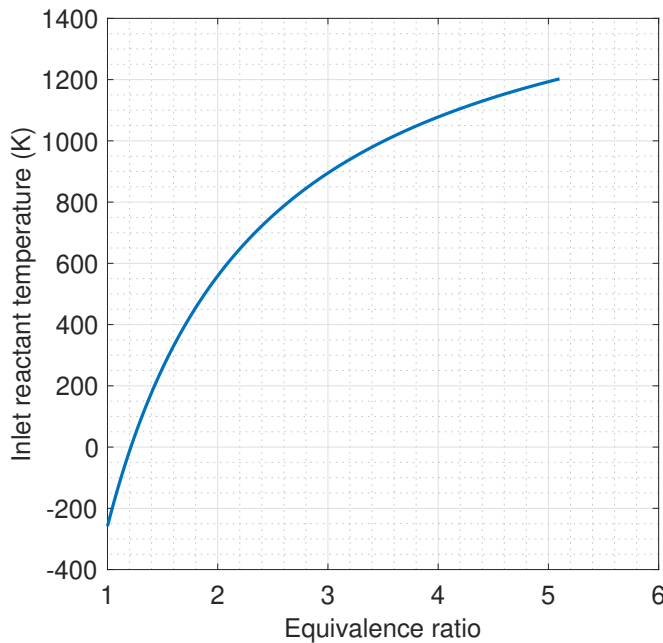


Figure 52: A chart showing the variation in inlet reactant temperature with equivalence ratio.

Using the definition of turbine isentropic efficiency $\eta_T = (h_3 - h_4)/(h_3 - h_{4s})$, the work output is therefore:

$$W_t = \dot{M}_{ex} \tilde{C}_{PP} \eta_t (T_3 - T_{4s}) \quad (121)$$

Where \dot{M}_{ex} is the molar flow rate of the exhaust gas ($kmols^{-1}$), \tilde{C}_{PP} is the molar specific heat capacity of the exhaust products ($kJkmol^{-1}K^{-1}$), η_t is the turbine isentropic efficiency, T_3 and T_{4s} are the temperatures at the turbine inlet and the outlet for an isentropic process respectively (K). Using an isentropic efficiency of 0.8 [?], the molar flow rate was $0.3246 kmols^{-1}$

6.6 Turbine cycle modifications

The cycle efficiency obtained from the simple cycle turbine was 33.2%, which is in the range of typical simple cycle efficiencies of 21-45% [?]. In order to increase cycle efficiency, modifications were added to the standard cycle including using a separate power turbine to increase efficiency, using waste oxygen from the electrolyser to decrease the mass flow rate of air and applying a heat engine to the hot exhaust leaving the turbine.

6.6.1 Split-shaft system

Due to the large size of the plant and the large variation in power output required, it is advantageous to use a split-shaft system which consists of 2 turbines. The first is used to transfer work to the compressor, which is called the gas generator. This must be coupled to the compressor and operates

at a high pressure. The second is the power turbine used to generate power being supplied to the grid, which operates at a lower pressure. This turbine is coupled with the load and must operate at US mains frequency of 60Hz (3600rpm). As the rotational speeds of the two turbines in a split shaft system are independent, the gas generator speed can be varied with the power demand to operate at maximum cycle efficiency [?].

Pressure Ratio The efficiency characteristics of the split-shaft system were recalculated as shown in Figure 53. It shows that going from a single shaft to a split-shaft turbine, the maximum efficiency shifts from a pressure ratio of 21 to 17, with a significant increase in efficiency across all pressure ratios. This pressure ratio also gives the maximum specific work output and the minimum ammonia flow rate. A lower combustion pressure has also been linked to fewer NO_x emissions and is safer [?], therefore $r_p = 17$ was used in this iteration of the model.

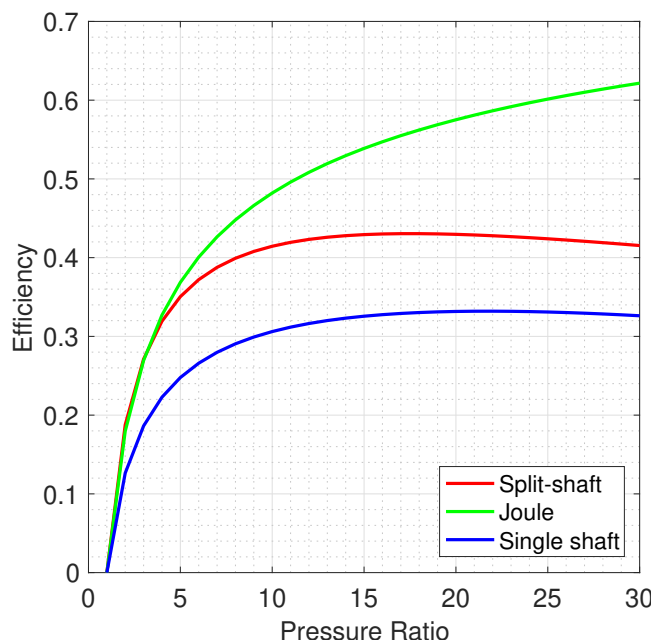


Figure 53: Chart showing the change in Joule efficiency, split-shaft efficiency and simple cycle efficiency across different pressure ratios

Intermediate Pressure Instead of one overall pressure ratio, the high and low pressure turbines will have their own pressure ratios r_{p1} and r_{p2} where $r_p = r_{p1}r_{p2}$. The high pressure turbine is used to generate the amount of work that is required by the compressor. This allows us to find the pressure ratio required for the first turbine using the compressor and turbine work equations from Sec-

tions 6.5.4 and 6.5.7:

$$r_{p1} = \left[1 - \frac{C_{p,a} T_1}{\eta_C \eta_T C_{p,p} T_3} \left(r_p^{\frac{\gamma-1}{\gamma}} - 1 \right) \right]^{\frac{\gamma}{1-\gamma}} \quad (122)$$

Using $r_p = 17$, the result is $r_{p1} = 3.01$ and $r_{p2} = 5.65$.

Changes to Model Results The effect of using a split-shaft turbine is shown in Table 37. The split-shaft turbine has a greater ammonia flow rate but also decreases the air flow required and increases efficiency by 10%. The large increase in efficiency and its increased suitability over a variable load justifies the use of the split-shaft turbine model.

Table 37: Salient model results from single shaft and split-shaft turbine configurations

Model Type	Single shaft	Split-shaft
Efficiency	33.20%	42.72%
NH_3^* flow rate (kmol/s)	0.3246	0.6423
Exhaust Temperature (K)	909.9	917.5
Equivalence Ratio	2.5	2.44

6.6.2 Additional Oxygen

In order to reduce the air flow rate in the compressor, additional oxygen can be added to the combustion chamber. Oxygen enriched combustion is typically used to increase the rate of combustion and increase flame temperature [?]. However, the combustor currently already has an excess of air, so the additional oxygen will not increase the flame temperature but will absorb the heat instead. By decreasing the mass flow in the compressor and increasing it in the turbine, there will be a decrease in compressor work and an increase in turbine work, which would theoretically increase cycle efficiency.

Both the electrolyser and the air separator produce very pure oxygen as a waste product. However, the oxygen from the air separator is close to ambient pressure and temperature so will require more energy to be used. In contrast, the electrolyser produces large amounts of high pressure oxygen, which can be expanded through a turbine before entering the combustion chamber, providing extra work. The results of adding different amounts of oxygen are shown in Table 38.

The increase in oxygen levels did not have the desired effect on efficiency. Although there was a reduction in air and ammonia flow rate and a small additional work from the expansion turbine, the temperature of the oxygen coming into the combustion chamber was still too low, and the heat input required to heat it was too high to increase cycle efficiency. The heat exchange network could not

Table 38: Salient model results from the addition of waste oxygen to combustion chamber

Oxygen flow rate (kmol/s)	0	0.5	1.0	1.5	2.0
Equivalence Ratio	2.44	2.23	2.03	1.82	1.62
NH_3^* flow rate (kmol/s)	0.6423	0.6425	0.6109	0.5823	0.5562
Heat in (MW)	210.5	234.8	248.2	262.9	303.3
Efficiency	42.74%	38.70%	36.24%	34.24%	30.73%

be used for heating due to the low usage time of the turbine. Therefore the extra oxygen modification was discarded in the final design.

6.6.3 Heat Engine

The exhaust gases coming out of the low pressure turbine still hold significant energy due to the high temperature. As this stream cannot be used in the heat exchange network and a combined heat and power system would require a combined cycle turbine, it was decided to run it through a simple heat engine, which converts heat into work. Equation 118 can be used to describe the heat recovered from the engine. The efficiency of a heat engine η_E is [?]:

$$\eta_E = \left(1 - \frac{T_C}{T_H}\right) \eta_{rel} \quad (123)$$

Where T_C and T_H are the cold and hot temperatures respectively (K) and the bracketed term represents the Carnot, or maximum possible efficiency for the temperature range $T_H - T_C$ and η_{rel} is the actual engine efficiency relative to the Carnot efficiency. Using a relative efficiency of 0.8, the heat engine will output 0.724MW at full load, meaning that the power output required is reduced to 89.3MW leading to an increase in efficiency as shown in Table 39. This justified the use of the heat engine so it was kept for the final design.

Table 39: Salient model results from the addition of a heat pump to the system

Model Type	No Engine	Engine
NH_3^* flow rate (kmol/s)	0.6423	0.6257
Heat in (MW)	211	207
Efficiency	42.72%	43.53%

6.7 Turbine Control

Variations in power demand of Maui would lead to different power demands from the gas turbine. Therefore a complex control system would need to be used to operate the turbine. A typical control system would have 3 controllers for temperature, acceleration and speed, which pass through a low

value select as shown in Figure 54. However, it was shown by Balagamuran (2009) [?] that temperature and acceleration are rarely selected so can be neglected. A simplified speed controller can be used instead. The structure of the closed loop transfer function with negative feedback is shown below in Figure 55.

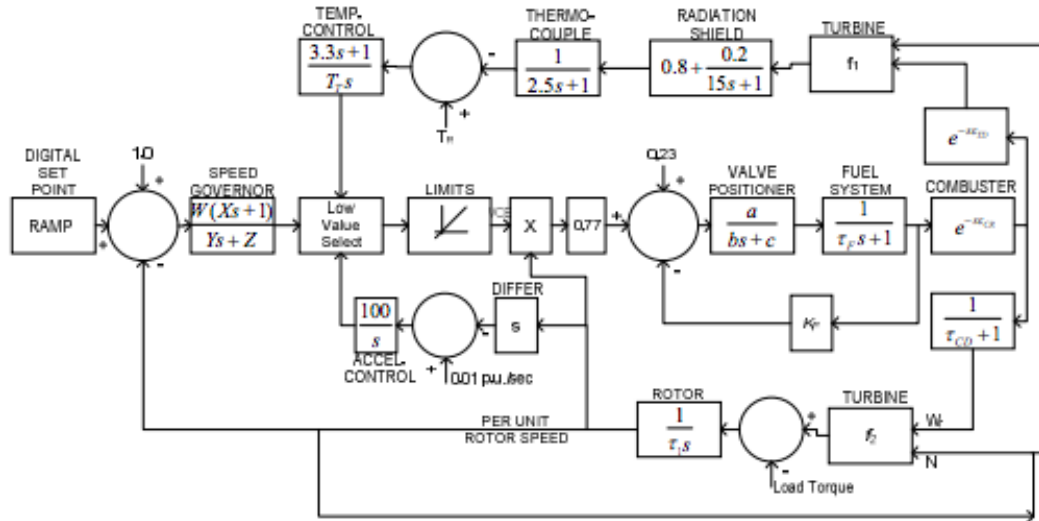


Figure 54: The full transfer function of a turbine with temperature, acceleration and speed control [?].

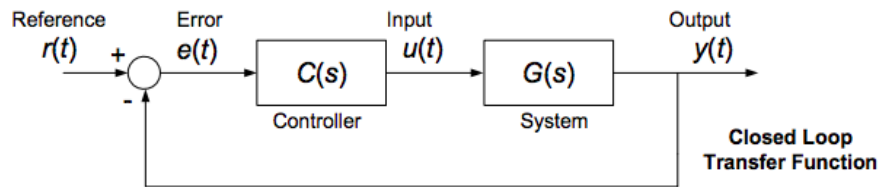


Figure 55: A basic control system [?].

6.8 PID Control

The controller used $C(s)$ will be a saturation limited anti-windup Proportional-Integral-Derivative (PID) controller. PID controllers respond to the error signal itself, in addition to the derivative and the integral of the error signal so that the rise time, settling time and peak overshoot can be controlled by adjusting the variables P , I , D and N that make up the coefficients of each term, where N is a noise filter term due used because the derivative term amplifies noise. When $I > 0$, stable PID controllers also have zero steady state error. The transfer function of the PID controller used in Simulink is shown below:

$$P + I \frac{1}{s} + D \frac{N}{1 + N \frac{1}{s}} \quad (124)$$

6.8.1 Turbine Transfer Function

The turbine transfer function $G(s)$, adapted from Balagamuram [?] consists of several different elements:

Fuel system: The fuel system applies the signal from the PID controller $u(t)$ to the active fuel control range, which excludes what is below the minimum load that is required to keep the turbine running under no load conditions and was calculated to be 45%. This is used to find the fuel flow rate required \dot{m}_f . The fuel valve is adjusted accordingly.

$$\dot{m}_f = \frac{1}{0.4s + 1} \frac{1}{0.05 + 1} (0.55u(t) + 0.45) \quad (125)$$

Turbine torque: Turbine torque is approximated as a linear function of fuel flow rate \dot{m}_f and rotor speed N .

$$T = 1.3(\dot{m}_f - 0.45) + 0.5(1 - N) \quad (126)$$

Rotor: The rotor system is used to convert the torque signal to a rotor speed using the rotor time constant, which was found to be 20s from turbines of similar size [?].

$$N = (\text{Turbine Torque} - \text{Load Torque}) \frac{1}{20s} \quad (127)$$

6.8.2 The Control Problem

The closed loop transfer function was built in Simulink as shown in Figure 56. The problem being modelled was a step change in load demand of an operating turbine so that start up and shutdown effects are neglected. A step change was chosen because the turbine is mostly used for sharp rises in power demand, which resembles a step change. The PID tuner built into Simulink was used to adjust the PID parameters to build a closed loop stable

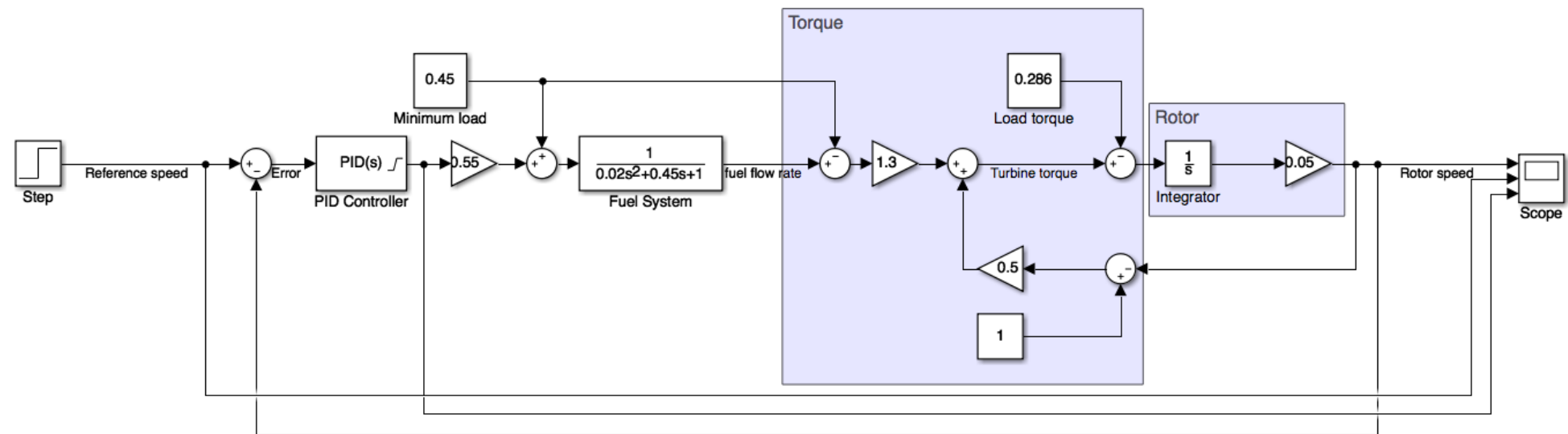


Figure 56: The control system modelled in Simulink.

system that would achieve the fastest rise time without exceeding a 10% maximum peak overshoot for step responses over 1MW. Overshoots in step responses less than 1MW were allowed to exceed 10% as the effect of the overshoot would be very small compared to the power output. The resulting model parameters and results across different sized step inputs are shown in Tables 40 and 41. The response of the rotor speed, reference speed and PID signal for the 5MW test are also shown in Figure 57.

Table 40: Parameters of the PID controller derived from Simulinks PID tuner

P	1.0502
I	0.04338
D	1.172
N	0.2379

Table 41: Results of the closed loop control system for different step inputs

Size of step input (MW)	0.5	1	5	10
Rise time (s)	38.4			
Settling time (s)	129			
Overshoot	15.6%	9.2%	5.7%	5.3%
Peak time (s)	58.8	69.5	81.5	83.2
Closed loop stability	Stable			

The model results show a stable rise in power output for all cases, with peak overshoot increasing in magnitude with a smaller step input and occurring earlier.

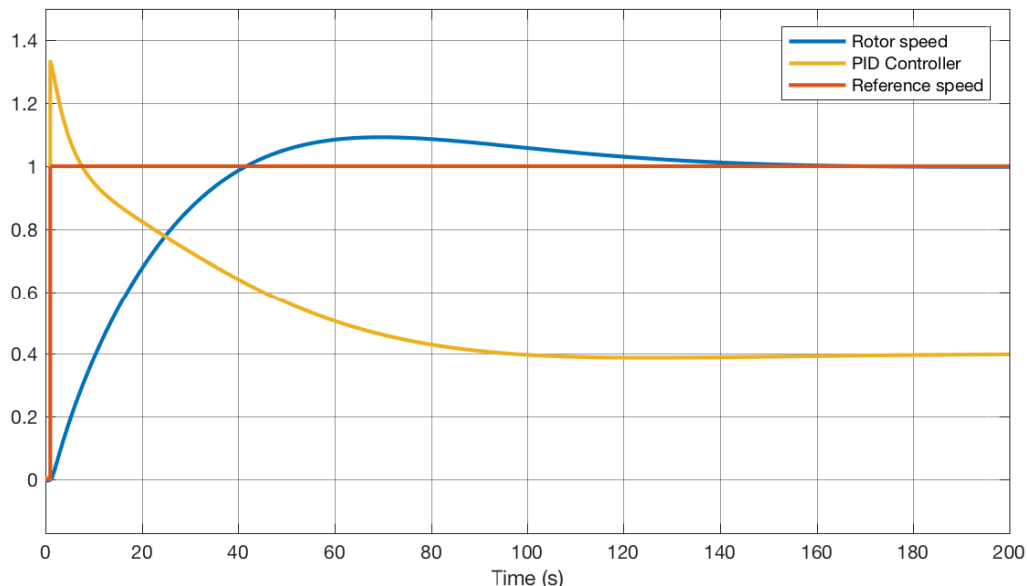


Figure 57: The 1MW step response of rotor speed, reference speed and PID signal

6.9 Turbine System Overview

The overall turbine diagram is shown in Figure 58. Stream and power data for one of the three turbines are shown in Tables 42 and 43.

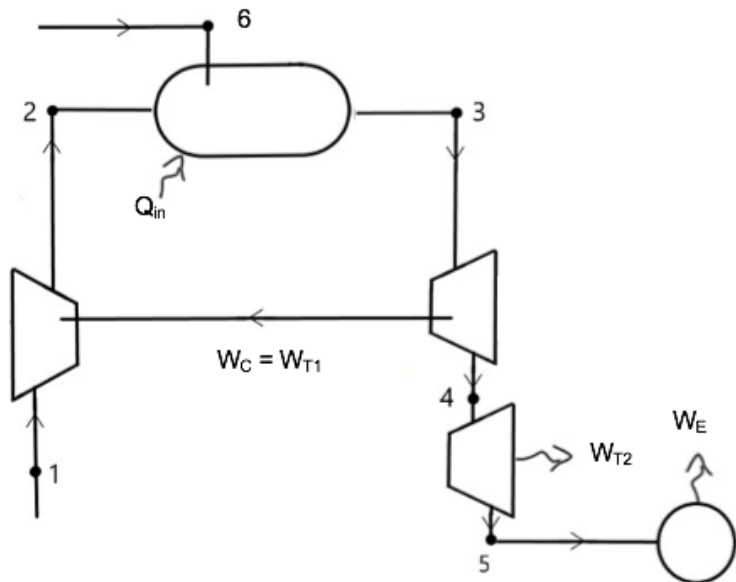


Figure 58: The turbine diagram, showing all streams, work inputs, outputs and heat inputs

Table 42: Thermodynamic and composition data for all streams of a single turbine operating at full capacity

State	Molar flow rate (kmol/s)							Temperature (K)	Pressure (kPa)
	O ₂	N ₂ *	N ₂	H ₂ O	NH ₃	H ₂	Total		
1	1.145	4.308	-	-	-	-	5.453	298.0	101.3
2								735.1	1722
3	0.676	4.305	0.313	0.939	-	-	6.233	1700	1722
4								1334	572.8
5	-	-	0.119	-	0.394	0.357	0.870	917.5	101.3
6								693	1722

Table 43: Heat inputs and work outputs of a single turbine

W _{T1}	78.9 MW
W _{T2}	89.3 MW
W _E	723.6 kW
Q _{in}	207 MW
Overall Efficiency	0.4353

6.10 Safety & Risk

The running of a large gas turbine has many associated risks; A safety and risk analysis was carried out for the gas turbine using a hazard and operability (HAZOP) study. This is to identify all potential hazards associated with the gas turbine coming from deviation to intended operation procedure. Causes and methods to mitigate these risks are split by turbine part and are outlined in Table 44. A safe turbine is achieved using continued monitoring at each section and high pressure relief valves.

Table 44: HAZOP study of the gas turbine

Deviation	Cause	Consequences	Action
Compressor			
Less air flow	Blocked air flow valve	Compressor stall - no pressure rise	Continued monitoring of inlet air flow, shut down compressor if no pressure rise
	Burst pipe	Build up of pressure in pipe, compressor stall	Pressure relief valve in pipe
More air flow	Broken air flow valve	Combustion conditions are too lean, ammonia released as exhaust	Continued monitoring of inlet air flow, shut down compressor if there is too much air
No air flow	Blocked air flow valve	Compressor stall, build up of pressure in pipe	Continued monitoring of inlet air flow, Pressure relief valve in pipe
Contaminated air flow	Impurities at the air inlet	large impurities can affect reaction, debris can damage machinery	Monitor the composition of the air at the compressor inlet, put plant in an area with clean air, filter out large debris
Higher temperature	Temperature fluctuations during the year	Combustion temperature is hotter leading to greater NO_x , damage to combustion vessel	Monitor combustion temperature and adjust air flow rate accordingly
Combustor			
More fuel flow	Broken fuel valve	Increased combustion temperature, depletion of ammonia reserves, risk of explosion	Continued monitoring of combustion chamber temperature, shut down if it exceeds 1800K
Less fuel flow	Blocked fuel valve	Mixture may be too lean to burn, ammonia released as exhaust, stored ammonia supply affected, pressure build up in pipe	Continued monitoring of fuel flow, shut down if no combustion, pressure relief valve in pipe
	Burst Pipe	Ammonia leaks to plant	Ammonia sensor nearby, evacuation at dangerous levels

	Insufficient ammonia store	No combustion	Continued monitoring of ammonia levels in storage, increase production if it is too low
No fuel flow	Blocked fuel valve, insufficient ammonia store	No combustion, no power generated	Continued monitoring of fuel flow, shut down if no combustion, pressure relief valve in pipe
Higher temperature	Greater dissociation achieved by pre-cracker	Greater NO_x emissions, damage to combustion vessel	Continued monitoring of combustion chamber temperature, shut down if it exceeds 1800K
Lower temperature	Lower input temperature, less dissociation of ammonia, no combustion	Less power generated in turbine	Continued monitoring of combustion chamber temperature, shut down if no combustion
Higher pressure	Greater rate of combustion, greater fuel/air flow	Damage to combustion chamber	Pressure sensors in combustion chamber, shut down if pressure exceeds 175kPa
Turbine			
Higher temperature	Greater dissociation achieved by pre-cracker	Damage caused to turbine machinery	Continued monitoring of combustion chamber temperature, shut down if it exceeds 1800K
Overall			
System shuts down	no fuel, compressor stall, turbine fault	No power generated	Regular maintenance checks

6.11 Costing

The main costs of the turbine system are capital and operation and maintenance (O&M) costs. Capital costs are the costs for building and installing the gas turbine system, operation and maintenance are required to keep the turbine running well throughout its lifetime. From literature, these are [?] [?]:

$$\text{Capital Cost} = 3[\text{Plant Output (kW)}] \times 763.6 [\text{Plant Output (MW)}^{-0.223}] = \$75.6 \text{ Million} \quad (128)$$

$$\text{O&M Cost} = 3 \times 5.8 [\text{Plant Output (MWh)}] = \$1.91 \text{ Million/year} \quad (129)$$

This is expensive, however because the turbines are used at peak hours when energy prices are high, they will generate a high revenue. Gas turbines have a lifespan of 30-40 years [?] so will not be replaced during the 25 years of plant operation. A full analysis of lifetime cost is carried out in Section 12.

6.12 Conclusions & Further Work

This chapter shows that the gas turbine system is an effective way to generate power during sharp rises in demand. It is cost effective, reliable, safe and is able to respond quickly to varying demand. The model also shows that it is relatively efficient for the amount of time that it is used. Additionally, it is more sustainable than typical turbines as the only pollutants released are small amounts of NO_x . Therefore, it is concluded that the turbine has managed to achieve its design targets outlined in Section 6.2.

One of the largest limitations of the model used was its inability to accurately predict the NO_x formation. The literature did not provide sufficient data for this problem but indicates that in addition to temperature, equivalence ratio also has a large effect on NO_x formation in nitrogen based fuels. This should be studied further across different NH_3/H_2 mixtures and different equivalence ratios to find the optimal conditions emitting the least amount of NO_x . If necessary, reduction of up to 70% of NO_x emissions can also be performed after combustion using selective non-catalytic reduction [?].

7 Solid Oxide Fuel Cell System

7.1 Introduction

The plant design is based around a hybrid system for power generation, combining a Solid Oxide Fuel Cell (SOFC) system with a gas turbine. The SOFC provides steady state power generation that will satisfy the baseline power demand, with the turbine instead used to accommodate for spikes in power demand. The SOFC is chosen for its high energy efficiency, and for its greater sustainability in comparison to other power generation methods. SOFCs produce no particulate matter or volatile organic compounds, and do not produce carbon dioxide or other gases that contribute to the greenhouse effect [?]. In addition to this, they are modular, meaning the baseline power generation can be increased or decreased very easily by simply adding or removing cells from the system [?]. Furthermore, they produce a high temperature exhaust that can be utilised to do additional work, thereby increasing the overall efficiency [?].

7.2 Design Objectives

The SOFC system must be able to produce at least 230 MW of power at steady state (see Section 9.6), with the most cost efficient and sustainable design possible. In this section, the design process of the SOFC shall be discussed, starting with an outline of the objectives and the operating principles. A mathematical model will be created from the design equations to determine the optimal configuration. This configuration will then be taken forward and a secondary gas turbine cycle will be designed and integrated into the system in order to further extract energy from the fuel cell exhaust. This will improve the overall system efficiency. Finally, a control system will be designed and used to set the ratio of the inlet flow of reactants into the fuel cell system.

7.3 Operating Principles

7.3.1 Overview

Fuel cells directly convert chemical energy to electrical energy by reacting a fuel with an oxidant. The fuel and oxidant flow along porous electrodes and react at the electrode/electrolyte interface. Either air or pure oxygen can be used as an oxidant. A variety of fuels can be used, provided they can be broken down into hydrogen, which is what specifically reacts with the oxygen.

There are two main types of SOFCs, the difference being which ions are conducted by the electrolyte. SOFC-Os have oxygen conducting electrolytes, whereas SOFC-Hs have hydrogen conduct-

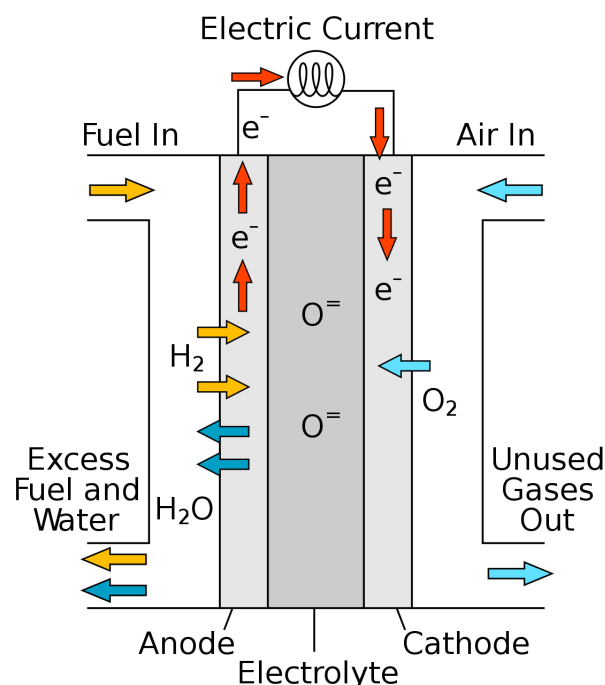


Figure 59: Simple diagram of SOFC-O operation [?]

ing electrolytes. A simple diagram of a SOFC is shown in Figure 59. The fuel cell is composed of an electrolyte, either side of which is an anode and a cathode. One of these components must be significantly thicker than the others in order to give structural stability [?]. The fuel flow comes into contact with the anode, and the air flow with the cathode, where they are broken down by the high temperatures into hydrogen and oxygen ions. These are absorbed through the electrodes and react at the electrode/electrolyte interface, known as the ‘triple-phase boundary’, or TPB (anode interface for SOFC-O, cathode interface for SOFC-H). These ions react to form water, and the movement of electrons creates a current. This current flows along the fuel cells, separated by a conducting interconnect, and is the primary power output of the SOFC system.

7.3.2 Cell Construction

The cell components must be made of materials with a similar coefficient of thermal expansion in order to prevent cracking when the fuel cell is heated up to operating temperature [?]. The most common choice of electrolyte in literature is yttria-stabilised zirconia (YSZ) - an oxygen conducting electrolyte - chosen for its high ionic conductivity, and mechanical and thermal stability at high temperatures [?]. It is also a very cost effective and sustainable choice, as it is found abundantly in the earth’s crust [?]. The anode also needs to be a good conductor, and ideally should catalyse the breakdown of ammonia to increase fuel utilisation. Nickel mixed with YSZ is a good choice, allowing for similar thermal properties as the electrolyte, but also acting as a catalyst for the breakdown of

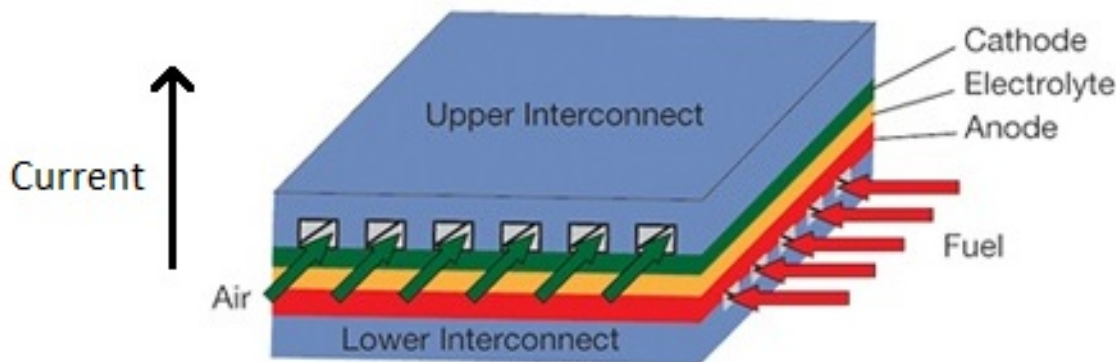


Figure 60: Diagram of a single fuel cell, that would be repeated in a vertical stack (adapted from [?])

ammonia. Using a nickel based anode means ammonia breakdown can be assumed to be 100% at the anode surface [?]. Similarly, the cathode is typically made of YSZ mixed with Strontium-doped Lanthanum Manganite (LSM), as LSM catalyses the decomposition of oxygen into ions [?]. These same materials were used in Zamfirescu's model [?], which formed the basis for the model designed in this project. Not mentioned in Zamfirescu's paper was the interconnect, which must conduct electricity well at the operating temperature while also providing structural support to the fuel cell stack. Typically, LaCrO_3 ceramics are used [?]. Fuel cells can either be planar or tubular in design, with literature suggesting that planar fuel cells have a greater power density, and are cheaper to manufacture, leading to a more cost efficient design [?]. Figure 60 shows the structure of a single planar fuel cell.

7.3.3 Cell Potential

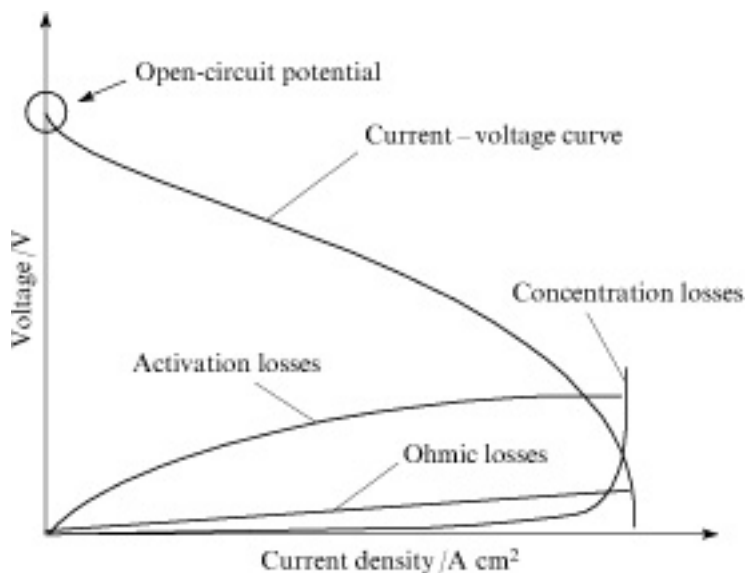


Figure 61: Typical voltage-current curve for a SOFC, showing the main potential losses [?]

Fuel cell performance is typically calculated using a graph of cell potential against current density, from which a curve for power density can be plotted, and the point of maximum power density can be observed. Figure 61 demonstrates a typical voltage-current density plot for a SOFC. The shape is characterised by the three main potential losses - activation losses, ohmic (or resistive) losses, and concentration losses. Activation losses are due to the activation energy of the electrodes, which is required for the reactions to start [?]. Ohmic losses are due to the resistive losses in the electrolyte as the electrons pass through it - the losses in the electrodes and the interconnects are considered negligible [?]. The concentration losses are due to the changing concentration gradients between the electrode surface and the TPB. The reaction is rate-limited by the rate at which ions are absorbed in the electrodes, so the concentration losses sharply increase at high current densities, where more reactants are present at the TPB, and the concentration gradient rapidly drops and no ions move across the electrodes [?]. The cell potential is calculated as the maximum theoretical voltage (the ‘Nernst Voltage’) minus the losses across the electrodes and electrolyte [?]:

$$V = E - \phi_{act,a} - \phi_{act,c} - \phi_\Omega - \phi_{conc,a} - \phi_{conc,c} \quad (130)$$

Where the Nernst voltage E is found from the Nernst equation [?]:

$$E = E^0 + \left(\frac{RT}{zF} \right) \frac{P_{H_2} \sqrt{P_{O_2}}}{P_{H_2O}} \quad (131)$$

$$E^0 = \frac{-\Delta G}{zF} = \frac{(\Delta H^0 - T\Delta S^0)}{zF} \quad (132)$$

z is the number of electrons exchanged in the reaction, F is Faraday’s constant, ΔG is the Gibbs free energy, ΔH^0 is the change in enthalpy of the reaction, ΔS^0 is the change of entropy of the reaction, R is the universal gas constant, T is the temperature, and P is the partial pressure of the substance in subscript, at the electrode surface. $\phi_{act,a}$ and $\phi_{act,c}$ represent the losses due to ‘activation overpotential’ of the anode and cathode, respectively. These can be derived from the Butler-Volmer expression [?], giving:

$$\phi_{act,\gamma} = \frac{RT}{F} \sinh^{-1} \left(\frac{J}{zJ_{0,\gamma}} \right) \quad (133)$$

Where γ represents the anode or cathode, J is the current density of the cell, and J_0 is the exchange current density of the electrode. $J_{0,\gamma}$ is given in literature as [?]:

$$J_{0,a} = \gamma_a \left(\frac{P_{H_2}}{P^0} \right) \left(\frac{P_{H_2O}}{P^0} \right)^m e^{\left(\frac{-E_{act,a}}{RT} \right)} \quad (134)$$

$$J_{0,c} = \gamma_c \left(\frac{P_{O_2}}{P^0} \right)^{0.25} e^{(-\frac{E_{act,c}}{RT})} \quad (135)$$

Where E_{act} is the activation energy of the electrode, P^0 is the ambient pressure, and γ_a , γ_c and m are experimentally determined constants. ϕ_Ω represents the resistive losses in the electrolyte, and is calculated using:

$$\phi_\Omega = J\delta_e R_\Omega \quad (136)$$

Where δ_e is the thickness of the electrolyte, and R_Ω is the resistivity of the electrolyte. $\phi_{conc,a}$ and $\phi_{conc,c}$ represent the losses due to ‘concentration overpotential’. These are derived using the Dusty-Gas Model and are given in literature [?]. The equations differ depending on the type of electrolyte used in the cell:

SOFC-O:

$$\phi_{conc,a} = \frac{RT}{2F} \ln \left(\frac{P_{H_2}^{TPB} P_{H_2O}}{P_{H_2} P_{H_2O}^{TPB}} \right) \quad (137)$$

$$\phi_{conc,c} = \frac{RT}{4F} \ln \left(\frac{P_{O_2}}{P_{O_2}^{TPB}} \right) \quad (138)$$

SOFC-H:

$$\phi_{conc,a} = \frac{RT}{2F} \ln \left(\frac{P_{H_2}}{P_{H_2}^{TPB}} \right) \quad (139)$$

$$\phi_{conc,c} = \frac{RT}{2F} \ln \left(\frac{P_{H_2O}^{TPB} \sqrt{P_{O_2}}}{P_{H_2O} \sqrt{P_{O_2}^{TPB}}} \right) \quad (140)$$

Where P^{TPB} is the pressure of the substance in subscript, at the triple-phase boundary, which is the point at which the reaction takes place. These pressures are derived using an extended form of the Stefan-Maxwell model [?] (re-written according to the nomenclature used in this report):

$$\frac{dy_i}{dx} = \frac{-N_i}{D_{i,k}^{eff}} - \frac{(y_j N_i - y_i N_j)}{D_{i,j}} \quad (141)$$

Where y is the mole fraction of the subscript gas (directly proportional to the partial pressure), N is the molar flux of the subscript gas, $D_{i,j}$ is the diffusion coefficient, and $D_{i,k}^{eff}$ is the effective Knudsen coefficient of the gas i . The current of the cell can be calculated by [?]:

$$I = \dot{n}zF \quad (142)$$

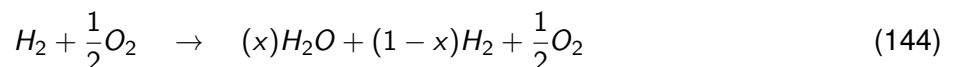
Where I is the current of the cell, and \dot{n} is the molar flow rate of hydrogen into the fuel cell. This is related to the molar flow rate of ammonia by the molar ratios of the chemical equations.

7.3.4 Cell Reaction

The reaction for ammonia decomposition is:



The reaction inside the fuel cell is:



Where x is the fraction of hydrogen that is utilised in the reaction. All terms in Equations 143 and 144 are in the gaseous state. From these we can see that the molar ratios of substances, and calculate the mole fractions of the substances at the electrodes before the reaction takes place. We can also calculate that the molar air to fuel ratio must be 3.57, and therefore is 3.57 by volume, by the ideal gas assumption. This assumption is valid given the high temperatures of the gases.

7.4 Design Procedure

7.4.1 Model Design

A model was designed using MATLAB in order to simulate the effect of changing the various design parameters on the cell's power density. The various properties of the gases involved in the reaction, and the material properties of the electrodes and electrolyte, were used as inputs, and the various design equations implemented to calculate the final cell potential. The Extended-Stefan-Maxwell equations formed two separate systems of ordinary differential equations, which were solved using the MATLAB function *ode45*. Plotting the cell potential and cell power density, against the current density allowed the maximum power output to be found graphically, and therefore the optimal operating conditions could be found.

7.4.2 Experimentation

By changing the operating conditions and material properties in the model, different conditions could be tested so that the optimal cell design could be found. Due to a limited variety of appropriate materials in literature, there were very few different parameters that could actually be changed, and therefore investigated. As such a direct comparison between a SOFC-O and a SOFC-H could not be found. The most important of these parameters were the operating temperature and pressure, and the thickness of the electrodes and electrolyte in the cell. A 'control' configuration was decided

on, so that results could be compared, and then each variable was changed to see the effect on the maximum power density.

The control configuration was heavily based on the design used by Zamfirescu et al. [?], using nickel mixed with YSZ for the anode, a YSZ electrolyte, and a LSM-YSZ cathode. Though the final design would require one component to be significantly larger than the other to give structural stability, they were all equally thick at 50 micrometres. This was so that the effect of changing the component thicknesses could be clearly demonstrated. The operating conditions were a temperature of 1073 K, and atmospheric pressure. For all tests, the ammonia decomposition was assumed to be 100% (due to the Nickel present at the anode, which catalyses the breakdown), and the hydrogen utilisation was assumed to be 80% [?].

7.4.3 Results

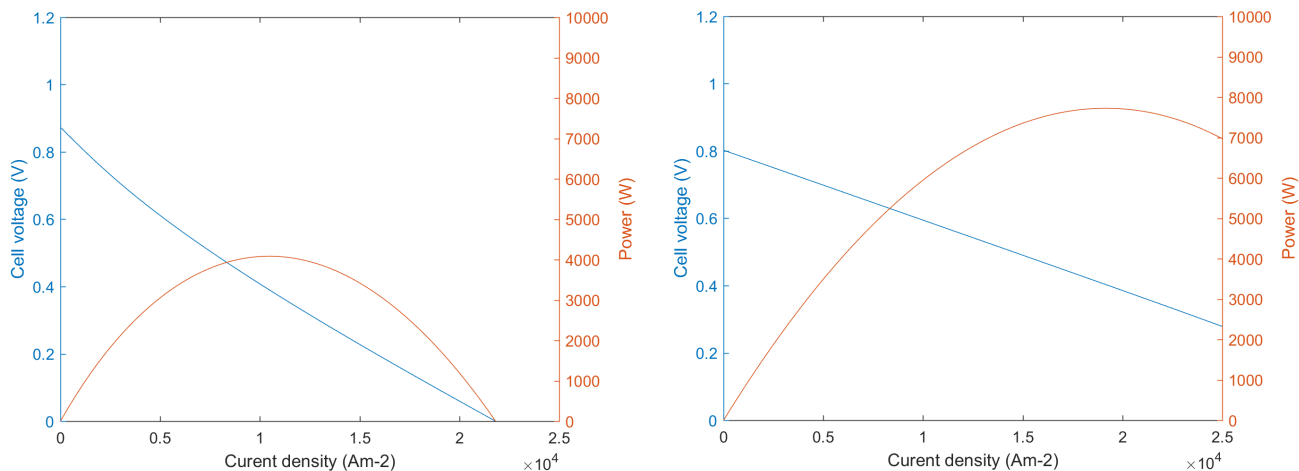


Figure 62: Voltage and Power vs Current Density for the control configuration (left) and an increased temperature of 1273 K (right)

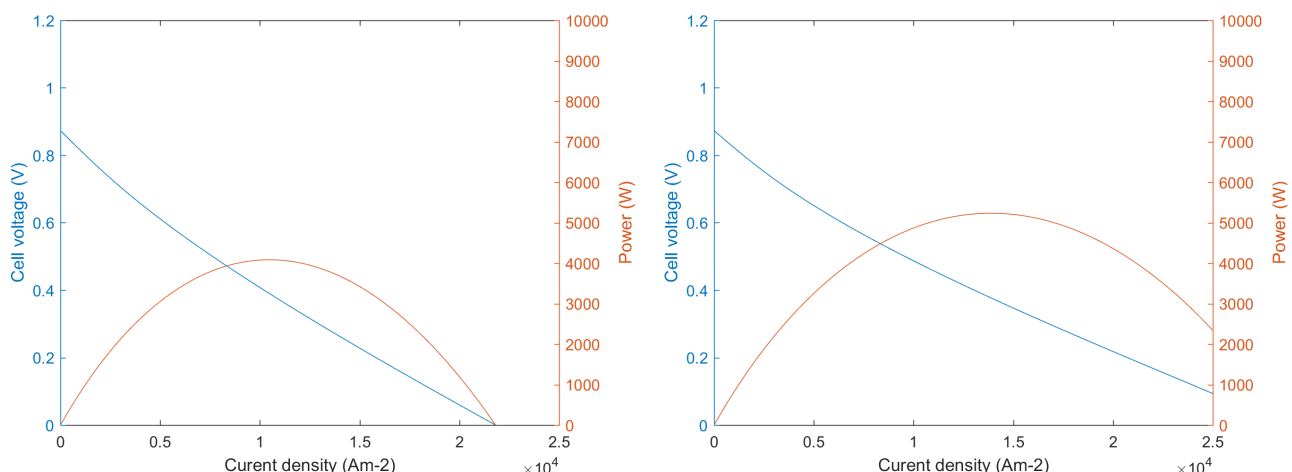


Figure 63: Voltage and Power vs Current Density for the control configuration (left) and an increased pressure of 5 bar (right)

The effects on the performance by changing the operating conditions are shown in Figures 62 and 63. Increasing temperature and pressure both increase the cell's maximum power density, but increasing temperature has the most significant effect. The effect of changing the support method is shown in Figure 64. It is clear from Figure 64 that an anode-supported cell has superior power density. The increased anode thickness causes the power density to increase, whereas the electrolyte and cathode supported cells result in significant decreases in power density. The electrolyte supported case can be explained by the significant increase in ohmic losses. The cathode supported case is likely an exaggerated result due to the failure of the ESM model to account for the rate of change of concentration gradient, causing it to drop rapidly, resulting in the very sudden increase in concentration losses. However, the conclusions drawn are supported by Villalba's thesis [?], and it is widely stated in literature that anode-supported cells are superior. This seems to be a consequence of the increased anode thickness, which slows down the rate of transfer of the water produced in the cell reaction. As such, there is less build up of water at the anode surface, and therefore a smaller drop in the partial pressure of hydrogen and the cell potential.

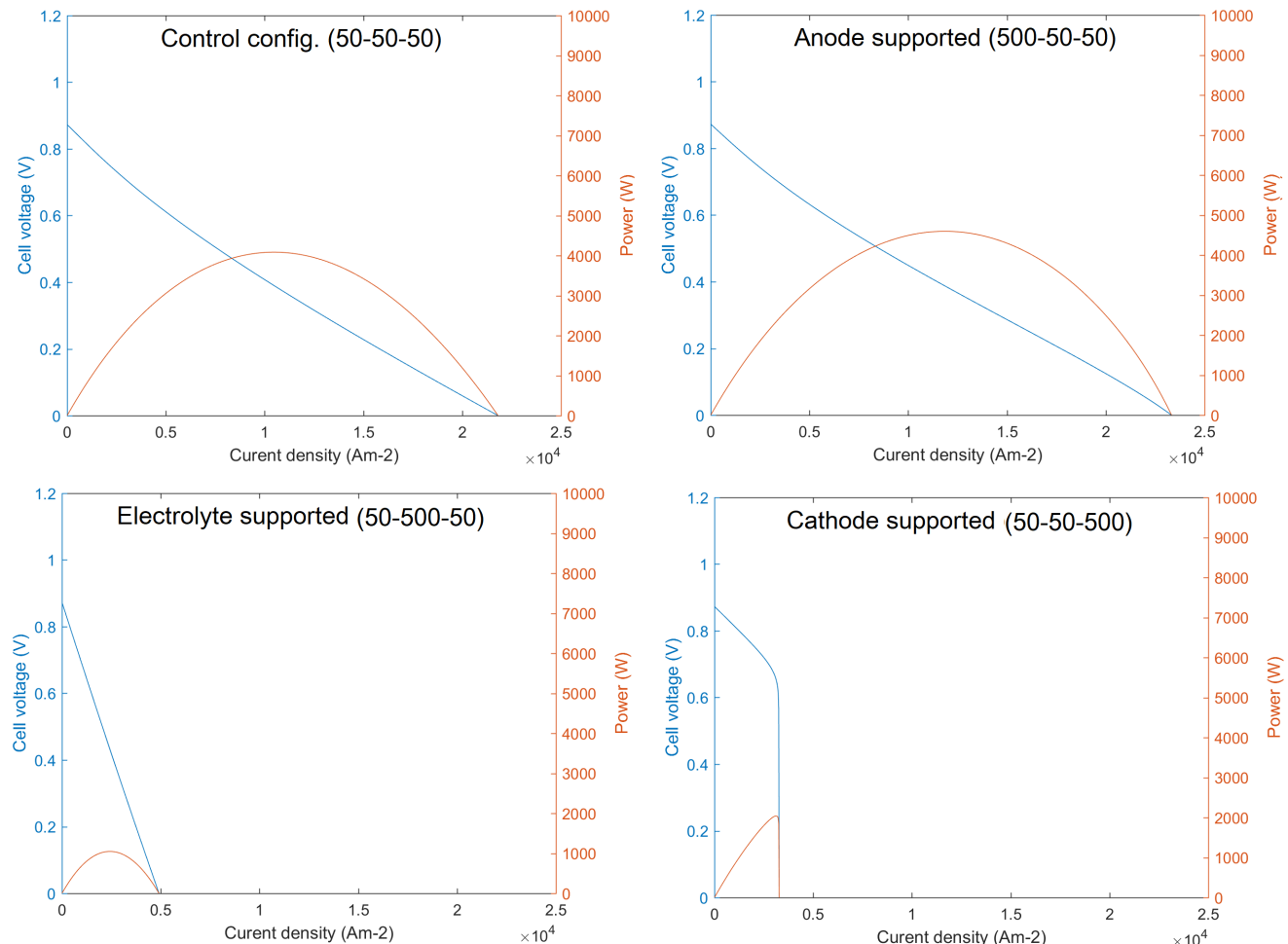


Figure 64: Voltage and Power Density vs Current Density for the 4 different support configurations
(Dimensions given in the form "Anode - Electrolyte - Cathode", in micrometres)

7.4.4 Final Cell Stack Design

Based on these conclusions, some further testing was performed and a final design was decided on: Ni-YSZ/YSZ/LSM-YSZ (500-20-30), at 1273 K and atmospheric pressure. The performance graph for this design is shown in Figure 65. These results can be verified by their similarity to Zamfirescu's results, as the model is very similar [?].

By choosing a cell area of $0.3 \text{ m} \times 0.3 \text{ m}$, currently the largest that can be produced [?], the power produced per fuel cell can be shown to be 870 W. To fulfill the demand of 230 MW, the cells themselves will need to produce 150 MW, as the integrated turbine will be able to produce the remaining 80 MW (see Section 7.5). Therefore, just under 172,500 cells will be required. Stacks of 1150 cells will be used, each producing just slightly over 1 MW, requiring 150 stacks in total.

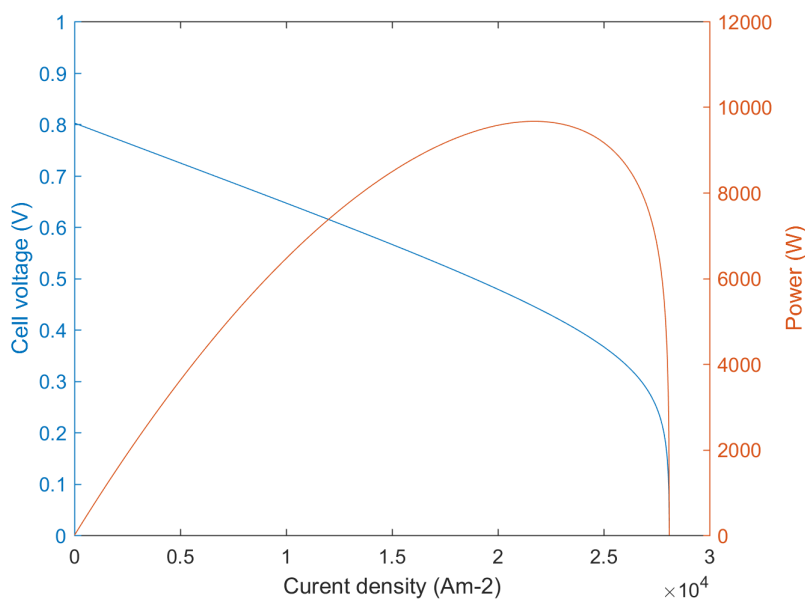


Figure 65: Voltage and Power Density against Current Density for the final cell design

7.4.5 Thermodynamic Analysis

The reaction in the cell is exothermic overall. Ammonia decomposition absorbs 37.278 kJ per mole of H₂ and the cell reaction produces 199.578 kJ per mole of H₂, so 162.3 kJ per mole of H₂ is produced overall - or 243.45 kJ per mole of NH₃. This heat can be used to heat up the inlet gases to the operating temperature. Therefore, the inlet temperature of the fuel and air can be calculated using the equation:

$$Q_{heat} - Q_{loss} = mc_p(T_{SOFC} - T_i) \quad (145)$$

Where T_i is the temperature of the inlet reactants, in Kelvin. As the value of c_p depends on the inlet temperature, it must be found iteratively. A short MATLAB script was devised for this purpose. Q_{heat}

could be calculated as the total energy produced by the reaction in the SOFC system, subtracting the energy released as electricity. Q_{loss} represents the heat loss from the SOFC system. This was found by calculating the one-dimensional overall heat transfer coefficient (HTC) between the fuel cell and its surroundings, and applying it to the total area of the stack.

$$Q_{loss} = UA(T_{SOFC} - T_{amb}) \quad (146)$$

Where U is the overall HTC, A is the total area of the SOFC stack, and $(T_{SOFC} - T_{amb})$ is the difference between the SOFC temperature and the ambient temperature.

To simplify this calculation, it is assumed that the fuel cell stacks have a uniform temperature of 1273 K. This assumption is acceptable provided the Biot number is less than 0.1. This can be calculated by:

$$Bi = h_{conv} \sum_i^n \frac{t_i}{k_i} \quad (147)$$

Where h_{conv} is the convective HTC of the overall body, t_i is the thickness and k_i is the thermal conductivity of component i . As the materials of the anode, cathode, and electrolyte are all variations of YSZ, we can assume the value of k_i to be the same for each. The values are given in Table 45.

Table 45: Table of component HTC's and thicknesses [?] [?]

Component	Conductive HTC ($\text{Wm}^{-1}\text{K}^{-1}$)	Thickness (m)
Interconnect	1.9	1×10^{-3}
Electrodes and Electrolyte	2.5	600×10^{-6}

h_{conv} is given as $16 \text{ Wm}^{-2}\text{K}^{-1}$ [?]. The Biot number is calculated as 0.012, therefore the assumption is valid. Due to the very high temperature of the system, heat losses from radiation are the most significant. The radiative heat transfer coefficient can be calculated using the equation [?]:

$$h_{rad} = \epsilon\sigma(T_{SOFC}^2 + T_{amb}^2)(T_{SOFC} + T_{amb}) \quad (148)$$

Where ϵ is the emissivity of the body, and σ is the Stefan-Boltzmann constant. Assuming an emissivity value of 0.8 [?], the coefficient is calculated as $121.8 \text{ Wm}^{-2}\text{K}^{-1}$. The conductive and convective heat transfer coefficients are also accounted for. The convective HTC is $16 \text{ Wm}^{-2}\text{K}^{-1}$ as given previously, and the conductive heat transfer is given by:

$$h_{cond} = \frac{k}{t} \quad (149)$$

Where k and t are the thermal conductivity and thickness of the insulation around the SOFC. The overall HTC can then be calculated by:

$$U = \frac{1}{\frac{1}{h_{rad}} + \frac{1}{h_{conv}} + \frac{1}{h_{cond}}} \quad (150)$$

The heat loss from the stack can be reduced significantly depending on the thickness of insulation, and the material used. The only insulator suitable for the high temperature of the SOFC stack is mineral wool [?], with a typical thermal conductivity of $0.04 \text{ Wm}^{-1}\text{K}^{-1}$ [?]. Heat loss against insulation thickness is plotted in Figure 66.

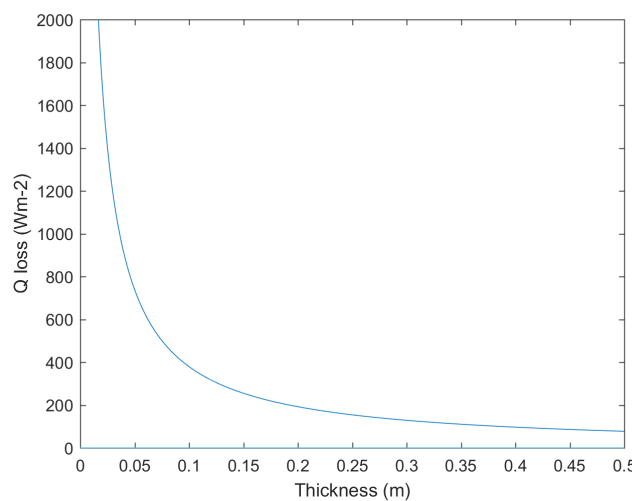


Figure 66: Heat loss per square metre against the thickness of insulation

It can be seen that diminishing returns occur almost immediately after a thickness of 0.05 m. As such, using this value, the total heat loss per cell is calculated using Equation 146, giving a heat loss per cell value of 1.488 W, which for the entire system is 256.68 kW. Using Equation 145 iteratively, recalculating the $c_p(T_i)$ value for the inlet gases each time, the required inlet temperature for the fuel and air is 600 K.

7.5 Integrated Gas Turbine

7.5.1 Secondary Gas Turbine Cycle

Knowing that the inlet temperature for the reactant streams is 600 K, the hot exhaust from the fuel cells can be used to heat the streams to this desired temperature. The fuel is stored as a liquid at 243 K and ambient pressure (see Section 5.8), so must first be heated slightly to convert it to the gaseous state. The gas can then be directed through a heat exchanger operating counter currently to the exhaust stream, where it is heated to 600 K. The exhaust flow can also be used to heat up

the air flow, from ambient temperature to 600 K, in the same way. The heat exchange can be calculated using:

$$(mc_p\Delta T)_{\text{exhaust}} = (mc_p\Delta T)_{\text{reactant}} \quad (151)$$

c_p for the fuel and air streams can be taken from the JANAF tables [?], and can be calculated for the exhaust stream at different temperatures by:

$$c_p = \sum_i^n c_{pi}y_i \quad (152)$$

Where y is the mole fraction of the component i in the exhaust mixture.

Table 46: Heat Exchanger stream temperatures

Heat Exchanger	Reactant inlet temp (K)	Reactant outlet temp (K)	Exhaust inlet temp (K)	Exhaust outlet temp (K)
HEX 1 (Fuel / Exhaust Streams)	243	600	1273	1205
HEX 2 (Air / Exhaust Streams)	298	600	1205	1030

It can be seen in Table 46 that the exhaust stream is still extremely hot, at 1030 K. This heat is used to drive a secondary gas turbine cycle, which is used to generate additional work and increase the overall efficiency of the system. By reducing the exhaust stream temperature to 298 K, it can safely be ejected to the atmosphere as seen in Figure 67. The temperature against entropy plot for the cycle is shown in Figure 68.

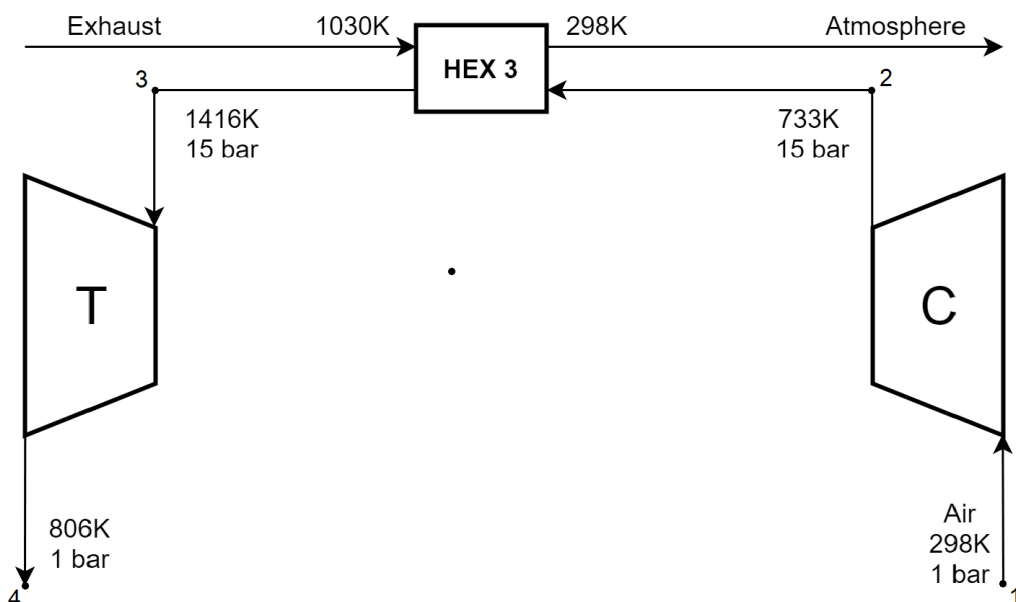


Figure 67: Diagram of the gas turbine cycle

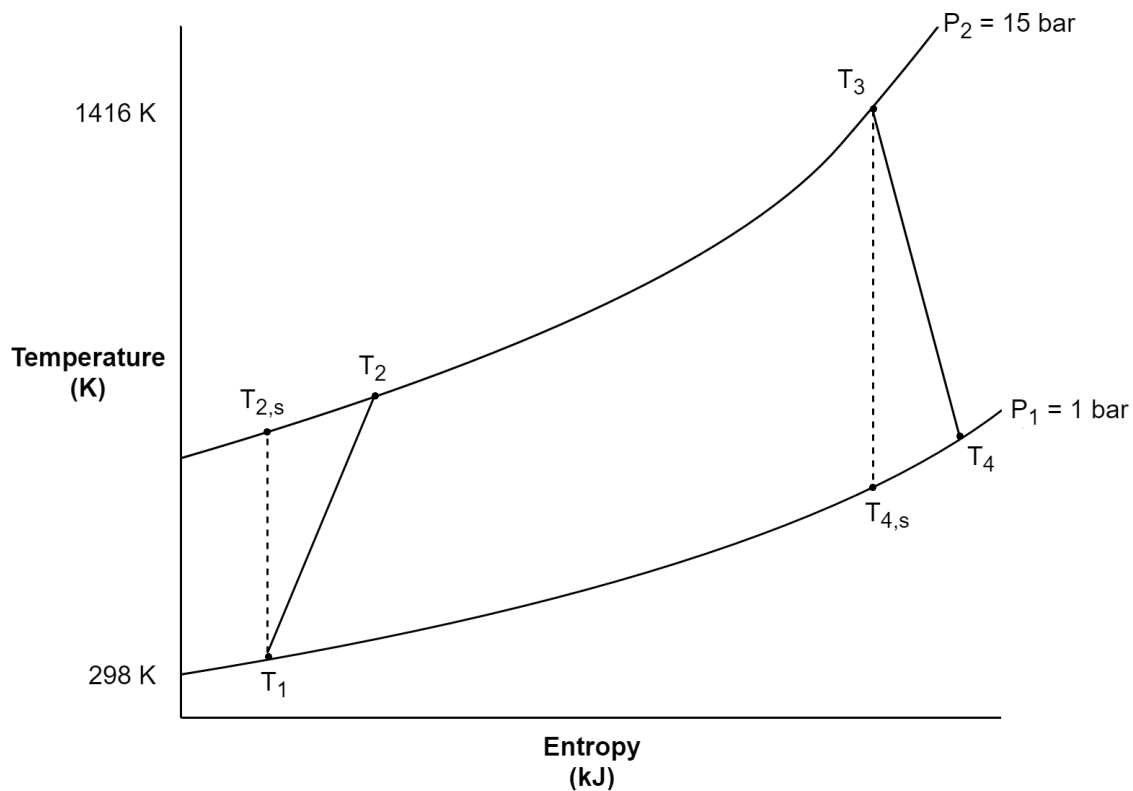


Figure 68: Temperature against Entropy plot for the gas turbine cycle

Modelling the secondary gas turbine cycle as a Brayton cycle, the cycle can be analysed with the following equations:

$$T_{2,s} = T_1 \left(\frac{P_2}{P_1} \right)^{\frac{\gamma-1}{\gamma}} \quad (153)$$

$$T_2 = T_1 + \frac{(T_{2,s} - T_1)}{\eta_c} \quad (154)$$

$$T_{4,s} = \frac{T_3}{\left(\frac{P_2}{P_1} \right)^{\frac{\gamma-1}{\gamma}}} \quad (155)$$

$$T_4 = T_3 - \eta_t (T_3 - T_{4,s}) \quad (156)$$

$$W_{in} = c_p (T_1 - T_2) (\dot{m}_{air}) \quad (157)$$

$$W_{out} = c_p (T_3 - T_4) (\dot{m}_{air}) \quad (158)$$

$$\text{Net power out} = W_{out} - W_{in} \quad (159)$$

Where T_i is the temperature at point i , P_i is the pressure at point i , γ is the ratio of specific heats of air, η_t and η_c are the isentropic efficiencies of the turbine and compressor respectively, c_p is the specific heat capacity, W_{in} is the work done on the gas by the compressor, W_{out} is the work done by the gas on the turbine, and \dot{m}_{air} is the mass flow rate of air through the cycle. T_1 and P_1 are the am-

bient conditions of atmospheric air, γ for air is 1.4, and η_t and η_c are assumed to be 0.8 [?]. T_3 is calculated using Equation 151 across a third heat exchanger, using T_2 as the inlet air temperature. This depends on P_2 , which is chosen to be 15 bar as operating under 12 bar was found to cause the power output to decrease with increasing mass flow of air. \dot{m}_{air} is determined graphically so as to optimise the value of T_3 , and subsequently optimise the net power produced by the cycle. This was done using MATLAB and produced the results shown in Figure 69.

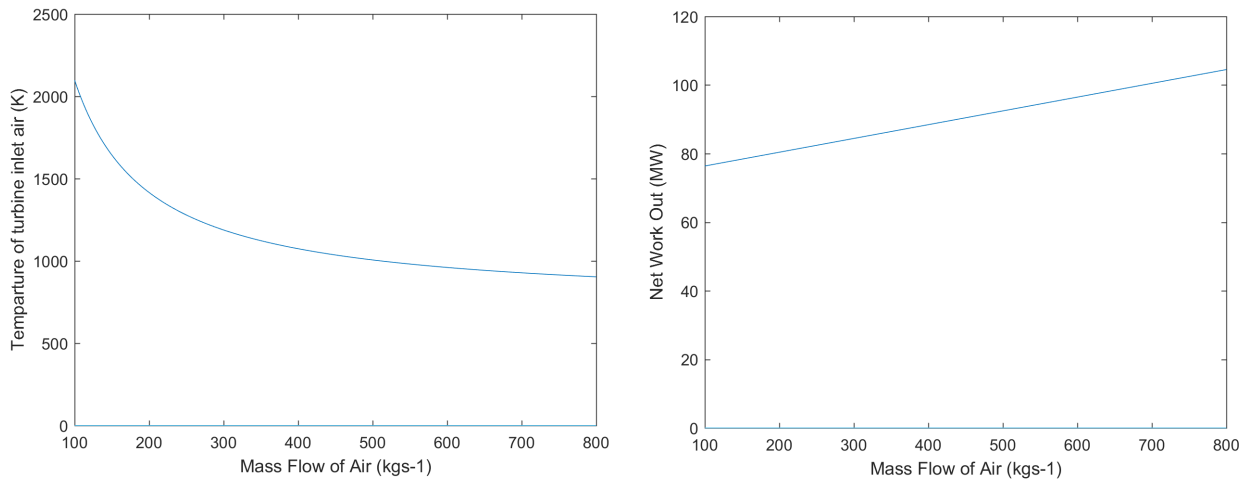


Figure 69: (Left) Temperature of turbine inlet air against mass flow rate of air
 (Right) Net work produced by the gas cycle against mass flow rate of air

Flow rates below 100 kgs⁻¹ were ignored as the temperatures were unfeasibly high. The turbine inlet temperature was constrained by the melting point of the turbine itself. Using the melting point of stainless steel as a guideline, at 1783 K [?], and erring on the side of caution, a mass flow rate of 200 kgs⁻¹ was taken, giving an inlet temperature of 1416 K, and a net work value of 80 MW. An advantage of this is that the power output can be increased simply by increasing the mass flow rate, if required.

7.5.2 Heat Exchangers

Knowing the desired temperatures of the various streams, the heat exchangers can be analysed in more detail. In order to properly estimate the cost of the plant, the areas of the heat exchangers must be calculated. The general equation for heat exchanger design is:

$$Q = UA\Delta T_{LM} \quad (160)$$

Where Q is the heat transferred, U is the overall heat transfer coefficient, A is the area, and ΔT_{LM} is the log mean temperature difference over the exchanger. Assuming the heat exchangers are ideal, with no losses, operating at constant pressure, and adopting the shell and tube design, the typical

values of heat transfer coefficients for a variety of stream combinations can be found. As all the streams are gases, not including steam, the value of the HTC lies between 10 and 50 $\text{Wm}^{-2}\text{K}^{-1}$ [?]. Taking a conservative average value of $25 \text{ Wm}^{-2}\text{K}^{-1}$ for all streams, the heat exchanger analysis is as follows:

Table 47: Summary of heat exchanger analysis

Heat Exchanger	$Q (\text{MW})$	$U (\text{Wm}^{-2}\text{K}^{-1})$	$\Delta T_{LM} (\text{K})$	$A (\text{m}^2)$
HEX 1	14.36	25	809	710
HEX 2	36.38	25	666	2185
HEX 3	146.11	25	410	14255

7.6 System Controller

As stated in Section 7.3.4, the desired air to fuel ratio (AFR) for molar equilibrium is 3.57. This ratio is desirable as it maximises the efficiency by allowing the reaction to take place while minimising the amount of wasted air or fuel that doesn't react. To achieve this, a controller was designed such that the AFR can be set by an operator, and any changes to the fuel flow will cause the air flow to change accordingly. The controller was designed using Simulink, and models the movement of valves that control the volume flow rate of fuel and air. The transfer function for a typical valve was found to be [?]:

$$G(s) = \frac{1}{\left(\frac{1}{52s} + 1\right)} \quad (161)$$

A valve ‘block’ was created in Simulink using this transfer function. Saturation was introduced, in order to accurately model the valves as the valves can only be fully open, partially open, or fully closed. Similarly, non-idealities are introduced to make the model more realistic, adding in errors to account for friction, or small pipe leakages etc. This formed the basis for the control plant, representing the fuel valve, and a feedback loop was created using a PID controller, where the input is a step change in fuel flow. The PID controller was then tuned to give an appropriately smooth and quick response, with the aim being a response time of less than one second. This plant was duplicated for the air valve, but with the input being the fuel flow multiplied by the AFR to give the optimal air flow. The results of the simulation are shown in Figure 70. The step change occurs at 0.2 seconds, and it is clear that a smooth response happens in under 0.1 seconds. The block diagram of the controller is shown in Figure 71, with the plant for each valve shown in Figure 72.

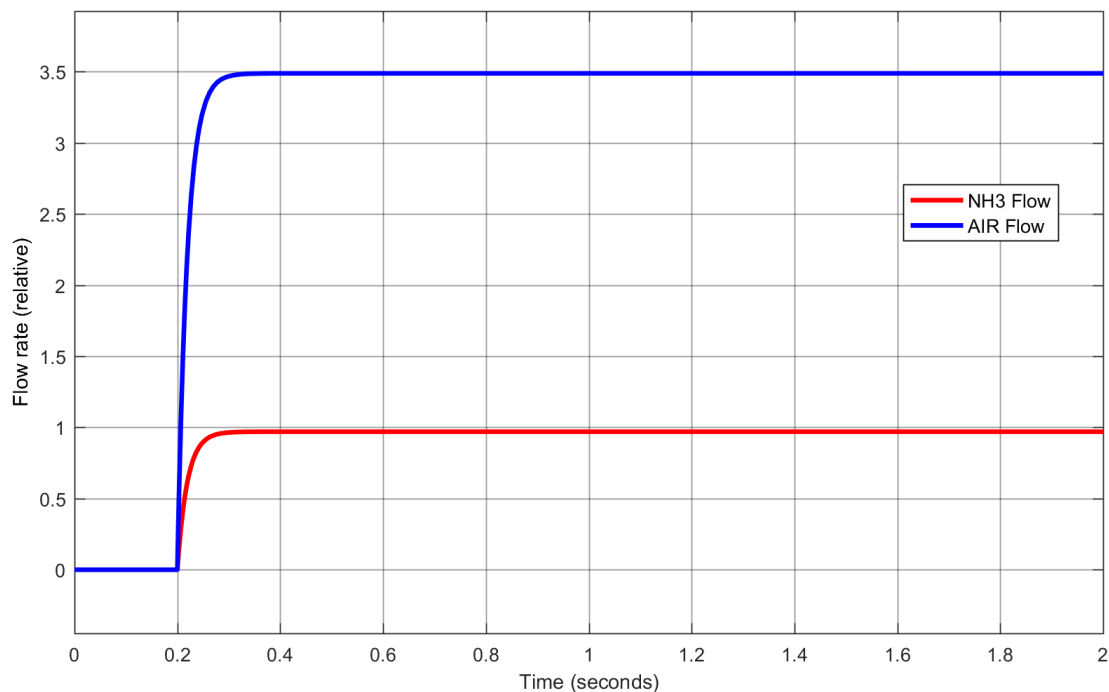


Figure 70: The controller response to a step change in desired fuel flow rate

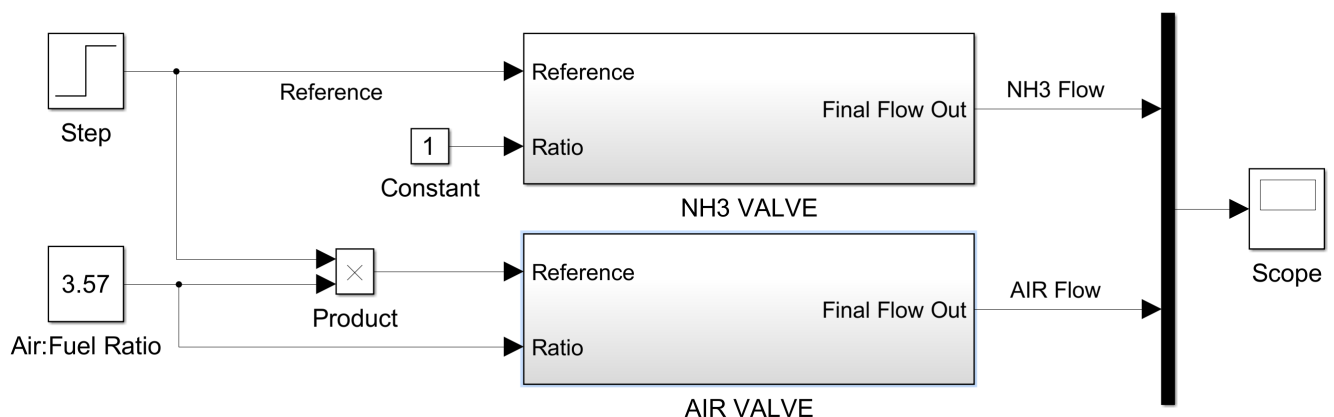


Figure 71: Overall plant diagram of the fuel and air valve controller

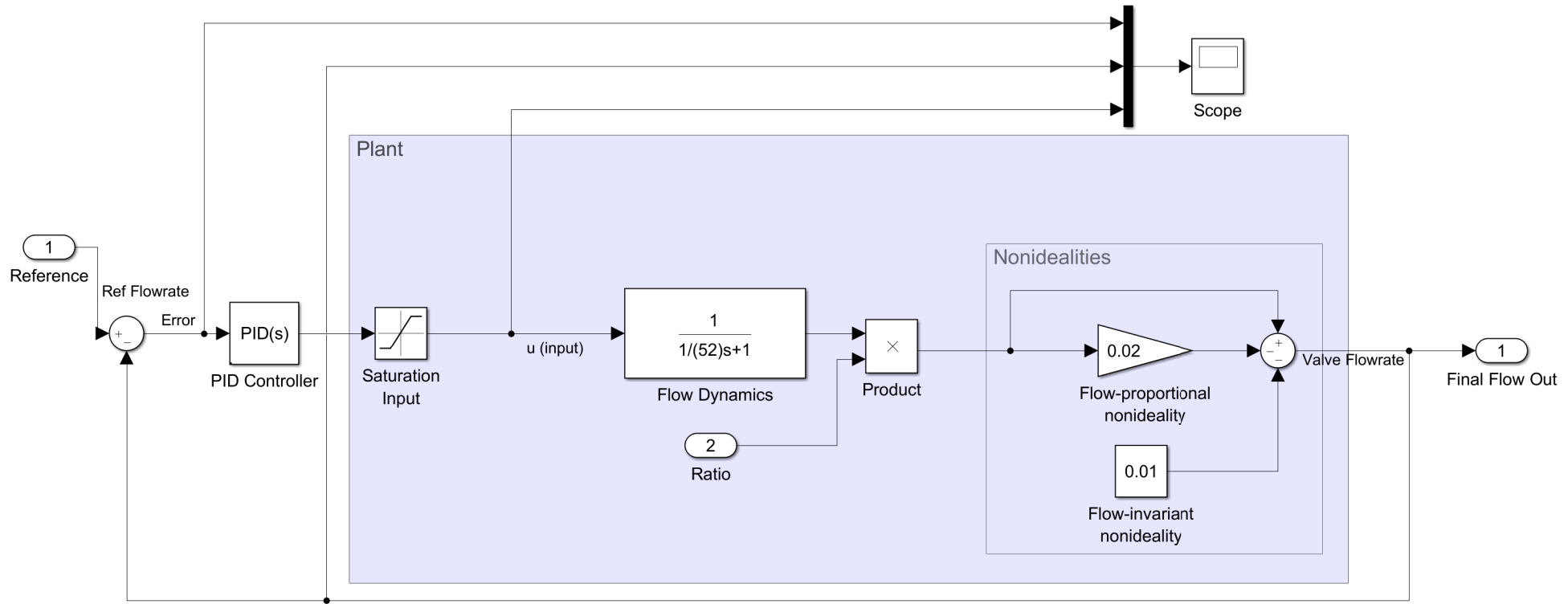


Figure 72: Zoom in of the individual valve control plants (identical for fuel and air)

7.7 System Overview

Table 48 gives an overview of the SOFC-gas turbine system characteristics. The overall efficiency of the system is calculated by the total net power output divided by the total energy of the fuel input:

$$\eta_{overall} = \frac{\text{Total Net Power Out}}{LHV_{(NH_3)} \cdot \dot{m}_{(NH_3)}} \quad (162)$$

Where LHV_{NH_3} is the ‘lower heating value’ of ammonia (found to be 18.6 MJkg^{-1} [?]), and \dot{m}_{NH_3} is the total mass flow rate of ammonia into the SOFC.

Table 48: Overview of the SOFC-integrated gas turbine system characteristics

Number of cells per stack	1150
Maximum power output of single stack (MW)	1.0
Number of fuel cells stacks	150
Total net power from SOFC (MW)	150
Total net power from turbine cycle (MW)	80
Overall efficiency	62.7%

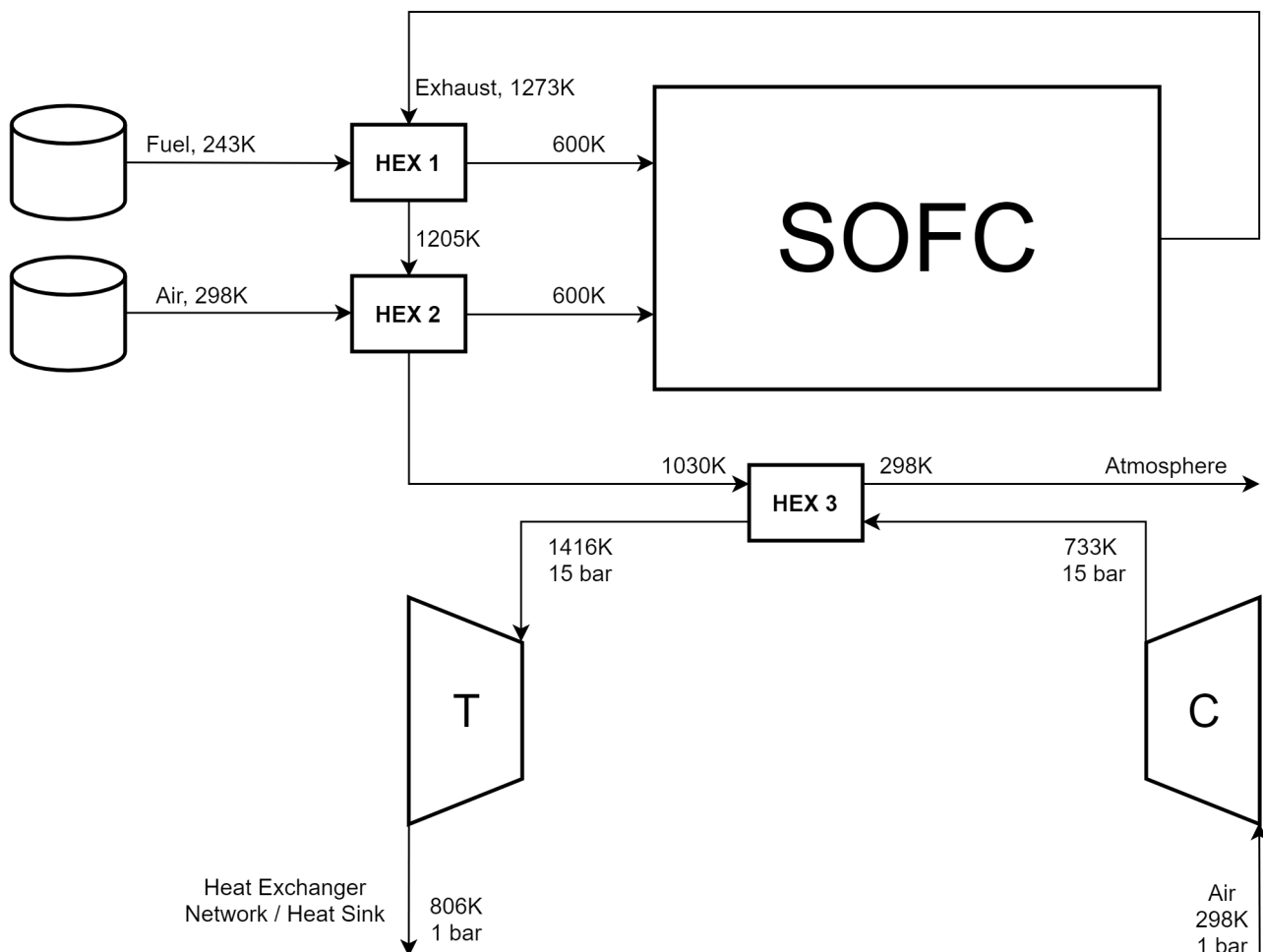


Figure 73: Diagram of overall SOFC-Gas cycle system

7.8 Cost Analysis

The purchase costs of the various components are shown in Table 49. The cost of the SOFC accounts for the cost of manufacture and testing, as well as accounting for various auxiliary systems such as the electronics, controls and sensory instruments, and assumes a sale price mark up of 50%. The final value given in the fuel cell financial report [?] also includes the supply of fuel, air and water - these values have been removed from the total, giving \$6200 per kW. The gas cycle components were found to be \$700 per kW generated [?]. The heat exchanger costs were calculated using [?]:

$$C_{HEX} = 130 \left(\frac{A}{0.093} \right)^{0.78} \quad (163)$$

Where C_{HEX} is the cost of the heat exchanger in USD, and A is the area of the heat exchanger in square metres.

Table 49: Cost of SOFC system components

Component	Cost per kW (USD)	Total Cost (millions of USD)
Fuel Cells	1.0	930
Gas Cycles	150	56
Heat Exchanger	Area (m ²)	Cost (millions of USD)
HEX 1	710	0.14
HEX 2	2185	0.33
HEX 3	14255	1.44

The fuel cells have a life span of approximately 5.5 years, so will need to be replaced every 5 years [?]. The total costs, including operation, labour costs and maintenance costs, are dealt with in detail in Section 12.

7.9 Sustainability Analysis

The integrated SOFC-gas turbine system is sustainable by design. The SOFC produces no particulate matter or greenhouse gases, and despite concerns about the production of nitrous oxides, these concerns have been shown to be unnecessary as the high operating temperature of the fuel cells mean the reaction is almost entirely complete [?]. As such, NO_x production is negligible provided the SOFC system is run at the specified temperature. The fuel cells themselves are constructed from very common materials, so there is no danger of any material shortage in future. Unlike most fuel cells, which run on hydrocarbons, the ammonia-fed fuel cell doesn't coke [?], giving it a much longer life span in comparison. The gas turbines are fed entirely with atmospheric air, and heated using the exhaust from the fuel cells. The combination of the fuel cells with the gas turbines significantly increases the efficiency of the system - over 60% in this case - much more efficient

than conventional power generation methods, which are typically around 40% efficient [?].

7.10 Safety and Risk Analysis

A Hazard and Operability (HAZOP) analysis was performed on the plan for the SOFC system in order to identify any potential risks of danger to personnel, as well as damage to the system itself. The results of this analysis are displayed in Table 50.

7.11 Further Considerations

Several improvements could be made to the analysis in this project, with the most significant improvements being made to the SOFC model. Firstly, the more accurate Dusty-Gas Model could have been used, instead of the Extended Stefan-Maxwell Model, as it takes into account the effect of diffusion and permeation mechanics on the concentration of the reacting species [?]. Due to implementation problems however, the Extended-Stefan-Maxwell model was used instead.

Secondly, the original intent of the model was to investigate a variety of different SOFC configurations, using different materials for the electrodes and electrolyte, and investigating the differences in performance between oxygen conducting SOFCs and hydrogen conducting SOFCs. However, due to the lack of literature and data regarding SOFC testing, there was very little variety in the materials used in the SOFCs, and a meta-study [?] comparing over 15 different configurations showed that the vast majority of electrodes and electrolytes were made of YSZ, with very minor differences due to different mixture compositions with other metals. For many of these mixtures, values for fundamental properties affecting SOFC performance were not available, and so could not be implemented properly into the model.

Finally, the heat exchangers could be designed in greater detail, looking at non-dimensional numbers such as the Reynold's number and the Nusselt number, which are based on the fluid properties but also the dimensions of the heat exchanger. This would allow for accurate values for the heat transfer coefficients. Heat losses could also be considered, as well as heat exchanger insulation. However, these changes are not so significant as the costs involved with the heat exchangers are negligible in comparison with the fuel cells themselves, and particularly in the grand scheme of the plant economics.

Table 50: HAZOP Analysis for the SOFC system

Guide Word	Deviation	Cause	Consequence	Action
NO	Air flow	Pipe leakage	No reaction, therefore no power output	Regular inspection of air flow equipment
		Damage to air inlet		
	Fuel flow	Pipe leakage	No reaction, therefore no power output, Ammonia leakage can ignite, and is toxic to humans	Regular inspection of fuel flow equipment, Check the ammonia storage/production facilities
		Damage to fuel inlet		
		No ammonia in storage/being produced		
	Heat input to SOFC STACKS	Faulty Heater	SOFC's can't be operated when needed	Regular inspection of heater
	Heat input to air and fuel flows	Heat exchangers are damaged	Reaction happens at a lower temperature, fuel efficiency decreases, dangerous compounds in exhaust	Regular inspection of exchangers, install heat sensors at inlets
MORE	Electricity output	Faulty wiring	No power output	Regular inspection
	Air flow	Faulty controller, SOFC not operating as required	Plant efficiency decreases	Regular inspection of controller, Design system to notify control staff
	Fuel flow		Fuel utilisation decreases	
	Power output		Wasted power production	
LESS	Air flow	Faulty controller, SOFC not operating as required	Power output reduced	As above
	Fuel flow			
AS WELL AS	Air contamination	Surrounding air is contaminated	Cathode active sites become blocked with impurities	Install air filters at air inlet
	Fuel contamination	Faults with storage or production facilities	Anode active sites become blocked with impurities	Install filters where possible, install contaminant sensors, cease operation with contaminated fuel
	NOx in exhaust	Low temperature reaction	Harmful gases released	Install NOx sensors in exhaust, do not allow operation below specified temperature
PART OF	No reaction, despite correct fuel and air flow	Electrodes and electrolytes are not connected properly/damaged	No power output	Regular inspection of SOFC stacks
REVERSE	NA	NA	NA	NA
OTHER THAN	Start up/Shut down	Maintenance	Large temperature change causes damage to cells due to expansion/contraction	Minimise need for additional maintenance

8 Heat Exchangers

8.1 Introduction

Within the plant, there are many different streams that need to be heated and cooled. By designing a network of heat exchangers, heat can be transferred between these streams, thus improving overall plant efficiency. The pinch analysis method described by Smith [?] [?] was used to design the heat exchange network so that streams are matched most effectively.

8.2 Stream data

The turbine system was excluded from the heat exchange network as it is only in use 5% of the generation time and thus cannot provide any useful heating/cooling most of the time. Data was gathered about the incoming and outgoing streams from each major process unit and is summarised in Table 51. Figure 74 also shows how these streams are linked to the process units in the plant.

The change in enthalpy ΔH from the inlet to the outlet of each of the streams was calculated using:

$$\Delta H = \dot{m}C_p(T_{in} - T_{out}) \quad (164)$$

where \dot{m} is the mass flow rate, C_p is the specific heat capacity and T_{in} and T_{out} are the temperatures at the inlet and outlet respectively. The product $\dot{m}C_p$ is the heat capacity flow rate denoted as CP . Negative changes in enthalpy correspond to hot streams that must be cooled (heat supply) and positive changes in enthalpy correspond to cold streams that must be heated (heat demand).

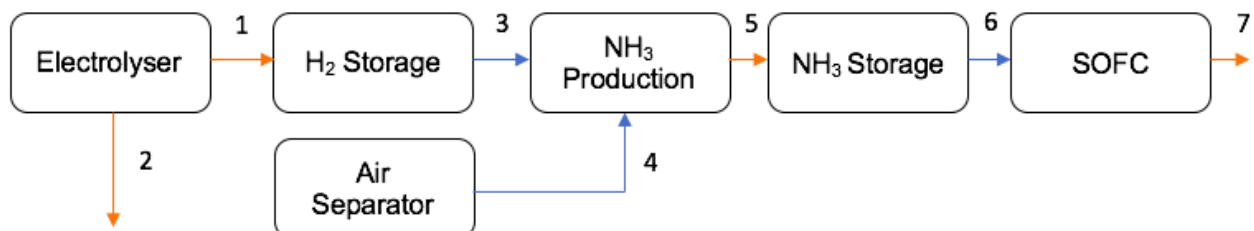


Figure 74: A diagram showing how different streams in the heat exchange network are related to the process units. Blue arrows represent cold streams that must be heated up and red arrows represent hot streams that must be cooled

Streams 2 and 7 are exhaust streams so they do not have to be fully cooled fully, and can be used as heating utilities with maximum power described in Table 51. This results in a total heat demand of 4.54MW and a total heat supply of 0.689MW with additional 124MW provided by hot streams 2 and 7. Therefore heating power must be supplied from streams 2 or 7 to fulfill heating requirements,

Table 51: Data for streams coming in and out of all major process units of the ESS plant

Stream	Composition	\dot{m} (kg/s)	C_p (kJ kg ⁻¹ K ⁻¹)	T_{in} (K)	T_{out} (K)	ΔH (kW)
1	H_2	0.4844	14.3	393	298	-658
2	O_2	35.75	0.919	393	298	-3119
3	H_2	0.5099	14.3	298	473	1276
4	N_2	2.34	1.04	288	473	450.2
5	NH_3	2.795	2.19	238	233	-30.6
6	NH_3	2.655	2.19	233	243	58.1
7	Air	200	1.01	898	298	-121200

extra heat that is not required for the network can be used as part of a cogeneration system.

8.3 Design Problem

A problem table, shown in Table 52, was used to summarise the temperature difference in each stream and to find the change in enthalpy across each temperature interval. For this table, the actual stream temperatures were shifted to guarantee that each heat exchanger will operate over a minimum temperature difference ΔT_{min} : $T_H^* = T_H - \frac{\Delta T_{min}}{2}$ for hot streams and $T_C^* = T_C + \frac{\Delta T_{min}}{2}$ for cold streams. A large ΔT_{min} means that less heat can be recovered, increasing utility costs. Decreasing ΔT_{min} will increase the heat recovered but will also increase the area of the heat exchangers required and the capital cost. It was set to 20K as the streams at the pinch points are gaseous, which require a larger ΔT_{min} than liquid streams [?]. Streams 2 and 7 were excluded from the problem table as they do not need to be cooled fully.

Table 52: Problem table for this design problem

T^* (K)	Stream & CP (kW K ⁻¹)					ΔT (K)	ΔH_{int} (kW)
	1 - 6.93	3 - 7.29	4 - 2.43	5 - 6.12	6 - 5.81		
483						100	-972
383		↑	↑			75	-209.3
308						10	45
298						10	69.3
288	↓					35	0
253					↑	10	-58.1
243						15	0
228				↓		5	30.6
223							

Using the problem table, the maximum cumulative negative enthalpy (greatest heat deficit) was -1181.3kW at 308K, the pinch point. This cannot be realised as it requires heat to be transferred up the temperature scale. To resolve this a hot utility of 1181kW was added. This heat cascades down the system to heat deficit intervals cooler in temperature as shown in Figure 75. The cascade diagram shows that the minimum heating and cooling requirements needed to satisfy the problem are 1181.3kW and 86.8kW respectively.

8.4 Pinch Design

Using the pinch design method, two separate networks were independently designed above and below the pinch. This is because minimum utility requirements cannot be met if heat is transferred across the pinch. To satisfy all stream requirements, two constraints also have to be met:

1. Above the pinch, the number of hot streams must be less than or equal to the number of cold streams so that cooling utilities are not needed.

2. The heat capacity flow rate of hot streams must be less than or equal to that of the cold stream they are matched with, so that no point has a temperature difference less than ΔT_{min} .

The reverse constraints apply below the pinch and are summarised in Table 53, which shows that the first constraint is not met above the pinch. Stream 1 was not hot enough to heat streams 3 and 4 so a fraction of stream 7 was added to the network to heat them (marked with *), which also allows the first constraint to be satisfied. Where there were multiple streams that can be matched, they were selected to give the greatest temperature difference, which reduces area of the heat exchangers and therefore the capital cost of the network required. Equation 164 was used to calculate enthalpy requirements and temperature coming out of each heat exchanger.

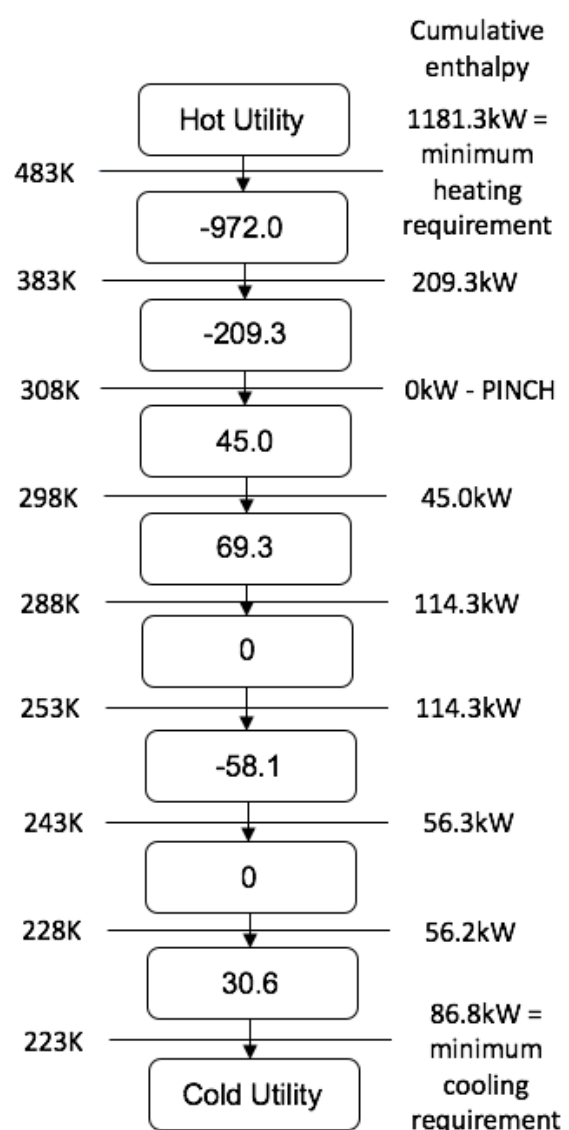


Figure 75: Cascade diagram for the heat exchange network.

Table 53: Constraints for pinch design of the heat exchange network. The top half of the table describes design constraints and the bottom half shows stream data. Hot streams are colored red and cold streams are colored blue.

Above pinch				Below pinch			
$N_H \leq N_C$				$N_H \geq N_C$			
$CP_H \leq CP_C$				$CP_H \geq CP_C$			
S1	6.93	S3	7.29	S1	6.93	S4	2.43
S7*	2.04	S4	2.43	S5	6.12	S6	5.81

Above the pinch, stream 1 was fully cooled using stream 3. Streams 3 and 4 both then required further heating utility in the form of stream 7. The flow rate of stream 7 must be less than 2.4kg s^{-1} to satisfy constraint 2 and was chosen to exactly satisfy the heating requirements of streams 3 and 4 while arriving at the pinch temperature resulting in a mass flow rate of 2.02kg s^{-1} . In total three heat exchangers were required: one as part of the main work and two as ‘heating utility’ from stream 7.

Below the pinch, stream 5 required cooling utility as no cold streams were cold enough to cool it. This left stream 1 to heat both streams 4 and 6. Stream 4 had a greater heating requirement so it was satisfied first. Stream 1 also requires cooling utility to remove the remaining heat. In total two heat exchangers and two cooling units were required. The full network is shown in Figure 76, heat transferred across heat exchangers and utilities are also shown in Table 54. Stream 2 was not needed for the final design as enough heating power was provided by stream 7.

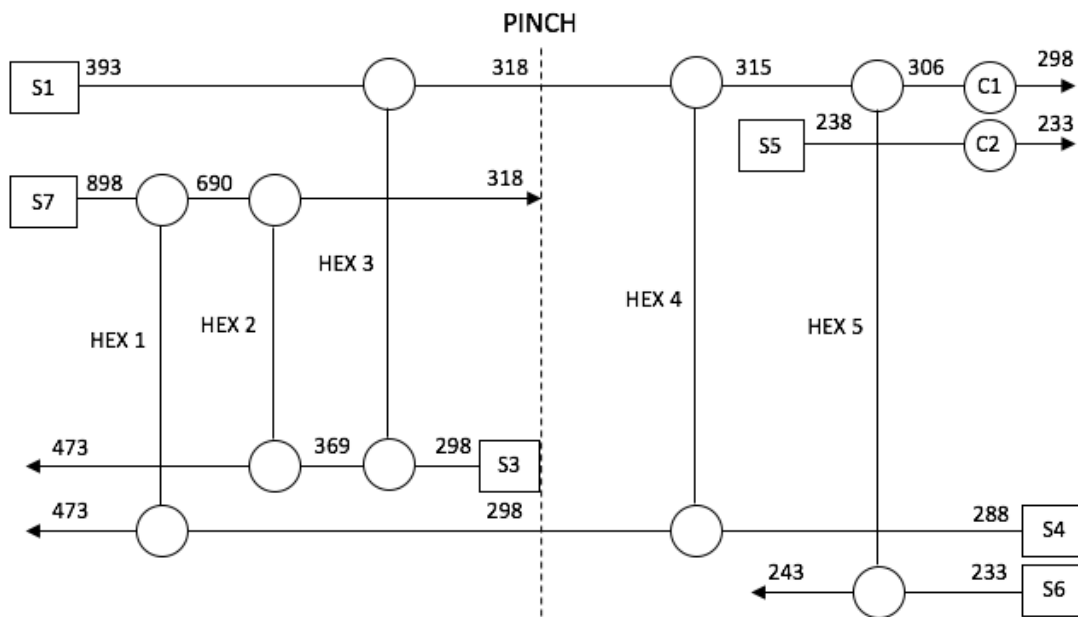


Figure 76: The final heat exchange network. Each pair of circles represents a heat exchanger, single circles represent cooling utility and temperatures (K) are shown at each isothermal segment.

From Table 54, five heat exchangers and two cooling utility units were required. The total cooling utility required was 86.8kW and the total heating utility (in the form of stream 7) was 1181.3kW. This

Table 54: Heat transferred in all heat exchangers and utilities in the network

Component	HEX 1	HEX 2	HEX 3	HEX 4	HEX 5	C1	C2
heat transferred (kW)	425.3	756.0	519.8	24.3	58.1	56.2	30.6

matches the minimum utility requirements calculated in Section 8.3, which shows that the heat exchanger network is one of the optimal configurations that can be designed.

Streams 1, 6 and 7 in the network have variable flow rates. This means that to satisfy stream requirements at all times, there will occasionally have to be heat transferred across the pinch, increasing the utility requirements. A control system would have to be designed to adjust the mass flow rates of stream 7 and cooling water used for C1 and C2 according to the varying demand.

8.5 Costing

From section 7.8, the capital cost of a heat exchanger varies with heat exchange area $A(m^2)$ as:

$$\text{Cost (Million \$)} = 130 \frac{A^{0.78}}{0.093} \quad (165)$$

The area of each heat exchanger was found using $Q = UA\Delta T_{LM}$ Where Q is the heat transferred, U is the overall heat transfer coefficient and ΔT_{LM} is the log-mean temperature difference across the heat exchanger. Due to the relatively small cost of the heat exchange network compared to the rest of the plant, approximate values for U were taken from existing data assuming that all heat exchangers operate with gases to give $U = 30Wm^{-2}$ [?]. The cost of the final network was \$241,000.

8.6 Conclusion

This chapter shows that the heat exchanger network satisfies all of the heating and cooling requirements in the plant and is a cost effective and reliable way to increase plant efficiency by reducing utility requirements from 5.2MW to 86.8kW.

9 Power Control and Plant Simulation

9.1 Introduction

Wind energy is very intermittent in its supply, and a method is needed for delivering power from an Energy Storage System (ESS) smoothly and efficiently.

Chemical plants typically operate in a steady state, which is why a simulation for this stop-start plant is very important. Another important note to stress is that this plant is the sole energy provider for the location, so it is responsible for any shortfalls or surpluses in demand, and therefore potential damage to consumers.

In this chapter a means of providing a large population a reliable, safe power supply in an efficient manner is developed, as well as a simulation of the plant to perform validation on.

9.2 Motivation

Electrical grids are dynamic systems - loads change throughout the day, as do supplies. A method for stabilising this system is beneficial to consumers as well as producers as significant deviations from the operating frequency ($\pm 4\text{Hz}$) will cause generator meltdowns, damaged industrial equipment, and brownouts [?]. Typically power distribution grids work within a tighter tolerance of $\pm 0.05\text{Hz}$ to avoid possible grid failure [?], with Figure 77 showing typical regulation methods and consequences for grid frequencies.

Important to note is that the ESS has *two* generation methods, the Solid Oxide Fuel Cell (SOFC) and the Ammonia Turbine. Each of these devices have differing performances - the turbine boasts an impressive start-up time, whereas the SOFC boasts a significantly better thermal efficiency.

Clearly a method that offers a highly efficient (as well as stable) grid will reduce both initial and operating costs - as this will reduce the number of wind turbines required, ammonia to be generated, and thus reduce plant size.

Control methods explored include Linear Quadratic Regulator (LQR), Proportional Integral Differential (PID) and others to explore the best way to control the chemical plant. This section also touches on Model Predictive Control (MPC) - an approach that was employed in industry since the 1980s with initial applications in chemical plants and oil refineries. The MPC is now commonplace in grid-balancing systems, as it offers optimal input, and takes account of constraints (such as maximum generation from a turbine). [?]

Classical control in the form of PID and LQR, while easier to implement, do not offer control over constraints, and therefore MPC is deemed a good candidate for the next iteration. MPC was not implemented as full system dynamics (at this stage in the design process) are not yet known.

9.3 Control Objectives

Fundamentally the task objectives are separated into two main criteria:

- Control Grid Frequency through supply and demand.
- Regulate SOFC and Turbine inputs for the most cost-efficient control method.

Most electrical grids ensure to keep net average frequency errors as zero for grid-based clocks to not run fast or slow. This report will not explore time-corrections. [?]

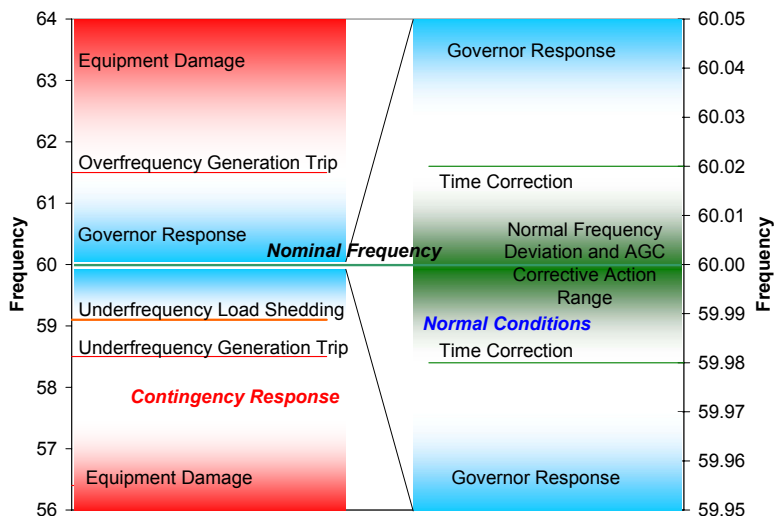


Figure 77: Frequency tolerances (in Hz) for grid operation [?]

9.4 System Dynamics

9.4.1 Electrical Grid

To begin the design, dynamics of electrical grids need to be understood, specifically how supply and demand feed into the frequency. Supplementing this is how Maui has a peak demand of 195MW, a yearly energy usage of 1200GWh, 55,301 residential and 9,356 commercial customers. [?]. This sizable demand means large fluctuations in the net power in the grid will occur, so an accurate model is needed.

It was observed that a net-positive power in the system ($P_{\text{net}} > 0$) causes an increase in the frequency ($\dot{\omega} > 0$) as the energy generated *must* go somewhere due to conservation of energy. The place the energy goes is the angular momentum of the rotating masses. The inverse is true for net-

negative powers, a decrease in frequency results.

To begin tackling this problem, it is possible to consider the grid like a flywheel as suggested by [?]. The governing equation is known as the *Swing Equation*, which models the electrical powers of every component as a *torque* (T_i) on a flywheel. This method makes sense, as the grid has an inertia associated with it, which is the rotational inertia of all power sources and sinks.

The inertia of the grid does vary with time - however for simplicity a time-invariant inertia J , (the inertia of my plant) is assumed. Grid inertia has a trend of decreasing with time, consumers are following a trend of moving away from bulky, solid-core transformers which offer an inertial component, to a low-inertia switch-mode power supplies [?]. This makes the control task more challenging as this will cause an increase in bandwidth of the system - by assuming a worst-case scenario of $J \approx J_{\text{plant}}$ should suffice since J will be tuneable with a *virtual inertia*, in Section 9.11.

To begin, the *Swing Equation* as suggested by [?] was considered:

$$P = T\omega_g \quad (166)$$

$$T = \frac{\partial}{\partial t}(J\omega_g) = J\dot{\omega}_g \quad (167)$$

$$\therefore \dot{\omega}_g = \frac{P_{\text{net}}}{J\omega_g} = \frac{T_{\text{net}}}{J}, \quad \text{where} \quad T_i \approx P_i\omega_{g0}^{-1} \quad (168)$$

This derivation assumed an operating point $\omega_{g0} = 120\pi$, as that is the grid's angular frequency of the proposed location and it is not expected to deviate much from it. The implication of this result is that a low inertia on the grid will cause *large* frequency rate of change for power mismatch.

9.4.2 Generation and Consumption Units

Since it was already known that each component's contribution can be written as $T_i \approx P_i\omega_{g0}^{-1}$, power can also be interpreted as a torque. For an initial design a first-order response from each component was assumed, with step responses like (by using a time constant k_i):

$$T_i(t) = T_{\max,i}(1 - e^{-k_i t}) \quad (169)$$

Which implies a transfer function for each component as:

$$\overline{G_i(s)} = \frac{\overline{T_i(s)}}{\overline{U_i(s)}} = \frac{T_{\max,i} k_i}{k_i + s} \quad (170)$$

The rise times can be assumed as $\frac{3}{t_{\text{rise},i}} \approx k_i$ as this gives an error of e^{-3} . If this is applied through to components, a set of parameters for the model (Table 55) can be generated.

Table 55: A table to capture the properties of the many systems in the ESS

Component	t_{rise}	k / mins^{-1}	η_{therm}	P_{\max} / MW	Minimum Use / %
Turbine	8 mins	0.375	0.65	250MW	10
SOFC	35 mins	0.0857	0.90	230MW	30
Electrolyser	1.2 mins	2.25	N/A	300MW	20
Cryo-Still	40 mins	4.50	N/A	-	30

9.4.3 Modelling Wind Power

As specified in the project brief, the only allowed power source are wind turbines. Wind turbines offer the ability to generate a lot of clean energy, but are very intermittent in their supply. For this design to be more accurate, a good model on how wind speed correlates with power generated was developed.

The wind turbine ‘GE Haliade-150-6MW’ was chosen as a good candidate, as it offers offshore 6MW generation, is domestic to the US market and has better specifications to its competitors. As suggested by [?], a reasonable approximation to the turbine model was found by considering a double-exponential model, which is of form:

$$P_{\text{gen}} = \begin{cases} P_{\text{rated}} \exp(-\tau_1 \exp(-v\tau_2)), & 0 \leq v < v_{\text{cutout}} \\ 0, & v_{\text{cutout}} \leq v \end{cases} \quad (171)$$

The wind turbine’s ‘cut-in’ speed is known, this is the speed at which the turbine begins to generate electricity. Also known is the ‘rated speed’, the speed at which the turbine generates maximum power. An *iterative convergent scheme* was setup in MATLAB (using gradient descent), and used the information in Table 56 to build the model and obtain time constants $\tau_1 = 70.9780$, $\tau_2 = 0.7130$.

Table 56: GE Haliade-150-6MW data from GE datasheet and private communication. [?]

P_{rated}	6000 kW
v_{cutin}	3 ms^{-1}
v_{cutout}	25 ms^{-1}
v_{rated}	12.5 ms^{-1}

Using the obtained constants, the characteristic steady-state power curve for the wind turbine can be plotted, as shown in Figure 78. By assuming that the turbine is always at steady state, it is easy to see estimating the wind power is a relatively simple task, by injecting wind speed in and multiply the result by the number of turbines in the field.

The NOAA supply historical data on hourly wind-speeds [?], as well as predicted future wind-speeds. This historical data-set was used to validate our model by considering how real-world wind-speed

works with energy generation. Using Equation 171 and using τ_1, τ_2 the yearly generated energy in Maui can be plotted.

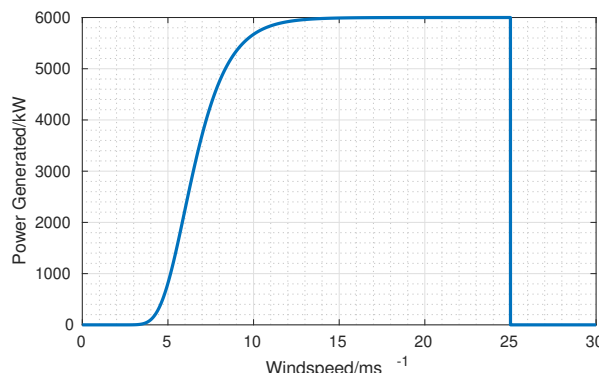


Figure 78: Approximated Steady State Power Response of the GE Haliade-150-6MW

Equation 171 was applied to the wind speed data-set with 65 turbines, to obtain the power data below in Figure 79.

The data obtained had values for every fifteen minutes, which although is a high resolution, a cubic spline fit gives an approximation on the second-by-second level. This is an approximation to what reality is with wind speed, however since turbine transfer functions for dynamic cases were not considered - this may make a good approximation to reality. The final supply profile used for testing is visible in Figure 81

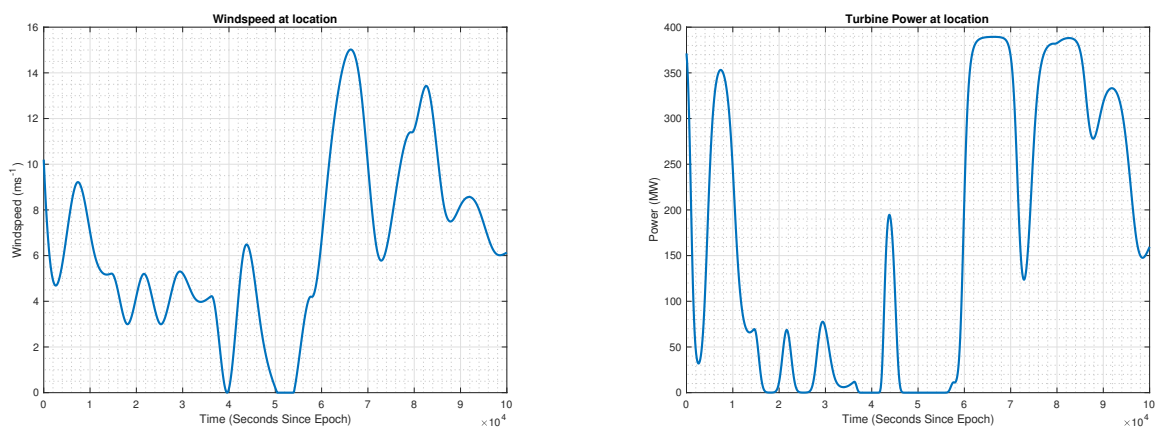
Similarly for demand, the EIA supply data sets for electrical demand [?], which were smoothed with cubic splines and cleaned for use later. An example of a typical daily load pattern is visible in Figure 80.

9.5 Plant Model in Simulink®

9.5.1 Motivation

To test designed controllers, a representation of the plant to experiment on is needed. Simulink¹ was used to build a model of the plant, and apply controllers to. The model is a *simplified version* of how the plant is expected to behave. The simplifications made and design decisions that were proceeded with are justified below.

¹Simulink is a Registered Trademark of The MathWorks Inc.



(a) Wind speed in Maui

(b) Electrical Power Obtained from 65 Wind Turbines

Figure 79: Wind speed Mapping to Electrical Power by Applying Equation 171 Over the First 10^5 Seconds of Data

9.5.2 Modelled Components

Components were simplified as how the many considered components will respond to changes of input are not known in detail. Since the plant controls P_{net} , the SOFCs and the Turbine are important to simulate on the generation, and the electrolyser on the consumption side.

Tanks were modelled by means of a integrator, fed with net flow-rates for each chemical species.

The cryogenic air-still is kept running continuously as it reduces the size of the part required to make the same amount of material. Another benefit is this negates the need to model the delay associated with priming the system before use. Cryogenic stills take on the order of hours to reach the temperature required for operation, so continuous running makes sense from a energy conservation standpoint too.

9.5.3 Assumptions

Components were assumed to behave as first-order, linear with no delays. There was also the assumption that there is no minimum utilisation for components, i.e. the control signal is $0 \leq u \leq 1$ such that for example the electrolyser can drain any power between 0 Watts and its maximum power, P_{max} . For material flow-rate, it was assumed the ammonia used in the turbine and the SOFC scaled linearly with utilisation, and gas generation from the electrolyser also scaled linearly with utilisation.

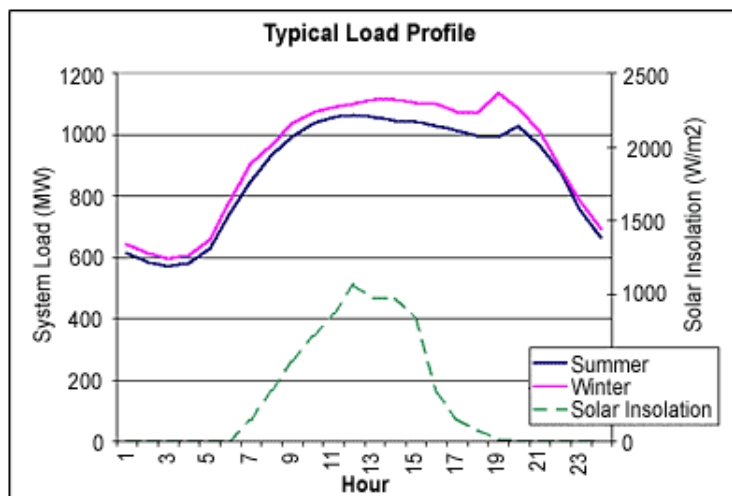


Figure 80: Typical load profiles for Hawaii, comparing summer and winter seasons. [?] (Note that this is for *Hawaii*, which includes Maui as well as many other consumers. Maui's peak power is on the order of $\approx 200\text{MW}$)

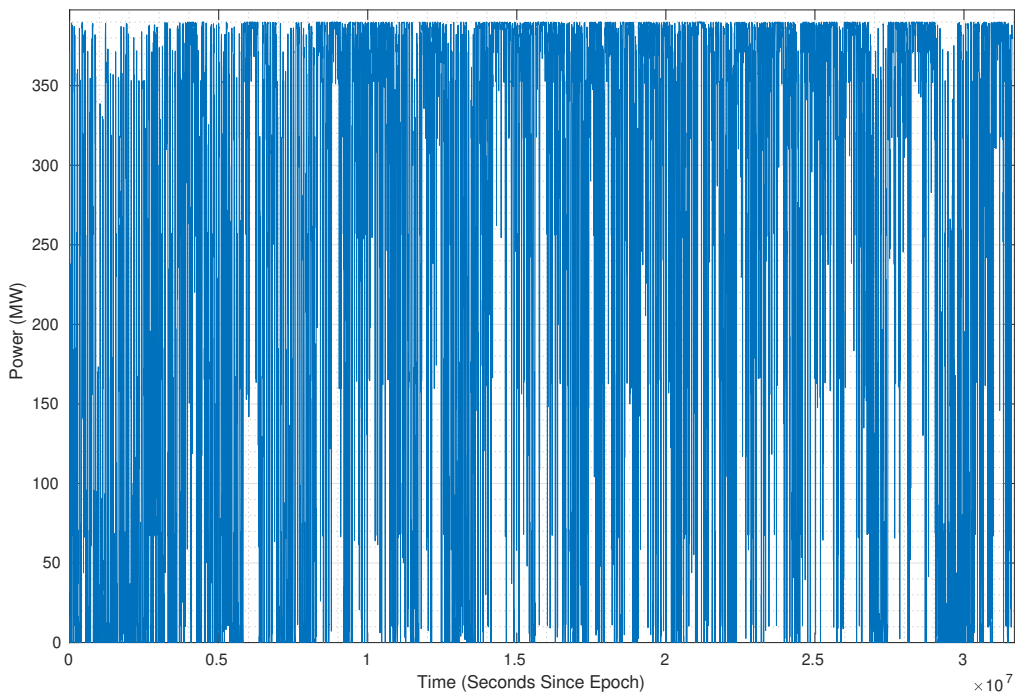


Figure 81: Wind Supply Curve for One Year (65 GE Haliade 150-6MW turbines)

9.5.4 Simulink Model Structure and Initial Implementation

Values for each block were left as variables to be determined by a supporting MATLAB script, with relevant data input from other sections of this investigation. This allowed for rapid prototyping, and gave the ability to quickly try different values for controller gains to observe responses. The model was subdivided into different components:

Global Plant is a block that includes the plant and controller. This is packaged in a convenient way as to apply different disturbances and observe performance. Supply and demand data were fed to this block by means of *Lookup Tables*, which took time as a variable in, and supplied the supply or demand for the given time. Lookup Table arrays were generated by the supporting MATLAB script. All blocks below are inside the ‘Global Plant’ block, modelled by Figure 83, which exists in the Testing Environment Figure 82.

Grid Dynamics in form of the ‘Swing Equation’ was packaged to allow for adding more complicated coupling or measurement effects - yet this was not implemented. Grid Dynamics is modelled in Figure 88.

Component Dynamics encapsulates the different behaviours of each component, including the limits on control inputs, rise times, maximum power, material flow-rates and room to make component models more complex. Component dynamics are modelled in Figure 86.

Controller allows for controllers to be applied with multi-state feedback, with room to add complexity. In the diagrams below (Figure 87) the LQR with augmented state is implemented.

Cryogenic Still simulates basic, steady state behaviour of the cryogenic still, observed in Figure 84.

Tanks and Haber Column simulates material volumes from flow-rates into a tank, and conversion of tank materials in the Haber Column. This system is modelled in Figure 85.

The diagrams overleaf show the Simulink plant that was used with this design study.

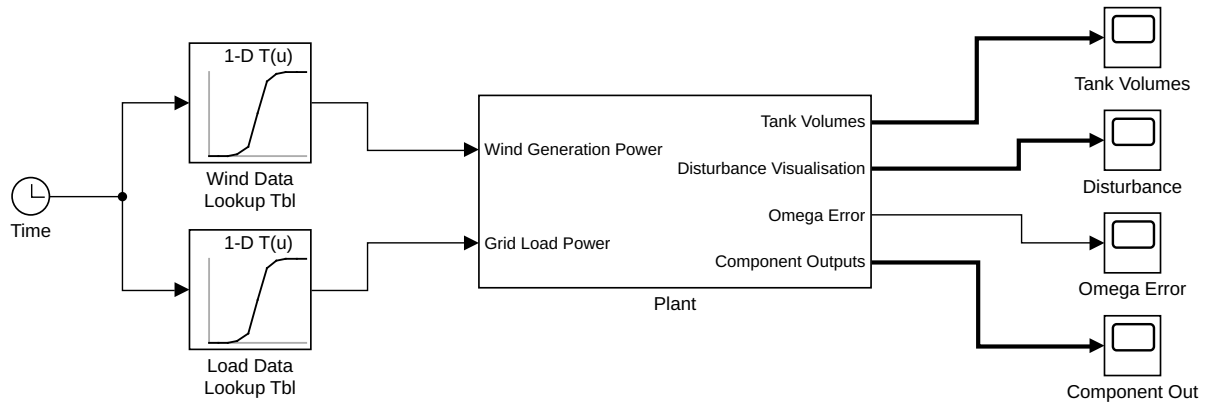


Figure 82: Plant in Testing Environment, *Lookup Tables* are used to feed real world data into the plant, and appropriate variables observed

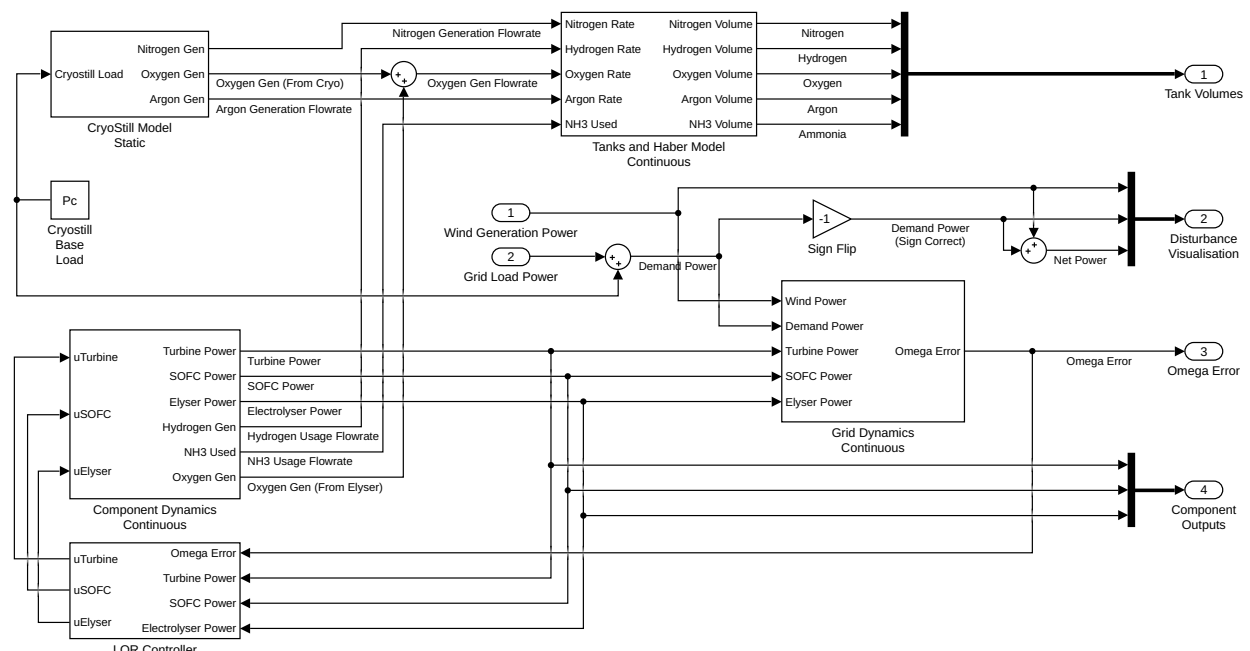


Figure 83: Plant with Controller Implemented, each important component is placed into a subsystem

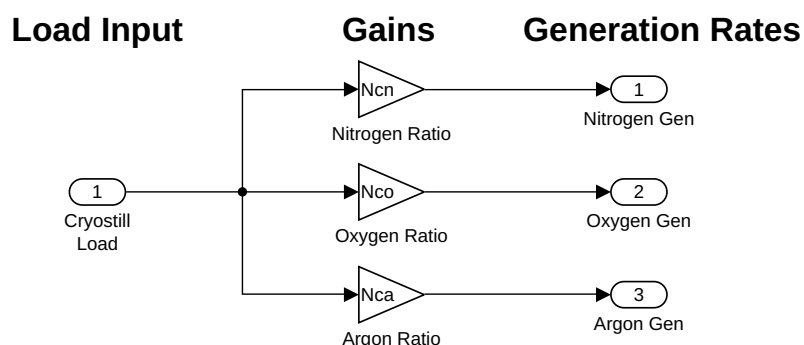


Figure 84: Steady State Cryogenic Still Model

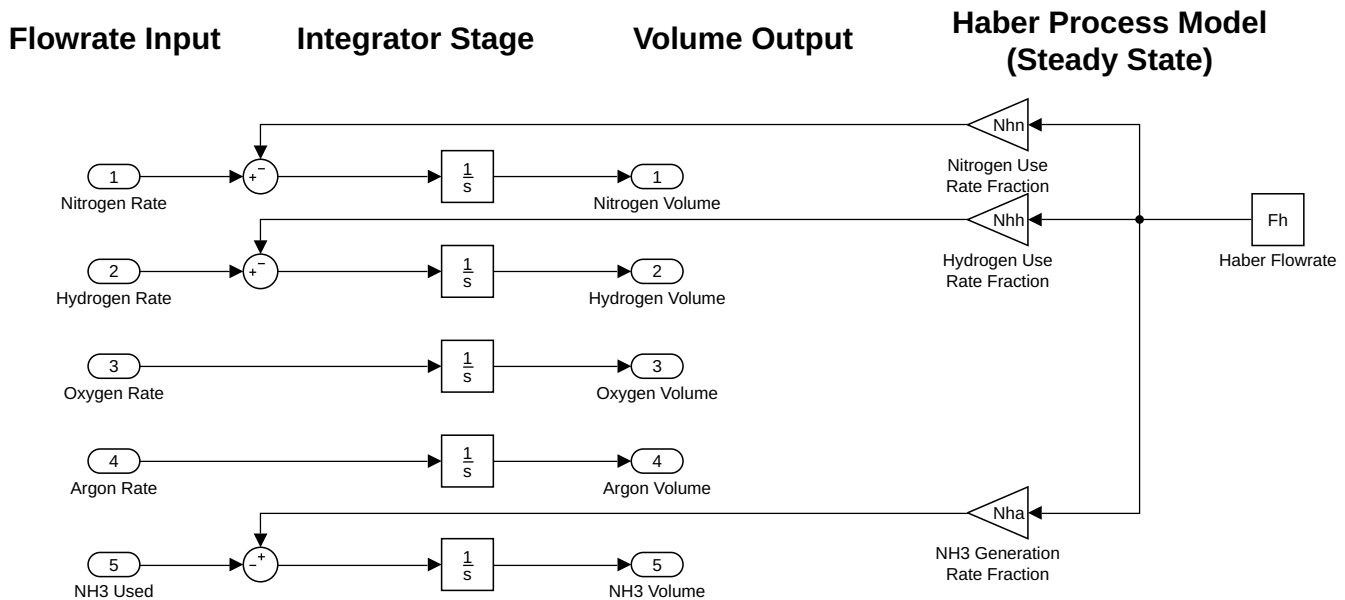


Figure 85: Tank and Steady State Haber Column Model, flow-rates are fed in and integrated for net volumes.

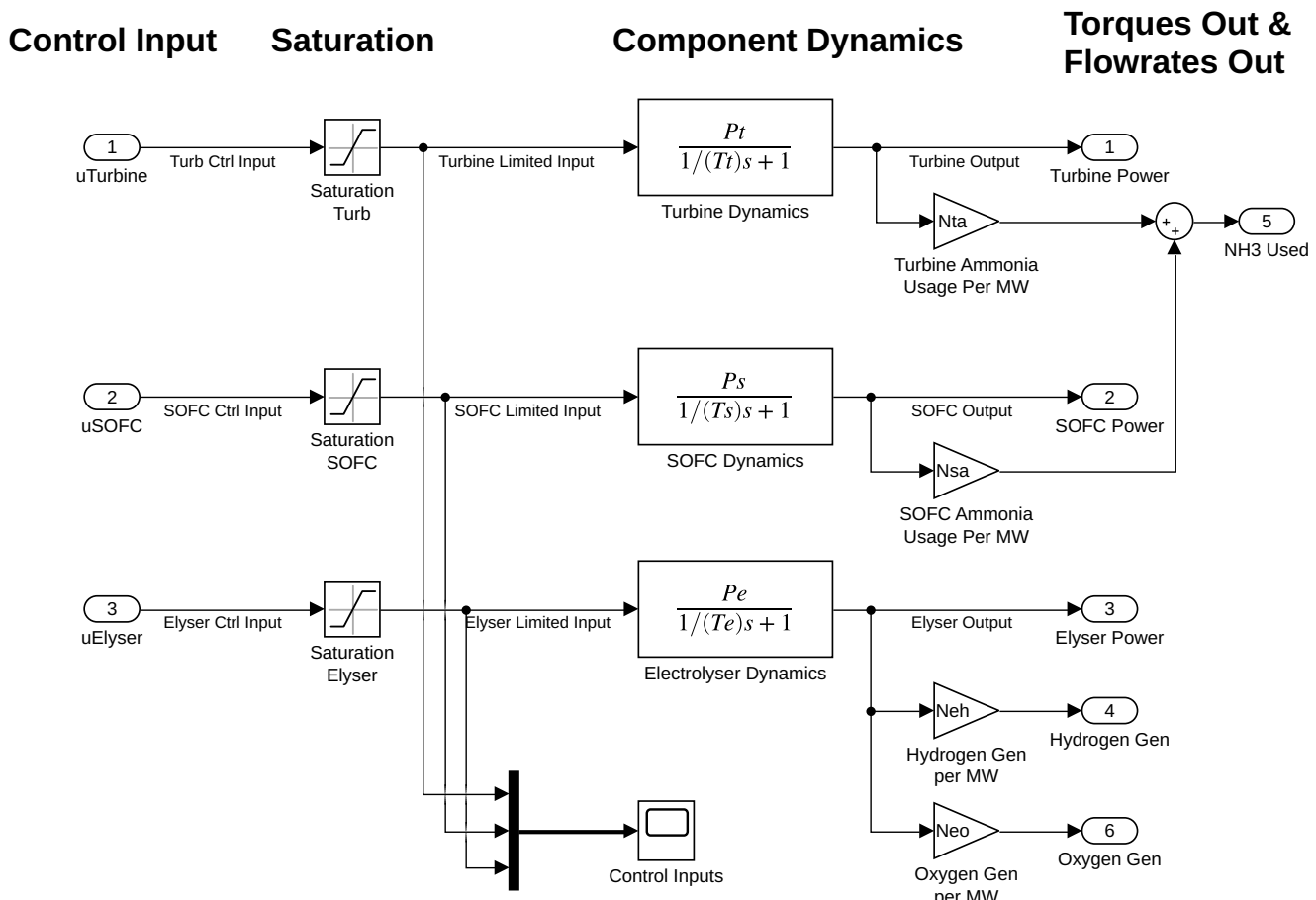


Figure 86: Component Dynamics (First Order Linear) with Saturation on Inputs.

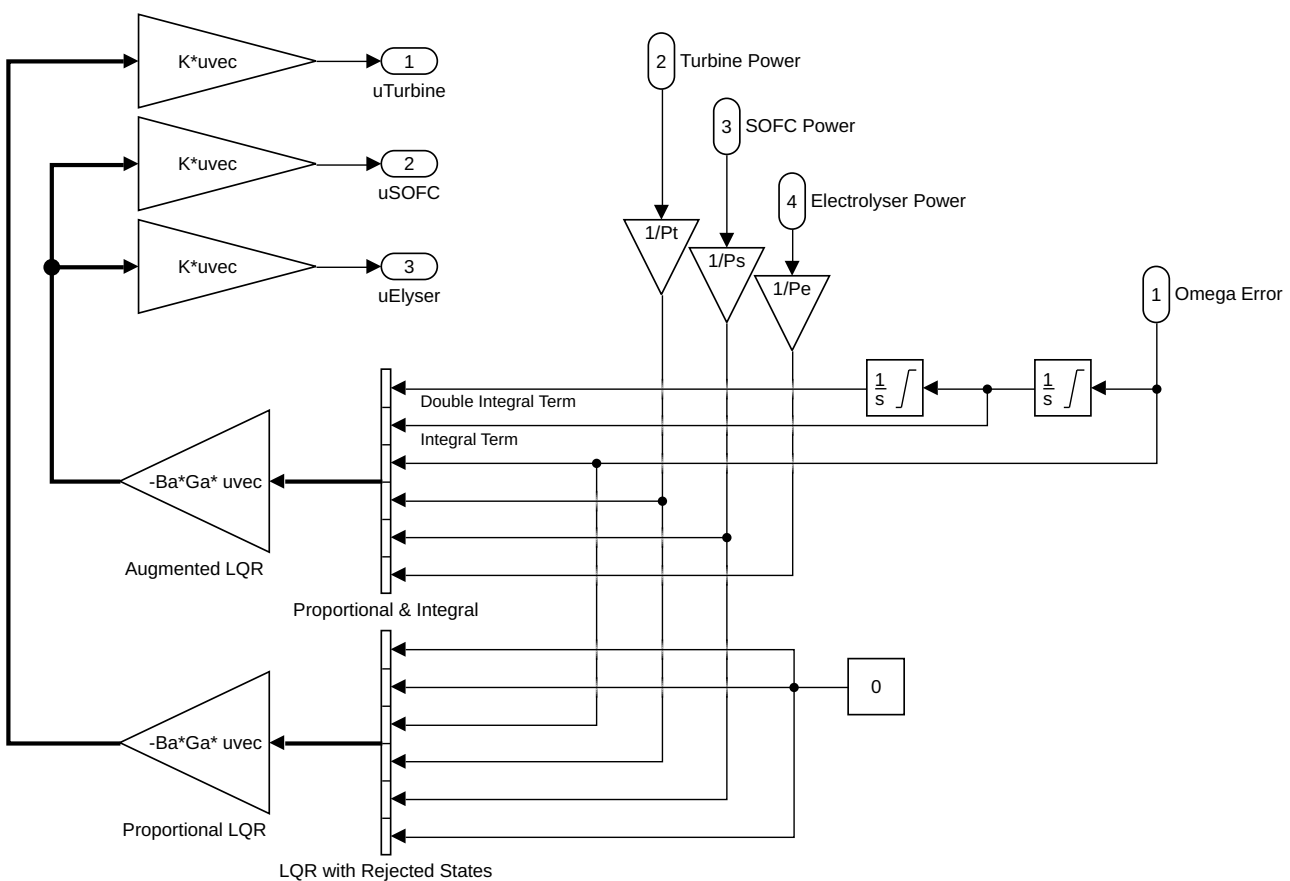


Figure 87: Controller Structure (LQR with Augmented State shown in Diagram).

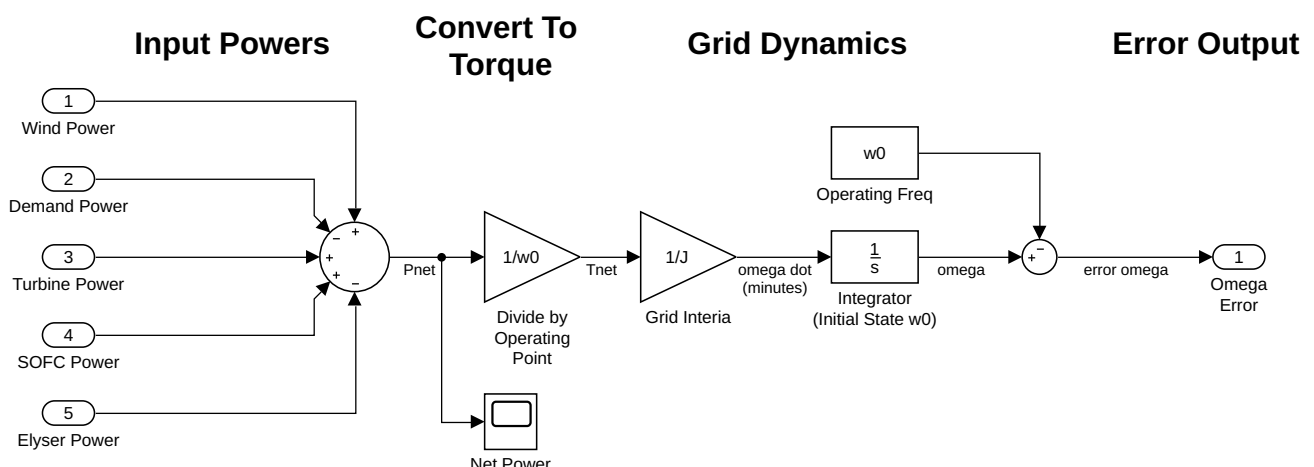


Figure 88: Grid Dynamics using Equation 167.

9.6 Plant Scaling

Plant scaling is a rather important section as it dictates the flowrates and storage requirements the plant has to adhere to, in order to satisfy consumer demand for the first design iteration.

The plant simulation was used with demand and wind data fed into a MATLAB program, which followed this process flow:

1. Program found the net energy in the system by subtracting load from wind generation.
2. Program assumed the net energy on the grid was zero, and all shortfalls and surplus were satisfied by the plant.
3. Program logged total energy generated, and total energy fed into plant for a year.

A flowsheet was then generated by using typical values from literature, with the assumption the gas turbine has a duty cycle of 5% of all generation. The material balance for the first design iteration was produced in Figure 89. These data were used to scale other components and to demonstrate that with approximate efficiency values from literature that this is a feasible project. Components were scaled by a safety factor applied to their predicted maximum use, 1.3 for the Gas Turbine, 1.2 for the SOFC, and 1.5 for the Electrolyser, with their respective powers in Table 55. A rather startling conclusion from this analysis is that the ESS stores far less energy than was originally expected.

The wind speeds in Maui are sufficiently high all-year-round to satisfy the bulk of consumer demand.

These data allowed for an idea of the plant's scale, and were used to find more detailed component parameters for the plant's dynamic simulation.

9.7 Plant-Controller Structure

9.7.1 Hierarchical Controller Structure

The design started by considering what controller is required to run the plant globally. Some components are nonlinear in their behaviour (however non-linearity is not implemented in the model), there are constraints on the operation of some components, and it would be beneficial to use predicted disturbances to control grid frequency in an optimal manner. An LQR based controller does not give the power to play with these properties, so a *Model Predictive Controller* (MPC) is preferred, but complicated to implement.

A MPC will allow the ability to generate an optimal control scheme for the plant - but are limited in

GENERATION UNITS		Energy into SOFC	Energy into Turbine	Total Energy In	Total NH3 tons/yr
Net Generated Energy (1yr) / MJ	1156300000	1751969696.9697	116836060.92	1868805757.89	83058.03
Combined Generation efficiency	SOFC efficiency		Turbine efficiency		
	0.62	0.627	0.433		
	SOFC duty		Turbine duty		
	0.95	0.95	0.05		
NH3 HHV ΔHc MJ/ton		NH3 LHV ΔHc MJ/ton	NH3 Precracked LHV ΔHc MJ/ton		
	22500	18557	19688.24		
HABER BOSCH					
Purge Fraction of Inlet	NH3 'into' Haber		H2 into Haber	N2 into Haber	
	5%	87429.51	15428.74	72000.77	
ELECTROLYSER					
Production of H2 (minimum)	Production (Safety Factor) H2		Elec.Energy Used MJ		
15428.74	16971.61		3435538888.19		
Safety Factor	Efficiency		H2 HHV ΔHc MJ/ton		
1.1	0.7		141700		
AIR SEPARATOR					
Production of N2 (minimum)	Production (Safety Factor) N2		Elec.Energy Used MJ		
72000.77	79200.85		31363536.39		
	Safety Factor		Energy Used Per Ton in MJ		
	1.1		396		
STORAGE					
Demand/supply max diff MJ	Safety factor		Max ammonia storage tons		
108864000	2		19006.85		
ENERGY BALANCE					
Net Into Plant	Net Used By Components		Energy In Balance	Extra Power Generated (%)	
4508500000	3466902424.57647		1041597575.42353	23.10	
Process Efficiency	Energy to Grid (Direct from Wind)		EGen per turb per year	Turbine Duty	
33.35%	3532620000		123709538.46	65.38%	

Figure 89: An approximate material balance flowsheet using efficiency factors from all components, demand and wind data.

that they run on discrete time, and will not offer a instantaneous response.

In the ideal scenario, the controller structure would be as in Figure 90.

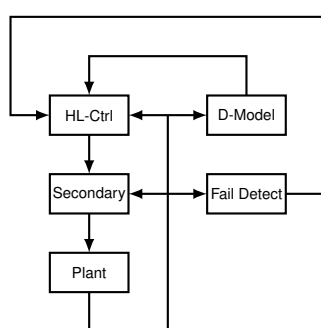


Figure 90: A simplified view of how the controllers and sensing tie together

The High-Level Controller (HL-Ctrl) would dictate how each component (Electrolyser, SOFC and Gas Turbine) would be used, given information on failure states, predicted future demand, and the current system state. This is explored in Sections 9.8 and 9.9.1.

The Secondary Controller would be a Virtual Inertia, a method used to simulate a large grid iner-

tia with more inexpensive methods. This is explored in Section 9.11, *but not in depth*.

Failure detection can be achieved via a Kalman filter as suggested by [?], and the information gained can inform the controller of possible constraints. This is mentioned in Section 9.12.

A Disturbance Model can aid in the case of MPC, future disturbance is *not known* in a causal system. By having a disturbance model, the system can predict (using a Markov Chain [?]) what the future state will be.

The ‘Plant’ block is where most of the design effort was focused, forming a model of the power-production and material balance will help greatly in deciding if this is a viable method of energy storage. This is explored below in moderate depth, using device parameters from Section 9.4 to be implemented in Section 9.5.

This topology would be ideal as the High-Level controller would dictate the control of the plant for the most cost-effective response. The Secondary (Virtual Inertia) controller would manage very fast changes in the system state - to ensure a low enough bandwidth for any High-Level controller operation. The High-Level controller would require state information from the disturbance model on future demand predictions, as well as the actual plant state (component actuation, grid frequency). Failure detection would be important in later iterations to guarantee the plant runs safely in all possible conditions - to ensure a stable electricity supply for consumers.

9.7.2 Process of Implementation

Implementation began by designing the core components of the plant. Approximate models for each component were formed. This allowed observations of responses to step requests, and from there constructed simple methods of control. Proportional, PID and LQR schemes were explored to check stability and find the optimal result. LQR was implemented, and model complexity was added.

Alongside development of the plant and classical controllers, methods on disturbance modelling were explored and data were collected to aid with the exploration piece of Model Predictive Control.

9.8 PID Considerations

A Proportional Integral Derivative (PID) controller was chosen as it contains an *integrator* which allows for no steady state tracking error, due to its infinite DC gain. On inspection it is clear that applying a PID for both the SOFC and the Gas Turbine is not beneficial. The Gas Turbine should not

run for DC loads, as this will use more ammonia and increase plant size (and therefore CAPEX and OPEX).

The design requirements prefer the SOFC to manage all disturbance that it can without turbine intervention. The SOFC had a PID applied, whereas the Gas Turbine had only a Proportional controller. The state observed was the frequency error from the set value, as its derivative correlates with net energy in the system.

Figure 91 shows diagrammatically how this is implemented, which was used as a starting point for the Linear Quadratic Regulator design. The control signal for the Electrolyser and SOFC is shared, as these two components *should not* be on at the same time. The signal to the Electrolyser is inverted as the control signals were defined earlier as $0 \leq u \leq 1$. These signals are clipped on entry to the ‘Component Dynamics’ block in Figure 86.

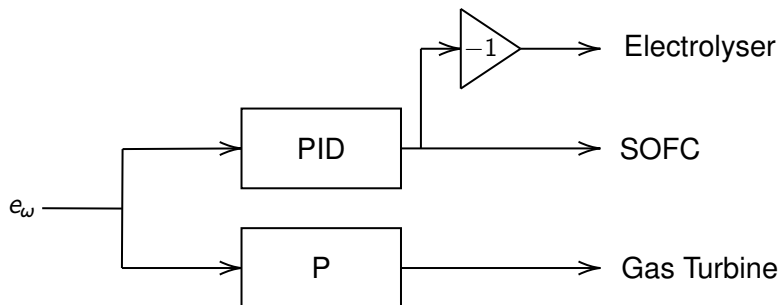


Figure 91: A diagram to show how PID is used in parallel with proportional control, using the same error signal.

9.9 LQR Problem Formulation

9.9.1 State Space System

The design begins by considering the system as a *State Space*, this takes into account **system dynamics**, **input effects**, and predicted **disturbance effects**. This model used the data generated from Table 55, and uses the system state \vec{x} to construct a model.

$$\frac{\partial \vec{x}}{\partial t} = \textcolor{red}{A}\vec{x} + \textcolor{blue}{B}u + \textcolor{green}{D}d \quad (172)$$

$$y = \textcolor{black}{C}\vec{x} \quad (173)$$

$$\vec{x} = \begin{bmatrix} e_\omega \\ T_t \\ T_s \\ T_e \end{bmatrix}, \quad u = \begin{bmatrix} u_t \\ u_s \\ u_e \end{bmatrix}, \quad d = \begin{bmatrix} d_{\text{demand}} \\ d_{\text{cryostill}} \\ d_{\text{wind}} \end{bmatrix}, \quad D = \begin{bmatrix} -1 & -1 & 1 \\ & \mathbf{0}_{4,3} \end{bmatrix} \quad (174)$$

$$A = \begin{bmatrix} 0 & J^{-1} & J^{-1} & -J^{-1} \\ 0 & -k_t & 0 & 0 \\ 0 & 0 & -k_s & 0 \\ 0 & 0 & 0 & -k_e \end{bmatrix}, \quad B = \begin{bmatrix} 0 & 0 & 0 \\ -k_t & 0 & 0 \\ 0 & -k_s & 0 \\ 0 & 0 & -k_e \end{bmatrix} \quad (175)$$

For this *State Space*, the angular frequency error term $e_\omega = \omega_g - \omega_{g0}$ was used, and loads were modelled by time-varying disturbance terms d_i .

Noiseless full-state feedback was assumed, as it is known can observe each property individually, and known methods on noise rejection exist. Should a state not be observable, an *observer* can be constructed to predict that state. [?]

9.9.2 Augmented Integrator State

To obtain integral action from the LQR, an ‘augmented’ state can be created, which is the integral of the error state measured [?]. This is executed through creating an augmented system:

$$\frac{\partial \vec{x}_a}{\partial t} = A_a \vec{x}_a + B_a u + D_a d \quad (176)$$

Such that:

$$\vec{x}_a = \begin{bmatrix} I_\omega \\ \vec{x} \end{bmatrix}, \quad A_a = \begin{bmatrix} 0 & 1 & 0 & 0 & 0 & 0 \\ & A & & & & \end{bmatrix}, \quad B_a = \begin{bmatrix} \mathbf{0}_{1,4} \\ B \end{bmatrix}, \quad D_a = \begin{bmatrix} \mathbf{0}_{1,3} \\ D \end{bmatrix} \quad (177)$$

This was repeated for an additional integral state, giving double integral (or gradient tracking) action.

9.9.3 Cost Function Structure

Producing the optimal LQR controller involves minimising the cost function J' :

$$J' = \int_0^\infty (\vec{x}^T Q \vec{x} + u^T R u) dt \quad (178)$$

Such that with feedback $u = -G \vec{x}$ an obtain optimal state feedback matrix G can be obtained.

MATLAB conveniently has the built-in function [lqr](#), which takes as arguments the weighting matrices Q and R and returns the gain matrix G .

As an aside, [lqr](#) works as a *known solution* to the above cost function is $G = R^{-1}(B^T P)$, where

P is found from solving the Algebraic Riccati Equation: $A^T P + PA - PBR^{-1}B^T P = 0$. [?]

This can be applied to a regular LQR and the LQR with augmented state, such that multi-state P and PI control can be achieved.

9.9.4 Parallel LQR with Augmented State

By using the same argument as in Section 9.8, the SOFC should manage all disturbance that it plausibly can without turbine intervention - just for the argument that the SOFC will use less ammonia and therefore reduce plant size. The SOFC therefore has to have integral action to reject DC error (as integrators have infinite gain at DC). The SOFC will also have a high gain, or a low cost associated with it. After some experimentation it was found that double integral action on the SOFC increased performance and reduced low frequency oscillations on high frequency load changes.

Turbine intervention is for large proportional error, so integral action is not desired. Turbine control also had higher cost associated with it, such that the SOFC is preferred if possible.

Overall the frequency error *must be inside tolerances* (recall Section 9.1), therefore cost associated with frequency error is the highest, with the integral terms tuned for best response.

9.9.5 Non-Idealities and Assumptions

In this analysis all components are assumed as first order, linear, have no time delay, and have the ability to supply positive and negative power. In reality the SOFC and Turbine can only give power to the grid, and the electrolyser can only take power from the grid, so the LQR method *will not be ideal*.

A parallel combination of the LQR and augmented-state LQR may also not be ideal - since some feedback terms are rejected, and each system is unaware of the other.

Inputs are also limited such that $0 \leq u \leq 1$, which is another non-ideality. With gains too high (input costs too low), control becomes bang-bang may lose the ability to finely regulate the system. Another consequence of my assumptions is that the plant can satisfy all demand put on it with zero error at DC.

Turbines have a cost associated with starting up - the amount of wear in a turbine (what defines the time between services) is determined by the number of spin-up events. The blades in the turbine undergo one stress cycle when the engine spools up to speed which (by Miners Rule) determines

the damage undertaken by the engine. Preventing unnecessary start-ups can be achieved by a threshold, which introduces *another non-ideality* into the system. Another non-ideality on the system is the limits on the integrator. Limits were imposed to prevent windup, and these were tuned for performance. Results from the implementation are analysed below in Section 9.10.

9.10 Controller and Plant Testing

9.10.1 Plant Tests

On creation of the plant, components needed to be tested to ensure operation were as expected. Step responses were observed for the components (Figure 92), which conformed to expectations (as in Table 55) and the test was deemed successful.

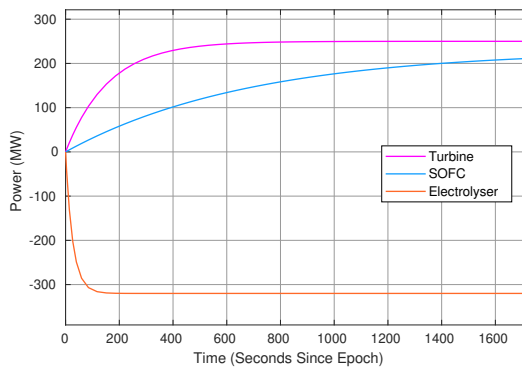


Figure 92: Tests conducted on Power Components with differing rise times.

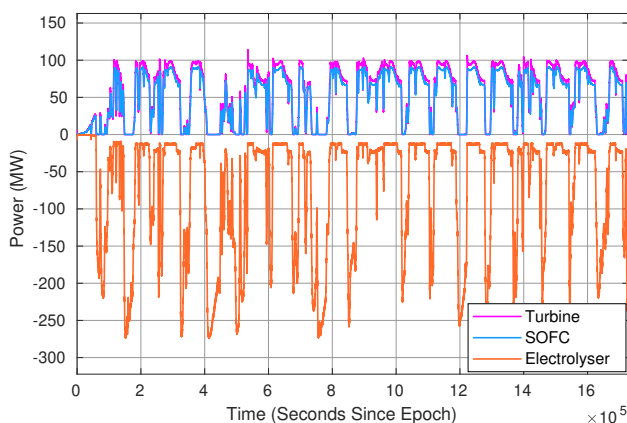
Tanks were tested and operated as expected, parameters for the Haber-Bosch, and cryogenic still were added and the plant behaved as expected.

An important note for all the controllers that were experimented on was that the electrical inertia J was reduced until the plant could no longer be controlled within tolerances, and then a small safety factor was added. Interestingly all controllers had a similar lower limit on the tolerable inertia. It was decided $J = 80 \cdot 10^3 \text{kgm}^2$.

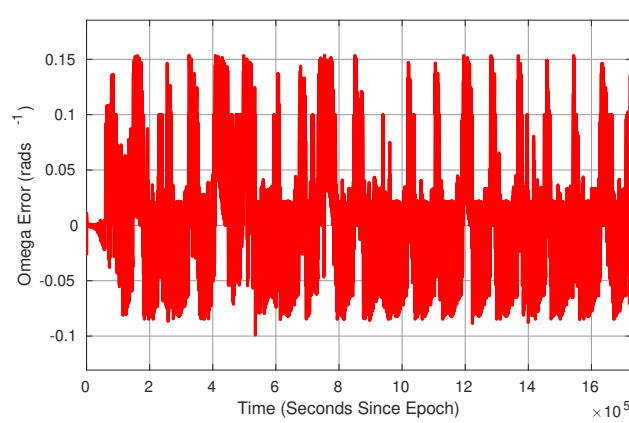
9.10.2 Proportional Control

A proportional control scheme was initially applied to observe how the system responds and check stability. Results of the simulation are visible in Figure 93.

System was found to be stable, but had steady state tracking errors. The turbine running at DC was not desirable, so a PID in parallel with a Proportional unit was applied as suggested in Section 9.8.

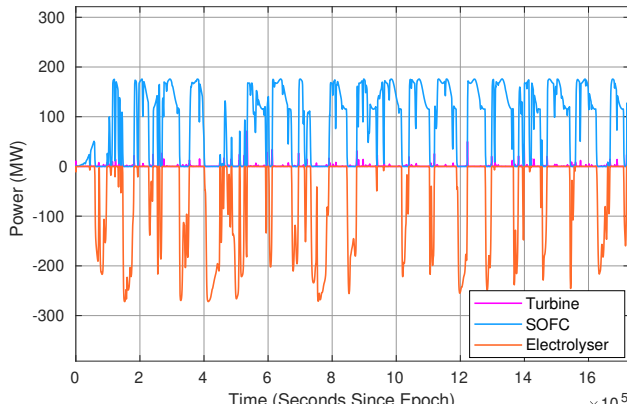


(a) Component powers.

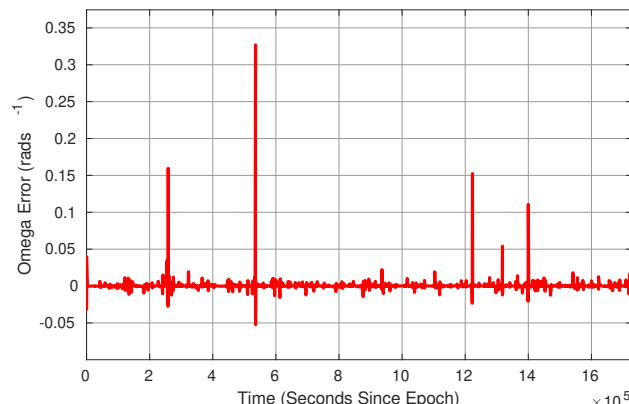
(b) Frequency error from 120π rads $^{-1}$.Figure 93: Simulation results from a 100 days of data, **Proportional Control Applied**, $P = 10$.

9.10.3 Plant with a PID/PD Combination

By implementing the same method as suggested in Section 9.8, the following results were yielded. Important to note was very strong performance from the controller, where very low frequency error is visible. This unfortunately came at the cost of an high ammonia use-rate, ending the 100 day simulation at -4200 tons of ammonia.



(a) Component powers.

(b) Frequency error from 120π rads $^{-1}$.Figure 94: Simulation results from a 100 days of data, **PID in Parallel with Proportional Control Applied**, $P = 10$, $I = 0.2$, $D = 0.8$, $P_{\text{turbine}} = 10$.

9.10.4 Plant with a Augmented LQR Combination

System was able to perform well under simulated harsh conditions, with a manageable frequency error.

Compared to PID, there is a significantly larger frequency error, however it is comfortably within tolerances. Interestingly the LQR used less ammonia than the PID, ending the 100 day simulation with -3850 tons of ammonia.

The Augmented LQR Combination was preferred and then run for a year, to ensure the material balance and error tolerance satisfied expectations.

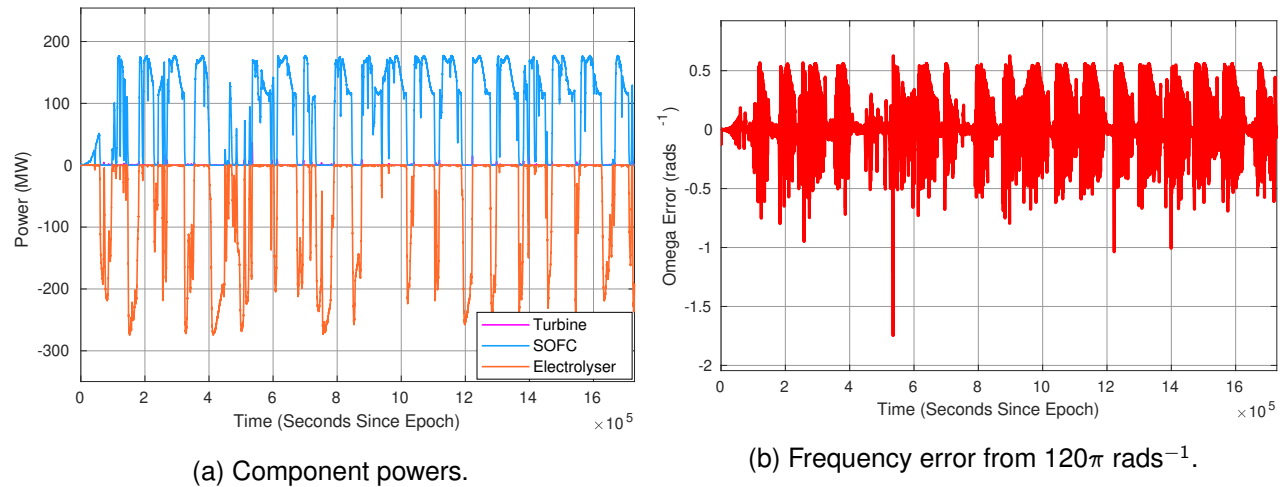


Figure 95: Simulation results from a 100 days of data, **Augmented State LQR in parallel with LQR Applied**.

9.10.5 Augmented LQR Year Simulation Results

Control application was successful. Grid Frequency throughout the year was controlled inside the \pm constraint, with the maximum visible error being $\approx 4 \text{ rads}^{-1}$.

Spread of frequency errors was small, as visible in Figure 96a, with the majority of the error close to 0. Figure 96b shows a time-series of a year's simulation, showing the grid is able to be controlled.

Material balance for a year was stable. As visible in Figure 97a no large excess of ammonia was produced, and for a first iteration the scaling as achieved in section 9.6 was *a good estimate*.

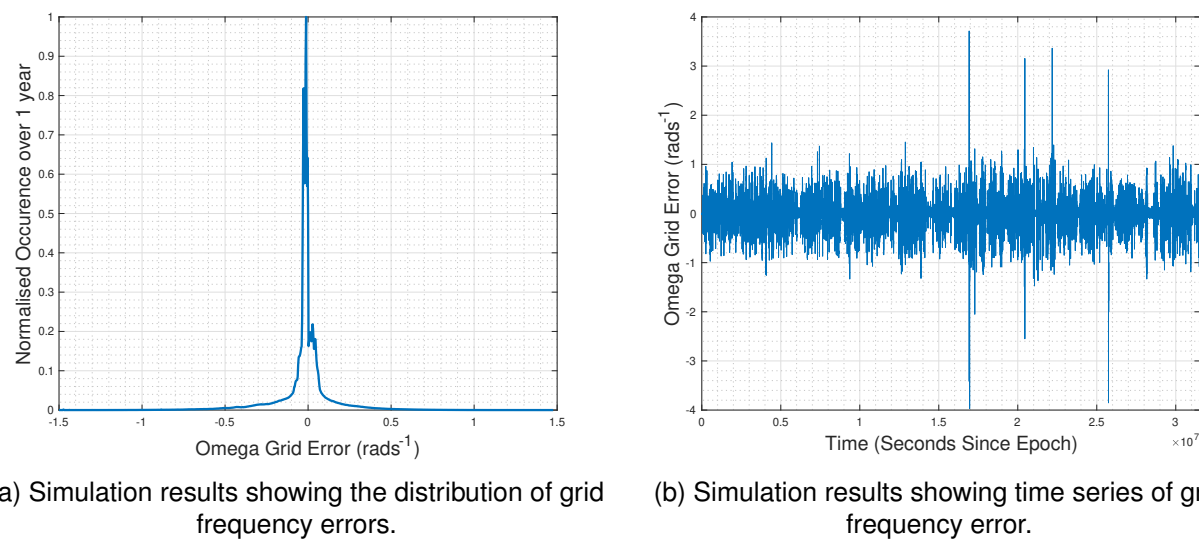
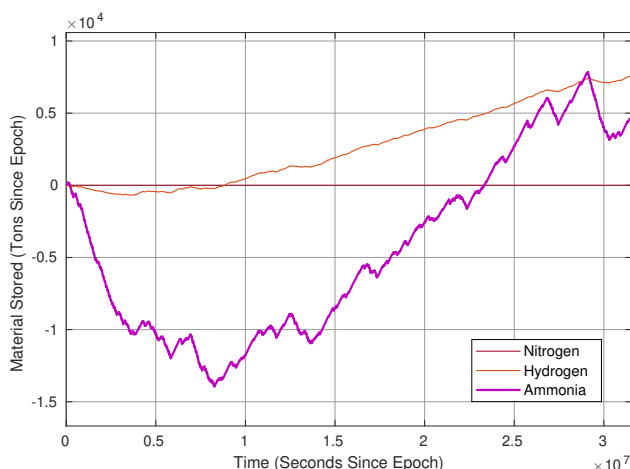
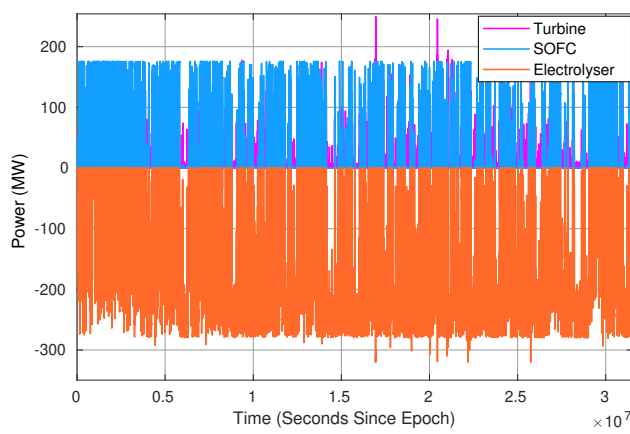


Figure 96: Simulation results from a 365 days of data, **Augmented State LQR in parallel with LQR Applied**.



(a) Simulation results showing material balance for a year.



(b) Simulation results showing component utilisation for a year.

Figure 97: Simulation results from a 365 days of data, **Augmented State LQR in parallel with LQR Applied.**

To conclude this section, the Linear Quadratic Regulator was a good candidate for controlling the plant, which appears viable given the year's material balance from the simulations run.

9.11 Secondary Controller - Virtual Inertia

9.11.1 Reason For Implementation

As discussed through this section, electrical grids require an 'inertial component' to reduce the bandwidth and aid in achieving stability of the system. Another way of looking at inertia is as a stored energy in the rotating generation units, this interpretation can be used in making an active, inexpensive inertia for the grid.

Implementing real inertia is expensive, as it requires the investment of the mass that will be rotating synchronously with the grid as well as the means of coupling the large inertia to the grid.

Especially problematic are the Wind Turbines and SOFCs, as they produce a DC current which is inverted to make AC for transmission. The power inverter is a switch mode system that has a small inertia, so an active method for increasing inertia is required.

9.11.2 Specification for Implementation

A control system with a battery-bank can be used to feed power into the grid. Batteries are DC units, whereas the grid is AC so an inverter is needed as well.

By re-using Equation 167 it is possible to make a control system that acts as a virtual inertia on the grid [?]. Solutions exist [?] that introduce a virtual inertia to the electrical grid.

The inertia used on the simulation found to give a compromise between fast response and tracking performance was $80 \cdot 10^3 \text{kgm}^2$, which would be used to define the scale of the virtual inertia.

9.12 Operation in Fail-States

When a fault is detected, the component would be taken offline. This removes it from the generated State Space, and means the controller has to adapt to stabilise the dynamics of the plant.

Should a generation-side component fail, the grid is at risk of not having enough energy and frequency dropping to dangerous levels. For this reason, the SOFCs and Turbine are paralleled, such that a single turbine *can be taken offline*, as more are able to step in and ensure operation.

Should all of one type of generation-side component fail, for example the SOFC, the turbine will have to make up all the load deficit. The turbine was not designed to have integral action, so there will be a proportional frequency error if another controller doesn't introduce integral action. Therefore failure detection should be used (through a Kalman filter as suggested by [?]) which will trigger the action of an integrator on the turbine.

Should a single electrolyser fail the remainder of active cells will consume the required amount of energy to sustain correct frequency. Should all the electrolyser units fail, the plant will have to dump power from the grid to prevent the frequency rising and damaging domestic equipment. This can be achieved by a *load bank* which is nothing more than an array of actively cooled resistors. Such systems are available for purchase and an example found can continuously dissipate 1MW [?].

Since simulations found a maximum net power on the grid of 250MW, 300 such resistive load dumps would be needed (safety factor of 1.2). The control signal from the electrolyser can be redirected to the load dumps, as they have a comparable response time.

Should a catastrophic failure occur causing the plant to not keep up with demand, *load shedding* will happen, which is a protective method to keep some of the grid alive and prevent a *black start*. This is discussed in more detail in section 9.13.3.

9.13 Risks and Challenges

9.13.1 Solar Power

Solar panel adoption in the United States is increasing year-upon-year, which (depending on solar isolation) can cause 'back-feed' events occurring like in Figure 98. An Energy Storage System would benefit in this case as the energy back-fed can be stored for later usage, in a similar way to

how the wind turbines perform. The challenge associated with this model is that since wind and load effects were considered, the MPC's disturbance prediction would have to incorporate the power supplied by solar panels as well, to ensure accurate control. As visible on the Figure 98, this is changing significantly every year, so more research would be required for this case. Another implication is that fewer wind turbines would be required, and the plant may end up generating excess Hydrogen and Ammonia.

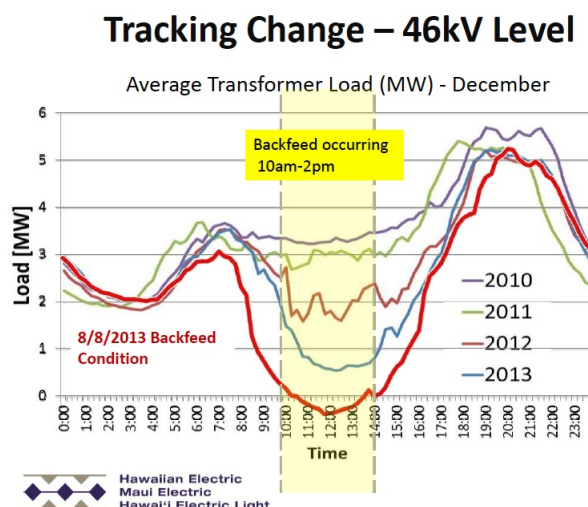


Figure 98: The Effect of Increased Solar Adoption [?]

9.13.2 Modelling Errors

The model developed in Section 9.5 is by no means a fully-accurate model of the plant. More work will have to be done in constructing deep models of each component for the removal of the bulk of the errors. Some other, not fully explored errors also include: Demand data was also approximated with cubic splines to give higher resolution data for simulation. Wind speed was approximated with cubic splines so better data at a higher resolution are required to form a more accurate model. Wind turbine dynamics were approximated as steady state for all wind speeds and the coupling to the grid was assumed to be perfect. A better understanding on how components couple to the electrical grid is crucial for this project to be better understood and more accurate.

9.13.3 Grid Black-start

Should an event occur that knocks the grid offline, a *black-start* will be required. This is challenging as the full 230MW grid load will be drawing power at the same time, and the act of switching on the power is a step request (which acts at a high bandwidth). Black-starts therefore take on the order of days to execute, in the UK the Restoration Time for 60% of the grid's demand is 24 hours [?].

A protocol would have to be written to deal with this rare but not-impossible risk, to ensure a fast recovery from disaster.

9.14 Conclusion

This section on power control and plant simulation was overall successful. The simulation proved useful in obtaining scaling figures for the plant, which were used in other sections, as well as validating the control scheme designed.

The controller survived far harsher conditions than those in reality, so robustness has been tested and the control scheme validated for the simplified case. In the case of real data applied the system, the maximum frequency error delta is no more than 4rads^{-1} which is within desired bounds. The material flows were validated to show the plant's scale is correct to a first order approximation, and the plant is in fact viable for this location.

10 Sustainability

A principal design target for the storage plant was that it must be sustainable. The plant impacts assessed in this section aim to judge if the plant:

Has a minimal environmental impact - this includes low resource consumption, waste, pollutant emission and greenhouse gas emissions.

Has an overall positive social impact - the social value of the plant must exceed the cost.

Issues associated with each design component are covered in their respective sections. This section will summarise these issues and include additional issues associated with the entire plant.

The plant will allow the whole of Maui to switch to a constant source of renewable energy, which currently make up only 24.8% of Maui's energy [?]. This would reduce lifecycle Greenhouse gas (GHG) emissions by up to 700 tonnes CO_2e/GWh [?]. The only direct GHG emissions from the plant are small amounts of NO_x from the gas turbine, which will only run 5% of the time, however there are minor indirect emissions from transport and construction. The waste products of the plant are pure oxygen, nitrogen and water which are not polluting gases. There is also a small amount of CO_2 that comes from the air separator but this comes from the air taken in so does not add net CO_2 to the atmosphere. The main inputs are air and seawater, which are abundant in the plant location. Therefore, the plant represents a large improvement to Maui's current environmental impact.

The construction and operation of the plant will require significant manpower, creating jobs and boosting the local economy of Maui. Residents will also benefit from gaining full access to clean energy and it allows the island to reach its renewable energy target of 100% by 2045 [?]. Although there will be minor visual and noise pollution, there will still be an overall positive societal impact.

11 Plant Safety

Ammonia based energy storage systems possess a many inherent risks, due to their operating conditions and chemical risks of the materials used. Over the past 50 years one major risk has been plant fires despite a steady decreased over time [27][35]. A number of studies have been conducted on the operation and source of risks and failure within Ammonia synthesis plants [27]. Two most high risk processes are hydrogen and ammonia storage and synthesis. In the case of hydrogen, the main factor is the storage of compressed gas. This is due to the risk of explosion of hydrogen gas under high temperature and pressure. Relief valves can be used to prevent over-pressurization and allow the release of gases. However, relief can form of explosive hydrogen gas clouds in certain atmospheric conditions, thus adequate monitoring of valve flow and subsequent ventilation of the outlet gas is required.

Ammonia has a number of chemical effects; whilst it is not considered a flammable hazardous product due to its high autoignition temperature (651 °C) and an explosive limit of 16-25% [27], the first of these being its corrosivity to many metals and alloys including copper and zinc, this means that any storage, piping or fittings to come into contact with ammonia should be made only from iron and steel as these do not suffer from ammonia corrosion. Despite its lower density than air evidence suggests that the formation of ammonia gas clouds at ground level is possible in certain environmental conditions [13]. These are largely dependent on wind speed and humidity. The impact of such releases can be varied, and the number of fatalities does not appear to correlate strongly to the amount of ammonia released. A 1400 ton release of ammonia in Lithuania (1989), the largest ever recorded, resulted in a 400km² affected area and a fatality rate of 7 people, whilst a 38 ton release of ammonia in South Africa (1973) resulted in 18 fatalities, the highest recorded involving ammonia. This was due to the proximity of a urban population, the speed of ammonia release - caused by brittle fracture - and the environmental conditions at the time[27]. Gaseous ammonia can cause severe irritation to the eyes, nose throat and lungs at high enough concentrations whilst contact with liquid ammonia can cause cryogenic burns. The main hazards associated with the levels of toxicity of ammonia and the levels of ammonia associated with each hazard are presented below.

Further information on the impact of exposure to ammonia can be found in the Acute Exposure Guideline Levels (AEGS) [25]. In order to minimise the hazards caused by ammonia release, a number of methods are available. The first of these is the positioning of the discharge valve sufficiently high above ground level to allow any high concentrations releases of ammonia to dilute.

Table 57: Ammonia exposure concentration hazards

Hazard	Concentration (PPM)
Threshold limit value (TLV)	25
Short term exposure limit (STEL)	35
Immediately dangerous to life and health (IDLH)	300
Severe eye and respiratory irritation - Permanent damage	400-700
Convulsive coughing and bronchial spasms	1700
Life threatening	2500
Death from suffocation	5000-10000

Furthermore, the installation of a mist extractor prevents liquid droplets of ammonia being released. This is needed as ammonia is toxic in water ecosystems, a 600 ton spill in Arkansas, USA (1971) resulted in the death of thousands of fish [27].

Despite these measures perhaps the most effective way of minimising the long-term risks is to limit the amount of gas released the plant. This can be done by recycling streams. In the case of the purge a membrane unit to recover hydrogen. In the ammonia storage tank vented gas is recycled through a refrigeration loop. The ammonia storage tank must be located outside of any plant buildings and at away from any densely populated urban areas. potable water sources and clear of any combustible materials. The site must be easily accessible by road to emergency vehicles and personnel. During any unattended operation constant monitoring of all liquid and vapour levels must take place.

References

- [1] L. Aparicio and J. Dumesic. Haber Bosch overall + conv. *Amm. Nitrate Proj.*, 1(9):452, 2008.
- [2] A. Araújo and S. Skogestad. Control structure design for the ammonia synthesis process. *Computers and Chemical Engineering*, 32(12):2920–2932, 2008.
- [3] R. Bañares-alcántara and M. Fiaschetti. Analysis of Islanded Amm.-based Energy Sto. Sys. (Oct.):1–150, 2014.
- [4] J. R. Bartels. A feasibility study of implementing an Ammonia Economy. *Digital Repository @ Iowa State University*, (December):102, 2008.
- [5] V. Belapurkar. Boil-Off in Refrigerated Amm. Tanks. pages 1–4, 2016.
- [6] J. M. Campbell. Gas-Liquid Separators Sizing Parameter. (December 2014):1–16, 2015.

- [7] D. C. Dyson and J. M. Simon. A kinetic expression with diffusion correction for ammonia synthesis on industrial catalyst. *Ind. and Eng. Chem. Fundamentals*, 7(4):605–610, 1968.
- [8] S. S. Elnashaie. Response To Comments On Simulation and Optimization of an Industrial Ammonia Reactor. *Ind. and Eng. Chem. Research*, 28(8):1267, 1989.
- [9] S. S. E. H. Elnashaie, A. T. Mahfouz, and S. S. Elshishini. Digital simulation of an industrial ammonia reactor. *Chemical Engineering and Processing*, 23(3):165–177, 1988.
- [10] S. Ergun and A. A. Orning. Fluid Flow through Randomly Packed Columns and Fluidized Beds. *Industrial & Engineering Chemistry*, 41(6):1179–1184, 1949.
- [11] W. Gellett, S. Szymanski, and P. Onsite. High Efficiency Low Cost Production Electrochemical Ammonia Production. *NH3 Fuel Conference, CA*, 2016.
- [12] L. J. Gillespie and J. A. Beattie. The thermodynamic treatment of chem. equilibria in systems comp. of real gases. *Jou. of the Amer. Chem. Soc.*, 52(11):4239–4246, 1930.
- [13] R. F. Griffiths and G. D. Kaiser. Production of dense gas mixtures from ammonia releases. *Jnl. of Haz. Mat.*, 6(1-2):197–212, 1982.
- [14] U. Guacci, F. Traina, G. Buzzi Ferrarla, and R. Barisone. On the Apln. of the Temkin Eqn. in the Eval. of Cat. for the Amm. Synt. *Ind. and Eng. Chem.*, 16(2):166–176, 1977.
- [15] V. Hacker, , K. Kordesch, and W. Vielstich. Amm. crackers. *Facilities*, 3:121–127, 2003.
- [16] A. M. Howatson, P. G. Lund, and J. D. Todd. Engineering Tables and Data. 1972.
- [17] T. B. Jekel, D. T. Reindl, and J. M. Fisher. Gravity Separator Fundamentals and Design. *Ammonia Refrigeration Convention & Exhibition*, (1998):23, 2001.
- [18] J. R. Jennings. Catalytic Ammonia Synthesis. Fundamentals and Practice. *Springer Science & Business Media*, page 451, 1991.
- [19] A. Jinasena, B. Lie, and B. Glemmestad. Dynamic Model of an Amm. Synt. Reactor Based on Open Inf. *9th EUROSIM Con. on Mod. and Sim. Oulu*, pages 943–948, 2016.
- [20] J. Kim, D. Um, and O. Kwon. Hydrogen production from burning and reforming of ammonia in a microreforming system. *Energy Conversion and Management*, 56:184–191, 2012.
- [21] V. Kyriakou, I. Garagounis, and E. Vasileiou. Progress in the Electrochemical Synthesis of Ammonia. *Catalysis Today*, 286:2–13, 2017.

- [22] H. Liu. Ammonia synthesis catalyst 100 years: Practice, enlightenment and challenge. *Cuihua Xuebao/Chinese Journal of Catalysis*, 35(10):1619–1640, 2014.
- [23] H. Z. Liu, X. N. Li, and Z. N. Hu. Development of novel low temperature and low pressure ammonia synthesis catalyst. *Applied Catalysis A: General*, 142(2):209–222, 1996.
- [24] Meps. Regional Steel Prices & Indices Country Steel Prices Steel Data. pages 1–2, 2018.
- [25] R. Michaels and R. Corp. Emer. Plan.: Crit. Eval. of AEGLs for Amm. 17(2):179–, 1998.
- [26] E. R. Morgan. Techno-Economic Feasibility Study of Ammonia Plants Powered by Offshore Wind. *University of Massachusetts - Amherst, PhD Dissertations*, page 432, 2013.
- [27] M. Ojha and A. K. Dhiman. Problem , Failure and Safety Analysis of Amm. Plant : a Review. *Int. Review of Chem. En.*, 2(October):631–646, 2010.
- [28] M. Penkuhn and G. Tsatsaronis. Comparison of different amm. synt. loop configurations with the aid of advanced exergy analysis. *Energy*, 137:854–864, 2017.
- [29] N. Pernicone, F. Ferrero, I. Rossetti, L. Forni, P. Canton, and P. Riello. Wustite as a new precursor of industrial amm. synt. cat. *App. Catalysis A: General*, 251(1):121–129, 2003.
- [30] A. Plus. Aspen Plus Ammonia Model. 2008.
- [31] J. A. S. Richard Turton, Richard C. Bailie, Wallace B. Whiting. *Analysis, Synthesis and Design of Chemical Processes Third Edition*, volume 53. 2013.
- [32] I. Rossetti, N. Pernicone, F. Ferrero, and L. Forni. Kinetic study of ammonia synthesis on a promoted Ru/C catalyst. *Ind. and Eng. Chem. Research*, 45(12):4150–4155, 2006.
- [33] Since Gas. Automatic Ammonia Cracker for Hydrogen Generation. pages 4–6, 2018.
- [34] M. Souders and G. G. B. Design of Fractionating Columns: I. Entrainment and Capacity. *Ind. and Eng. Chem.*, 26(1):98–103, 1934.
- [35] G. P. Williams. Safety perf. in amm. plants: VI. *Proc. Saf. Prog.*, 18(2):78–81, 1999.

12 Overall Financial Analysis

Initial Capital Investment

The cost estimations for the plant were performed using the 'Total Purchasing Cost Estimate' (TPCE) method [?]. This calculates values for the various aspects of the plant's construction by scaling them relative to the purchase price of the major plant components. Table 58 shows the purchase prices of the main plant components, and Table 59 shows the various scaling factors chosen. In the interest of a conservative estimate, the largest scaling factors were taken from the range of values given.

Table 58: Purchase Cost of major plant components (data sourced from previous sections)

Component	Price (Millions of USD)
Electrolyser	15.8
Cryo Separator	9.40
Reactor	15.48
Main Turbine	75.60
HEX Net	0.24
Wind Farm	975.00
SOFC/GT system	987.91
TOTAL COST	2079.43

Table 59: Values calculated by TPCE method

Expense	% TPCE	Cost (Millions of USD)
Purchase	100	2079.43
Installation	14	291.12
Instrumentation	8	166.35
Piping	20	415.89
Electrics	10	207.94
Building	18	374.30
Yard Improvement	5	103.97
Service Facilities	20	415.89
Land	2	41.59
TOTAL DIRECT COST	197	4,096.48
Engineering Supervision	21	436.68
Construction Expenses	14	291.12
TOTAL INDIRECT COST	35	727.80
Contractors fee	14	291.12
Contingency	35	727.80
FIXED CAPITAL INVESTMENT	281	5,853.20
Working Capital	42	873.36
TOTAL CAPITAL INVESTMENT	323	6,716.56

Operating Costs

The plant operating costs are also calculated using the TPCE method, but with some additional complications. Labour costs are calculated separately, and the values are calculated proportional

to the Total Capital Investment instead of the purchase cost. A summary of the operating costs can be seen in Table 60.

Labour costs were calculated assuming 250 operators are required to be working at the plant at any one time, based on data for a coal power plant of similar power output [?]. This was multiplied by 3 so that every hour of the data would be covered over 8 hour shifts. The average salary for a plant operator in the US was found to be \$70,000 [?]. A total of 750 operators being paid \$70,000 a year results in a cost of \$52.5 million per year. This was multiplied by a safety factor of 10 to account for staff not tied directly to the plant operation, such as administration and security.

The SOFCs must be replaced every 5 years, so this cost will be included in the annual operating costs. This cost is found as the purchase cost for the SOFC system, plus 14% to account for the installation process, spread equally over 5 years. The other expenses from Table 58 are ignored, as these parts are assumed to be covered by the annual maintenance costs.

In Table 60, 'indirect expenses' accounts for administrative, distributing and marketing expenses, while 'general overhead' accounts for property taxes, personal and property liability insurance, maintenance of plant roads, cafeteria expenses, etc.

Table 60: Operating costs for the plant

Annual Expense	Calculation	Cost (Millions of USD)
Labour	Calculated separately	525.00
Supervision	20% of Labour Cost	105.00
Maintenance	6% of TCI	402.99
Indirect Expenses	3% of TCI	201.50
General Overhead	15% of Labour + Supervision + Maintenance	690.45
SOFC Replacement	20% of (Purchase Cost of SOFC + 14%)	225.24
TOTAL	Sum of all values in this table	2,150.18

Financial Overview

The levelised cost of electricity per kWh produced is calculated using Equation 179:

$$\text{Unit Cost of Production} = \frac{\text{Total Operating Cost per Year} - \text{Annual Investment Repayment}}{\text{Total kWh Produced per Year}} \quad (179)$$

The plant produces a total of 1.688×10^{10} kWh every year, and the annual investment repayment is calculated using Equation 180:

$$\text{Annual Investment Repayment} = \text{Total Capital Investment} \times \frac{i(1+i)^n}{(i+1)^n - 1} \quad (180)$$

Where i is the interest rate and n is the repayment period in years. i is assumed to be 10%, to ac-

count for the high risk involved with investing in new technology, and n is taken to be the currently planned lifetime of the plant, 25 years. This results in an annual repayment of \$735.88 million. Using Equation 179, the unit cost of production is found to be \$0.17 per kWh. This is much higher than the average sale price of electricity in the US, at \$0.12 per kWh, but much lower than the average sale price in Hawaii, which is \$0.28 per kWh [?]. This gives a large range of potential sale prices to select, with a very high mark-up being achievable while still being very competitive in Hawaii's energy market. Using an example sale price of \$0.225 per kWh, the forecast is shown in Table 61.

Table 61: Annual Revenue, Cost and Profit for the plant

Sale Price per kWh (USD)	\$0.225
Total Energy produced per year (kWh)	1.688×10^{10}
Annual Revenue (USD)	\$3.798 bn.
Annual Expense (USD)	\$2.890 bn.
Annual Net Profit (USD)	\$0.908 bn.
Total Net Profit after 25 years (USD)	\$22.697 bn.
Return on Investment after 25 years	337.9%

Conclusion

It is clearly demonstrated in the cost analysis that the plant is very profitable. However, this is almost entirely due to Hawaii's uniquely expensive energy market. Hawaii's energy is predominantly produced using petroleum, which has to be imported from the US mainland to Hawaii, 2000 miles away in the Pacific Ocean [?]. This drives up the price per kWh enormously, and so a very lucrative opportunity is created, whereby electricity generated on the island itself can be sold for much higher than cost price. The cost price shown in Table 4 has been chosen conservatively, and could be set much higher for greater profitability.

It is worth noting that the plant, as it has been modelled in this report, would not be feasible on the US mainland due to the relatively high unit cost per kWh. At \$0.17 per kWh (or \$170 per MWh), it is relatively competitive when compared to some other renewable energy sources, such as solar power and offshore-wind farms (without an ESS), as shown in Figure 99. However, it is still much higher than conventional power generation methods, such as coal-fired power stations. Economies of scale can be capitalised on in order to reduce this cost further, by building an even larger plant to cover a larger demand.

Estimated Levelized Cost of New Electric Generating Technologies in 2018 (2011 \$/megawatthour)

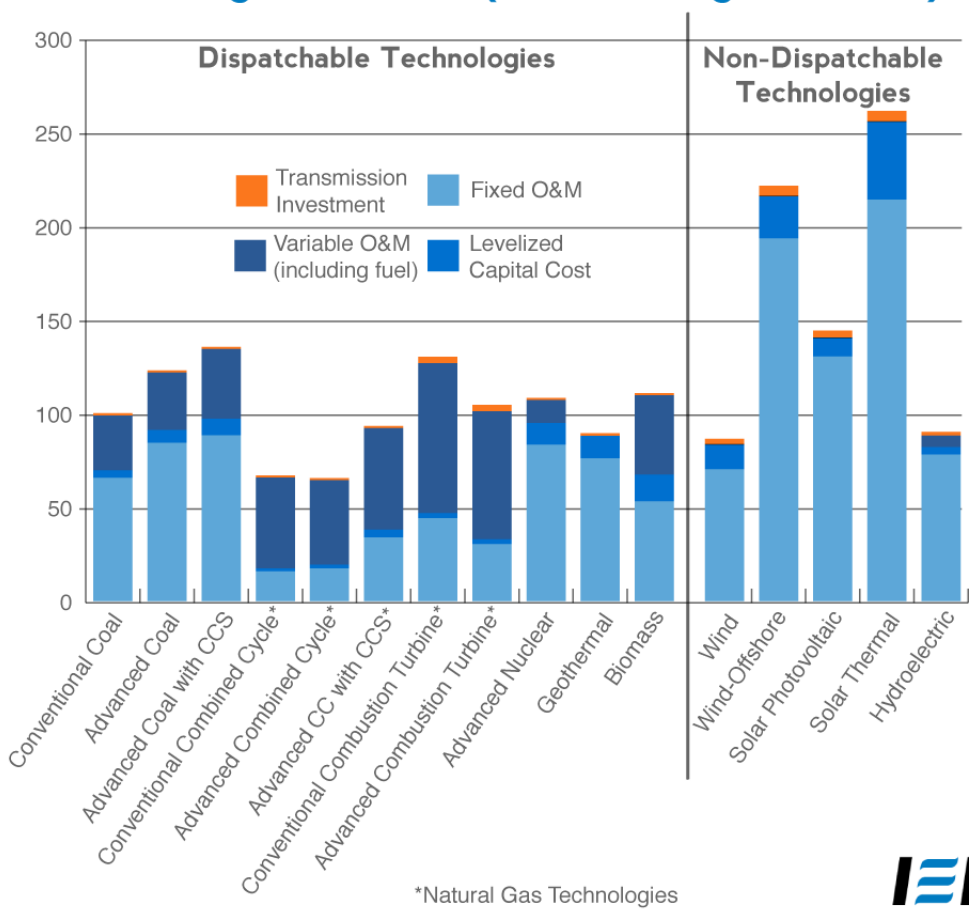


Figure 99: Unit cost of production per MWh for various power generation methods [?]

13 Conclusion

The main objective of this project is to design an ammonia-based ESS to power the island of Maui using wind energy harvested from a windfarm. The plant designed consists of six major components in order to achieve the goal: hydrogen formation by electrolysis of water, nitrogen separation from air by cryogenic distillation, ammonia synthesis by Haber-Bosch process with iron-based catalyst, ammonia gas turbine, solid oxide fuel cell network and power control system. With a planned lifetime of 25 servicing years, the plant is designed to be sustainable and fully self-sufficient. All raw materials are naturally obtainable, and no harmful byproducts are produced or released in waste, purge or exhaust streams.

Meeting the Demand The power demand of Maui is to be met by the application of a hybrid power generation system: SOFCs and gas turbine. Gas turbine (with max power of 270MW) has a much shorter rise time than SOFCs (with max power of 230MW), and can be used as a temporary power supply as SOFCs ramp up. Hence as SOFCs are warming up, gas turbine can smooth out the transition for power generation and accommodate for short-term power spikes; SOFCs can then take over and provide continuous power generation to meet baseline demand. Both units have built-in failsafe capacity and can be ran in conjunction in the event of high power demand, and is therefore sufficient to meet the fluctuating demand profile of 100-190 MW as required.

Material Balance Around 90,000 tpy of ammonia is produced from 74,000 tpy of nitrogen from cryogenic distillation and 16,000 tpd of hydrogen from electrolysis of water, which is stored and later decomposed to release energy. To allow for possibility of demand fluctuation, power demand and ammonia supply are not perfectly matched; a marginal amount of excess ammonia and hydrogen is produced which can be flared to achieve a zero overall material balance.

Sustainability To assess the plant's sustainability, the plant is judged upon two main criteria: environmental impact and societal impact.

With reference to each design component's environmental sustainability assessment:

1. Main inputs are air and seawater, which are abundant and naturally obtainable.
2. Minimal amount of CO_2 produced from separation of air does not contribute towards the increase in net CO_2 level in the atmosphere.

3. Other waste products of the plant are high-purity nitrogen, oxygen and water, and are all non-toxic in nature.
4. The only direct source of Greenhouse gas emission is from the gas turbine, which will only be run 5% of the time.

On the societal side, the construction and operation will create jobs and boost the local economy of Maui, with full access to clean energy available upon the operation of the plant. The plant will allow Maui to reach its renewable energy target of 100% by 2045.

To summarise, the sustainability analysis of the plant has shown that it is highly sustainable, and that it has a minimal environmental impact whilst achieving an overall positive societal impact.

Safety and Risk Due to the operating conditions and chemical risks involved in a plant of this magnitude, safety and risk aspects of individual plant components are carefully considered, researched and presented in their respective "Safety and Risk" sections. HAZOP studies have been conducted to components where applicable, highlighting likely modes of failure as well as devising counter-measures to reduce the risks.

Financial Analysis The cost estimations for the plant are performed using the 'Total Purchasing Cost Estimate'. Total purchase cost of major plant components and various aspects of the plant's construction and cost of operation are estimated to be \$6680 million, with the largest shares of component purchase cost from the windfarm and SOFCs at around \$1000 million individually. Levelised cost of electricity is \$0.17 per kWh of electricity produced, which is relatively competitive compared to the average sale price of \$0.28 per kWh in Hawaii, despite being much higher than US national average of \$0.12 per kWh. The financial analysis of the plant has shown that it is highly feasible for the location chosen, and that it is relatively competitive compared to alternative renewable energy sources.

Future Research Analysis of the proposed design showed that the project is highly feasible in areas of meeting power demand, sustainability and profit turning. In reality, EES of this scale is highly complex and will require more in-depth and rigorous investigation, e.g. refined controller design, more accurate thermodynamic and box emission assessment. This report offers an idealistic design draft of ESS, such that a more intricate design can be pursued in the future.